Ultrafast dynamics of coherent intersubband polarizations in quantum wells and quantum cascade laser structures

DISSERTATION

zur Erlangung des akademischen Grades
doctor rerum naturalium
(dr. rer. nat.)
im Fach Physik

eingereicht an der
Mathematisch-Naturwissenschaftlichen Fakultät I
Humboldt-Universität zu Berlin

von
Herrn Dipl.-Phys. Felix Eickemeyer
geborem am 03.01.1973 in Heidelberg

Präsident der Humboldt-Universität zu Berlin:
Prof. Dr. J. Mlynek

Dekan der Mathematisch-Naturwissenschaftlichen Fakultät I:
Prof. Dr. M. Linscheid

Gutachter:

1. Prof. Dr. Thomas Elsässer
2. Prof. Dr. Klaus Ploog
3. Prof. Dr. Manfred Helm

eingereicht am: 27. Mai 2002
Tag der mündlichen Prüfung: 3. Juli 2002

Abstract

In this thesis we investigate the ultrafast dynamics of carriers and coherent intersubband polarizations in quasi-two-dimensional semiconductor nanostructures and devices. In particular, we study n-type modulation doped multiple quantum wells and quantum cascade laser structures based on the GaAs/AlGaAs material system using ultrafast spectroscopy in the mid-infrared spectral range (3-20 mu). A novel experimental setup is developed allowing for the first time the controlled phase and amplitude shaping of ultrafast field transients in the mid-infrared wavelength range.

We study the feasibility of coherent nonlinear control of intersubband polarizations. Amplitude and phase-controlled mid-infrared field transients from our new laser source induce resonant intersubband excitations in n-type modulation doped GaAs/AlGaAs quantum wells. The transmitted electric field transients are directly measured by ultrafast electro-optic sampling. We demonstrate for the first time coherent control of linear intersubband polarizations with subpicosecond dephasing times by applying two phase-locked pulses with variable relative phase. A saturation of the intersubband excitation by more than 0.2 is achieved with mid-infrared pulses of only 1 pJ pulse energy.

We present for the first time a direct time-resolved experimental study on electrically driven quantum cascade laser structures. These studies provide insight into the dynamics of electron transport, which can not be obtained by stationary measurements. The ultrafast quantum transport of electrons from the injector through the injection barrier into the upper laser subband is investigated in femtosecond mid-infrared pump-probe experiments. In this way we directly monitor the ultrafast saturation and subsequent recovery of electrically induced gain. For forward bias and spectral positions around the gain maximum we observe pronounced gain oscillations. This gives direct evidence for a coherent wave packet motion from the injector into the upper laser subband via resonant tunneling even at the high electron density present in a quantum cascade laser structure. After saturation the electrically induced gain is completely recovered within 1 ps at low lattice and carrier temperatures.

Keywords:
ultrafast spectroscopy, semiconductor, nanostructure, intersubband, quantum cascade laser, electron transport, resonant tunneling, quantum well, coherent control, mid-infrared, pulse shaping

Kurzfassung

In dieser Arbeit untersuchen wir die ultraschnelle Dynamik von Ladungsträgern und kohärenten Intersubbandpolarisationen in quasi-zweidimensionalen Halbleiternanostrukturen und Halbleiterbauelementen. Insbesondere werden n-Typ modulationsdotierte multiple Quantentöpfe und Quantenkaskadenlaserstrukturen basierend auf dem Materialsystem GaAs/AlGaAs mit der Methode der ultraschnellen Spektroskopie im mittleren Infrarot (3-20 mu) studiert. Ein neuartiger experimenteller Aufbau ist entwickelt worden, der zum ersten Mal das phasen- und amplitudenkontrollierte Formen von ultraschnellen Feldtransienten im mittelinfraroten Spektralbereich erlaubt.

Wir untersuchen die Möglichkeit der kohärenten Kontrolle von Intersubbandübergängen. Amplituden- und phasenkonntrollierte Feldtransienten im mittleren Infrarot, die mit unserer neuen Laserquelle erzeugt werden, induzieren resonante Intersubbandanregungen in n-Typ modulationsdotierten GaAs/AlGaAs Quantentöpfen. Die transmittierten elektrischen Feldtransienten werden mit Hilfe des ultraschnellen elektro-optischen Abtastverfahrens gemessen. Unter Anwendung zweier phasengekoppelter Mittinfarotpulse variabler relativer Phase zeigen wir erstmalig die kohärente Kontrolle an linearen Intersubbandpolarisationen mit Dephasierungszeiten unterhalb einer Pikosekunde. Eine Sättigung von mehr als 0.2 wird bei einer Mittinfrarotpulsenergie von nur 1 pJ erreicht.

Es wird erstmalig ein direktes, zeitaufgelöstes Experiment an elektrisch betriebenen Quantenkaskadenstrukturen vorgestellt. Diese Untersuchung ermöglicht den Einblick in die Dynamik des Elektronentransports, der mit stationären Methoden nicht meßbar ist. Der ultraschnelle Quantentransport der Elektronen vom Injektor durch die Injektionsbarriere in das obere Lasersubband wird in Femtosekunden-Mittinfrarot-Anreg-Abtast-Experimenten untersucht. Auf diese Weise beobachten wir die ultraschnelle Sättigung und die nachfolgende Wiederherstellung des elektrisch induzierten Gains. Wir beobachten ausgeprägte Gainoszillationen bei angelegtem Vorwärtsstrom und an spektralen Positionen am Gainmaximum. Dies ist ein direkter Beweis für eine kohärente Wellenpaketspropagation vom Injektor in das obere Lasersubband mittels resonantem Tunneln trotz der hohen Ladungsträgerdichte in Quantenkaskadenlasern. Nach der Sättigung ist der elektrisch induzierte Gain bei niedrigen Gitter- und Ladungsträgertemperaturen innerhalb einer Pikosekunde vollständig wiederhergestellt.

Sclagwörter:
ultraschnelle Spektroskopie, Halbleiter, Nanostruktur, intersubband, Quantenkaskadenlaser, Elektronentransport, resonantes Tunneln, Quantentopf, kohärente Kontrolle, mittleres Infrarot, Pulsformung

Contents

Chapter 1

Introduction

One of the most significant directions in semiconductor physics in the last decades has been the progressive miniaturization of devices. On one hand this has led to the explosive growth in computer technology. On the other hand, the opportunity to fabricate structures with characteristic dimensions on the nanometer length scale has led to the investigation of a whole range of novel physical phenomena. Such physical phenomena gave and still give rise to new generations of devices, which rely on completely different physical principles than their predecessors.

A very important class of nanometric structures are the quasi-two dimensional semiconductor nanostructures [1]. These structures consist of two different semiconductor materials, which are deposited alternately on each other. The technical development of growth techniques allows one to control the thicknesses of these layers within one atomic monolayer. In this way, potential wells and barriers in the conduction and valence band along the stack axis are formed resulting in two-dimensional carrier confinement within the plane of the layers. As a consequence, the quantization of electronic states leads to a series of valence and conduction subbands with energy spacings much smaller than the fundamental bandgap.

These subbands give rise to low-energy optical excitations between consecutive valence or conduction subbands, so-called intersubband transitions. The transition energies are located in a range corresponding to the infrared wavelength range ($\lambda = 1.5$–100 μm). This spectral regime is of large technical interest. Many important gases, from byproducts of fossil fuel burning to constituents of human breath, have characteristic absorption lines in the mid-infrared ($\lambda = 3 - 20\,\mu$m) as a result of molecular rotational-vibrational transitions. Another important example is free-space optical data communication, which is possible in the so-called atmospheric windows around wavelengths of 5 and 10 μm. Hence, an important goal in semiconductor research is to exploit the optical properties of semiconductor nanostructures to develop new opto-electronic device structures. Two of the most successful devices based on intersubband transitions are long-wavelength photodetectors [2] and electrically pumped, unipolar semiconductor lasers, called quantum cascade lasers [3].

A prerequisite for further performance improvements of existing devices and the development of future applications is a thorough understanding of the mechanisms governing the optical and electronic properties of semiconductor nanostructures. Since the timescale of the interactions among the carriers and between the carriers and the lattice is as short as a few femtoseconds ($1\,\text{fs} = 10^{-15}$ s), ultrafast nonlinear spectroscopy represents a suitable means of investigating these processes [4]. Ultrafast spectroscopy allows for the preparation of a well-defined nonequilibrium state and the subsequent real-time monitoring of the relaxation into the initial state on a femtosecond time scale. This nonlinear technique has provided deep insight into the fundamental relaxation dynamics of intersubband excitations [5]. Those studies are elemental for further investigations concerning existing device structures and possible device applications.

Femtosecond spectroscopy in the mid-infrared spectral range has recently attracted considerable interest in the ultrafast community since it has a broad potential for the study of the ultrafast dynamics of elementary excitations in condensed matter [6, 7]. The ultimate goal of such investigations is not only to initiate and probe ultrafast dynamics, but to coherently control the dynamics of such elementary excitations [8, 9]. This requires amplitude and phase control of the excitation pulses. So far, however, it was not possible to carry out coherent control experiments in the mid-infrared spectral range because a suitable light source for shaped mid-infrared pulses was lacking. In this thesis we present the first tabletop system including a laser light source, which allows for a controlled amplitude and phase shaping, and a full characterization of the generated electric field transients.

This thesis is further aimed to investigating two different two-dimensional semiconductor nanostructures using the methods of ultrafast spectroscopy:

(i) Ultrafast coherent control of intersubband transitions in quantum wells

Intersubband transitions in quantum wells display very high absorption cross sections of up to 10^{-13} cm^2 and—for an energy separation larger than an optical phonon—a carrier lifetime in the excited subband between several hundreds of femtoseconds and a few picoseconds [5]. These properties make intersubband transitions in quantum wells interesting for optical switching. Ultrafast switch on and switch off times should be attainable by coherent control of optical polarizations within their dephasing time without being limited by the longer carrier relaxation times. In this thesis, we study the feasibility of coherent nonlinear control of intersubband polarizations in GaAs/AlGaAs quantum wells by weak ultrashort electric field-transients. Coherent polarizations on the transition between the $n = 1$ and $n = 2$ conduction subband are generated by shaped mid-infrared transients at a megahertz repetition rate and their coherent emission is amplitude- and phase-resolved by electro-optic sampling.

(ii) Electron transport in quantum cascade structures

A milestone in semiconductor nanophysics was the development of the quantum cascade laser [3]. It represents the first unipolar laser light source based on optical intersubband transitions in a coupled multiple quantum well structure. The quantum cascade laser is an electrically driven laser where electrons cascade down a potential staircase. Thereby the electrons sequentially pass so-called injector regions, which act as an electron reservoir, and active regions, which represent a three-level laser system. Since its invention, tremendous performance improvements have been attained, e. g., continuous wave operation at room temperature [10]. Very recently the first quantum cascade laser has been developed emitting in the Terahertz spectral regime [11].

Although the design and production of these structures have reached a high degree of sophistication, direct experimental information on the microscopic mechanisms is still poor. An important issue is the transport of electrons from the injector into the active region. Optimum design strategies try to enhance the injector–active region coupling via resonant tunneling and, at the same time, to prevent the carriers from propagating into the continuum [12]. The underlying physical picture relies on coherent electron transport, which, however, has not yet been demonstrated experimentally. From a theoretical point of view, the degree of coherence in quantum transport is determined by the interplay between electron wave packet propagation and dissipative scattering processes [13]. Thus, a detailed investigation of the ultrafast gain dynamics provides better insight into the quantum cascade laser physics.

So far, a direct time-resolved experimental characterization of electrically driven quantum transport—which represents a quasi-stationary *nonequilibrium* state of the electron gas—has not been performed. We want to emphasize that this situation differs strongly from the well-studied motion of electron wave packets that have been impulsively photo-excited from an *equilibrium* initial state of matter (e. g., Bloch oscillations [14]). In this thesis, we present the first direct time-resolved experimental study of the quantum transport of electrons from the injector into the active region of a quantum cascade laser structure.

This thesis is organized as follows. In chapter 2 we briefly introduce the methods of ultrafast spectroscopy which we will focus on. Then we discuss the schemes for the generation and characterization of femtosecond mid-infrared pulses. Subsequently, we present our new method of shaping ultrafast mid-infrared pulses. In chapter 3 we give an introduction to the optical and electronic properties of quasi-two-dimensional heterostructures. A review from literature is provided concerning the ultrafast dynamics of intersubband excitations and vertical electron transport. In chapter 4 we investigate the feasibility of coherent control in multiple quantum well structures. The presentation of single pulse and phase-locked pulse pair experiments is followed by a detailed qualitative and quantitative analysis of the data. Chapter 5 deals with the development of an experimental technique to combine ultrafast spectroscopy with high-current electrical pumping of semiconductor device structures. As a first application we present a linear transmission change experiment to measure the spectral characteristics of the current-induced optical gain of the investigated quantum cascade structure. These studies represent the basis for the electron transport experiment carried out in chapter 6. In this chapter time-resolved transmission change studies are presented on various quantum cascade structures. A detailed analysis of the data follows which aims to determine the characteristics of electron transport in such structures.

Chapter 2

Ultrafast spectroscopy in the mid-infrared spectral range

In this chapter, we discuss the technological aspects for ultrafast spectroscopy in the mid-infrared spectral range. This method has a broad potential for time-resolved investigations of phenomena in condensed-matter since numerous elementary excitations exist in this low-energy range. Recently, ultrafast time-resolved mid-infrared studies on such diverse systems as liquid water [15], peptides [16], high-temperature superconductors [17], and semiconductor nanostructures [18] have been carried out. For the coherent control of the excitations in these systems, which is of great fundamental and technical interest [8, 9], a light source is required allowing for the controlled shaping and full characterization of ultrashort mid-infrared pulses. Here, we present a new light source for the generation, shaping, and complete characterization of femtosecond mid-infrared field transients.

After a brief introduction to the basic theoretical concepts we start with the presentation of the time-resolved experimental techniques used in this thesis. Next, we provide a comprehensive description of the generation, shaping, characterization, and theoretical analysis of femtosecond mid-infrared pulses.

2.1 Electromagnetic waves and nonlinear optics

The interaction of a light field $\vec{E}(\vec{r},t)$ with matter leads to a polarization $\vec{P}(\vec{r},t)$ which acts as a source for a new electromagnetic wave. For the phenomena discussed in this thesis the classical, i.e., non-quantized description of electromagnetic waves is appropriate and sufficient. The wave equation reads:

$$\nabla \times \nabla \times \vec{E} + \frac{1}{c^2}\frac{\partial^2 \vec{E}}{\partial t^2} = -\frac{1}{\epsilon_0 c^2}\frac{\partial^2 \vec{P}}{\partial t^2} \tag{2.1}$$

In most cases one can expand P into a power series of the electric field:

$$\vec{P}(\vec{r},t) = \vec{P}^{(1)}(\vec{r},t) + \vec{P}^{(2)}(\vec{r},t) + \vec{P}^{(3)}(\vec{r},t) + ...$$

where

$$P_i^{(1)}(t) \;=\; \int_0^\infty \chi_{ik}^{(1)}(\tau)\, E_k(t-\tau)\, d\tau$$

$$\begin{aligned} P_i^{(2)}(t) &= \int_0^\infty \int_0^\infty \chi_{ikl}^{(2)}(\tau_1, \tau_2)\, E_k(t-\tau_1)\, E_l(t-\tau_2)\, d\tau_1\, d\tau_2 \\ &\vdots \end{aligned}$$

$\chi^{(1)}$ is the linear optical susceptibility tensor in the time representation, $\chi^{(2)}$ is the second-order nonlinear optical susceptibility tensor, and so forth. For frequencies far away from any resonance the susceptibilities become quasi-instantaneous and can be approximated by a delta function. This corresponds to frequency independent susceptibilities in the frequency representation, e.g., $d^{(2)}(\omega_1, \omega_2) = const.$ Effects like difference-frequency mixing and the electro-optic effect, which will play an important role later on, are treated within this regime. In the vicinity of a resonance, however, a closer look on the interacting medium is needed and the quantum mechanical apparatus has to be applied. In the next section we will give an example where the resonant medium is described as a quantum mechanical two-level system.

Often, it is useful to rewrite the wave equation (2.1) by splitting the polarization into a resonant part $\vec{P}_{Res}$ and a part resulting from the linear interaction with the host medium $\vec{P}_H$

$$\vec{P} = \vec{P}_H + \vec{P}_{Res}$$

P_H gives rise to the "background" refractive index $n(\omega)$. Next, we split the electric field and the polarization field into a slowly varying amplitude and a plane wave at the center frequency Ω

$$\begin{aligned} \vec{E} &= \frac{1}{2}\, \vec{E}(z,t)\, e^{i(\Omega\, t - k(\Omega)\, z)} + cc. \\ \vec{P} &= \frac{1}{2}\, \vec{P}(z,t)\, e^{i(\Omega\, t - k(\Omega)\, z)} + cc. \end{aligned}$$

where $k(\Omega) = \frac{n(\Omega)}{c}\,\Omega$. Considering transverse, plane waves propagating in z direction and using the slowly varying amplitude approximation the wave equation (2.1) yields [19]

$$\left(\frac{\partial}{\partial z} + \frac{1}{v_{gr}(\Omega)} \frac{\partial}{\partial t} \right) E(z,t) = i\, \frac{\Omega}{2\, \epsilon_0\, c\, n(\Omega)}\, P_{Res}(z,t) \tag{2.2}$$

where v_{gr} is the group velocity defined by

$$\frac{1}{v_{gr}(\Omega)} = \left. \frac{dk(\omega)}{d\omega} \right|_{\omega=\Omega}$$

2.1.1 Coherent interaction of light with a two-level system

In this section we discuss the resonant interaction of light with a medium which can be described as a quantum mechanical two-level system. The system consists of the ground state $|0\rangle$ and the excited state $|1\rangle$ which are the eigenstates of the system Hamiltonian H_0

$$\begin{aligned} H_0\, |0\rangle &= \hbar\, \omega_0\, |0\rangle \\ H_0\, |1\rangle &= \hbar\, \omega_1\, |1\rangle \end{aligned}$$

An appropriate formalism allowing for a statistical description of the two level system is the density matrix formalism [20, 21, 22, 23]. The density matrix is the operator

$$\rho = \sum_{m,n} p_{mn}\, |m\rangle\langle n| \ , \quad m,\, n \,\epsilon\, \{0, 1\}$$

The diagonal elements of the density matrix denote the occupations in states $|0\rangle$, $|1\rangle$ ($p_{00} + p_{11} = 1$) and the non-diagonal elements describe the polarizations, i.e., the coherent superpositions of states $|0\rangle$ and $|1\rangle$. The expectation value of an observable A is the trace of $\rho\, A$

$$\langle\, A \,\rangle = \mathrm{Tr}\,(\rho\, A)$$

The time evolution of the density matrix is described by the von Neumann equation [20]

$$\frac{\partial\, \rho(t)}{\partial\, t} = -\,\frac{i}{\hbar}\,[\, H_0 + V(t)\,,\, \rho(t)\,] - \hat{\Gamma}\Big(\rho(t) - \rho(-\infty)\Big) \tag{2.3}$$

$V(t)$ is the interaction term describing the interaction of the two-level system with the electromagnetic wave $E(t)$ by the dipole operator $\hat{\mu}$ and the dipole moment μ

$$V(t) = -\hat{\mu}\, E(t)\;, \quad \hat{\mu} = \begin{pmatrix} 0 & \mu \\ \mu & 0 \end{pmatrix}\;, \quad \rho(-\infty) = \begin{pmatrix} 1 & 0 \\ 0 & 0 \end{pmatrix} \text{ for } T \to 0$$

The relaxation term $\hat{\Gamma}(\rho)$ describes phenomenologically the scattering processes between states $|0\rangle$, $|1\rangle$ and the host medium, which leads to depopulation of the excited state with the lifetime T_1 and to dephasing of the polarizations with a phase relaxation time T_2

$$\hat{\Gamma}(\rho) = \begin{pmatrix} \frac{\rho_{00}}{T_1} & \frac{\rho_{10}}{T_2} \\ \frac{\rho_{01}}{T_2} & \frac{\rho_{11}}{T_1} \end{pmatrix}$$

Dephasing consists of two contributions, the dephasing due to depopulation and a pure dephasing described by T_2^*:

$$\frac{1}{T_2} = \frac{1}{T_2^*} + \frac{1}{2\,T_1}$$

The scattering mechanisms leading to depopulation and dephasing have to be considered in more detail for the particular system under investigation.

Up to now, we have presented the main equations which can be used to calculate the time evolution of the two-level system under the influence of an electromagnetic wave. Under certain conditions these equations can be simplified. First, we assume that the light field is nearly resonant with the $|0\rangle$–$|1\rangle$ transition, i.e., $\Delta\omega \equiv \Omega - (\omega_1 - \omega_0) \ll \Omega$. Next, we split the expectation value for the dipole operator in a slowly varying and an oscillatory part

$$\langle\, \hat{\mu}\,\rangle = \frac{1}{2}\,\langle\, p\,\rangle\, e^{i(\Omega\, t - k\, z)} + cc.$$

We identify the polarization P_{Res} and the occupation of the upper state n_{ex} with the quantities defined above in the following way:

$$P_{Res} = N_0\,\langle\, p\,\rangle\;, \quad n_{ex} = \rho_{11}$$

where N_0 is the carrier density. Finally, we apply the rotating wave approximation neglecting the high frequency terms [24] to get the Maxwell-Bloch equations:

$$\left(\frac{\partial}{\partial\, z} + \frac{1}{v_{gr}(\Omega)}\,\frac{\partial}{\partial\, t}\right) E \;=\; i\,\frac{\Omega}{2\,\epsilon_0\, c\, n(\Omega)}\, P_{Res} \tag{2.4}$$

$$\left(\frac{\partial}{\partial\, t} + \frac{1}{T_2} - i\,\Delta\omega\right) P_{Res} \;=\; i\,\frac{\mu^2\, N_0}{\hbar}\, E\,(1 - 2\, n_{ex}) \tag{2.5}$$

$$\left(\frac{\partial}{\partial\, t} + \frac{1}{T_1}\right) n_{ex} \;=\; i\,\frac{1}{4\,\hbar}\,(E\, P_{Res}^* - E^*\, P_{Res}) \tag{2.6}$$

These coupled differential equations describe the time evolution of the electric field and the two-level system. We will use them later in the discussion of the coherent nonlinear propagation of ultrafast electric field transients through intersubband resonances.

2.1.2 Pump-probe spectroscopy

The experimental technique used in this thesis to investigate the ultrafast dynamics of carriers and coherent polarizations in semiconductor nanostructures and devices is the time-resolved or pump-probe transmission spectroscopy. Such an experiment is shown schematically in Fig. 2.1.

An intense light pulse (pump) excites the sample in a defined nonequilibrium state. This causes a change of the optical properties of the sample. A weak probe pulse subsequently measures the transmission as a function of the time delay t_D between the pump and probe pulses. The temporal resolution of the experiment for an optically thin sample is determined by the pulse lengths of the pump and probe pulses. It is independent of the response time of the detector. The term “ultrafast”is used when the pulse duration of the pump and probe pulses is less than one picosecond (10^{-12} s). The shortest pulses that have been generated so far have a duration of 3.8 fs [25, 26].

The pump-probe signal is a nonlinear signal which can be described in a perturbative approach in lowest order by the third order nonlinear polarization $P^{(3)}$ [23]. Here, the pump field interacts twice and the probe field interacts once with the sample. The pump-probe signal is calculated assuming an optically thin sample of thickness L. After interaction with the sample the detected probe field $E_{det}(z,t)$ follows from equation (2.2)

$$E_{det}(L,t,t_D) = E_{pr}(0,t) + i\,\frac{\Omega\, L}{2\,\epsilon_0\, n(\Omega)\, c}\, P^{(3)}(t,t_D) \tag{2.7}$$

and the detected probe intensity $I_{det}(t_D)$ reads

$$I_{det}(t_D) = \int_{-\infty}^{+\infty} dt\, |\, E_{det}(L,t,t_D)\,|^2 \tag{2.8}$$

The pump-probe signal (differential transmission) is defined as the normalized difference between the probe field intensity with and without the pump field [27]:

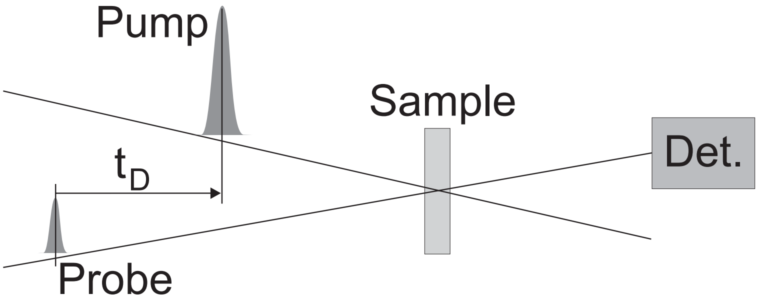

Figure 2.1: Setup for time-resolved transmission spectroscopy. The strong pump pulse excites the sample. A subsequent weak probe pulse measures the transmission of the sample as a function of time delay t_D.

$$
\begin{aligned}
\frac{\Delta T}{T_0}(t_D) &= \frac{I_{det}(t_D) - I_{det}(-\infty)}{I_{det}(-\infty)} \\
&= \Bigg(-\frac{\Omega\, L}{\epsilon_0\, c\, n(\Omega)} \operatorname{Im} \int_{-\infty}^{\infty} dt\, E^*_{pr}(0,t)\, P^{(3)}(t,t_D) \\
&\quad + \frac{\Omega^2\, L^2}{4\, \epsilon_0^2\, c^2\, n(\Omega)^2}\, |P^{(3}(t,t_D)|^2 \Bigg) / I_{det}(-\infty) \\
&\approx -\frac{\Omega\, L}{\epsilon_0\, c\, n(\Omega)} \operatorname{Im} \int_{-\infty}^{\infty} dt\, E^*_{pr}(0,t)\, P^{(3)}(t,t_D) / \int_{-\infty}^{\infty} dt\, |\, E_{pr}(0,t)\, |^2 \qquad (2.9)
\end{aligned}
$$

This approximation assumes that the electromagnetic field generated by the induced third-order polarization is significantly smaller than the probe field. In a similar way the dispersed pump-probe signal $\frac{\Delta T}{T_0}(\omega, t_D)$ can be obtained by the Fourier transform with respect to t [27]

$$
\frac{\Delta T}{T_0}(\omega, t_D) = -\frac{\Omega\, L}{\epsilon_0\, c\, n(\Omega)} \operatorname{Im} \frac{P^{(3)}(\omega, t_D)}{E_{pr}(0,\omega)} \qquad (2.10)
$$

In the interpretation of the pump-probe signal one has to pay attention to the so called coherent artifacts. They occur for negative time delays t_D and in the temporal overlap of the pump- and probe pulses. A detailed discussion of such phenomena can be found in Refs. [28, 29, 27]. Here, we want to briefly discuss the coherent artifacts in the frame of the quantum mechanical two-level system using the third order nonlinear polarization. Depending on the time ordering of the pump- and probe pulse interactions different contributions can be distinguished as depicted in Fig. 2.2. The first contribution is the so-called perturbed free-induction decay (PFD). Here, the linear polarization $P^{(1)}$ generated by the probe field, which decays with the dephasing time T_2 (free-induction decay), is perturbed by the subsequent interaction with the pump field. The PFD causes signals for negative delay times, in particular if the dephasing time T_2 is longer than the pulse length [31, 27]. It occurs

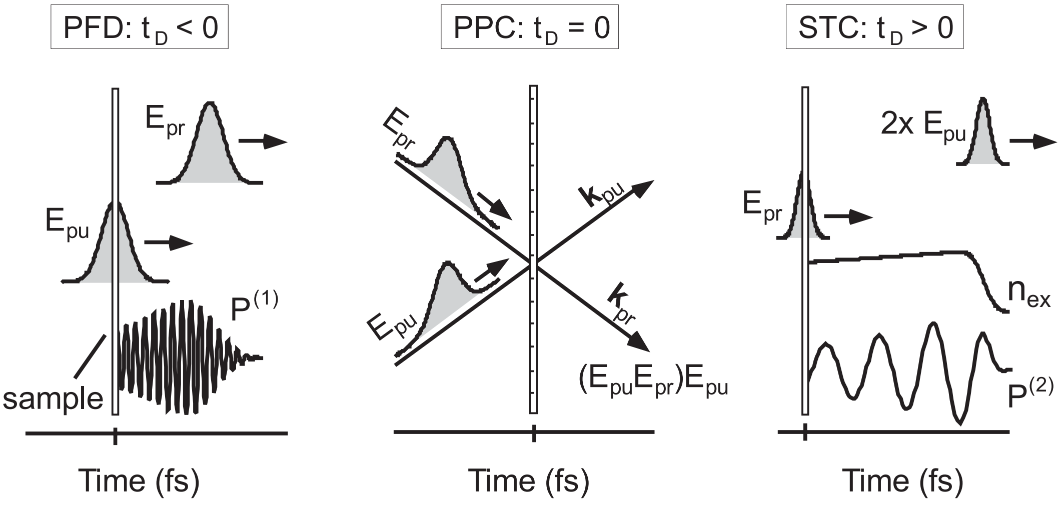

Figure 2.2: Depending on the time order of the interaction of the pump- and probe fields with the sample three contributions to the pump-probe signal can be distinguished [30].

only in the dispersed pump-probe signal since in the spectrally integrated signal the spectral contributions destructively interfere.

The pump-probe coupling (PPC) contribution occurs during the temporal overlap between the pump and probe pulses [31, 27]. The interference of the pump field and the probe field generates a transient excitation grating in the sample which leads to diffraction of pump light into the probe direction. It can be positive or negative depending on the relative phase of the transient grating and the diffracted light. These two components, PFD and PPC, which are usually called coherent artifacts, are unavoidable features in pump-probe spectroscopy. They complicate the analysis of the pump-probe signal in the time range before and around delay zero.

The signal in the time regime when the probe pulse interacts after the pump pulse without temporal overlap is called sequential transmission change (STC). In this regime the pump-probe signal reflects the dynamics of populations and of quantum coherences in the sample. The dynamics of optical polarizations generated by the pump pulse do not influence the pump-probe signal in this time regime.

In this thesis, three different techniques were used to characterize the ultrafast dynamics of carriers and coherent polarizations in semiconductor nanostructures and devices:

1. Spectrally integrated detection: The probe pulses are measured spectrally integrated after interaction with the sample. The advantage of this technique is a relatively simple setup. In this thesis, we use the spectrally integrated detection technique for linear transmission change measurements of a quantum cascade laser structure. The sample is pumped electrically and probed with ultrashort mid-infrared pulses. Spectral information is obtained by tuning the center-wavelength of the probe pulses. Thus, the measured signal as a function of the center frequency of the probe pulse is the convolution of the lineshape function of the excited transition with the spectrum of the probe pulse.

2. Pseudo two-color pump-probe spectroscopy [27]: The probe pulses are spectrally resolved after interaction with the sample, i.e. the dispersed pump-probe signal [Eq. (2.10)] is measured. Here, the spectral characteristics of the excitation can be measured with a high spectral resolution. We use this technique later for the electron transport studies in quantum cascade structures. It is important to note that for the interpretation of the experimental data all possible contributions (PFD, PPC, and STC) have to be considered.

3. Full characterization of spectral phase and amplitude: Here, the full information about the probe pulse is obtained by resolution of the spectral amplitude and phase after the interaction with the sample. A technique for the complete pulse characterization is electro-optic sampling. It was first applied to THz pulses by Auston et al. [33] and is nowadays a standard technique in this spectral range. With electro-optic sampling the electric field of a pulse is measured directly [Eq. (2.7)] resulting in time transients as shown in Fig. 2.3. By Fourier transforming those transients the spectral amplitude and phase is obtained. In this thesis, we use electro-optic sampling for the characterization of shaped mid-infrared pulses and for the study of coherent nonlinear propagation of ultrafast electric field transients through intersubband resonances.

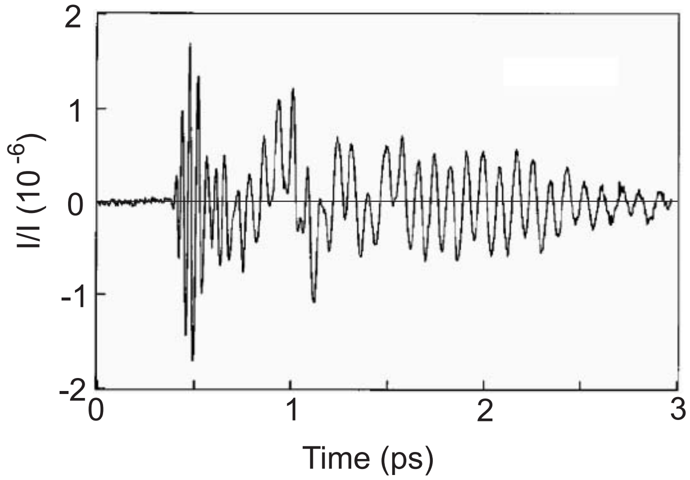

Figure 2.3: Temporal waveform of the THz radiation measured with electro-optic sampling [32].

2.2 Generation of ultrashort mid-infrared pulses

In this thesis ultrafast pump-probe spectroscopy is carried out in the mid-infrared wavelength range. Up to now, there is no light source available generating tunable ultrashort mid-infrared pulses directly. Therefore we use nonlinear optical techniques to convert femtosecond near-infrared pulses available from conventional Ti:sapphire laser systems to the desired wavelength range. Here, this is done in two different schemes. The first scheme uses phasematched difference frequency mixing in gallium selenide (GaSe) of components within the broad spectrum of single, 14 fs pulses from a cavity-dumped Ti:sapphire laser. This represents a highly compact source for the generation of mid-infrared pulses of 100 to 200 fs duration which are tunable from 7 to 20 μm at megahertz repetition rates. The second scheme is based on a 1 kHz regenerative amplifier and an optical parametric amplifier. The mid-infrared pulses are then generated by phasematched difference frequency mixing in GaSe covering the wavelength range from 3 to 20 μm. In that way, pulse energies of up to 1 μJ and pulse durations as short as 50 fs are obtained.

2.2.1 Low-intensity mid-infrared pulses at 2 MHz repetition rate

In this section we will first present a cavity-dumped Ti:sapphire laser providing ultrashort near-infrared pulses at a repetition rate of 2 MHz. This design corresponds to the laser demonstrated by Pshenichnikov et al. [34, 35]. The output pulses are used to generate ultrafast mid-infrared pulses via phasematched difference frequency mixing. In the following, this concept is discussed experimentally and theoretically in detail as it is the basis for pulse shaping presented later.

2.2.1.1 Cavity-dumped Ti:sapphire laser

In recent years, Ti:sapphire (Ti^{3+}:Al_2O_3) has become the most important laser medium in femtosecond technology. The advantage is its very broad fluorescence spectrum [36] with a maximum around 780nm. Another very useful property of this crystal is its high third order

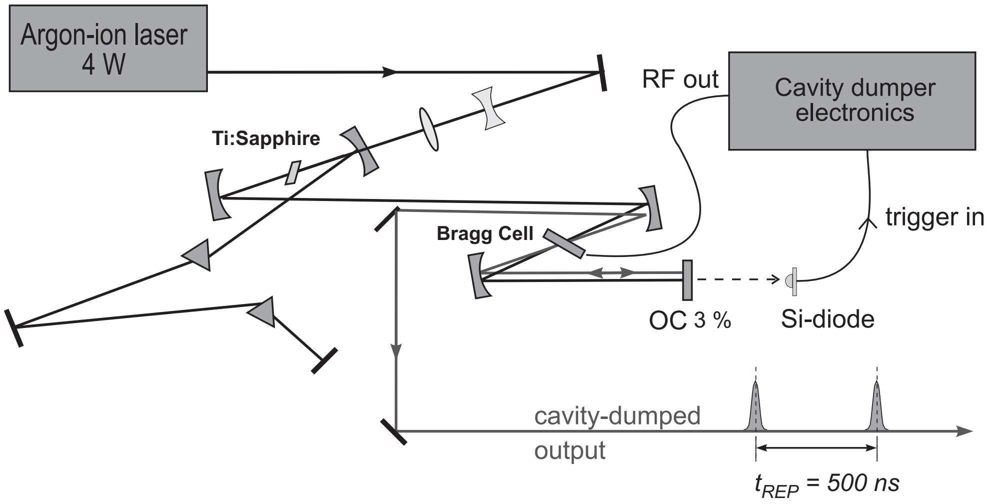

Figure 2.4: Setup of the cavity-dumped Ti:sapphire laser, pumped by approximately 4 W from a commercial Ar^+-ion laser ($\lambda = 514$ nm). Pulses with 14 fs duration and energies of typically 35 nJ are obtained at a repetition rate of 2 MHz.

nonlinear coefficient so that ultrashort pulses via Kerr lens modelocking can be generated without the help of an additional nonlinear optical element. The setup of the laser used in this thesis is shown in Fig. 2.4. The laser cavity contains a 4 mm long Ti:sapphire crystal and a fused-silica acousto optic modulator (Bragg cell). The Ti:sapphire crystal is pumped by 4 W from an Ar^+-ion laser. The group velocity dispersion (chirp) accumulated in the cavity is compensated with a pair of fused silica prisms. This oscillator runs intra-cavity with a repetition rate of 84 MHz. An electric pulse sent to the piezoelectric transducer in the Bragg cell generates a periodic grating which leads to the diffraction of a femtosecond pulse out of the cavity. In this way we get pulses with energies of typically 35 nJ and nearly bandwidth limited pulse lengths of 14 fs with a spectral width of 67 nm at a repetition rate of 2 MHz (Fig. 2.5).

2.2.1.2 Phasematched difference frequency mixing

The near-infrared pulses derived from the cavity-dumped Ti:sapphire laser are used for the generation of mid-infrared pulses. The scheme presented here is based on phasematched difference frequency mixing of frequency components within a single near-infrared pulse in a GaSe crystal [37]. Compared to non-phasematched optical rectification with the same material [38, 39] the average power obtained with phasematching is about 100 times higher.

Fig. 2.6 illustrates the concept of phasematched mid-infrared generation with a single pulse in a GaSe crystal. We apply *type-I* phasematching which means that an ordinary wave with frequency ω and an extraordinary wave with frequency $\omega + \Delta\omega$ are mixed to generate an ordinary wave with the difference frequency $\Delta\omega$ and zero phase mismatch Δk:

$$\begin{aligned}\Delta k &\equiv \Delta k(\omega, \Delta\omega, \theta) = k_{eo}(\omega + \Delta\omega, \theta) - k_o(\omega) - k_o(\Delta\omega) \\ &= \frac{1}{c}\Big(n_{eo}(\omega + \Delta\omega, \theta) \cdot (\omega + \Delta\omega) - n_o(\omega) \cdot \omega - n_o(\Delta\omega) \cdot \Delta\omega\Big) \\ &= 0\end{aligned}$$

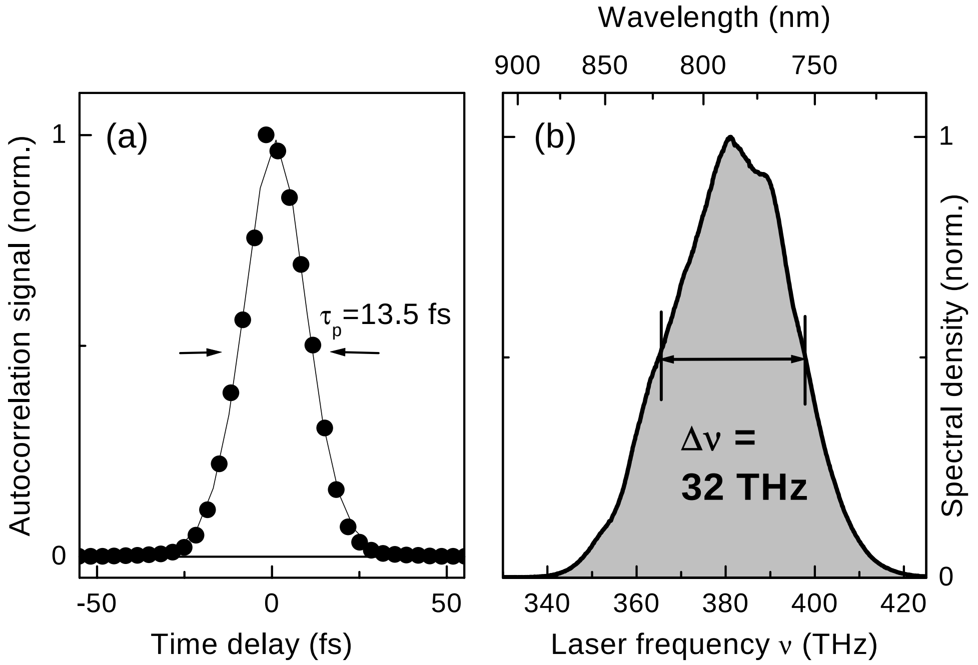

Figure 2.5: (a) Autocorrelation trace of the cavity-dumped pulses measured via second harmonic generation in a KDP crystal (circles). The sech^2 fit (line) corresponds to a pulse duration of $\tau_p = 13.5$ fs. (b) Pulse spectrum of the near-infrared pulse centered at $\lambda = 780$ nm with a spectral width of 67 nm (32 THz).

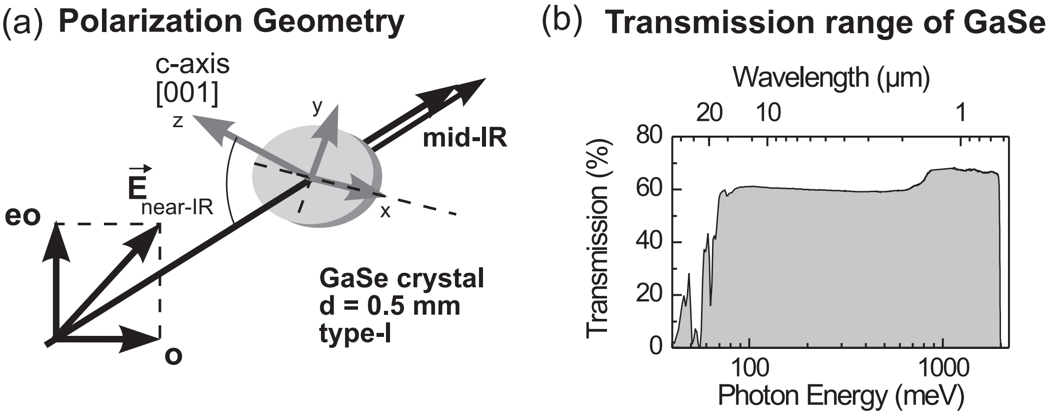

Figure 2.6: (a) Polarization geometry of a near-infrared pulse generating a mid-infrared pulse via type-I phasematched difference frequency mixing in a 0.5 mm thick GaSe crystal. (b) Transmission range of GaSe in the near- and mid-infrared spectral range.

k_o and k_{eo} are the wave vectors, n_o and n_{eo} are the frequency dependent indices of refraction of GaSe for the ordinary and the extraordinary wave [40]. To achieve type-I phasematching the incident beam propagates in the yz-plane [Fig. 2.6 (a)] of the GaSe crystal. By rotating the crystal around the x-axis the phasematching angle θ is adjusted. The polarization of the input pulses enclose an angle of 45° with respect to the plane of incidence so that one single input pulse provides both polarization components [ordinary (o) and extraordinary (eo)] for a type-I process. In this way mid-infrared pulses are generated via difference frequency mixing within the broad spectrum of a single near-infrared input pulse. We choose GaSe because of its strong nonlinearity and favorable transparency properties in the near- and mid-infrared spectral range [see Fig. 2.6 (b)]. The generated mid-infrared pulse E^{MIR} can be described by a single equation which is derived in detail in appendix A:

$$\begin{aligned} E^{MIR}(z,\Delta\omega) &= \frac{4\,\Delta\omega^2\,d(\theta)}{c^2\,k_o(\Delta\omega)}\,e^{-i\,k_o(\Delta\omega)\,z} \\ &\cdot\int d\omega\,A_o^{NIR}(\omega)\left(A_{eo}^{NIR}(\omega+\Delta\omega,\theta)\right)^{\star}\,\frac{e^{i\,\Delta k\,L}-1}{\Delta k}+cc. \end{aligned} \tag{2.11}$$

where A_o^{NIR} and A_{eo}^{NIR} are the envelopes of the ordinary and extraordinary components of the generating near-infrared pulse, $d(\theta)$ is the effective nonlinear susceptibility, and $L = 0.5$ mm is the GaSe thickness.

To see for which frequency $\Delta\omega$ the electric field $E^{MIR}(z,\Delta\omega)$ is non-negligible one has to look closer at the phasematching term $\left|\frac{e^{i\,\Delta k\,L}-1}{\Delta k}\right|$. For thick crystals as used here the phasematching term is nonzero only if the phase mismatch $\Delta k(\omega,\Delta\omega,\theta)$ is close to zero. Since $k_{eo}(\omega,\theta)$ depends on the angle θ the phase matching condition is fulfilled for a narrow range of $\Delta\omega$ frequencies.

Mid-infrared pulse parameters By rotating the GaSe crystal, i.e., by adjusting the phasematching angle, the center frequency of the mid-infrared pulses is tunable in a wide range from 7 to 20 μm as shown in Fig. 2.7 (a). The generation of higher wavelengths is restricted by the transparency range of the GaSe crystal [see Fig. 2.6 (b)]. The lower wavelength side is limited by the spectral width of the near-infrared pulses [Fig. 2.5 (a)]. The solid lines in Fig. 2.7 (a) are calculated spectra from the model described above. These calculations, which use as parameters only the data for the ordinary and extraordinary refractive indices [40], reproduce the measured spectra quite accurately. With an upconversion technique pulse lengths of 165 fs at $\lambda = 14\,\mu$m and 95 fs at $\lambda = 9.5\,\mu$m were measured [41]. A thorough characterization of the spectral phase and amplitude is done with the electro-optic sampling technique as discussed later in this chapter.

With a calibrated HgCdTe mid-infrared detector the pulse energies were measured. Pulse energies as a function of photon energy are shown in Fig. 2.7 (b). A peak energy of around 2.5 pJ is obtained for wavelengths in the range from 10 to 14 μm. It decreases rapidly for higher and lower wavelengths. Pulse energies of a few pJ seem to be very small. Assuming a rectangular shaped pulse with an energy of $I^{Pulse} = 1$ pJ and a pulse length of $\tau_p = 200$ fs one finds that in the focus, which is typically $d_{foc} = 70\,\mu$m in diameter, the pulse reaches an electric field strength of

$$E^{MIR} = \sqrt{2\,\frac{S^{MIR}}{c\,\epsilon_0}} = \sqrt{2\,\frac{I^{Pulse}}{c\,\epsilon_0\,\tau_p\,\pi\,\left(\frac{d_{foc}}{2}\right)^2}} = 10\,\frac{kV}{cm}$$

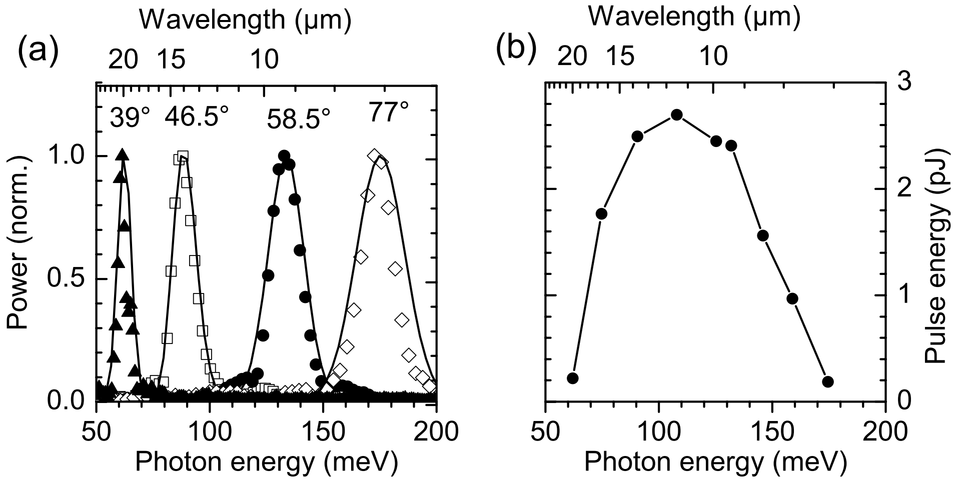

Figure 2.7: (a) Normalized power spectra (symbols) of the femtosecond mid-infrared pulses generated by phasematched difference frequency mixing of frequency components within a single near-infrared pulse in GaSe for different phasematching angles as indicated. Solid lines: calculated spectra using the model described in the text. (b) Measured mid-infrared pulse energies.

In high quality semiconductor nanostructures, this field is actually sufficient to generate nonlinear effects as we will see in chapter 4.

Very often, however, much higher pulse energies are needed. Using the mid-infrared pulse generation technique of phasematched difference frequency mixing we need a near-infrared system with much higher pulse energies. Unfortunately, then the rather simple scheme with a single near-infrared pulse generating the mid-infrared pulse in GaSe is not applicable as we run into the problem of strong two-photon absorption. A technique which circumvents this problem is presented in the next section.

2.2.2 High-intensity mid-infrared pulses at 1 kHz repetition rate

In this section we present a laser source for high-intensity mid-infrared pulses at 1 kHz repetition rate. The mid-infrared pulses are generated in a three-stage scheme. First, high-power, ultrashort near-infrared pulses are generated in a 1 kHz regenerative Ti:sapphire laser system. In a second stage, these pulses are used to generate tunable, near-infrared pulses in an optical parametric amplifier. Finally, mid-infrared pulses are generated via difference frequency mixing. We restrict the presentation to the most important points. A detailed description can be found in [41, 42]. This laser system is used for the time-resolved experiments on quantum cascade lasers.

2.2.2.1 Regenerative amplification and optical parametric amplification

The scheme for the generation of ultrafast, high-power near-infrared pulses is shown in Fig. 2.8. It is based on chirped pulse amplification (CPA) [43]. Here, weak 50 fs near-infrared

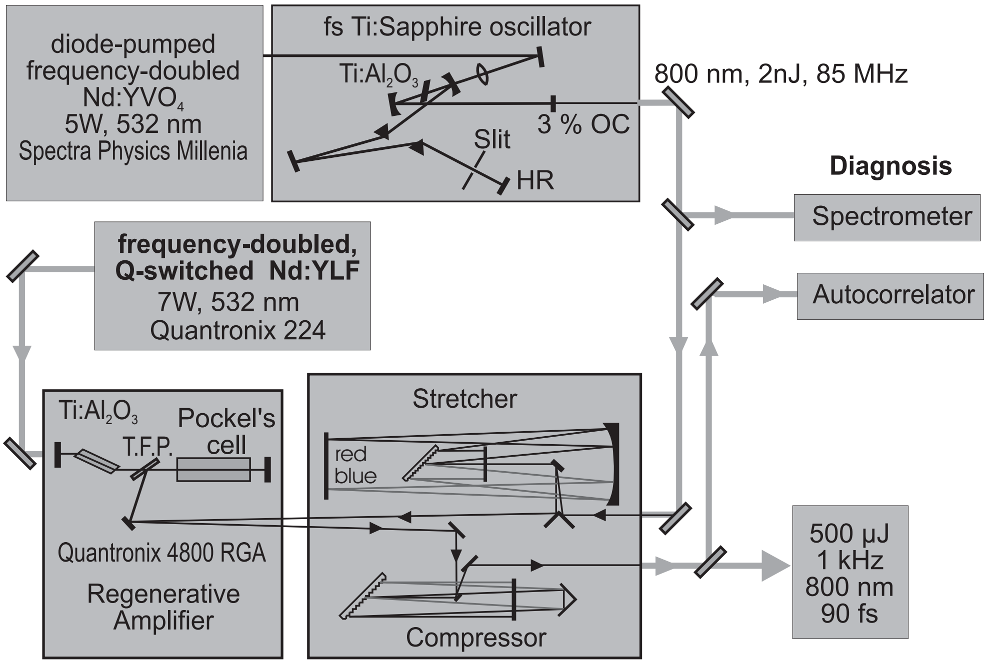

Figure 2.8: Chirped pulse amplification laser system for the generation of amplified femtosecond pulses (T.F.P.=thin film polarizer, HR=high reflector, OC=output coupler) [41].

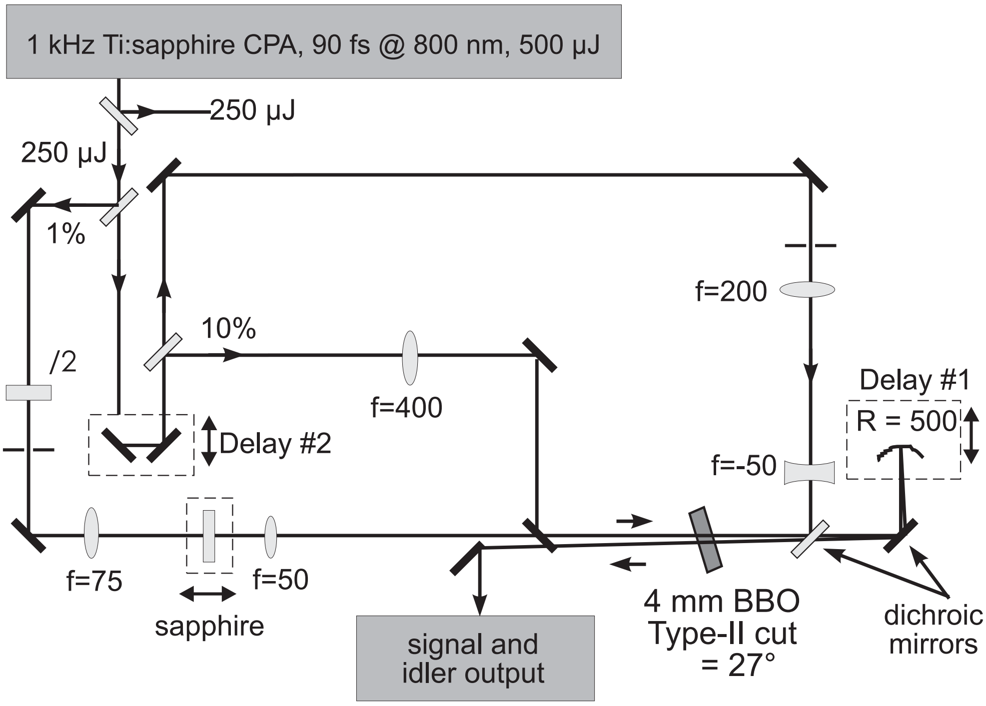

Figure 2.9: Two-stage optical parametric amplifier for the generation of tunable femtosecond signal and idler pulses in the near-infrared spectral range (λ =1-2 μm) [41].

pulses centered at 800 nm are generated in a Ti:sapphire oscillator with a repetition rate of 85 MHz and a pulse energy of 2 nJ. In a next stage, these pulses are temporally stretched to a pulse length of approximately 300 ps with a grating pulse stretcher to decrease significantly the peak power below the damage threshold of the following elements. These stretched pulses are then amplified in several round trips in a regenerative amplifier containing a 20 mm long Ti:sapphire crystal in the cavity, which is pumped by 7 mJ pulses from a synchronized frequency-doubled Nd:YLF laser. A Pockel's cell couples the pulses in and out with a repetition rate of 1 kHz. Finally the pulses are re-compressed to a pulse length of 80 to 100 fs in a grating compressor. The pulse energy now is typically 500 μJ.

In a further stage (see Fig. 2.9), near-infrared pulses ($\lambda = 1 - 2\,\mu$m) are generated in an optical parametric amplifier (OPA). Only half of the output power of the regenerative amplifier is needed. A small fraction ($\approx 1\,\%$) of the amplified 800 nm pulses is focused into a sapphire plate generating a white-light continuum, which is used for seeding. A fraction of 10 % is spatially and temporally overlapped with the seed pulses in a BBO crystal to generate in a first stage signal and idler pulses with pulse energies of together 200 nJ in the range between 1.2 and 2.2 μm via type-II phasematching. In a second stage these pulses are spatially and temporally overlapped with the resulting 90 % of the pump pulses at a different position of the BBO crystal and thereby amplified to pulse energies of together $70 - 80\,\mu$J.

2.2.2.2 Difference frequency mixing with signal and idler pulses

The mid-infrared pulses are generated via difference frequency mixing of signal and idler pulses in a 1 mm thick, type-I oriented GaSe crystal. For this, the setup shown in Fig. 2.10 was constructed. The temporal overlap is adjusted with a delay stage that separates signal and idler pulses using broadband dichroic mirrors. A telescope generates an effective focal length of 700 mm which leads to signal and idler foci of 500 μm diameter at the GaSe crystal. By adjusting the GaSe and BBO crystal angles appropriately, type-I phasematching occurs. Behind the GaSe crystal, residual signal and idler components are suppressed using suitable long-pass interference filters with onset wavelengths in the mid-infrared. A reference

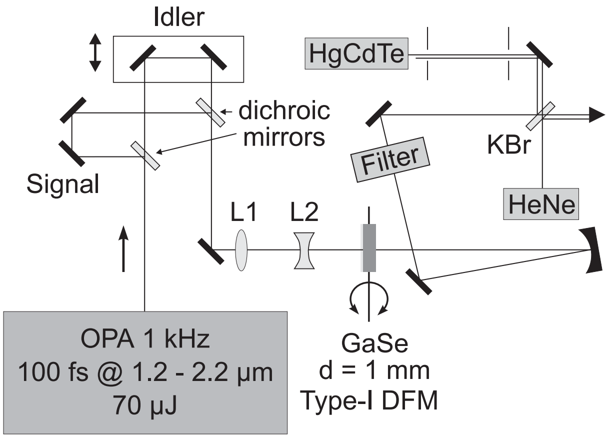

Figure 2.10: Mid-infrared generation via difference frequency mixing of signal and idler pulses in GaSe (L_1: $f = 150$ mm, L_2: $f = -100$ mm). The filter behind the GaSe crystal is needed to block residual signal and idler pulses. A HeNe laser beam is overlapped with the mid-infrared beam [41].

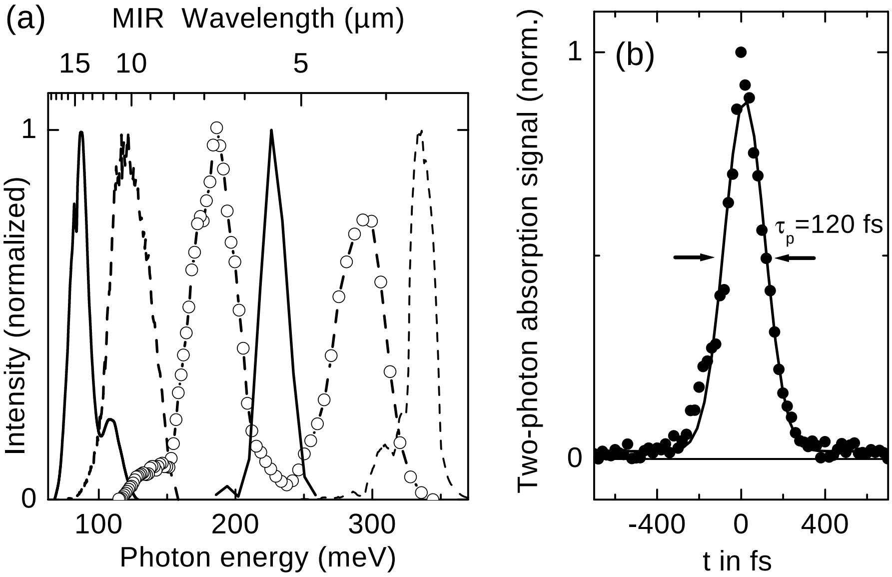

Figure 2.11: (a) Spectra of the mid-infrared femtosecond pulses generated with phasematched difference frequency mixing of signal and idler pulses for several phasematching angles [42]. (b)Autocorrelation trace of a mid-infrared pulse centered at $\lambda = 10\,\mu$m measured via two-photon absorption in InSb. The measured autocorrelation width corresponds to a pulse length of $\tau_p = 120$ fs.

beam is split off using a KBr plate. It is overlapped with the beam of a HeNe adjustment laser. In this way, steerability of the mid-infrared beam throughout the rest of the setup is accomplished.

Mid-infrared pulse parameters As in the high-frequency laser system, the pulses are tunable by adjusting the phasematching angle of the GaSe crystal. In addition to this the wavelengths of the signal and idler pulses have to be adjusted. The tuning range is wider than for the high-frequency system, it is in the spectral range between $3 - 20\,\mu$m. The pulse length is $\tau_p = 120$ fs for $\lambda = 10.0\,\mu$m [Fig. 2.11 (b)]. It varies strongly with the center wavelength as depicted in table 2.1. For wavelengths longer than $10\,\mu$m the pulse lengths increase rapidly. For a wavelength of $12.5\,\mu$m the pulse duration is 360 fs, which is far from the bandwidth limit. For these longer wavelengths pulse lengthening occurs as a result of dispersion in the GaSe crystal and subsequent optics. This can partly be compensated with

Table 2.1: Pulse lengths τ_p for different center wavelengths λ [42].

λ / μm	τ_p / fs
5.5	54
9.6	108
10.0	120
12.5	360

a pulse compressor as has been shown in [42].

The intensity of the mid-infrared output is measured directly using a sensitive thermopile detector. Smaller average powers for the experiments are determined with a calibrated HgCdTe detector. The pulse energy is 1 μJ around $\lambda = 5\,\mu$m and falls off inversely proportional to the photon energy at longer wavelengths (approximately constant number of photons per pulse).

2.3 Characterization of ultrashort mid-infrared pulses

In this section we discuss the electro-optic sampling technique [44, 45, 46]. It represents a very powerful method to characterize ultrashort pulses as it measures directly the electric field. Hence, it yields the complete spectral information of the field transient. Electro-optic sampling has become a standard technique in terahertz spectroscopy [33, 47, 48] and was applied for ultrafast pulses with wavelength down to the mid-infrared [32, 49]. For shorter wavelengths, however, it can not be applied as it would demand reference pulses to be shorter than available nowadays.

After a discussion of the principle of electro-optic sampling we address questions concerning the appropriate polarization directions for the mid-infrared beam and the near-infrared reference pulses. Then we study the wavelength range for which this technique can be applied. Finally, we demonstrate the electro-optic sampling technique by sampling some typical mid-infrared field transients.

Electro-optic sampling The basic idea of electro-optic sampling is the following. The electric field of the mid-infrared pulse induces a change of birefringence in a crystal via the electro-optic effect, i.e., it generates a change in the index ellipsoid of the crystal (appendix B). A short near-infrared pulse measures this electro-optic modulation as a function of time delay via the phase retardance Γ induced by the birefringence.

A suitable sensor crystal is ZnTe since it has sufficient transparency properties in the near- and mid-infrared spectral range and a large eletro-optic coefficient [32]. We will see later that the phase retardance Γ is proportional to the amplitude of the mid-infrared electric field: $\Gamma \sim E^{MIR}$. Γ can be measured in the setup shown in Fig. 2.12 (a). The linearly polarized near-infrared beam is focused collinearly with the mid-infrared beam on the ZnTe crystal. This is achieved by leading the near-infrared beam through a hole in the off-axis mirror (OA). Behind the ZnTe crystal the near-infrared beam is slightly elliptically polarized because of the birefringence induced by the electric field of the mid-infrared pulse. It passes successively a $\lambda/4$ wave plate and a Wollaston polarizer (WP) to generate two symmetrically arms whose intensity difference is measured with a pair of balanced photo diodes (BPD).

The intensity difference is the phase retardance which will be shown now. To calculate the expected effect we use the matrix representation of optical elements affecting the polarization of the near-infrared pulse (C). The incident, linearly polarized near-infrared beam $\vec{E}_{in} = (E, 0)\, e^{i(\omega t - k z)}$ is transformed into the elliptically polarized beam $\vec{E}_{out}$ by passing the ZnTe crystal and the $\lambda/4$ waveplate in the following way [see Fig. 2.12 (b)]

$$\begin{aligned}
\vec{E}_{out} &= \frac{1}{2} M_{\lambda/4}\, M_{ZnTe}\, \vec{E}_{in} + cc. = \frac{1}{2} M_{\lambda/4}\, M(\Gamma)\, \vec{E}_{in} + cc. \\
&= \frac{1}{2} \frac{1}{\sqrt{2}} \begin{pmatrix} 1 & e^{i\frac{\pi}{2}} \\ e^{i\frac{\pi}{2}} & 1 \end{pmatrix} \begin{pmatrix} \cos\frac{\Gamma}{2} & e^{i\frac{\pi}{2}}\, \sin\frac{\Gamma}{2} \\ e^{i\frac{\pi}{2}}\, \sin\frac{\Gamma}{2} & \cos\frac{\Gamma}{2} \end{pmatrix} \vec{E}_{in} + cc.
\end{aligned}$$

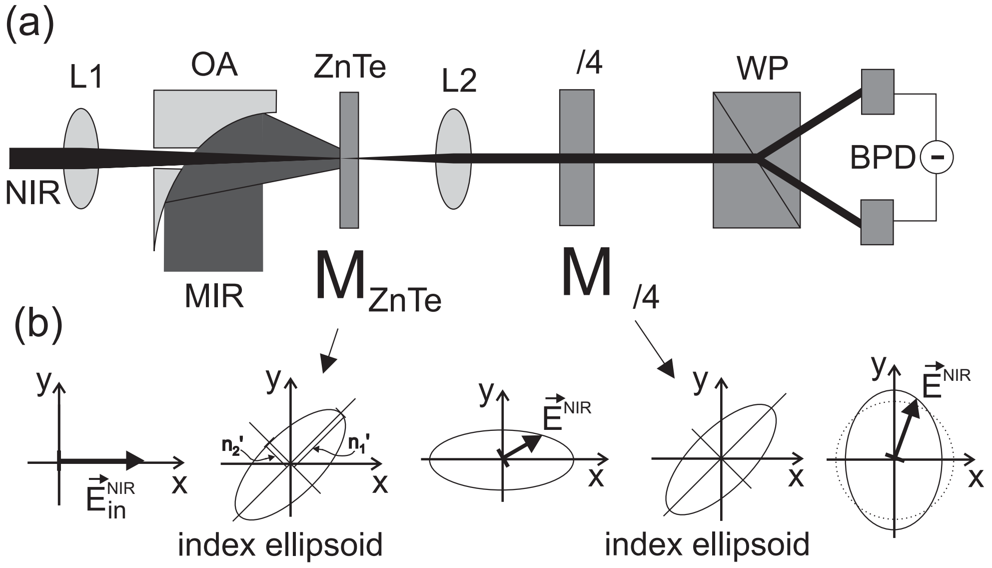

Figure 2.12: Principle of measurement of the electric field of a mid-infrared pulse using electro-optic sampling. (a) The mid-infrared beam and a near-infrared reference beam are focused onto the ZnTe crystal ($f_{L1} = 200$ mm, $f_{OA} = 100$ mm, $f_{L2} = 100$ mm). The reference beam passes a $\lambda/4$ wave plate and a Wollaston polarizer (WP) before it is measured with a pair of balanced photo diodes (BPD). (b) Evolution of the polarization of the near-infrared reference beam. The incoming beam is polarized along the x axis. Under the influence of the mid-infrared induced index-ellipsoid [for n_1' and n_2' see formula (D.6)] of the ZnTe crystal it becomes slightly elliptically polarized. The index-ellipsoid of the $\lambda/4$ wave plate transforms the slightly elliptically polarized beam into a slightly "non-circularly"polarized beam which is necessary to get two symmetric arms after passing the Wollaston polarizer.

$$= \frac{1}{2}\frac{E}{\sqrt{2}} \begin{pmatrix} \cos\frac{\Gamma}{2} - \sin\frac{\Gamma}{2} \\ e^{i\frac{\pi}{2}}\left(\sin\frac{\Gamma}{2} + \cos\frac{\Gamma}{2}\right) \end{pmatrix} e^{i(\omega\, t - k\, z + \varphi)} + cc. = \begin{pmatrix} E_{out,x} \\ E_{out,y} \end{pmatrix}$$

The diodes measure the time integrated difference signal Δ_E

$$\begin{aligned} \Delta_E &= \lim_{T\to\infty} \frac{1}{T} \int_0^T (E_{out,y})^2 - (E_{out,x})^2 \, dt \\ &= \frac{E}{2}\left(\left(\cos\frac{\Gamma}{2} + \sin\frac{\Gamma}{2}\right)^2 - \left(\cos\frac{\Gamma}{2} - \sin\frac{\Gamma}{2}\right)^2\right) \\ &= E\,\sin\Gamma \end{aligned}$$

For $\Gamma \ll 1$ this results in the normalized difference signal

$$\Delta \equiv \Delta_E/E = \Gamma \sim E^{MIR} \tag{2.12}$$

By varying the time delay t_D between the mid- and the near-infrared pulses the electric field of the mid-infrared pulse is measured directly as illustrated in Fig. 2.13. Thus, the complete information about the spectral phase and amplitude is obtained.

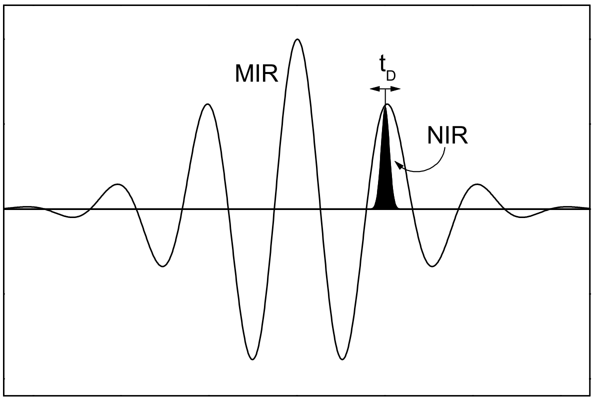

Figure 2.13: The Principle of electro-optic sampling: A short near-infrared reference pulse (NIR) measures the birefringence induced by the electric field of the mid-infrared pulse (MIR) as a function of the time delay t_D.

Polarization geometry The non-vanishing components of the electro-optic tensor $\mathbf{r}_{ZnTe}$ for ZnTe at a mid-infrared wavelength of 10.6 μm [50] are

$$r_{41} = r_{52} = r_{63} = 3.9 \cdot 10^{-12}\, \frac{\mathrm{m}}{\mathrm{V}} \tag{2.13}$$

We choose a thin ZnTe plate being $< 110 >$ oriented [32] and both the mid- and near-infrared propagation directions being perpendicular to the ZnTe surface. Under these conditions we show in appendix D that the maximum phase retardance $\Gamma = \frac{\omega}{c}\, n^3\, r_{41}\, E^{MIR}\, L$, where L is the crystal thickness, is obtained for a polarization configuration as depicted in Fig. 2.14.

Wavelength range Eq. 2.12 is exact for a static mid-infrared field. Here, however, we want to measure the electric field of an ultrashort mid-infrared pulse with center frequency Ω. As A consequence, two points have to be taken into account:

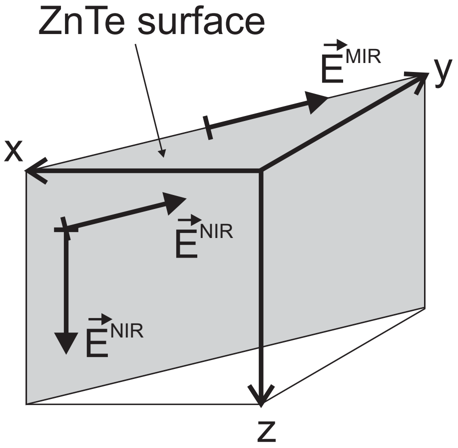

Figure 2.14: ZnTe surface and polarizations of the near- and mid-infrared beam yielding the maximum effect (for the near-infrared beam there are two possibilities).

- The difference between the group velocity of the near-infrared pulse and the phase velocity of the mid-infrared pulse [51]: First we consider the near-infrared reference pulse to be negligibly short and centered at a frequency ω_0. $\delta(x)$ is the group/phase velocity mismatch time after having passed a distance x in the crystal

  $$\delta(x) = \left(\frac{1}{v_{gr}(\omega_0)} - \frac{1}{v_{ph}(\Omega)} \right) x$$

  with the group velocity of the near-infrared $v_{gr}(\omega_0)$ and the mid-infrared phase velocity $v_{ph} = \frac{c}{n(\Omega)}$. The mid-infrared field $E^{MIR}(x)$ measured by the near-infrared pulse is

  $$E^{MIR}(x) = E^{MIR} \cos(\Omega \cdot \delta(x) + \varphi)$$

  where φ is the phase of the mid-infrared wave (which depends on the time delay t_D between the near- and mid-infrared pulse). The electro-optic effect induced by the mid-infrared pulse is averaged along the crystal

  $$\tilde{\Delta} = \frac{\omega}{c} n(\omega_0)^3 r_{41} \int_0^L E^{MIR}(x)\, dx$$

- The finite pulse length of the near-infrared pulse. This effect is modelled by the convolution with the normalized envelope of the near-infrared pulse

  $$I^{NIR}(x_0) = I_{norm}\, e^{-4 \ln 2 \left(\frac{n(\omega)\, x_0}{c\, \tau_p} \right)^2}$$

  where the near-infrared pulse length is $\tau_p = 14$ fs.

Taking into account these two points the measured normalized differential signal reads

$$\Delta^{eff}(\Omega, L, \varphi) = \frac{\omega}{c} n(\omega_0)^3 r_{41} \int_0^L \int_{-\infty}^{\infty} E^{MIR}(x - x_0) \cdot I^{NIR}(x_0)\, dx_0\, dx$$

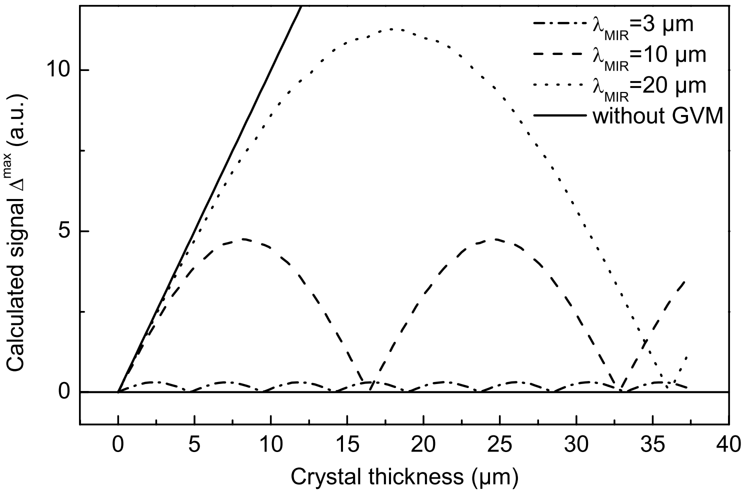

Figure 2.15: Difference signal $\Delta^{max}(L)$ plotted as a function of the crystal thickness L for $\lambda_{MIR} = 3\,\mu$m (dash-dotted line), $10\,\mu$m (dashed line), $20\,\mu$m (dotted line) and for a situation without group velocity mismatch.

Both effects distort the signal because they act differently on different frequency components of the mid-infrared pulse. Note that for different crystal thicknesses L the measured signal $\Delta^{eff} = \Delta^{eff}(\varphi)$ experiences a phase shift. φ_{max} is the phase where the signal reaches its maximum ($\Delta^{max} \equiv \Delta^{eff}(\varphi_{max})$).

In Fig. 2.15 the difference signal $\Delta^{max}(L)$ is plotted as a function of the crystal thickness L for $\lambda_{MIR} = 3$, 10, and 20 μm and for a situation without group velocity mismatch. As can be seen, for shorter mid-infrared wavelengths the effects described above become more serious. Consequently, a thinner ZnTe crystal is required. For $\lambda_{MIR} = 10\,\mu$m the maximum difference signal is obtained at a crystal thickness of 8 μm. As we will sample ultrafast mid-infrared pulses with center frequencies between 10 μm and 12 μm we have used a crystal thickness of $L = 10\,\mu$m.

Experimental data Typical mid-infrared electric field transients generated via phase-matched difference frequency mixing in a GaSe crystal and measured with electro-optic sampling are shown in Fig. 2.16. In (a) the electro-optic signal is shown as a function of time delay between the mid-infrared pulse and a near-infrared reference pulse. In (b) the mid-infrared pulse has passed a 6 mm thick potassium bromide (KBr) window. The respec-

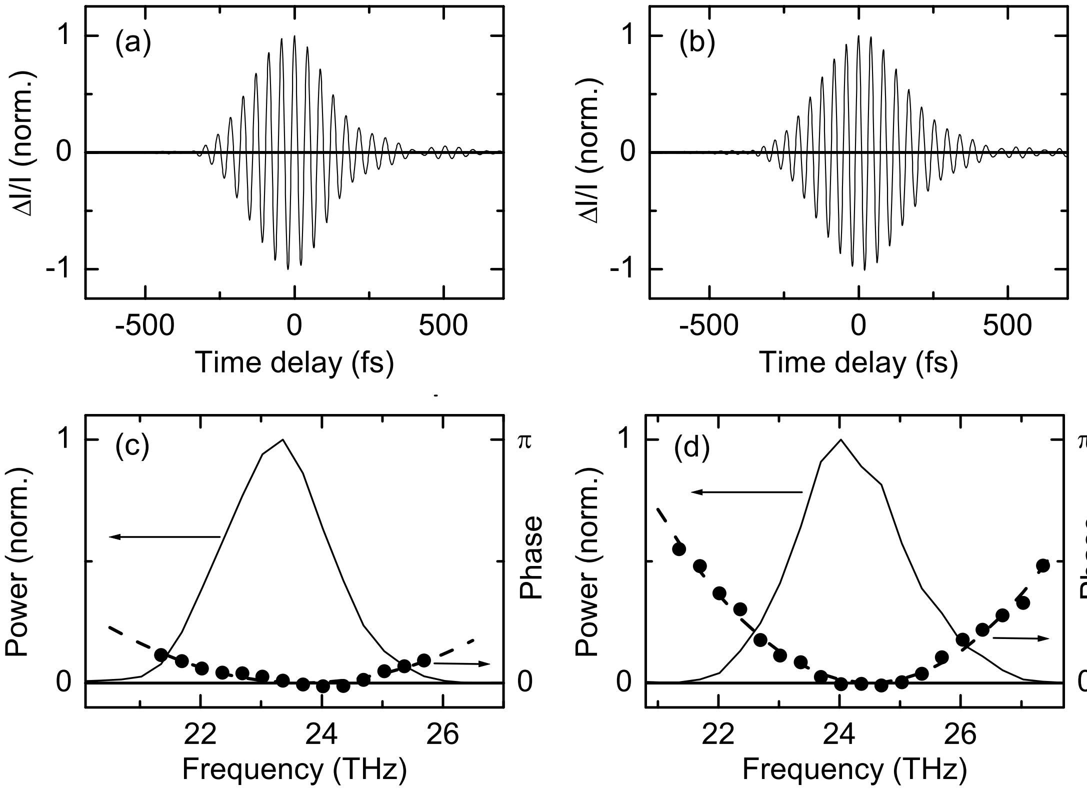

Figure 2.16: (a) Mid-infrared electric field transients measured with electro-optic sampling. The mid-infrared pulse was generated via phasematched difference-frequency mixing in a GaSe crystal. (b) Field transient after passing 6 mm KBr. (c), (d) Power spectra (solid line) and spectral phases (circles) gained from the Fourier transform of the respective transients. Dashed lines: Quadratic fit with a chirp $\partial^2 \Phi / \partial \omega^2$ of (c) 37 fs^2 and (d) 90 fs^2.

tive power spectra [Fig. 2.16 (c),(d): solid lines] and the spectral phases [Fig. 2.16 (c),(d): circles] were obtained by the Fourier transforms of the transients. The pulse in Fig. 2.16 (a) has a linear chirp $\partial^2 \Phi / \partial \omega^2$ of 37 fs^2. After having passed the KBr window the linear chirp increases to 90 fs^2. Hence, 6 mm KBr account for a linear chirp of 53 fs^2. With the Sellmeier equation for KBr

$$n_{KBr}^2(\lambda) = 1.39408 + \frac{0.79221 \cdot \lambda^2}{\lambda^2 - 0.146^2} + \frac{0.01981 \cdot \lambda^2}{\lambda^2 - 0.173^2} + \frac{0.15587 \cdot \lambda^2}{\lambda^2 - 0.187^2} + \frac{0.17673 \cdot \lambda^2}{\lambda^2 - 60.61^2} + \frac{2.06217 \cdot \lambda^2}{\lambda^2 - 87.72^2}$$

(λ in μ) a linear chirp of 52 fs^2 after the passage of 6 mm KBr is calculated which is in good agreement with the measured one.

In conclusion, we have seen that electro-optic sampling is an excellent method to determine the spectral phase and amplitude of a mid-infrared pulse. This is used in the following to characterize shaped mid-infrared pulses.

2.4 Shaping of ultrashort mid-infrared pulses

In this section we present a novel technique to shape ultrashort mid-infrared pulses. It is based on a two-stage scheme. In a first stage, ultrashort near-infrared pulses are shaped with a programmable pulse shaper. In a second stage, these pulses generate shaped mid-infrared field transients via phasematched difference frequency mixing in a GaSe crystal. This indirect technique is capable to phase *and* amplitude shape the mid-infrared field transients within its given spectral width.

Direct amplitude shaping in the mid-infrared has been accomplished recently using amplitude masks in a zero-dispersion stretcher [41, 42]. With some effort, this direct technique can, in principle, be extended to also phase shape mid-infrared pulses. However, the advantage of our method is that it combines two well known techniques: near-infrared pulse shaping and mid-infrared generation via phasematched difference frequency mixing, which can be modelled quite accurately by the theory described in section 2.2.1.2.

In the following, we first present the technique of pulse shaping in the near-infrared spectral range using an array of liquid crystals before we come to the new concept of mid-infrared pulse shaping.

2.4.1 Pulse shaping in the near-infrared

In a first stage, near-infrared pulses are shaped in a programmable pulse shaper. An exact control of this shape is essential for the subsequent mid-infrared pulse shaping. We start presenting the setup using a 128-pixel liquid crystal array. We calculate the transmission and phase of each pixel induced by a voltage applied on each of the pixels individually. Then we explain the calibration of the pulse shaper. Finally we present an intrinsic technique to characterize the shaped near-infrared pulses at any position of the optical setup.

Experimental setup The basic idea of pulse shaping in the near-infrared spectral region is to phase and amplitude modulate the frequency components within an ultrashort near-infrared pulse. First experiments used lithographically etched masks [52, 53]. Nowadays, programmable acousto-optic modulators [54] and liquid crystal modulators (LCM) [55, 56, 57] are used. In this thesis we have used the LCM technique. The apparatus was developed

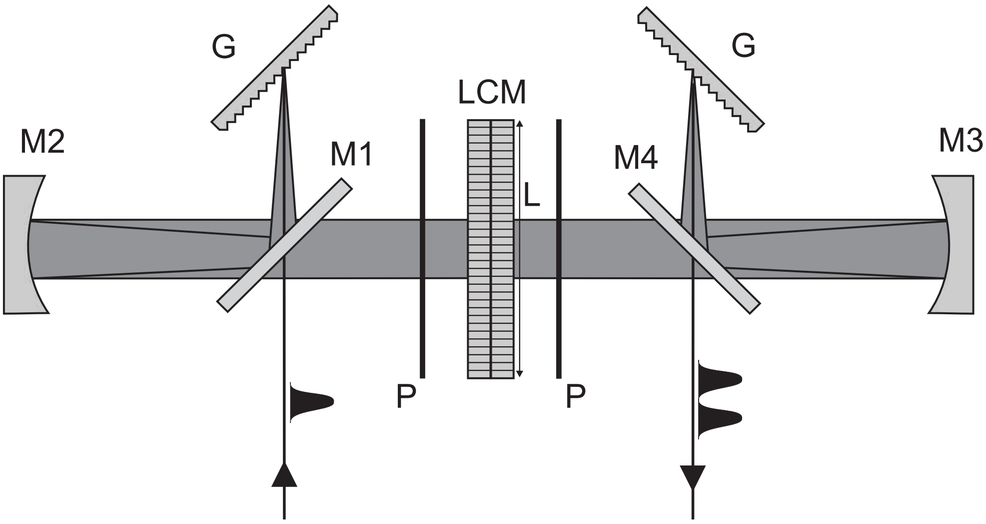

Figure 2.17: Setup of the near-infrared pulse shaper. The incoming pulse is spectrally dispersed by the grating G (600 l/mm). With a plane gold mirror (M1) the beam is reflected onto the spherical gold mirror M2 ($f_{M2} = f_{M3} = 15$ cm). Here, the spectral components are collimated and focused onto the liquid-crystal-modulator (LCM). Before and after the LCM they pass a polarizer (P). With the spherical gold mirror M3 and the plane gold mirror M4 the spectral components are re-focused onto the grating G yielding a parallel, shaped near-infrared beam.

by Wefers and Nelson [58] in cooperation with CRI. It consists of two liquid crystal arrays with 128 pixels each, which are glued upon each other. In the setup (see Fig. 2.17) we placed the LCM into a 4-f zero dispersion stretcher. The incident near-infrared beam is dispersed at the first grating and focussed onto the LCM with a spherical mirror. Hence, a certain polarized frequency content of the pulse passes a pixel of the first and a pixel of the second LCM array. These two pixels represent two degrees of freedom which we can use to modulate the phase and amplitude of the corresponding frequency content as we will see later. The length L of the LCM is 12.8 mm. The frequency range passing the LCM is approximately double the FWHM (full width at half maximum) of the near-infrared pulse spectrum ($\Delta\lambda = 70$ nm). We use a 600 l/mm grating and a curved mirror with $f = 150$ mm.

Calculation of transmission and phase The electric field $\vec{E}_{in}$ of a frequency component λ yields after transmission of the polarizers P and the LCM pixelpair, each of thickness l, (see appendix C)

$$\begin{aligned}\vec{E}_{out}(U_1, U_2) &= P \cdot M(-45^\circ) \cdot \begin{pmatrix} e^{i\,\frac{2\pi}{\lambda}\,\bar{n}_0\,l} & 0 \\ 0 & e^{i\,\frac{2\pi}{\lambda}\,n_2(U_2)\,l} \end{pmatrix} \\ &\quad \cdot \begin{pmatrix} e^{i\,\frac{2\pi}{\lambda}\,n_1(U_1)\,l} & 0 \\ 0 & e^{i\,\frac{2\pi}{\lambda}\,n_0\,l} \end{pmatrix} \cdot M(45^\circ) \cdot P\,\vec{E}_{in} \\ &\equiv S(U_1, U_2)\,\vec{E}_{in}\end{aligned}$$

where $n_1(U_1)$ and $n_2(U_2)$ are the refractive indices of the pixel pair, which is controlled by the voltages U_1 and U_2 (U_1, $U_2 = 0...10$ V),

$$S(U_1, U_2) \quad = \quad e^{i\,\frac{2\pi}{\lambda}\,(\bar{n}_0 + n_0)\,l}\; e^{i\,\frac{\varphi_1+\varphi_2}{2}} \begin{pmatrix} \cos\frac{\varphi_1-\varphi_2}{2} & 0 \\ 0 & 0 \end{pmatrix}$$

with the phases

$$\begin{aligned} \varphi_1 \quad &\equiv \quad \varphi_1(U_1) = \frac{2\pi}{\lambda}\,(n_1(U_1) - n_0)\;l \\ \varphi_2 \quad &\equiv \quad \varphi_2(U_2) = \frac{2\pi}{\lambda}\,(n_2(U_1) - \bar{n}_0)\;l \end{aligned}$$

The phase factor $e^{i\,\frac{2\pi}{\lambda}\,(\bar{n}_0+n_0)\,l}$ could, in principle, be used to control the absolute phase of the shaped near-infrared pulse. Here, however, it will be neglected as we are not interested in an absolute phase. With $\vec{E}_{in} = (E, 0)$ the transmission is

$$T(U_1, U_2) = \frac{\mid E_{out}(U_1, U_2) \mid^2}{\mid E_{in} \mid^2} = \frac{\cos(\varphi_1 - \varphi_2) + 1}{2}$$

and the phase shift

$$\Delta\varphi(U_1, U_2) = \frac{\varphi_1 + \varphi_2}{2}$$

In this way, phase and amplitude control of all corresponding frequencies is achieved. Hence, with the limitation of 128 pixelpairs we can arbitrarily shape a near-infrared pulse within a certain spectral bandwidth.

Calibration Since the voltage dependence of the phases $\varphi_1(U_1)$ and $\varphi_2(U_2)$ depend on parameters of the LCM, which are not known, we have to determine this experimentally. In a first step we measure the transmissions $T(U, U_0)$ and $T(U_0, U)$ with a fixed voltage U_0 for each pixel with a photodiode. With these transmissions we define the phase ψ

$$\begin{aligned} \psi(U, U_0) \equiv \varphi_1(U) - \varphi_2(U_0) &= \arccos[2\,T(U, U_0) - 1] \\ \psi(U_0, U) \equiv \varphi_1(U_0) - \varphi_2(U) &= \arccos[2\,T(U_0, U) - 1] \end{aligned}$$

Now we set $\varphi_2(U_0) \equiv 0$, which is reasonable since we are not interested in an absolute phase of the near-infrared pulse. This results in the calibration equations

$$\begin{aligned} \varphi_1(U) \quad &= \quad \psi(U, U_0) \\ \varphi_2(U) \quad &= \quad \psi(U_0, U_0) - \psi(U_0, U) \end{aligned}$$

Characterization of shaped near-infrared pulses Many techniques have been developed to characterize ultrashort near-infrared pulses. Standard techniques for phase and amplitude characterization of the spectral components of an ultrashort near-infrared pulse are, e.g., frequency resolved optical gating (FROG) [59] and spectral phase interferometry for direct electric-field reconstruction (SPIDER) [60]. The disadvantage of such techniques is that they require additional setups. Thus, they measure the pulse characteristics somewhere in these setups and not at the position of the experiment. With the pulse shaper, however,

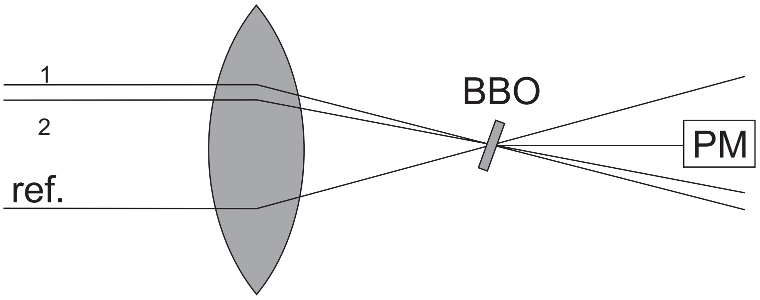

Figure 2.18: Cross-correlation in a BBO crystal of two frequency components ω_1 and ω_2 of the near-infrared pulse with a short reference pulse. The cross correlation signal is measured with a photo-multiplier (PM). The relative phase of ω_1 and ω_2 can be obtained by this technique.

we have an intrinsic possibility to characterize the phase and amplitude at any desired position. To be more precise, with the pulse-shaper we measure the phases of the spectral components. The spectral amplitude is then measured with a conventional monochromator. This technique which is called direct optical spectral phase measurement (DOSPM) [61] is based on the temporal interference of two spectral components $E_{\omega_1}(t) = \cos(\omega_1 t + \varphi(\omega_1))$ and $E_{\omega_2}(t) = \cos(\omega_2 t + \varphi(\omega_2))$ with frequencies ω_1, ω_2 and phases $\varphi(\omega_1)$, $\varphi(\omega_2)$ of the spectrum to be investigated. The measurement of the resulting temporal beats is carried out by cross correlation with a nearly transform-limited reference pulse in a thin BBO crystal. The setup is shown in Fig. 2.18. Two oscillators are selected from the shaped spectrum by adjusting the transmission of all pixelpairs to zero except of those corresponding to the desired two frequency portions. Since it is not possible to set the transmission of pixelpairs to exact zero, the passing light causes an additional cross correlation signal superimposed on the proper one. To suppress this sufficiently we increased the intensity of the two oscillators by increasing their frequency content. For one oscillator we used the frequency portion passing five pixelpairs. The interference of these two oscillators give a temporal beat signal

$$\begin{aligned} I(t) &= \left(E_{\omega_1}(t) + E_{\omega_2}(t)\right)^2 \\ &\sim \cos^2\left(\frac{\omega_1+\omega_2}{2}t + \frac{\varphi(\omega_1)+\varphi(\omega_2)}{2}\right) \times \cos^2\left(\frac{\omega_1-\omega_2}{2}t + \frac{\varphi(\omega_1)-\varphi(\omega_2)}{2}\right) \end{aligned}$$

In the cross correlation only the low frequency part $\cos^2\left(\frac{\omega_1-\omega_2}{2}t + \frac{\varphi(\omega_1)-\varphi(\omega_2)}{2}\right)$ survives while the high frequency part is averaged out due to the non-collinear second-harmonic generation and the phase instability with respect to the reference pulse. Scanning a complete set of frequency doublets we can determine the phase information of the shaped near-infrared pulse. Cross correlation curves for two different frequency doublets of a pulse with an intensity spectrum as shown in Fig. 2.19 (a) are shown in Fig. 2.19 (b). The phase data generated with this technique and the corresponding pulse shapes are shown in Fig. 2.19 (c). As can be seen, this technique works quite well and there are no ambiguities as, e.g., with FROG. We can characterize the shaped near-infrared pulse directly at the position of the GaSe crystal where we want to generate the shaped mid-infrared pulses. The disadvantage of this technique is that it is rather time consuming. One complete phase data measurement needs around thirty minutes.

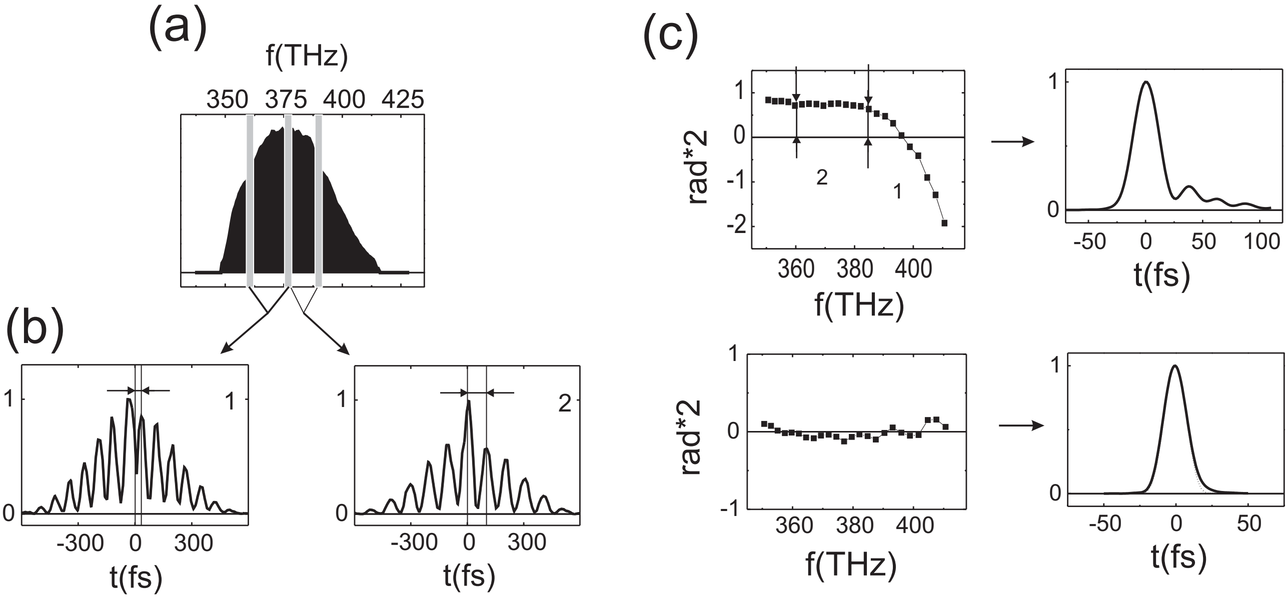

Figure 2.19: Phase characterization of a near-infrared pulse with the intensity spectrum shown in (a). (b) Cross-correlation curves of two spectral components with a short near-infrared pulse. (c) Scanning over the whole spectral range results in the complete phase diagram and thus the pulse shapes. In a first step, the phase of a chirped near-infrared pulse was measured (upper panels). In a second step, the phase was changed with the pulse shaper to get a bandwidth limited pulse (lower panels).

2.4.2 Pulse shaping in the mid-infrared

Experimental setup The complete experimental setup for our new technique of pulse shaping in the mid-infrared wavelength range is shown schematically in Fig. 2.20 (a). The near-infrared pulses are generated in a cavity-dumped, modelocked Ti:sapphire oscillator as described in section 2.2.1.1. In our setup, shaped mid-infrared pulses are obtained in a two-stage scheme: first, the near-infrared beam is shaped in a programmable pulse-shaper. In this way, amplitude- and phase-shaped near-infrared pulses are generated. In the second step, phasematched difference-frequency mixing of different spectral components of these pulses in a 0.5-mm-thick GaSe crystal (section 2.2.1.2) provides femtosecond mid-infrared electric field transients. We apply free-space electro-optic sampling, to measure the shaped mid-infrared electric-field transients (section 2.3).

Experimental data In Fig. 2.21 mid-infrared waveforms are shown which are generated by a near-infrared, phase-locked pulse pair. The near-infrared pulse pair was obtained by programming the pulse shaper so that the near-infrared spectral amplitude has the shape

$$A_{\Delta t}(\omega) = \frac{A_0(\omega)}{2}\left(e^{-i\,\frac{\omega\,\Delta t}{2}} + e^{i\,\frac{\omega\,\Delta t}{2}}\right) = A_0(\omega)\,\cos\frac{\omega\,\Delta t}{2}$$

where $A_0(\omega)$ is the spectral amplitude of the unshaped near-infrared pulse and Δt is the pulse distance. For a near-infrared pulse distance of $\Delta t = 800$ fs [Fig. 2.21 (a)], $\Delta t = 500$ fs [Fig. 2.21 (b)], and $\Delta t = 200$ fs [Fig. 2.21 (c)] a mid-infrared pulse pair with the same pulse distance is obtained. The respective mid-infrared intensity spectra obtained from the

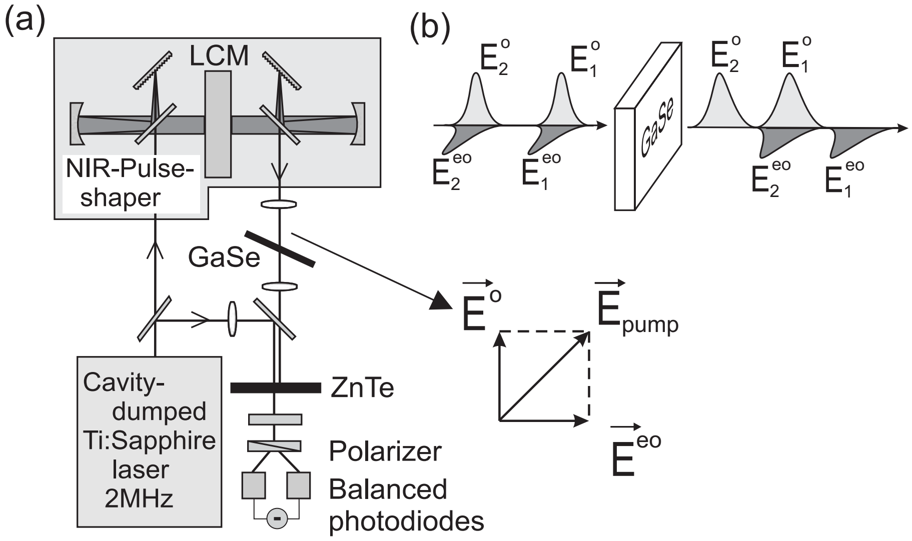

Figure 2.20: (a) Experimental setup for the generation and characterization of amplitude- and phase-shaped femtosecond pulses in the wavelength range from 7 to 20 μm. The ultrafast electric field transients are generated by phasematched difference frequency mixing in a GaSe crystal of shaped near-infrared pulses using a liquid crystal modulator (LCM). The electric field transients generated are directly measured using ultrafast electro-optic sampling. (b) Schematic showing the propagation of the ordinary (o) and extraordinary (eo) components of two phase-locked near-infrared pump pulses. Group velocity mismatch between the ordinary and extraordinary wave leads to coincidence of the extraordinary component of the second pulse with the ordinary of the first.

Fourier transforms of the transients are shown in Fig. 2.21 (d)-(f) (circles). The fit curves (solid lines) are functions $\cos(\Delta t/2 \cdot \omega)$ multiplied with the spectra for a single pulse (dashed lines).

What happens if the near-infrared pulse distance is further reduced to 60 fs is shown in Fig. 2.22. In 2.22 (a) a typical mid-infrared waveform is shown which was generated by a single (i.e. unshaped) near-infrared pump pulse. The corresponding spectrum is centered at $\lambda = 13.7$ μm with a spectral width (FWHM) of approximately 2 THz ($\sim 1.3\,\mu$m) as shown in the inset. We then impose a linear spectral phase $\Phi(\omega)$ on the near-infrared pulse, which delays the near-infrared and, consequently, the mid-infrared field transient by 60 fs as shown in Fig. 2.22 (b). Next, we programmed the pulse shaper to produce a pair of in-phase near-infrared pump pulses with 60 fs separation. The resulting mid-infrared transient is shown in Fig. 2.22 (c). In addition to the transients generated by the two pulses individually, i.e., the expected superposition of the transients in Figs. 2.22 (a) and (b), we find a second pulse centered around 400 fs, well after the maxima of the two phase-locked pulses. To explore this phenomenon further, we used the pulse shaper to create near-infrared pulse sequences with pulse separations being either one half or one full oscillation period of the $\lambda = 13.7\,\mu$m carrier wavelength of the mid-infrared light. In Fig. 2.23 we plot the electric field transients generated by a pair of phase-locked pump pulses separated by (a) $\Delta t = 23$ fs (equal to half the mid-infrared period) and (b) $\Delta t = 46$ fs (equal to a full mid-infrared period). The solid and dashed lines correspond to a relative phase $\Delta\Phi$ between the phase-locked pump pulses of $\Delta\Phi = 0$ and $\Delta\Phi = \pi$, respectively. The inset shows an enlarged time window around 400

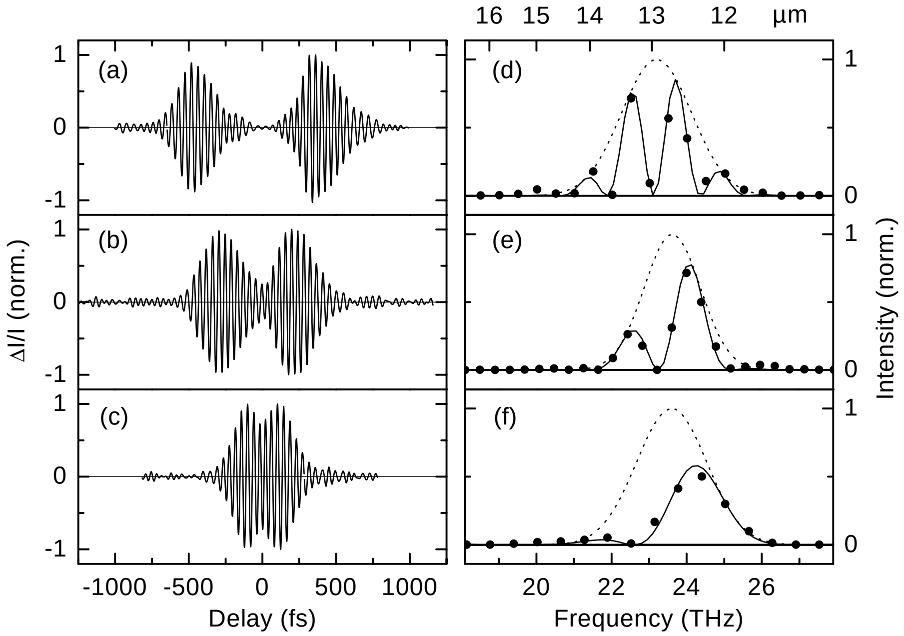

Figure 2.21: Electric field transients of mid-infrared pulses measured with free-space electro-optic sampling. The pulses centered at $\lambda = 13.0\,\mu$m are generated by a pair of phase-locked pump pulses with (a) $\Delta t = 800$ fs, (b) $\Delta t = 500$ fs, and (c) $\Delta t = 200$ fs separation. (d)-(f) Corresponding intensity spectra obtained from the Fourier transforms of the time transients (circles). The respective fit curves (solid lines) are sine functions multiplied with the spectra for a single pulse (dashed lines).

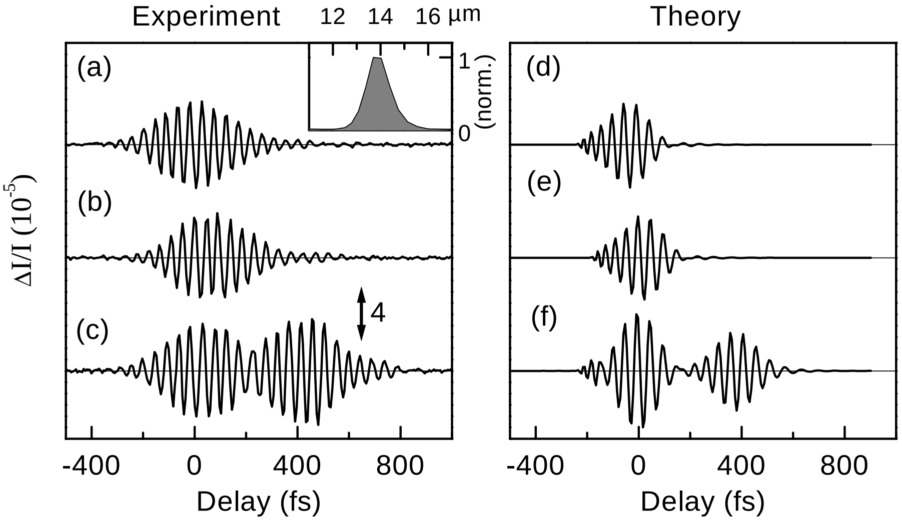

Figure 2.22: Electric field transients of mid-infrared pulses centered around $\lambda = 13.7\,\mu$m. They are generated by a pair of phase-locked pump pulses with 60 fs separation. (a),(b) Transients generated when each pump pulse is applied separately. (c) Applying two pump pulses. Inset: Fourier transform of the waveform of a single pulse, showing the pulse spectrum. (d)-(f) Corresponding theoretical curves from the model discussed in appendix A.

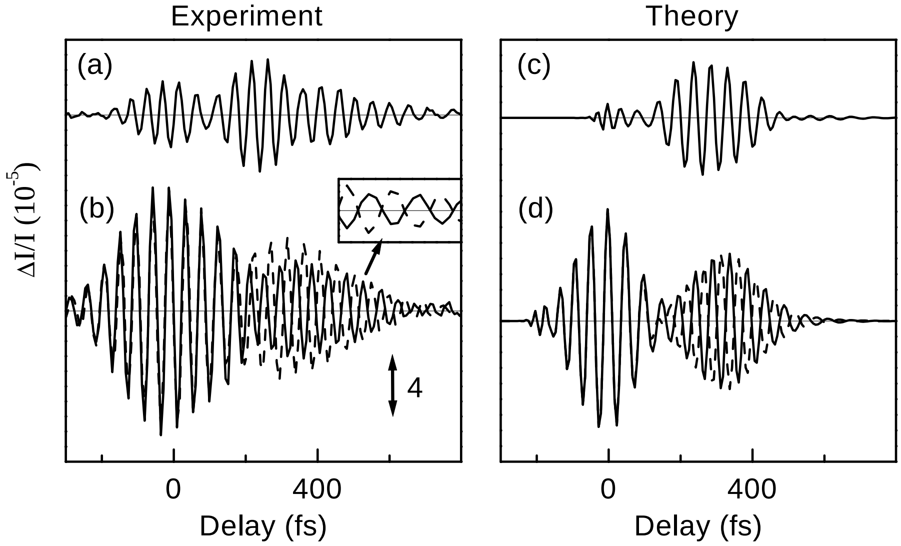

Figure 2.23: Mid-infrared waveforms generated by two near-infrared pulses with distances of (a) $\Delta t = 23$ fs (corresponding to a $\lambda/2$ retardance of the mid-infrared phase) and (b) $\Delta t = 46$ fs. The relative phase between the phase-locked near-infrared pump pulses, $\Delta\Phi$, is 0 (solid curves) and π (dashed curves). Inset, enlarged time-window around 300 fs. Corresponding model calculations are shown in (c) and (d).

fs, in which the waveform shows the following interesting behavior: the amplitude depends only weakly on the coarse separation between the phase-locked pump pulses, while the phase changes by π as we vary the relative phase between the pump pulses by the same amount. In contrast, in the time range around delay zero we obtain the expected behavior: (i) we observe either destructive [Fig. 2.23 (a)] or constructive [Fig. 2.23 (b)] interference between the two generated mid-infrared fields and (ii) the phase of the electric field transients is independent of the relative phase between the pump pulses as expected for optical rectification.

Discussion The peculiar behavior observed in our experiments is explained by the following picture: At the entrance of the GaSe crystal we have two pump pulses, $E_1(t)$ and $E_2(t) = E_1(t + \Delta t)$, each consisting of an ordinary $\vec{e}_o$ and an extraordinary $\vec{e}_{eo}$ component, i.e.,

$$\begin{aligned} \vec{E}_1(t) &= \frac{E_1(t)}{\sqrt{2}}(\vec{e}_o + \vec{e}_{eo}) \quad \text{and} \\ \vec{E}_2(t) &= \frac{E_2(t)}{\sqrt{2}}(\vec{e}_o + \vec{e}_{eo}) \end{aligned}$$

The two pump pulses generate the nonlinear polarizations

$$\begin{aligned} P_1^{NL}(t)\,\vec{e}_o &= \chi^{(2)} : E_1(t)\,\vec{e}_o : E_1(t)\,\vec{e}_{eo} \\ P_2^{NL}(t)\,\vec{e}_o &= \chi^{(2)} : E_2(t)\,\vec{e}_o : E_2(t)\,\vec{e}_{eo} \end{aligned}$$

via the optical rectification part of the $\chi^{(2)}$ tensor. Applying these pump pulses separately, we obtain the corresponding mid-infrared field transients [Figs. 2.22 (a,b)]. Now, as we apply the pulse pair $E_1(t) + E_2(t)$, the nonlinear polarization

$$P_{1/2}^{NL} = P_1^{NL}(t) + P_2^{NL}(t) + P_X^{NL}(t)$$

contains in addition to the self-terms P_1^{NL} and P_2^{NL} a cross term

$$P_X^{NL}(t)\,\vec{e}_o = \chi^{(2)} : E_1(t)\,\vec{e}_o : E_2(t)\,\vec{e}_{eo} + \chi^{(2)} : E_2(t)\,\vec{e}_o : E_1(t)\,\vec{e}_{eo}\ ,$$

depending on the electric fields of both pulses. Close to the entrance of the GaSe-crystal the self terms dominate and, thus, generate two mid-infrared pulses separated by the same delay as the corresponding pump pulses [Fig. 2.20 (b)]. In this early stage of the generation process, the cross term vanishes due to the poor temporal overlap between $E_1(t)$ and $E_2(t)$. For situations in which Δt is below the mid-infrared pulse duration the two self-terms merge into one pulse and constructive or destructive interference of the mid-infrared fields takes place according to the specific Δt. This effect explains the electric field transients around delay zero in Figs. 2.22 (c) and 2.23 (a,b). The waveforms observed around 400 fs, however, are caused by the cross terms. As the group velocities of the extraordinary and the ordinary pump pulses are different in GaSe the extraordinary part of the second pump pulse meets the ordinary part of the first pump pulse at a later position in the crystal depending on the distance between the pump pulses. Here, the contribution due to the respective self-term vanishes and the cross-term generates the second mid-infrared pulse around 400 fs. The large delay between the mid-infrared pulse pair relative to that of the pump pulses is connected to the mid-infrared/ near-infrared group velocity mismatch being much larger than that between ordinary and extraordinary pump waves. In contrast to the field transients generated by the the self-terms, the waveform caused by the cross-term is quite sensitive to the relative phase between the two pump pulses. It is obvious from the equation for P_X^{NL} that the phase of the mid-infrared field is directly connected to the relative phase between the two pump pulses [cf. solid and dashed lines in Fig. 2.23 (b)].

Model calculations Our qualitative picture is fully confirmed by detailed model calculations according to the theory derived in appendix A, which takes into account the frequency dependent refractive indices of all three interacting waves. The theoretical curves shown in Figs. 2.22 (d,e,f) and 2.23 (c,d) reproduce all the main features observed in the respective experiments as predicted by our above arguments. We attribute the relatively minor quantitative differences to a small chirp on the input pulses and to dispersion in the mid-infrared optics between the GaSe and ZnTe crystals, neither of which is included in the theory. These results on mid-infrared pulse pair generation elucidate all the essential new nonlinear optics that determine the shape of the mid-infrared field transients.

Towards arbitrary pulse shaping in the mid-infrared So far, we have experimentally demonstrated temporal phase and amplitude control of femtosecond mid-infrared pulse pairs. The generation of the mid-infrared field transients is well described by the theory in appendix A. Hence, the question is: Can we extend this concept to generate arbitrary mid-infrared pulse shapes? For this, we recall formula (2.11) which describes the mid-infrared generation with an extraordinary component A_{eo}^{NIR} and an ordinary component A_o^{NIR} of a near-infrared pulse:

$$A^{MIR}(\Delta\omega) = \int d\omega\, A_o^{NIR}(\omega + \Delta\omega)\left(A_{eo}^{NIR}(\omega)\right)^{\star}\,\alpha(\omega, \Delta\omega, L, \theta) \tag{2.14}$$

with the phase mismatch function

$$\alpha(\omega, \Delta\omega, L, \theta) = \frac{4\,\Delta\omega^2\, d}{c^2\, k(\Delta\omega)} \cdot \frac{e^{i\,\Delta k(\omega,\Delta\omega,\theta)\,L} - 1}{\Delta k(\omega, \Delta\omega, \theta)}$$

Now, we assume that A_{eo}^{NIR} and A_o^{NIR} can be controlled individually. One of the latter, e.g., A_{eo}^{NIR} we choose as a Gaussian pulse with very small bandwidth centered at ω_0, i.e., $A_{eo}^{NIR}(\omega) = 2\,\pi\,\delta(\omega - \omega_0)$. As an example, this pulse could be a picosecond pulse. Eq. (2.14) now yields

$$A^{MIR}(\Delta\omega) = \alpha(\omega_0, \Delta\omega, L, \theta)\, A_o^{NIR}(\omega_0 + \Delta\omega)$$

Since this formula can be inverted, an arbitrary mid-infrared field A^{MIR} can be generated with the corresponding near-infrared field A_o^{NIR}. Of course, this is possible only within the given frequency bandwidth of the near-infrared pulse. A very simple case is that of a thin crystal ($L \ll \frac{1}{\Delta k}$). Here, the phase mismatch can be neglected and the generated mid-infrared field directly equals the near-infrared field except for a frequency shift of ω_0. For a thick crystal, a non-negligible phase mismatch results in the narrowing of the generated mid-infrared spectrum.

This method requires that we can control the ordinary and extraordinary components of the near-infrared pulse individually. A straightforward technique would be to use two near-infrared pulse shapers. The measurements discussed above, however, pave the way for a much simpler technique using only one pulse shaper. We have seen that the ordinary component of the first pulse of a pulse pair meets the extraordinary component of the second after having passed a certain distance in the GaSe crystal. This results in the cross term. Since we can shape both pulses of a pulse pair individually with the near-infrared pulse shaper the only resulting requirement is the suppression of the self-terms. This could be accomplished, e.g., by separating the two components from each other in time by passing them through a birefringent crystal before they enter the GaSe crystal. This scheme for the generation of arbitrarily shaped mid-infrared pulses is shown in Fig. 2.24.

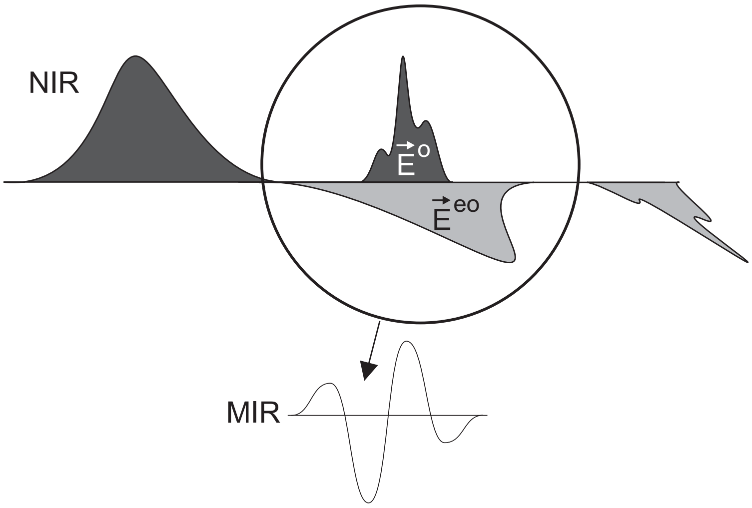

Figure 2.24: Scheme of the generation of arbitrarily shaped mid-infrared pulses.

Chapter 3

Coherent dynamics of intersubband transitions

In this chapter we introduce the basics about the coherent dynamics of intersubband transitions in quasi-two dimensional semiconductor nanostructures. This physics plays a fundamental role for the time-resolved experiments discussed in this thesis, i.e., coherent control of intersubband excitations in quantum wells and carrier transport in semiconductor devices (quantum cascade lasers).

We start with a short introduction into the electronic and optical properties of quasi-two dimensional semiconductor nanostructures. We discuss the optical transitions occurring between quantized subbands due to the carrier confinement. The known characteristics about intersubband absorption and the ultrafast dynamics of intersubband excitations are reviewed. As a first application we present a concept for coherent control of intersubband transitions.

In the subsequent section, electron transport in coupled quantum well systems is discussed. Transport in terms of resonant tunneling in double quantum wells and superlattices is explained and experimental studies are discussed. Finally, the quantum cascade laser is introduced. Here, electron transport plays an essential role. We review the current status and open questions concerning electron transport in quantum cascade structures and explain the experimental concept employed for the ultrafast electron transport studies carried out in this thesis.

3.1 Quasi-two dimensional heterostructures

Modern techniques like molecular beam epitaxy [62, 63, 64] or metal-organic vapor phase epitaxy [65] allow the controlled growth of low-dimensional semiconductor nanostructures on an atomic length scale. The basic principle is illustrated in Fig. 3.1 (a): A sequence of nanometer-thick layers using material systems like GaAs/AlGaAs, GaInAs/InP, GaInAs/AlInAs, or Ge/Si are deposited alternately on each other. In this thesis, we will concentrate on the material system GaAs/AlGaAs.

The different band gaps of the individual materials lead to a carrier confinement along the growth direction giving rise to new electronic and optical properties, which will be discussed in the following.

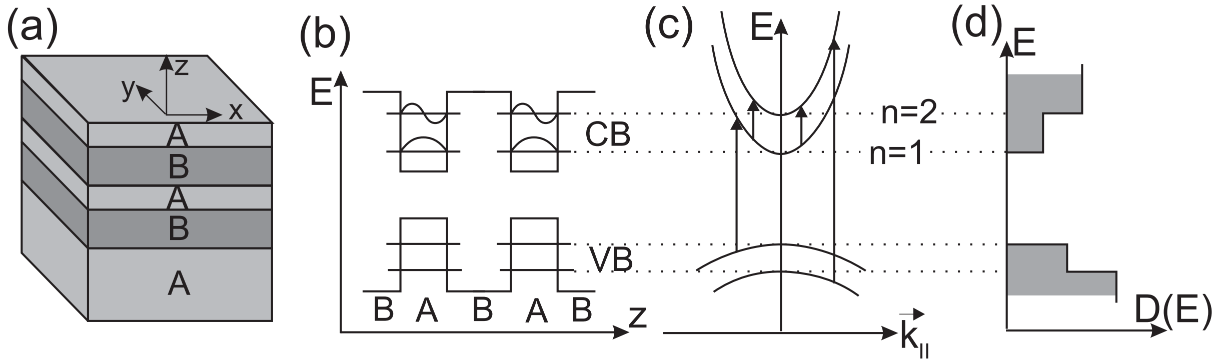

Figure 3.1: (a) Thin layers of different materials A (e.g. GaAs) and B (e.g. AlGaAs) are grown alternately on each other. (b) Due to the conduction band (CB) and valence band (VB) discontinuity the carriers are confined in the potential wells leading to discrete levels. (c) The carriers can propagate freely in x- and y-direction leading to a subband structure. (d) Step-like density of states in the conduction and valence band.

3.1.1 Electronic and optical properties

The bandgap discontinuity in growth direction (z-direction) leads to rectangular shaped potential wells and barriers for the carriers in the valence and the conduction band [Fig. 3.1 (b)]. The distribution of the bandgap discontinuity among the valence and conduction band depends on the specific material system. In z-direction the carriers are confined in the so-called quantum wells according to the one-dimensional Schrödinger equation, which reads in the effective mass approximation [24]

$$\left(-\frac{\hbar^2}{2\, m^{eff}}\, \frac{\partial^2}{\partial\, z^2} + V(z)\right) \zeta_n(z) = E_n\, \zeta_n(z)$$

Here, ζ is the envelope function of the electron (hole), m^{eff} is the electron (hole) effective mass, and V is the confinement potential. The confinement leads to a quantized motion in z-direction with eigenenergies E_n $(n = 1, 2, ...)$ as depicted in Fig. 3.1 (b). The energy positions of the different levels can be tailored by varying the quantum well widths. Since the carriers can move freely parallel to the layers (x, y–direction) the quantized energy levels represent the bottom of two-dimensional subbands [Fig. 3.1(c)] with different effective masses and nonparabolicities according to the details of the band structure. Another important consequence of the quantum confinement in z-direction is a step-like density of states as depicted in Fig. 3.1 (d), in contrast to the square-root dependence in bulk material.

In the first part of this chapter we will concentrate on multiple quantum well structures, where the barriers are much thicker than the penetration depth of the envelope wavefunction into the barrier. Here, the coupling between different quantum wells can be neglected. Quantum well structures, where the barriers between adjacent quantum wells are thin so that their coupling can't be neglected are called superlattice structures. The coupling between quantum wells is quite important for device structures like the quantum cascade laser. We will discuss such effects later.

The subbands in the individual bands give rise to a new kind of electronic transition, the intersubband transitions. Such transitions can occur due to scattering (e.g. carrier-phonon or carrier-carrier scattering), due to spontaneous emission of a photon, or induced by an

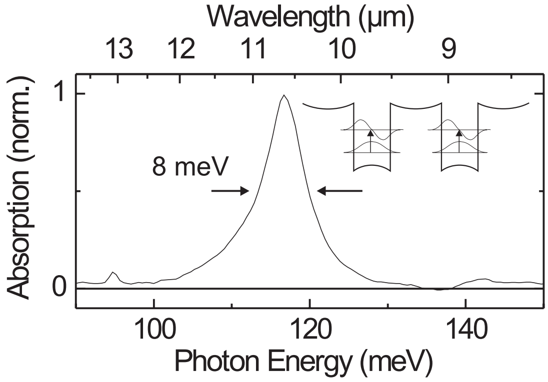

Figure 3.2: Intersubband absorption [(n=1)→(n=2)] of a modulation-doped GaAs/$Al_{0.35}Ga_{0.65}As$ multiple quantum well structure with a doping of 6×10^{11} cm^{-2} measured at 15 K. The quantum well thickness is 9 nm and the barrier thickness 20 nm [69].

optical field. For typical layer thicknesses on the order of 10 nm the energy splitting of the subbands corresponds to wavelengths in the mid-infrared wavelength range.

Optically induced intersubband transitions are frequently studied in n- or p-doped multiple quantum well structures. Modulation-doped structures contain a layer of impurities in the center of the barriers, e.g., Si-δ-doping in AlGaAs barriers between GaAs wells, spatially separated from the quantum wells. The donors provide free electrons forming a quasi-two dimensional electron plasma in the lowest subband of the quantum wells. The spatial separation of electrons and ionized impurities modifies the potential energy profile of the free carriers. Additional potential minima in the barriers and potential maxima in the wells occur (see inset of Fig. 3.2). In the structures investigated in this thesis the well potential for the electrons is much deeper than the barrier minima which results in a complete electron transfer to the wells and in a strong confinement of the carriers in the lowest subbands.

In a symmetric quantum well, optical transitions only between subbands of different parity, e.g., 1–2, 2–3, or 1–4, are dipole-allowed and result in intersubband absorption and emission. The intersubband dipole is oriented along z so that only the z-component of an electromagnetic wave (P polarization) induces an electronic intersubband transition. However, very small contributions of S polarized absorption is measured, which is due to k·p mixing between valence and conduction band states [66].

The energy position of an intersubband transition is correlated with the energy separation between the subbands. Due to the identical sign of the subband curvature the intersubband absorption is concentrated in narrow lines, in contrast to the broad optical spectra of interband absorption. Thus, intersubband transitions are characterized by very large absorption cross sections [67, 68]. The finite linewidth of the intersubband absorption is due to different broadening mechanisms, which will be discussed in the next section.

3.1.2 Intersubband absorption

Optical intersubband transitions were first observed in high-density inversion layers of heterostructures in the 1970s [70, 71]. In the GaAs/AlGaAs system stationary intersubband absorption has been discussed in a large amount of studies, including Refs. [67, 68, 72, 73]. Typical linewidths range from ≈ 3 meV [73] to 25 meV [72]. In Fig. 3.2 the intersubband absorption spectrum of a n-type modulation-doped GaAs/AlGaAs multiple quantum well structure with a well width of 9 nm, a barrier thickness of 20 nm, and a doping of 6×10^{11} cm^{-2} is displayed. The peak position of this line is at 116 meV. The linewidth (FWHM) has a value of 8 meV. The decay dynamics of the macroscopic intersubband polarization determines the shape and width of the intersubband line. There are different broadening mechanisms determining the linewidth of the intersubband absorption which will be briefly discussed in the following [5]:

- Homogeneous broadening: Any scattering process which changes the relative phase between the involved subbands result in a damping of the macroscopic intersubband polarization. The relevant scattering mechanisms are electron-electron scattering, electron-phonon scattering and disorder scattering. Neglecting any memory effects (Markovian limit) these scattering processes lead to a Lorentzian shaped absorption line. It is characterized by the decay time of the coherent polarization T_2. This decay time was already introduced in chapter 2 as a phenomenological damping term in the density matrix formalism of a quantum mechanical two-level system.

- Inhomogeneous broadening: In most cases the system cannot be characterized by a two-level system with a single transition energy. Typically there is an *inhomogeneous* distribution of those. The destructive interference of the different oscillators accounts additionally for the decay of the macroscopic polarization. The main mechanisms contributing to such an inhomogeneous broadening are structural disorder like fluctuations of the potential well width or fluctuations of the alloy composition and intrinsic effects like the different effective masses of the subbands and nonparabolic subband dispersions [74].

- Many-body effects: The picture of independent two-level systems as presented above is an approximation. In particular at high carrier concentrations the coupling of different oscillators via the Coulomb interaction has to be taken into account. This changes the behavior of the system with respect to the interaction with an electromagnetic wave leading to a change in the shape, width, and position of the intersubband absorption line. A prominent many-body effect is the depolarization shift [75]. A collective charge density oscillation in z–direction induced by a coherent excitation leads to an oscillating charge separation. Consequently, the Coulomb-interaction among the carriers results in an additional back-driving force for the carriers and shifts the transition frequency to higher energies (blue shift). In addition, this effect also leads to a narrowing of the absorption line [76].

  Many-body effects are very significant in case of wide wells, i.e., large intersubband dipoles, and high carrier concentrations. Here, the mere single-particle picture is not adequate to describe the position and width of the intersubband line.

3.1.3 Ultrafast dynamics of intersubband excitations

The different processes responsible for the line broadening discussed above take place on an ultrafast timescale. The methods of ultrafast spectroscopy, especially pump-probe spectroscopy and four-wave mixing, have given a deep insight into these mechanisms

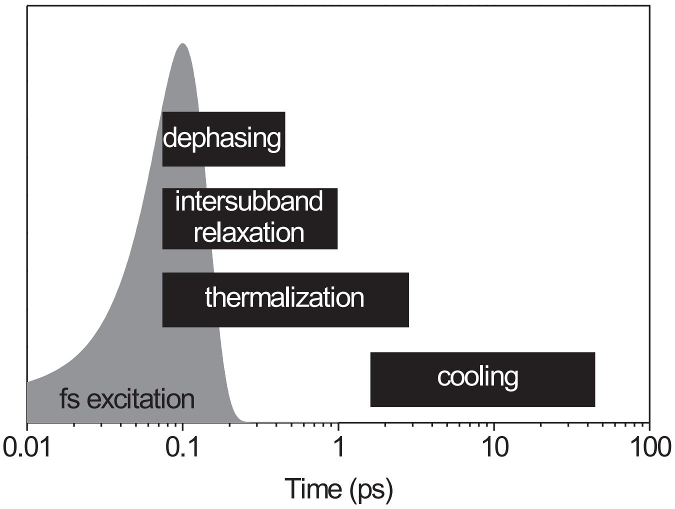

Figure 3.3: Schematics of the different timescales of ultrafast processes occurring after a femtosecond intersubband excitation.

[77, 78, 18, 5, 41, 79, 69]. In addition to those dephasing processes, ultrafast spectroscopy reveals also information about carrier redistribution mechanisms. After excitation with an ultrashort pulse, the carrier system undergoes several stages of relaxation before it returns to the thermodynamic equilibrium. Carrier relaxation can be classified by four temporally overlapping regimes as shown in Fig. 3.3 [4]. In the following, we summarize the main mechanisms for carrier relaxation after resonant intersubband excitation in the case of modulation doped GaInAs/AlInAs and GaAs/AlGaAs quantum well structures with subband spacings substantially larger than the energy of a linear-optical (LO) phonon. We restrict our discussion to low carrier concentrations for which many-body effects are less important.

- Dephasing of coherent polarizations: The resonant interaction of a coherent ultrashort pulse with an intersubband transition creates a coherent, macroscopic optical polarization between the optically coupled states with equal in-plane momenta. Additionally it creates an occupation of electron states in the upper subband which was unoccupied before.

  In the quantum mechanical density-matrix formulation for a single two-level system as discussed in the previous chapter the coherent polarization is identified with the off-diagonal elements of the density matrix and the occupations are described by the diagonal elements. The intersubband polarizations dephase on a time scale of several hundreds of femtoseconds for intersubband spacings of $\approx 100-200$ meV as determined in four-wave mixing experiments [18, 69]. Dephasing mechanisms are electron-electron, intraband LO phonon and electron-impurity scattering. Such processes result in a *homogeneous* broadening of the intersubband transition. As the structures considered are modulation doped the electron gas in the quantum wells is spatially separated from the ionized donors in the barriers. This leads to a reduced ionized impurity scattering of electrons with a characteristic scattering time of 1–2 ps [80], which is much longer

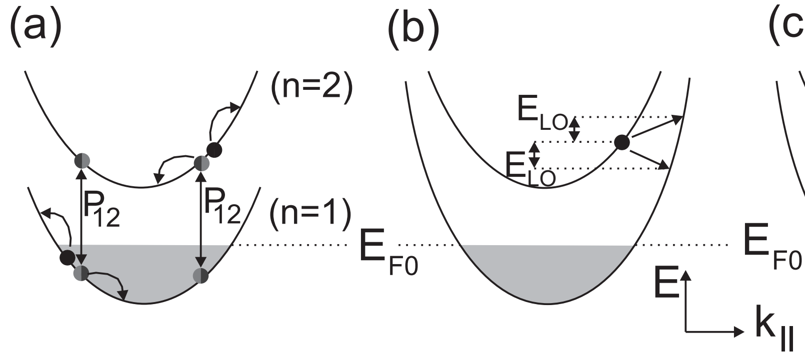

Figure 3.4: Main mechanisms of carrier relaxation after an ultrafast, coherent optical excitation (E_{F0}–Fermi energy). (a) For negligible inhomogeneous broadening the main mechanism for dephasing of the macroscopic intersubband polarization P_{12} is electron-electron scattering. (b) If the subband spacing is higher than the LO phonon energy the main intersubband relaxation mechanism is electron-LO phonon scattering. For large subband spacings, the electrons are transferred into states in the lower subbands with high in-plane momenta. (c) Thermalization is dominated by Coulomb scattering between high- and low-energy carriers which leads to a heating of the cold electron plasma.

than the observed dephasing times. At low temperatures (10 K) the LO phonon absorption by electrons is negligible. For electron concentrations below $\approx 10^{12}$ cm^{-2}, which will be present in the sample investigated in the subsequent chapter, the Fermi energy is below the LO phonon energy so that LO phonon emission is also negligible. Intersubband population relaxation plays a minor role for dephasing as it occurs with a longer time constant as will be discussed below [77, 78, 41, 69]. Hence, the main scattering mechanism leading to a homogeneous dephasing at low temperatures and low electron concentrations is electron-electron scattering as depicted in Fig. 3.4 (a). It should be noted that a theoretical analysis of intersubband dephasing by electron-electron scattering has not been performed until now.

An additional damping mechanism for the macroscopic intersubband polarization exists in the case of *inhomogeneously* distributed two-level systems due to structural disorder or intrinsic effects as described above. The rigid macroscopic phase relationship existing for short moments after excitation is destroyed due to the time evolution of these oscillators with different frequencies. Nowadays, high quality GaAs/AlGaAs quantum wells show negligible inhomogeneous dephasing as was shown by time-resolved four-wave mixing experiments [69].

- Intersubband relaxation: Electrons which are excited by optical excitation into the higher subbands can relax into lower subbands due to the interaction with electrons via Coulomb scattering and with the lattice via phonon scattering. For subband spacings far above the LO phonon energy this leads to the population of states in the lower subband with large in-plane momenta [see Fig. 3.4 (b)]. The relaxation time depends on the subband spacing. Because of the $1/k^2$-dependence of the electron-LO phonon scattering rate, a subband spacing resonant to the LO phonon energy results in a much shorter relaxation time than a subband spacing far above the LO phonon energy. This behavior is exploited in quantum cascade lasers to ensure a short lifetime in the lower laser subband.

In intersubband pump-probe measurements it was observed that the relaxation times were independent of the electron concentration [78, 41]. Thus LO phonon scattering is the main relaxation mechanism. The same measurements yielded typical intersubband relaxation time constants of around $\approx 0.5 - 1.5$ ps for subband spacing above the LO phonon energy, which is in good agreement with theoretical models [81].

- Thermalization: Intersubband relaxation results in a carrier distribution in the lower subband far away from thermal equilibrium. Subsequent scattering leads to a carrier redistribution, which transforms the system from an athermal into a quasi-equilibrium distribution. As part of the excess energy from the optical excitation remains in the carrier system, this quasi-equilibrium is characterized by an elevated electron temperature. The main scattering mechanisms for thermalization are electron-phonon scattering transferring excess energy to the lattice and Coulomb scattering between high- and low-energy carriers which leads to a heating of the cold electron plasma.

  Using intersubband pump-interband probe experiments the thermalization was experimentally monitored [78, 41]. Athermal electron distributions created by ultrafast intersubband excitation were observed for delay times up to 2 ps. The data were well reproduced by ensemble Monte Carlo simulations [82]. These calculations show that electron thermalization at low lattice temperatures occurs mainly due to electron-electron scattering [see Fig. 3.4 (c)] with rates strongly reduced by Pauli blocking and screening and due to the picosecond supply of hot electrons from the upper subband.

  In contrast to these low temperature results, sub-100 fs thermalization times were observed at room temperature [83].

- Carrier cooling: After the carrier system is transferred into a Fermi distribution with an electron temperature substantially higher than the lattice temperature the final relaxation stage is carrier cooling. The main cooling mechanisms involve LO phonon and, to a lesser extent, acoustic phonon scattering.

  Intersubband pump-interband probe experiments were used to measure the dynamics of carrier cooling [78, 41]. It was found that within 25 ps the Fermi distribution cools down to 50 K independent on the plasma density in a range of electron concentrations between 1.5×10^{11} and 1.5×10^{12} cm^{-2}.

3.2 Coherent control in semiconductor nanostructures

Semiconductor nanostructures have a broad potential in applications like optical switching [84] and modulation [85] with ultrafast switch-on and switch-off times. Moreover, they are important model systems for coherent control of material excitations on ultrafast time scales [9].

In the following we will discuss some important studies on coherent control in semiconductor nanostructures that have been done so far.

Most research has concentrated on interband and excitonic excitations in quasi-two dimensional quantum wells for which different schemes of coherent control of optical polarizations and photoinduced electric currents have been realized. In quasistationary experiments, the nonlinear coupling of intersubband excitations and excitonic transitions has been studied

[86]. A strong change in the interband absorption spectrum due to the resonant coupling of the lowest subbands by a high-power laser was observed, the so-called optical quantum-confined Stark effect.

Further, coherent control of photocurrents have been demonstrated. Haché et al. [87] studied the coherent generation and control of photocurrent in bulk GaAs via interband absorption with a phaselocked pulse pair. Of great interest is the manipulation of carrier populations, because it represents an important step towards ultrafast optoelectronics and all-optical switching. Coherent control of excitons has been reported by Heberle et al. [9]. They coherently controlled the generation and destruction of excitons in quantum wells by the time delay of a sequence of two phase-locked optical pump pulses. A later probe pulse recorded the resulting exciton density. Here, the long exciton dephasing times enable the generation and destruction of excitons for pump pulse distances of several picoseconds.

Concepts for coherent control involving intersubband excitations have been investigated in a number of theoretical studies. Hu and Pötz [88] studied the coherent control of optical gain from electronic intersubband transitions in semiconductors. Neogi et al. [89] demonstrated that interband transitions in semiconductor quantum wells can be manipulated by the optimization of a pulsed intersubband control-light field.

Only few experiments addressed the properties of coherent intersubband polarizations and their application for coherent optical switching. In Ref. [90] coherent charge oscillations after interband excitation in a quantum well were observed by monitoring the emitted electromagnetic radiation. With a phaselocked pulse pair, Dupont et al. [91] controlled the direction of the emission of photoexcited electrons via bound-to-free transitions in AlGaAs/GaAs quantum well superlattices.

Coherent control of bound-to-bound intersubband transitions, however, has not been done so far. Due to the very high absorption cross section of such transitions sizable intersubband excitations should be reachable with very weak ultrashort electric field-transients resonant to the intersubband transition.

Experimental concept for coherent control of intersubband transitions The ultrafast dynamics of intersubband excitations in quasi-two dimensional semiconductors are well understood. The high structural quality of state-of-the-art GaAs/AlGaAs quantum wells results in a strong reduction of disorder-induced inhomogeneous broadening of intersubband resonances, leading to rather narrow intersubband absorption spectra with comparatively long dephasing times. Hence, those structures are supposed to be ideal model systems for coherent control of intersubband resonances on a sub-picosecond time scale.

The new methods of controlled shaping and time-resolved detection of electric field transients in the mid-infrared presented in the previous chapter now allow to investigate and directly manipulate coherent intersubband excitations in the time domain. In the experiments presented in the next chapter, we investigate the coherent nonlinear manipulation of intersubband populations and polarizations in GaAs/AlGaAs quantum wells by weak ultrashort electric field-transients resonant to the intersubband transition. Coherent polarizations on the transition between the $n = 1$ and $n = 2$ conduction subband are generated by shaped mid-infrared transients at a megahertz repetition rate. The re-emitted free induction decay is measured with electro-optic sampling.

3.3 Carrier transport in semiconductor nanostructures

Ultrafast spectroscopy provides a powerful tool to investigate and coherently control the dynamics of intersubband excitations. Now, we discuss the use of ultrafast spectroscopy to investigate the dynamics of transport in quasi-two dimensional semiconductor nanostructures. For nanostructure devices, such as the quantum cascade laser, carrier transport plays a fundamental role and its detailed understanding is a prerequisite for further performance improvements of these structures.

Vertical transport in semiconductor nanostructures is inherently connected with tunneling—a quantum-mechanical phenomenon that has no classical analogue. As tunneling takes place on an ultrafast timescale, all-optical techniques, such as pump-probe spectroscopy, four-wave-mixing spectroscopy, etc., are appropriate methods to study transport in semiconductor nanostructures. Time-resolved all-optical studies of tunneling began in the late 1980s [92] and much effort has been undertaken in this field until now. In the following, we want to consider briefly transport studies in double quantum well and superlattice structures before we discuss transport in quantum cascade structures. Finally, we will consider open questions connected with electron transport in semiconductor nanostructures and present an experimental concept to elucidate those.

3.3.1 Coupled quantum wells

So far, we have considered single quantum wells or multiple quantum well structures with thick barriers for which there is practically no coupling between subsequent quantum wells.

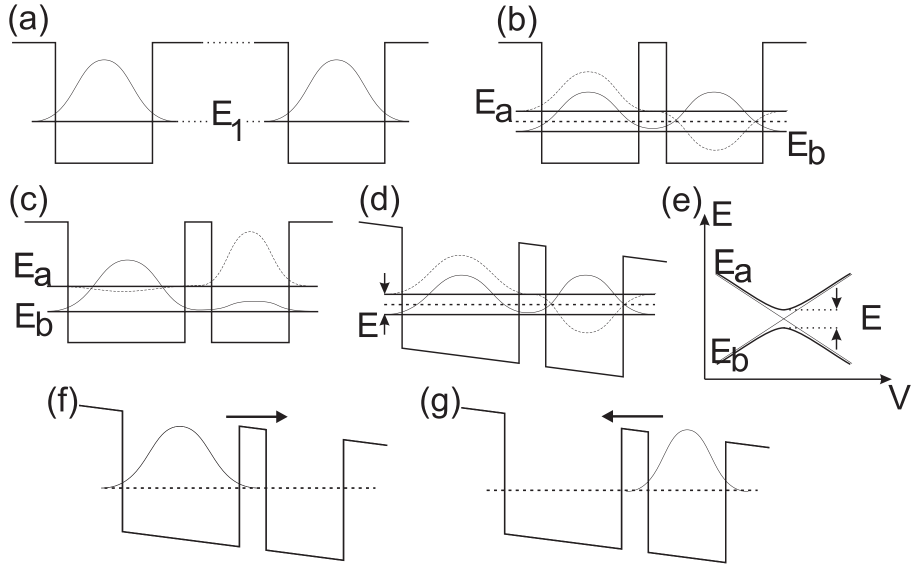

Figure 3.5: Coupling of quantum wells. (a) Symmetric double quantum wells with large barrier width (negligible coupling). (b) The small barrier width leads to a coupling of the quantum wells. The corresponding states are the binding $|\,b\rangle$ and the anti-binding $|\,a\rangle$ state with an energy splitting $\Delta E = E_a - E_b$. (c) Asymmetric double quantum well. (d) Resonant situation with applied bias. (e) Fan chart for an asymmetric double quantum well structure with applied bias V. (f) Wavepacket $|\,l\rangle = \frac{|\,b\rangle+|\,a\rangle}{\sqrt{2}}$. (g) Wavepacket after $T_{osc}/2$, $|\,r\rangle = \frac{|\,b\rangle-|\,a\rangle}{\sqrt{2}}$.

In this case, the quantum wells can be treated independently. When the barrier thickness becomes smaller, coupling between the wells has to be taken into account. This is schematically depicted in Figs. 3.5 (a) and (b), where the well widths are equal. In Fig. 3.5 (a) the barrier is very thick so that coupling can be neglected and the eigenstates are localized in the respective wells. In Fig. 3.5 (b) the barrier is thin so that there is coupling between the two wells. As a consequence, an energy splitting with energies E_a and E_b occurs and the respective electron states, the so-called binding ($|\, b\rangle$) and anti-binding ($|\, a\rangle$) states, are delocalized over both wells. The energy splitting or tunnel coupling $\Delta E \equiv E_a - E_b$ is determined by the barrier thickness and the barrier height. Such a resonant situation can also be obtained for asymmetric, coupled double quantum wells with applied bias. In Fig. 3.5 (c) the lowest two states of an asymmetric, coupled double quantum well are shown. The lowest state is mainly localized in the wide well and the other state is mainly localized in the narrow well. Due to the coupling of the two wells the two states have nonzero probability density in both wells. Under a suitable bias these two states become resonant [Fig. 3.5 (d)] and we observe the same behavior as described above. In Fig. 3.5 (e) the energies of the two states as a function of the applied bias are schematically shown (fan chart). The minimal energy splitting ΔE is observed at resonance.

After the coherent excitation of an electronic wavepacket, e.g., by optical excitation with a pulse which is spectrally broader than $\Delta\omega = \Delta E/\hbar$, an oscillatory motion is expected. Such a wavepacket consisting of a coherent superposition of the binding and the anti-binding state reads

$$|\, ab, \phi\rangle(t) = \frac{1}{\sqrt{2}}\Big(|\, b\rangle + |\, a\rangle\, e^{i\left(\frac{\Delta E}{\hbar}t+\phi\right)}\Big) \tag{3.1}$$

In Fig. 3.5 (f) a wavepacket localized in the left well

$$|\, l\rangle = |\, ab, 0\rangle(0) = \frac{|\, b\rangle + |\, a\rangle}{\sqrt{2}}$$

is shown. As time elapses, this wavepacket tunnels through the barrier and after a time $\frac{T_{osc}}{2}$ (tunneling time) it is localized in the right well [Fig. 3.5 (g)]

$$|\, r\rangle = |\, ab, 0\rangle(\frac{T_{osc}}{2}) = \frac{|\, b\rangle - |\, a\rangle}{\sqrt{2}}$$

After one oscillation period the wavepacket is localized again in the left well

$$|\, l\rangle = |\, ab, 0\rangle(T_{osc})$$

From Eq. (3.1) it can be easily seen that the oscillation period is directly connected with the energy splitting by the relation

$$T_{osc} = \frac{h}{\Delta E}$$

Assuming the energy eigenstates $|a\rangle$ and $|b\rangle$ as a single, homogeneously broadened 2-level system dephasing leads to an exponential damping of the oscillation with a damping rate $\Gamma = 1/T_2$. The normalized spatial displacement of the wavepacket in z-direction yields

$$z(t) = e^{-t/T_2}\, \cos(\omega_{osc}\, t + \phi)\,, \quad \omega_{osc} = \frac{2\,\pi}{T_{osc}}$$

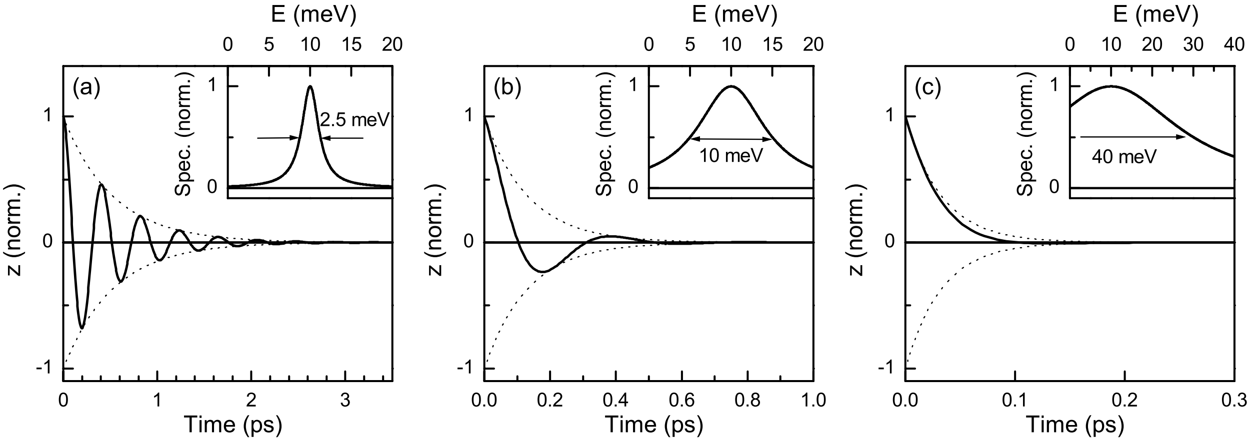

Figure 3.6: Exponentially damped oscillation $z(t) = e^{-t/T_2}\cos(2\pi\,t/T_{osc})$ as a function of time. The oscillation period is $T_{osc} = 410$ fs corresponding to an energy splitting of $\Delta E = 10$ meV. (a) Oscillation for a damping time $T_2 = \frac{4}{\pi}\,T_{osc}$, i.e., $2\,\hbar\,\Gamma = 0.25\cdot\hbar\,\omega_{osc} = 2.5$ meV. (b) Oscillation for a damping time $T_2 = \frac{1}{\pi}\,T_{osc}$, i.e., $2\,\hbar\,\Gamma = \hbar\,\omega_{osc} = 10$ meV. (c) Oscillation for a damping time $T_2 = \frac{1}{4\pi}\,T_{osc}$, i.e., $2\,\hbar\,\Gamma = 4\cdot\hbar\,\omega_{osc} = 40$ meV. Inset: Fourier transforms of the respective transients.

as shown in Fig. 3.6 (a). The Fourier transform of the exponentially damped oscillation yields a Lorentz line (Insets of Fig. 3.6)

$$\tilde{z}(\omega) = \frac{1/T_2}{(1/T_2)^2 + (\omega_0 - \omega)^2}$$

with the homogeneous linewidth $2\,\Gamma = 2/T_2$. The coherence of the oscillation strongly depends on Γ. For $\Gamma \geq \omega_{osc}$ the oscillation is heavily damped [Fig. 3.6 (c)] so that the original wavepacket is completely dephased after one oscillation. We define electron transport as coherent if $\Gamma < \omega_{osc}$ [Fig. 3.6 (a)] and incoherent if $\Gamma > \omega_{osc}$ [Fig. 3.6 (c)].

So far, we have only considered the case of resonant tunneling. Also non-resonant tunneling plays an important role for transport in semiconductor nanostructures. For simplicity, we will not discuss non-resonant tunneling now but we will come back to this point in the discussion of the transport measurements on quantum cascade structures.

In the following we want to discuss some important experimental studies related to vertical electron transport in semiconductor nanostructures.

Tunneling in biased quantum well structures was first observed by Oberli et al. [93]. The authors used a biased, asymmetric, coupled double quantum well structure based on the GaAs/AlGaAs material system. Carriers were generated in one of the quantum wells via sub-picosecond interband photoexcitation and the subsequent luminescence was measured time-resolved. The tunneling time was identified with the photoluminescence decay time. As expected, a strong reduction of the tunneling time was observed if the two states in the respective quantum wells are resonantly coupled. Wavepacket oscillations between the wells of a biased, asymmetric GaAs/AlGaAs double quantum well were observed by Leo et al. [94]. They created an electronic wave packet in the wide well via ultrafast interband photoexcitation and traced the oscillatory motion of this wave packet by degenerate four-wave mixing and by pump-probe spectroscopy. In a further experiment by Roskos et al.

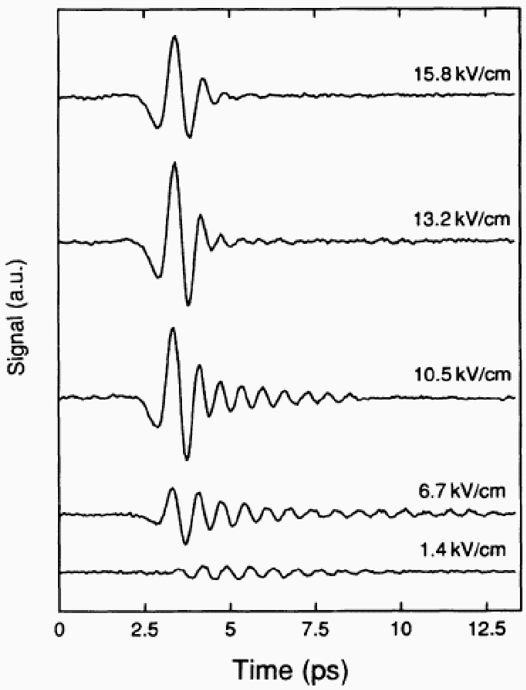

Figure 3.7: Measured coherent electromagnetic transients emitted from an asymmetric double quantum well for different bias fields [95].

[95] such a wave packet oscillation was directly observed by time-resolved detection of the THz emission from this spatial charge oscillation as shown in Fig. 3.7. In resonance, several oscillations were observed at carrier densities on the order of 10^9 cm^{-2}. From the decay of the coherent electromagnetic signal at resonance a dephasing time of $T_2 \approx 7$ ps was deduced compared to an oscillation period of $T_{osc} \approx 1$ ps.

Tunneling was also studied in superlattice structures with many coupled quantum wells. Here, wavepacket oscillations—the so-called Bloch oscillations—were observed. [96, 1]. The first Bloch oscillations were observed with four-wave-mixing experiments in a semiconductor superlattice by Feldmann et al. [14]. The oscillations have been induced by femtosecond interband excitation and monitored in real-time. Martini et al. [97] studied the coherent THz emission from interband excited Bloch oscillations as a function of excitation density. Pronounced oscillatory motions with an oscillation period $T_{osc} \approx 600$ fs were found for electron concentrations of up to several 10^9 cm^{-2}, whereas a rapid damping of the oscillations occurs at higher carrier densities as shown in Fig. 3.8 (a). For the homogeneous linewidth of the oscillation $2\,\Gamma = 2/T_2$ [Fig. 3.8 (b)] as a function of the excitation density n_{ex} they derived the linear expression

$$\Gamma(n_{ex}) = \Gamma(0) + \nu \cdot n_{ex}\,, \quad \Gamma(0) = \frac{1}{\hbar} 1.2 \text{ meV}\,, \nu = \frac{1}{\hbar} 9 \cdot 10^{-11} \text{ meV} \cdot \text{cm}^2 \cdot n_{\text{well}} \qquad (3.2)$$

For $n_{ex} < 10^{10}$ cm^{-2} the dephasing times are higher than the oscillation period and the transport is coherent. For higher carrier densities the transport is incoherent.

So far, we have seen that transport in double quantum wells and superlattices can be described in terms of tunneling. It is coherent for electron sheet densities $< 10^{10}$ cm^{-2}. In electrically driven device structures like quantum cascade lasers, however, the carrier sheet

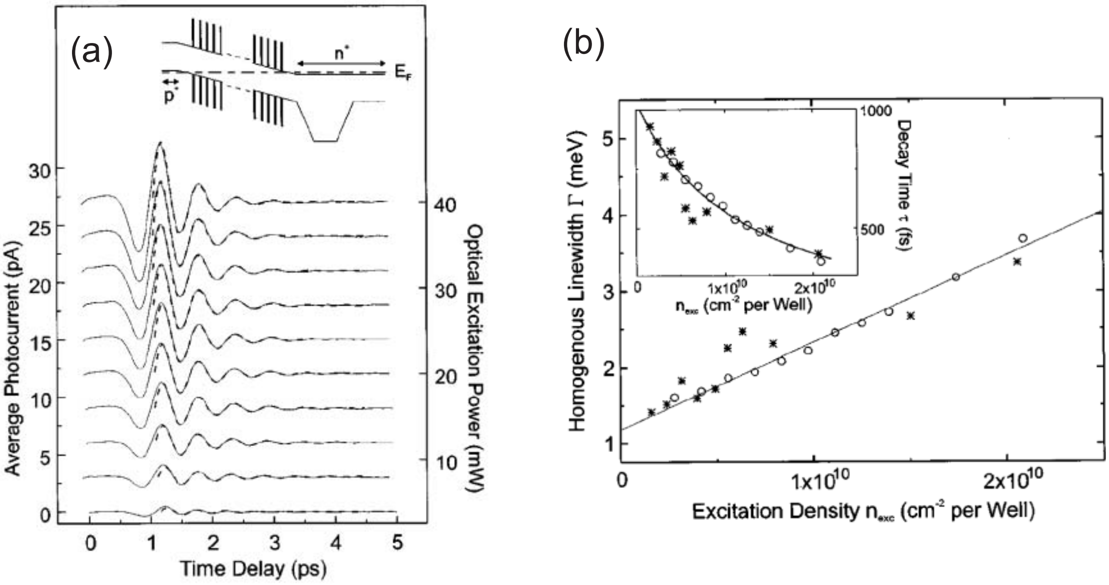

Figure 3.8: (a) Measured coherent electromagnetic transients emitted from a GaAs/AlGaAs superlattice structure for various optical excitation powers. (b) Homogeneous linewidth Γ and decay time constant (inset) of the THz pulses as a function of excitation density [97].

densities are typically $\approx 4 \times 10^{11}$ cm^{-2}. Extrapolating the data measured by Martini et al. using equation (3.2) one would expect dephasing times of ≈ 30 fs at such elevated electron densities. For a typical energy splitting on the order of 10 meV ($h/10$ meV $= 410$ fs) this suggests that the transport in such structures is expected to be fully incoherent. However, such dephasing times have never been measured experimentally.

It is important to note that in the experiments described above, electronic wavepackets were generated via interband excitation, where the dephasing times are strongly influenced by electron-hole interaction. To study electron transport in unipolar devices, a measurement avoiding the generation of both electrons and holes at the same time is necessary. This has not been done so far.

3.3.2 Quantum cascade structures

Light amplification exploiting intersubband transitions was first predicted by Kazarinov and Suris in 1971 [98]. It took another two decades, however, until the first laser based on intersubband transitions, the so-called quantum cascade laser was experimentally demonstrated by Faist et al. [3]. This laser works at 10 K in pulsed operation with a peak power of 8 mW. The emission wavelength is $\lambda = 4.2\,\mu$m. So far, quantum cascade lasers have been demonstrated using the InGaAs/AlInAs and GaAs/AlGaAs material systems.

In the following, we explain the basic working principle of quantum cascade lasers before we illustrate the progress that has been done since its first realization. Finally, we discuss the techniques that have been used so far for the characterization of quantum cascade laser structures and the physical insight that have been gained from those techniques.

3.3.2.1 Basics of quantum cascade lasers

In Fig. 3.9 the conduction band diagram of a GaAs/AlGaAs quantum cascade laser under bias is shown. Typical quantum cascade lasers consist of 20-30 periods each containing an injector region and an active region. To minimize space-charge effects caused by carrier injection under applied bias, the injector region is *n*-type doped. The doping concentration per period is typically 2–4 $\times\ 10^{11}$ cm^{-2}. The active region acts as a three-level laser system. To achieve population inversion between subband 3 and subband 2 the active region is designed so that the energy separation between subband 2 and subband 1 is almost resonant to the LO phonon energy. In this way, intersubband relaxation from subband 2 to subband 1 by emission of LO phonons is strongly enhanced, which results in a lifetime of subband 2 on the order of $\tau_2 \approx 300$ fs whereas the lifetime of subband 3 is typically $\tau_3 \approx 1$ ps. Electrons leave the active region by tunneling through a thin exit barrier into the following injector region. The injector region acts as an electron reservoir. It is a superlattice which consists of typically 5 quantum wells. It is designed in such way that under applied bias the coupling between adjacent quantum wells leads to the formation of minibands which ensures an efficient carrier transport. The minigap prevents electrons residing in the upper laser subband 3 from leaking into the continuum states. A crucial point is the carrier injection from the injector into the upper laser subband 3 in the active region. Under an appropriate bias, the injector subband g becomes resonant with subband 3. This leads to an efficient carrier injection via resonant tunneling. However, the very high carrier density in the injector leads to high carrier-carrier scattering rates. This results in a strong damping of the coherent wavepacket propagation and, thus, a less efficient carrier injection. We will come back to this point below.

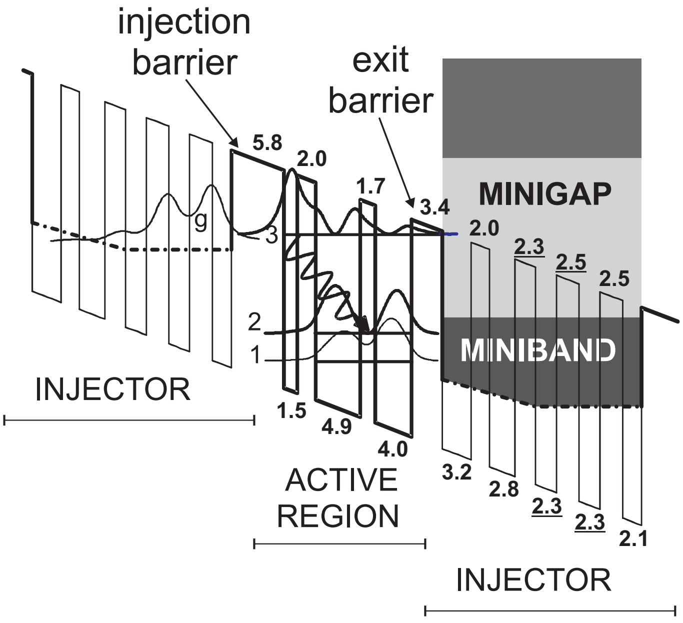

Figure 3.9: Bandstructure of a GaAs/AlGaAs quantum cascade laser [99]. Displayed are states in subbands g, 3, 2, and 1. The numbers are barrier and well widths in nm. The underlined numbers indicate the doped wells and barriers.

3.3.2.2 History and current status of quantum cascade laser devices

Since the invention of the quantum cascade laser, tremendous progress has been made. One year after the development of the first quantum cascade laser continuous wave operation at cryogenic temperatures [100] and pulsed mode up to room temperature [101] was attained. Single-mode laser output was achieved in 1996 with the distributed feedback design [102]. The quest for higher power and longer wavelength devices led to the invention of the superlattice active region in 1997 [103]. Until this time, quantum cascade lasers have been demonstrated exclusively with the material system InGaAs/AlInAs grown on InP substrates. In 1998, Sirtori et al. [99] demonstrated the first quantum cascade laser based on the material system GaAs/AlGaAs grown on GaAs substrates. One year later a superlattice laser was grown using the same material system [104] and in 2001 room temperature operation was shown [105]. In the mean time, picosecond self-mode-locked pulses from quantum cascade lasers [106] and ultra-broadband laser emission in the wavelength range from $6-8\,\mu$m [107] were explored. A recent breakthrough was the demonstration of continuous wave operation of a quantum cascade laser at room temperature [10]. Another milestone was the development of a THz quantum cascade laser emitting at a wavelength of $70\,\mu$m [11].

At present, efforts are underway to reduce the emission wavelength to 1.55 μm, i.e., into the communications wavelength, and to achieve femtosecond self-mode-locked pulses [108]. Further research activity towards an increased family of material systems, e.g. Sb-based structures [109, 110], strained InGaP/InGaAs [111] or Si/SiGe-based structures [112] is under way.

Future performance improvements strongly rely on a detailed understanding of the microscopic processes in such devices where many open questions are left to answer.

3.3.2.3 Experimental characterization of quantum cascade structures

For the characterization of quantum cascade laser structures there exist several standard techniques. The most common are electroluminescence, photocurrent, light output power versus current and voltage-current measurements. From those techniques useful information about intersubband transitions, gain characteristics, and—to a lesser extent—stationary distribution functions can be obtained. Information about electron transport, which is a dynamic process, can be—if at all—only derived indirectly.

In the following, we will briefly introduce the standard techniques mentioned above. Then we will discuss the information obtained by them and compare it with theoretical studies. Finally, we will discuss in more detail studies on electron transport which have been done with these techniques.

Standard techniques In Fig. 3.10 (a) the voltage-current (V-I) characteristics of a GaInAs/AlInAs quantum cascade laser is shown [113]. At an applied bias of > 5 V the structure is aligned, which leads to a rapid decrease of the electric resistance. At a bias of ≈ 6 V the device starts lasing as shown by the light output-current (L-I) characteristics [Fig. 3.10 (b)]. This device lases at a wavelength of $\approx 8.2\,\mu$m [see inset of Fig. 3.10 (b)].

Intersubband photocurrent (PC) spectra for a GaAs/AlGaAs quantum cascade laser structure are shown in Fig. 3.11 (c) [114, 115]. It results from photoexcitation of carriers residing in the lowest energy bands (in particular subband 1) into subband 3 at small bias. Photocurrent spectra provide information about the 1–3 subband spacing at low bias. In

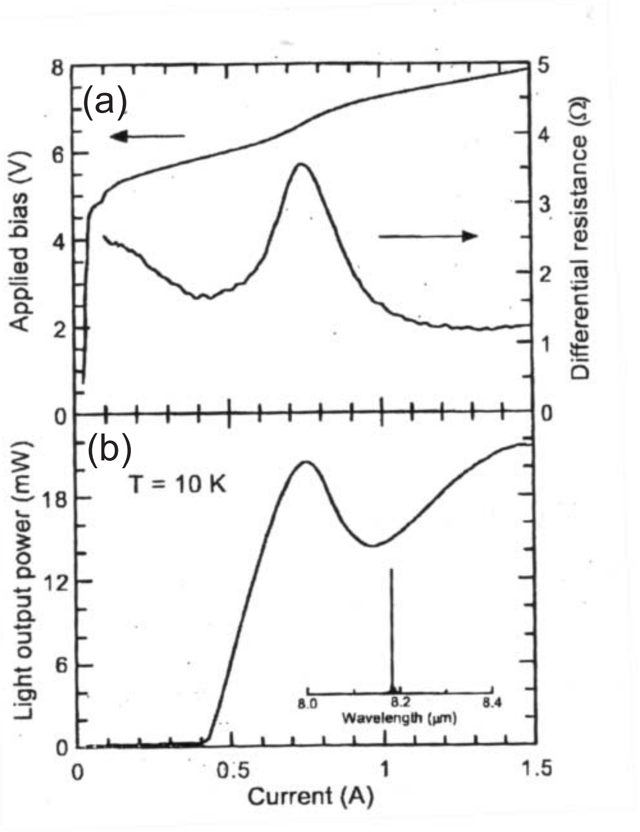

Figure 3.10: (a) Voltage versus current (V-I) characteristics and differential resistance of a GaInAs/AlInAs quantum cascade laser operating at 10 K in pulsed mode. (b) Light versus current characteristics. In the inset, a low-resolution spectrum, showing the emission wavelength, is presented [113].

Fig. 3.11 (d) electroluminescence data for the same sample with an applied bias as indicated are shown. Electroluminescence is due to spontaneous emission of electrons from the upper laser subband into the lower subband. If the lower laser subband is empty then the spectral shape of the gain coefficient can be determined from the electroluminescence spectrum by $g(\hbar\,\omega) \sim I_{EL}(\hbar\,\omega)/\omega^3$. However, the latter assumption cannot be made in general, so that the electroluminescence provides only a rough estimate of the gain spectrum.

Gain measurements To get more detailed information about the gain coefficient in quantum cascade lasers, various techniques have been developed [116, 117]. A standard technique to determine the gain is the Hakki-Paoli technique [118]. Here, optical gain is extracted from the fringe contrast of the Fabry-Perot modes of the cavity below threshold using a Fourier analysis of the subthreshold spectra [119, 116]. Detailed theoretical studies on gain were carried out by Wacker and Lee [120]. They used a fully self-consistent quantum mechanical approach based on the theory of nonequilibrium Green's functions [121, 13]. These calculated gain spectra are in good agreement with experimental results. We will come back to the experimental determination of the gain later.

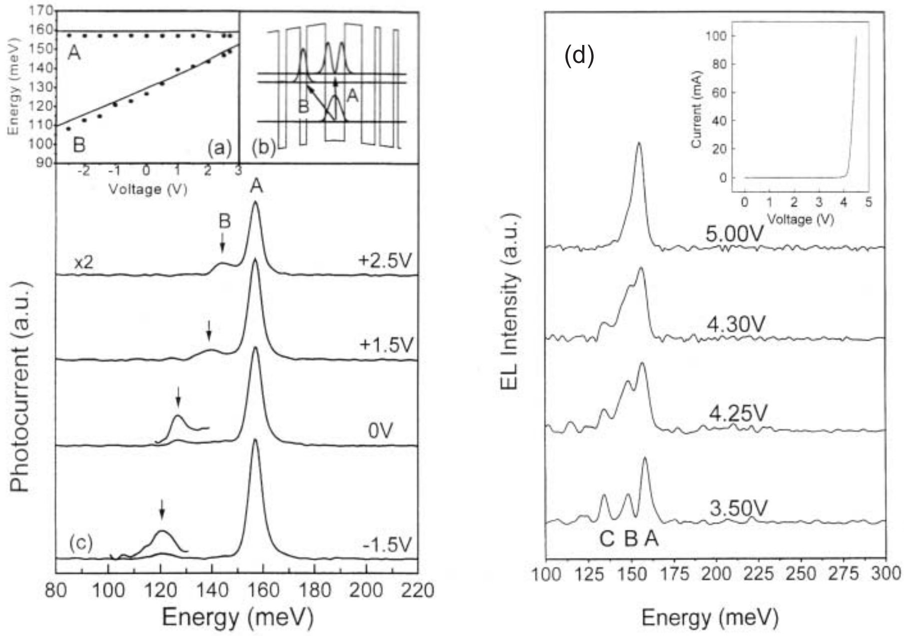

Figure 3.11: (a) Measured (dots) and calculated (lines) bias dependence of the photocurrent transitions A and B indicated in (b) of a GaAs/AlGaAs quantum cascade laser structure. A Stark shift of peak B is observed in the low temperature (T=10 K) photocurrent spectra shown in (c). (d) Electroluminescence spectra as a function of the applied bias. Inset: Current voltage characteristics [114, 115].

Electron distributions An important question is the electron distribution in quantum cascade lasers. From electroluminescence and interband photoluminescence studies in laser structures without resonator, Wilson et al. [114, 115] estimated the bias dependence of the electron distribution. Troccoli et al. [122, 123] carried out detailed electroluminescence studies. From these studies the authors concluded that the electron distribution is thermalized with an electron temperature of $T_e \approx 200$ K. From theoretical studies, a quasi-thermalized electron distribution due to the very high electron-electron scattering rates was found with electron temperatures much higher than the lattice temperature [124, 125, 126]. However, a direct experimental determination of the electron distribution in quantum cascade lasers, which would clarify many unsolved questions, is still lacking.

Electron transport Since electron transport is a dynamic process stationary techniques can only provide indirect information. In the following we will discuss the relevant theoretical and experimental studies done so far.

Theoretical work on electron transport in electrically driven superlattices began with the seminal work of Kazarinov and Suris in 1971 [98, 127]. They calculated current-voltage characteristics using the density matrix formalism in a tight binding approximation. They predicted the occurrence of a negative differential resistance under an appropriate bias. In

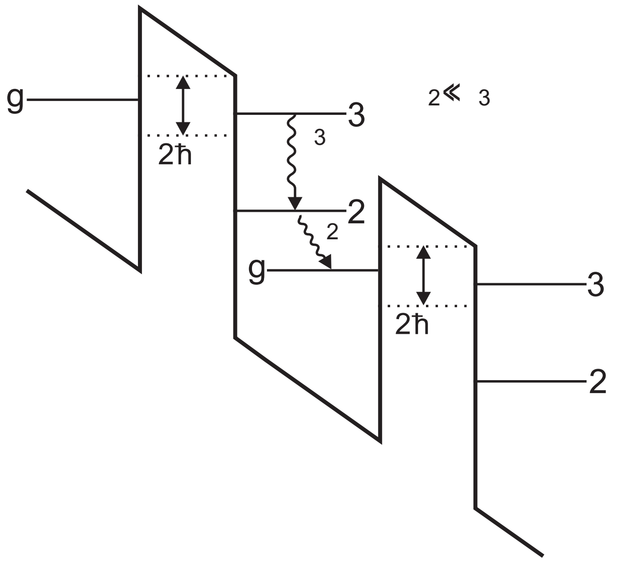

Figure 3.12: Schematics of the structure considered in the work of Kazarinov and Suris [98, 127]. $2\,\hbar\,\Omega$ is the coupling between subsequent quantum wells. In their calculation, it is assumed that $\tau_2 \ll \tau_3$.

the nomenclature of the quantum cascade laser, the current density reads [see Fig. 3.12]

$$I(V) = e\,N_s\,\frac{2\,|\,\Omega|^2\,T_2}{1 + (\frac{E_g - E_3}{\hbar})^2\,T_2^2 + 4\,|\,\Omega|^2\,T_2\,\tau_3} \tag{3.3}$$

where $E_g - E_3$ is the energy detuning from resonance, N_s is the sheet electron density in the injector, $2\,\hbar\,\Omega$ is the tunnel coupling, and T_2 is the irreversible dephasing time of the $g-3$ polarization. At an appropriate bias V_{res}, subband g is in resonance with subband 3, i.e., $E_g - E_3 = 0$, and the maximum current density

$$I_{max} = e\,N_s\,\frac{2\,|\,\Omega|^2\,T_2}{1 + 4\,|\,\Omega|^2\,T_2\,\tau_3} \tag{3.4}$$

is obtained. Increasing the bias beyond resonance leads to a decrease of the current, i.e., to a negative differential resistance.

Sirtori et al. studied the resonant alignment of the subband g and subband 3, which is a prerequisite for resonant tunneling through the injection barrier [113]. They measured the voltage (V-I curve) and light output power (L-I curve) as a function of current for various GaInAs/AlInAs quantum cascade devices (Fig. 3.10). The authors interpreted the features around $I \approx 0.75$ A as an indication of resonant tunneling through the injection barrier arising from the alignment of subband 3 and subband g. A negative differential resistance as theoretically predicted is not seen in Fig. 3.10 (a). The authors argue that the internal impedance of the circuitry is much bigger than $|dV/dI|$, which hinders the observation of a negative differential resistance. In addition, structural inhomogeneities will also wash out any pronounced structures in the V-I characteristics. The L-I characteristics [Fig. 3.10 (b)] has been interpreted as a quenching of resonant tunneling for $I > I_{RT}$. The laser output power drops in correspondence of the peak of the dV/dI since at this voltage the injector is not aligned anymore with the subband 3.

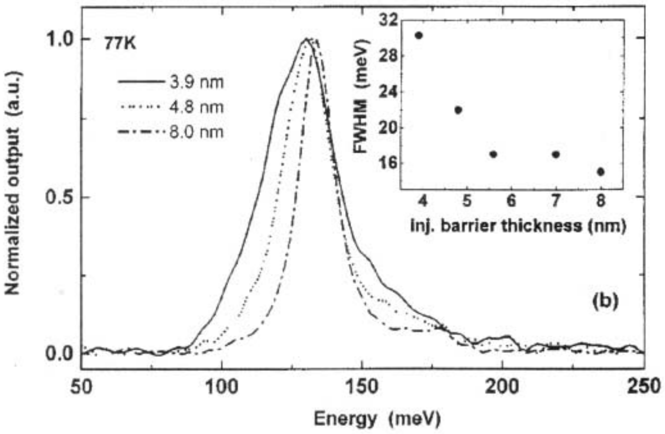

Figure 3.13: Normalized electroluminescence spectra for GaAs/AlGaAs quantum cascade laser structures similar to [116] with various injection barrier thicknesses at $I = 6$ kA/cm^2. Inset: FWHM of the measured electroluminescence spectra as a function of the barrier thickness [12].

A further justification of the picture of resonant alignment of subband 3 and subband g for an appropriate bias was given by the measurements of Barbieri et al. [12]. They studied electroluminescence (EL) spectra of GaAs/AlGaAs quantum cascade laser structures without resonator. In Fig. 3.13 the normalized electroluminescence spectra under an applied current of $I = 6$ kA/cm^2 are shown for identical structures differing only in the thickness of the injection barrier. Two distinct peaks separated by $2\,\hbar\,\Omega$ as expected for a strong tunnel coupling are not seen because of the strong homogeneous and inhomogeneous broadening of the 3–2 transition. In the inset of Fig. 3.13 the full width at half maximum of the electroluminescence spectra is shown. The electroluminescence width increases with decreasing barrier width in good agreement with the calculated energy splitting $2\,\hbar\,\Omega$.

Indication of resonant alignment was also observed by photocurrent and electroluminescence measurements carried out by Wilson et al. [114, 115]. In Fig. 3.11 (c) intersubband photocurrent spectra of a GaAs/AlGaAs quantum cascade laser structure are shown. For increasing bias the subbands A and B move closer together. For higher currents subband 1 is depleted and intersubband photocurrent vanishes. Resonant alignment is then observed in electroluminescence measurements [3.11 (d)]. The two peaks corresponding to A–2 and B–2 transitions move closer together with increasing bias and merge into a single peak for $U > 4$ V when resonant alignment is reached.

A more thorough investigation about the role of the dephasing time T_2 for transport through the injection barrier was done by Sirtori et al. [113]. Based on the calculations of Kazarinov and Suris [equation (3.4)] they identified two different transport regimes depending on the magnitude of the quantity $4\,|\,\Omega|^2\,T_2\,\tau_3$. The weak injector-active region coupling regime occurs for $4\,|\,\Omega|^2\,T_2\,\tau_3 \ll 1$. This implies that the dephasing time T_2, which is assumed to be in the same order as τ_3, is much shorter than the tunneling time $\frac{\pi}{2\,\Omega}$. Here, the current density is dominated by what they call incoherent tunneling, i.e., scattering ($I_{max} = e\,N_s\,2\,|\,\Omega|^2\,T_2$). The second regime is the strong coupling regime. It occurs when $4\,|\,\Omega|^2\,T_2\,\tau_3 \gg 1$. In this regime $I_{max} = e\,N_s/(2\,\tau_3)^2$, i.e., the current is controlled by the lifetime of subband 3 (τ_3). The transport through the injection barrier is dominated by resonant tunneling. An important statement of the authors is: This "is the configuration in which we want to operate the lasers in order to always ensure very fast electron injection into the upper laser state (n=3), without being limited by the tunneling rate"[113].

To calculate the quantity $4\,|\,\Omega|^2\,T_2\,\tau_3$ they determined the dephasing time T_2 from the electroluminescence width. A value of $T_2 \approx 50 - 100$ fs was gained. However, the electroluminescence width is determined by the energy splitting $2\,\hbar\,\Omega$ and the 3–2 intersubband dephasing, and is additionally broadened by structural inhomogeneities. T_2, which is the dephasing time of coherent superpositions of states in subband g and subband 3, cannot be determined by the electroluminescence width.

With the assumption of a unique dephasing time $T_2 = 100$ fs—without any experimental proof—, they derived a value for the quantity $4\,|\,\Omega|^2\,T_2\,\tau_3$ ranging from 0.7 to 11.6 for different laser devices. This suggests that most of the investigated laser devices work in between the strong coupling regime and the weak coupling regime and, hence, the transport from the injector into the active region cannot be described in a strictly coherent picture. We would like to emphasize that the whole study in Ref. [113] relies critically on the dephasing time T_2 which is, however, not yet determined experimentally.

To clarify the coherence of charge transport, Iotti and Rossi carried out semiclassical Monte Carlo simulations taking into account carrier-carrier and carrier-phonon scattering [125, 126, 128]. From their calculations they derived voltage-current characteristics and observed a good agreement with experimental data [128]. Moreover, they derived voltage-current characteristics using a quantum mechanical density matrix calculation neglecting carrier-carrier scattering. They observed similar results as derived from the respective semiclassical calculation. From this, they claimed that the semiclassical picture, in which quantum coherences are neglected, is sufficient to describe transport processes in the quantum cascade laser. In conclusion they claimed that energy-relaxation and dephasing processes are strong enough to destroy any phase-coherence effect on a picosecond time scale. However, since the voltage-current characteristics is a macroscopic phenomenon this is only correct for global transport through the entire structure. Microscopic transport, e.g. transport through the injection barrier, can not be described in this picture. To model this, a full quantum calculation is necessary which has not yet been presented.

3.3.3 Open questions and experimental concept

Electron transport in double quantum wells and in superlattices is coherent for electron concentrations $< 10^{10}$ cm^{-2}. For the high electron concentrations ($\approx 4 \times 10^{11}$ cm^{-2}) present in unipolar semiconductor devices like the quantum cascade laser, electron transport has not yet been directly observed. It is important to note that all techniques that have been applied so far to characterize such devices are stationary techniques which give no direct information about dynamic processes.

The quantum cascade laser is designed in the spirit of coherent electron transport [113] but the high electron-electron scattering rates suggest a minor role of quantum coherences [128]. In the experiments discussed above a clear indication of resonant alignment of states in the injector and states in the active region is obtained which is necessary for resonant tunneling. However, it is still unclear whether this transport is coherent or incoherent.

To clarify the nature of electron transport at such elevated electron densities time-resolved measurements are needed. For this, the well-known methods of ultrafast spectroscopy have to be combined with high-current pumping of device structures. In this thesis, we will present the first experiment of this kind. To study electron transport from the injector into the upper laser subband we will use femtosecond mid-infrared pump-probe spectroscopy.

Chapter 4

Coherent nonlinear propagation of ultrafast electric field transients through intersubband resonances

The generation and optical control of intersubband excitations provides interesting perspectives for fast optical switching. In this chapter we demonstrate coherent control of intersubband polarizations in quantum wells on a sub-picosecond time scale.

In the following, we first introduce the GaAs/AlGaAs quantum well sample investigated. One reason for choosing this particular structure is that it has been already characterized in our group using other experimental techniques [69, 41]. The orientation of intersubband dipoles perpendicular to the layers requires a suitable beam propagation geometry to ensure a strong coupling with the electric field. This is discussed in detail as it plays also an important role for the experiments presented in the subsequent chapters. Then we explain the experimental setup using the detection and generation scheme for ultrashort mid-infrared pulses developed in chapter 2. The results of linear and nonlinear propagation of single pulses and of phase-locked pulse pairs through intersubband resonances is presented in the subsequent section. Finally, we analyze the data in the framework of Maxwell-Bloch equations for a homogeneously broadened two-level system.

4.1 Sample properties

For the experiment, an n-type modulation-doped GaAs/AlGaAs multiple quantum well structure is used. It was grown by molecular beam epitaxy at the Paul-Drude-Institut (PDI) in Berlin. A semi-insulating GaAs (100) wafer is used as substrate to guarantee a large transmission in the mid-infrared. The substrate thickness is 300 μm. The sample consists of $N_{QW} = 51$ GaAs quantum wells of 10 nm width separated by $\mathrm{Al_{0.35}Ga_{0.65}As}$ barriers of 20-nm thickness, which ensures a negligible coupling between the individual quantum wells. The center of the barriers is δ-doped with Si at concentrations of $n_{2D} = 5 \times 10^{10}$ cm^{-2}. At low temperatures, the electrons transfer completely from the ionized donors into the wells resulting in a degenerate electron gas with a Fermi energy of 2 meV at 15 K. A 1.25-μm thick $\mathrm{Al_{0.35}Ga_{0.65}As}$ spacer layer was grown on top of the structure to optimize the optical coupling as will be discussed below. Finally, a 10-nm cap layer covers the sample.

Fig. 4.1 (a) shows the conduction band potential and the corresponding electronic prob-

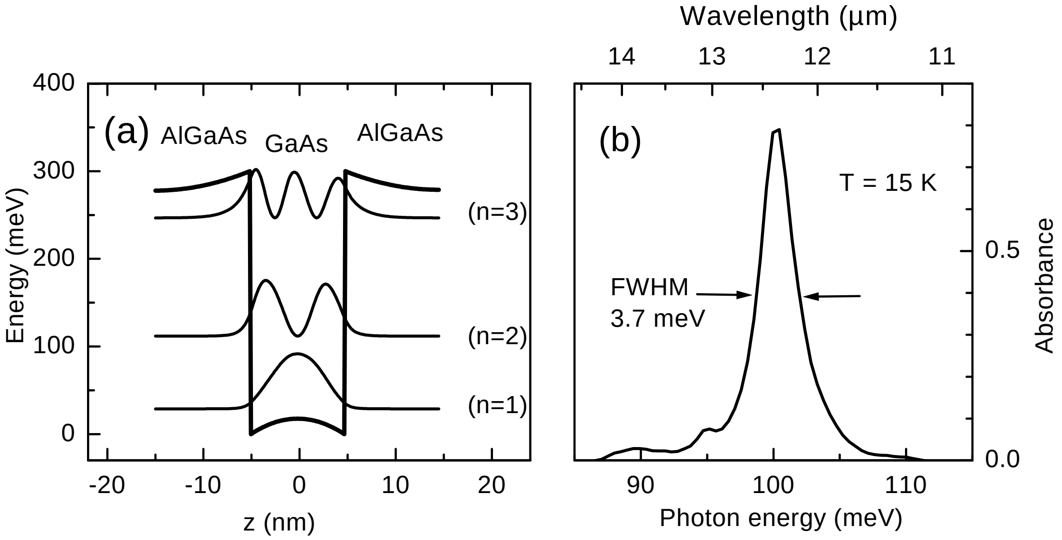

Figure 4.1: (a) Conduction band potential and corresponding probability densities $|\zeta_n(z)|^2$ for the GaAs/Al$_{0.35}$Ga$_{0.65}$As multiple quantum well sample. (b) Intersubband absorbance (from subband 1 to subband 2) [69].

ability density functions. The three energetically lowest subbands are confined inside the 10-nm wide well. The $n = 1$ to $n = 2$ absorbance spectrum $a(\omega)$ measured in the beam propagation geometry described below is shown in Fig. 4.1 (b) [69]. At $T = 15$ K it displays a very small linewidth of $\Delta E_{IS} = 3.7$ meV centered at $\lambda = 12.4$ μm. The absorption at $\lambda = 12.4$ μm is $A_{abs} = a \ln(10) \approx 84$ %.

In pump-probe experiments carried out by Kaindl et al. [69], an intersubband relaxation time $T_1 = 550 \pm 50$ fs was determined. The same authors did also time-resolved four-wave mixing experiments. These experiments show that the intersubband absorption lineshape is dominantly homogeneously broadened. Subband non-parabolicities and many-body effects caused by the Coulomb interaction among the electrons play a minor role for the low electron concentration in this sample. Hence, the 1–2 intersubband transition can be modelled in good approximation by a homogeneously broadened two-level system. At low temperatures, a dephasing time of $T_2 = 320$ fs was measured, which is independent of the excitation intensities up to an excitation of 30 % of all carriers. The contribution of population relaxation to dephasing $[1/(2\,T_1) \approx 0.9\ \text{ps}^{-1}]$ is only ≈ 30 % of the observed value. Thus there is significant pure dephasing due to electron-electron scattering.

4.2 Geometry of beam propagation

Since intersubband dipoles are oriented along the stack axis (z-direction), beam propagation perpendicular to the substrate is inadequate to assure a strong coupling. Tilting the substrate results only in a weak coupling as any beam incident on the sample propagates in the sample almost perpendicularly to the surface because of the high refractive index of the GaAs substrate ($n_{GaAs} = 3.23$ at $\lambda = 10$ μm). To achieve a strong coupling with the light field, we choose the prism-like geometry shown in Fig. 4.2. The beam enters at the side facet of the prism parallel to the layers. With a suitable choice of the prism angles the desired angle

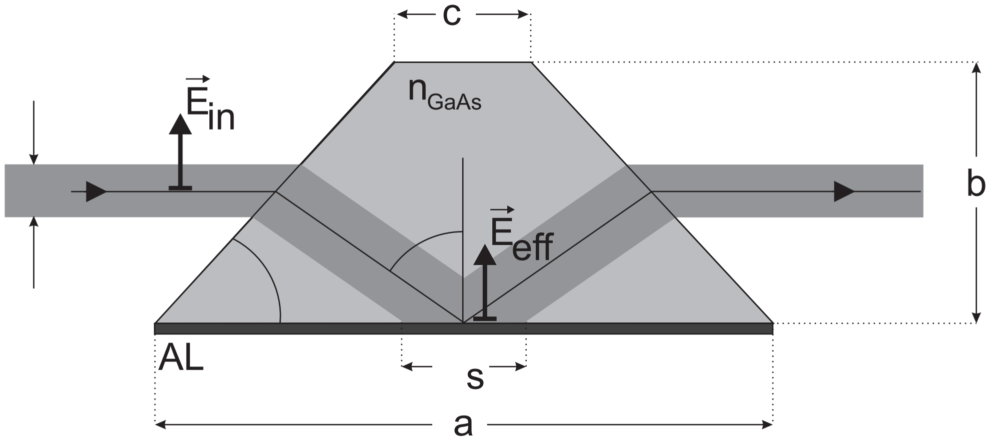

Figure 4.2: Schematics of the prism geometry of a GaAs/AlGaAs sample with substrate thickness b, refractive index n_{GaAs} and active layers (AL). δ is the focus diameter and $\vec{E}_{in}$ the electric field of the incident beam. δ_s is the projection of the focus diameter onto the plane of the layers. $\vec{E}_{eff}$ is the effective electric field experienced by the electrons in the antinode of the standing wave.

of incidence can be obtained. With a given thickness b of the substrate and a beam focus diameter δ we determine the optimal angle of incidence α and, concomitantly, the prism angle β and the length a. The latter two are the relevant quantities for the fabrication of the prism-shaped sample.

From geometrical considerations we get a prism angle $\beta(\alpha)$ by solving the equation

$$\alpha = \beta(\alpha) + \arcsin\left(\frac{1}{n_{GaAs}} \cos\beta(\alpha)\right)$$

and further

$$a = b\frac{\sin(\alpha+\beta)}{\sin(\alpha)\cdot\sin(\beta)} \quad \text{and} \quad c = a - 2\frac{b}{\tan(\beta)}$$

Two quantities play an important role for the design of the prism geometry:

- the area enhancement, i.e., the area of the focus projected onto the plane of the layers divided by the focus:
$$A(\alpha) = \frac{\delta_s(\alpha)}{\delta} = \frac{\cos(\alpha - \beta(\alpha))}{\cos(\alpha)\cdot\sin(\beta(\alpha))}$$
- The electric field E_{eff} polarized perpendicular to the layers, which is experienced by electrons in the antinode of the standing wave due to total reflection of the light from the base plane of the prism. Taking into account the reflection at the prism surface, E_{eff} reads without any absorption

$$E_{eff} = 2\cdot\frac{\sin(180^\circ - 2\,\beta)}{n_{GaAs}\cdot\sin(90^\circ + \alpha - 2\,\beta)}\cdot E_{in} \tag{4.1}$$

In the experiments we would like to have a high effective electric field at the intersubband dipoles. In Fig. 4.3 (a) the effective electric field and the area enhancement are shown as a

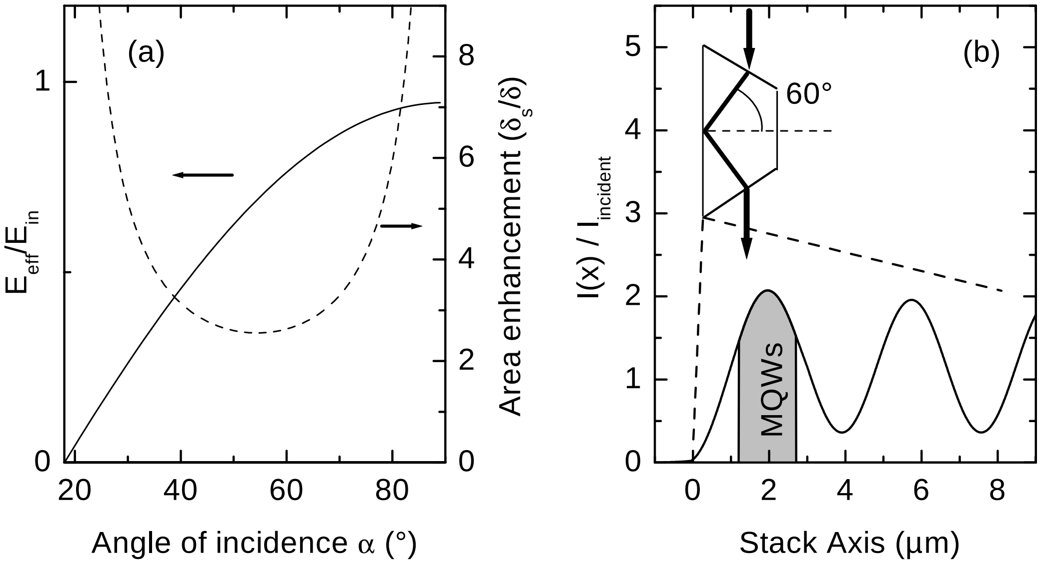

Figure 4.3: (a) Normalized effective electric field amplitude E_{eff}/E_{in} (solid line) and area enhancement (dashed line) plotted as a function of the angle of incidence. (b) Calculated intensity pattern of the standing wave arising close to the interface sample/glue due to total internal reflection.

function of α. At an angle of incidence of $\alpha = 60°$ the effective electric field E_{eff} is 75 % of the incident field E_{in}. The focus area is enhanced by a factor of $A = 2.63$ at this angle. For $\alpha > 60°$ the area enhancement increases rapidly. Since we will later use the same geometry for measurements on mesa shaped quantum cascade structures, where a small focus is very important, we decide to use an angle of incidence of $\alpha = 60°$.

For $\alpha = 60°$ we get $\beta = 48°$. For a substrate thickness of $b = 300$ μm we calculate

$$a = 790\,\mu\text{m} \quad \text{and} \quad c = 250\,\mu\text{m}$$

For the fabrication, the sample is glued ($n_{glue} \approx 1.5$) onto a sample holder. Due to the large difference of the refractive indices there is total reflection at the interface sample/glue $[\alpha_{tot} = \text{asin}\,(n_{glue}/n_{GaAs}) = 28°]$ at an angle of incidence of $\alpha = 60°$. The superposition of the incident and the reflected field yields a standing wave with its node at the surface sample/glue and a wavelength $\lambda_{sw} = \lambda/(2 \cdot n_{GaAs} \cdot \cos\alpha) = 3.9\,\mu$m for $\lambda = 12.5\,\mu$m. In Fig. 4.3 (b) the intensity pattern of the standing wave is plotted. It is calculated using the matrix transfer formalism (see, e.g., Ref. [129]) including the anisotropic dielectric functions of the doped active region to account correctly for the properties of intersubband transitions. Since the electric field is zero at the interface sample/glue a AlGaAs spacer layer of 1.25-μm thickness was grown on top of the multiple quantum well layers to shift them to a position of maximum intensity.

4.3 Experimental setup

The experimental setup is shown in Fig. 4.4. Near-infrared 14 fs pulses centered at a wavelength of 780 nm with a repetition rate of 2 MHz are generated in a cavity-dumped

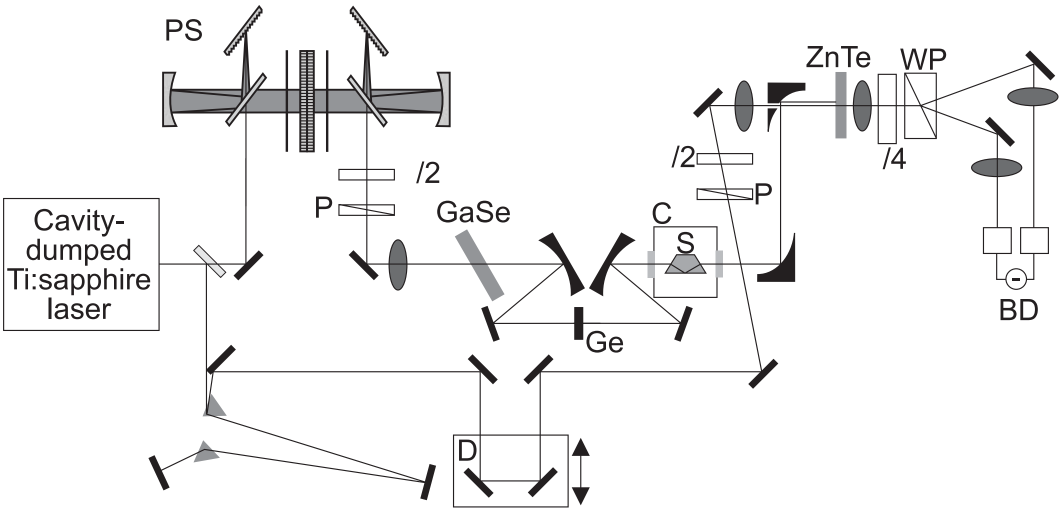

Figure 4.4: Experimental setup for the study of coherent nonlinear propagation of ultrafast electric field transients through intersubband resonances (PS: Pulse shaper, $\lambda/2$, $\lambda/4$: waveplates, P: Polarizer, GaSe: 0.5 mm thick GaSe crystal, Ge: 1 mm thick Ge plate, C: Cryostat, S: Sample, ZnTe: 10 μm thick ZnTe plate, WP: Wollaston polarizer, BD: Pair of balanced diodes, D: Delay stage).

mode-locked Ti:sapphire oscillator. The pulses are amplitude- and phase-shaped in a programmable pulse shaper (PS) to generate tailored mid-infrared transients by phasematched difference-frequency mixing in a 0.5-mm-thick GaSe crystal. In that way single pulses and phase-locked pulse pairs in the mid-infrared are generated as described in detail in section 2.2.1. The pulse energies are adjustable without additional filters. Residual near-infrared light is filtered at a germanium (Ge) plate. After interaction with the sample (S) the time-dependent electric field of the transients is measured by ultrafast electro-optic sampling. The shaped mid-infrared pulses are centered at the maximum of the intersubband line, i.e., at a wavelength of 12.4 μm. All the experiments have been performed at a lattice temperature of 15 K.

4.4 Experimental data

In Fig. 4.5 (a,b) data for a single pulse with an energy[1] of $I^{pulse} = 0.1$ pJ are shown. This figure shows the electric field transients of a single pulse transmitted through an undoped reference sample of identical shape E_{Ref} [Fig. 4.5 (a)] and of a single pulse transmitted through the quantum well sample E_{QW} [Fig. 4.5 (b)]. The field transient transmitted through the quantum well sample is distinctly different from the transient through the reference sample. Instead of a single pulse, two pulses can be observed. The amplitude of the first pulse, which is centered around $t = 0$ is approximately a factor of 3 larger than the amplitude

---

[1] The determination of the pulse energies of the 2 MHz laser system with such low mid-infrared intensity is difficult. We use a MCT detector, which is calibrated with a 1 kHz, high-intensity, mid-infrared source. In this calibration the response of the different preamlifiers in the different systems has to be taken into account giving rise to a large systematic error of around 50 % for the absolute values of I^{pulse}. The relative pulse energies in our experiment, however, are known with an accuracy of 5 %.

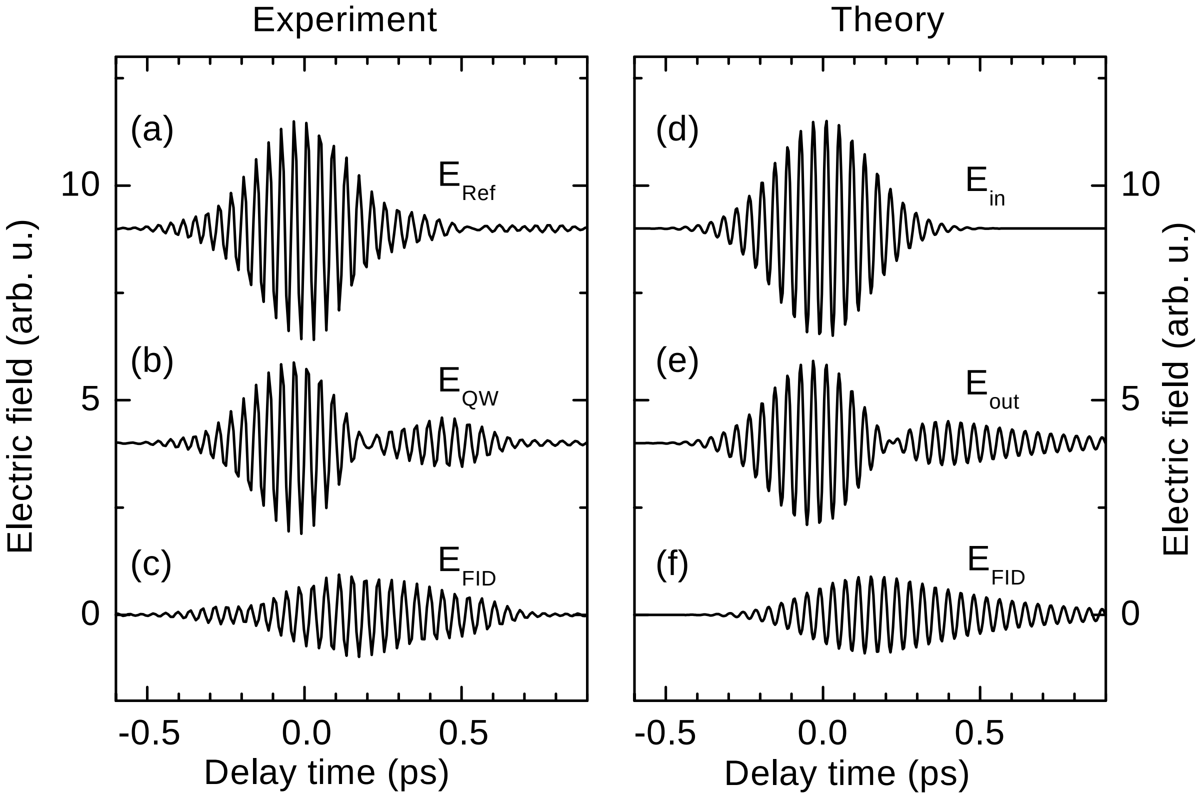

Figure 4.5: Measured and calculated electric field transients for low excitation through an undoped reference sample (a,d), through the quantum well sample (b,e) in response to a single pulse. The difference of the curves in the upper and middle panels, i.e., the free-induction decay of the intersubband excitation is displayed in (c,f).

of the second, weaker pulse centered around $t = 0.4$ ps. In Fig. 4.5 (c) we plot the difference between the transients $E_{FID} = E_{QW} - E_{Ref}$, which represents the response of the multiple quantum well systems. Since the wave propagation geometry through the two samples is not exactly the same, e.g., the base planes of the samples might enclose a small angle, a small systematic shift in the amplitude and phase between the time transients transmitted through the reference sample and the quantum well sample is taken into account. E_{FID} is called the free induction decay of the intersubband polarization, which will be discussed in detail in the next section.

For the figures presented in the following we keep the sequence E_{Ref} (upper trace), E_{QW} (middle trace), and E_{FID} (lower trace) within the respective panels.

In Fig. 4.6 we present data, where two phase-locked mid-infrared pulses with amplitudes E_1 and $E_2 \approx 1/2\, E_1$ and a separation of $\tau_{12} = 400$ fs are applied. $\tau_{el} = 300$ fs is the length (FWHM) of the electric field envelopes. The relative phase between the pulses is (a) $\Delta\Phi = 0$ and (c) $\Delta\Phi = \pi$.

In Fig. 4.7 we present results for excitation with single mid-infrared pulses with different electric field amplitudes. Experimental data for low excitation ($I^{pulse} = 0.1$ pJ) and for stronger excitation ($I^{pulse} = 1.0$ pJ) are shown in Figs. 4.7 (a) and 4.7 (b), respectively (note the different ordinate scales). With increasing amplitude of the exciting electric field one finds a decreasing ratio of the amplitudes of E_{FID} and E_{Ref}. In Fig. 4.7 (c) this

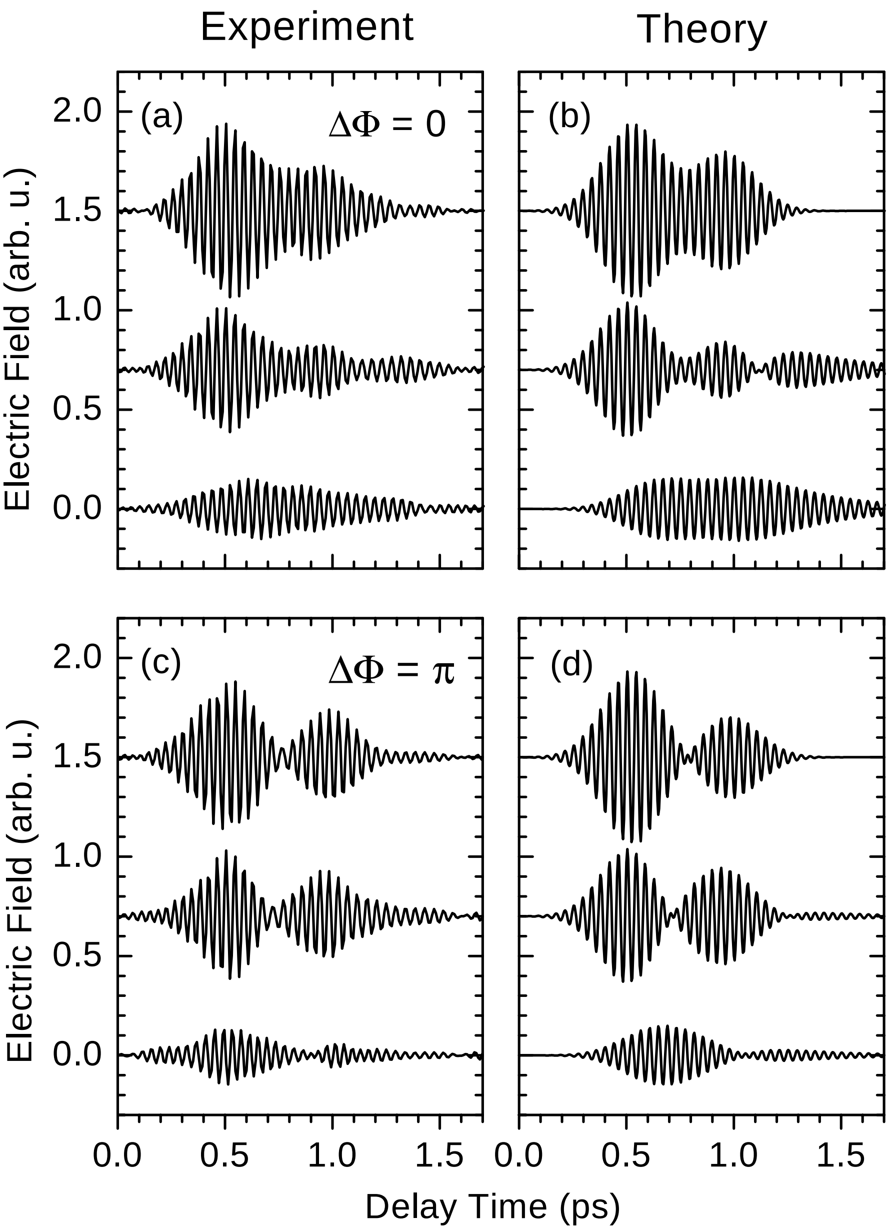

Figure 4.6: Coherent control of intersubband excitation using two phase-locked mid-infrared pulses with $t_D = 400$ fs separation and relative phases of (a),(b) $\Delta\Phi = 0$ and (c),(d) $\Delta\Phi = \pi$. Each panel shows the incident pulses (upper traces), the pulses sent through the quantum well sample (middle traces), and the respective difference (lower traces) being the re-emitted free induction decay of the coherent intersubband polarization. Left panels: Electric field transients obtained with ultrafast electro-optic sampling. Right panels: Model calculations based on Maxwell-Bloch equations.

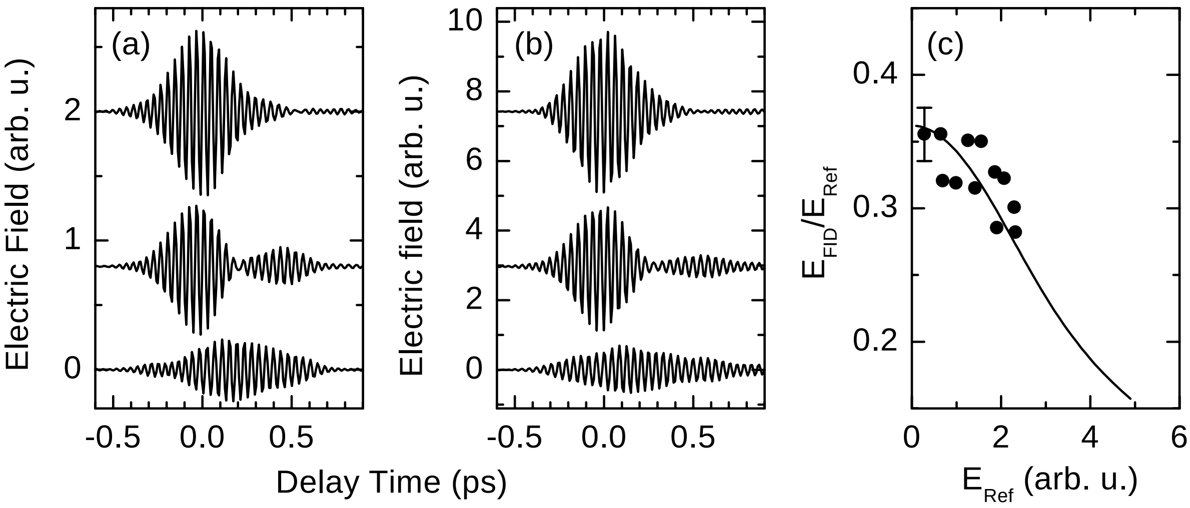

Figure 4.7: Measured electric field transients through the reference sample (upper traces), through the quantum well sample (middle traces), and the free induction decay of the intersubband excitation (lower traces) in response to a single pulse for (a) low ($I^{pulse} = 0.1$ pJ) and (b) high ($I^{pulse} = 1.0$ pJ) excitation fields. (c) Ratio between the field amplitudes of the re-emitted free induction decay E_{FID} and the excitation pulse E_{Ref} as a function of E_{Ref} obtained from individual measurements of the field transients (symbols) and calculated using the Maxwell-Bloch equations as discussed above (solid line).

ratio E_{FID}/E_{Ref} as a function of E_{Ref} is summarized. Each circle has been measured in an independent experiment. For the highest incident field amplitudes this ratio is approximately 20 % smaller than for the lowest incident field amplitudes.

4.5 Discussion

Now, we analyze the experimental data presented in the previous section. We will start with a qualitative discussion of the underlying physics. Finally, we present model calculations using the Maxwell-Bloch equations [Eqs. (2.4-2.6)].

4.5.1 Qualitative analysis

Free induction decay In the experiment shown in Fig. 4.5 (b), a single mid-infrared pulse is propagated through the quantum well sample. The center frequency is resonant to the intersubband transition. The interaction with the intersubband dipoles leads to a macroscopic intersubband polarization with a phase shifted by 90° relative to the incident pulse. This macroscopic polarization emits an electromagnetic wave, again shifted by 90°. Hence, this re-emitted wave destructively interferes with the incident pulse. The re-emitted light is called the free induction decay E_{FID}. It gives rise to the second component of the electric field in Fig. 4.5 (b). Since the incident pulse and the free induction decay have a phase difference of 180°, the re-emitted light can be directly extracted from the data by subtracting the transients $E_{FID} = E_{QW} - E_{Ref}$ [Fig. 4.5 (c)]. The free induction decay rises with the integral of the exciting field E_{Ref} and decays on a time scale of several hundreds of femtoseconds. This decay time is determined by the dephasing time T_2 which was measured previously by four-wave mixing experiments ($T_2 = 320$ fs) [69].

We want to emphasize that in contrast to previous experiments on coherent intersubband excitations reported in literature our experiment allows a direct measurement of the coherent intersubband polarization as a function of time. In particular, this includes both amplitude and phase. The authors of Refs. [38, 90] presented electric field correlation measurements which contain (without any further characterization of the reference pulse) only information on the spectrum of the emitted light. To determine the actual time structure of the emitted field one additionally needs information about the spectral phase.

Spectral amplitude and phase The advantage of our measurement technique is that we have access to the spectral amplitude and phase of the data. In Fig. 4.8 (a) the spectral intensities of the field transients through the reference sample $|E_{Ref}(\omega)|^2$ (open squares) and through the quantum well sample $|E_{QW}(\omega)|^2$ (circles) are plotted. These curves are obtained by the Fourier transform of the transients. The solid line is the expected spectrum of the field transient through the quantum well sample for the linear case. It is obtained by multiplying $|E_{Ref}(\omega)|^2$ with the transmission of the quantum well sample $T(\omega) = 10^{-a(\omega)}$ [cf. Fig. 4.1 (b)]). The measured curve is in good agreement with the calculation indicating that the excitation is linear. A thorough calculation of the degree of excitation will be given below. The information obtained by the intensity spectrum is equivalent to a linear absorption measurement.

In Fig. 4.8 (b) the spectral phase of $E_{Ref}(\omega)$ subtracted from the spectral phase of

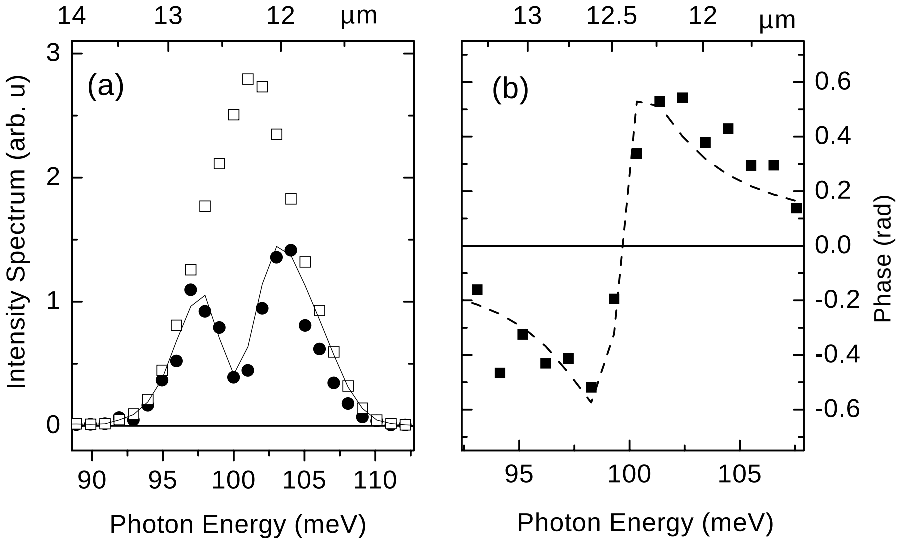

Figure 4.8: (a) Intensity spectra of the field transients through the reference sample $|E_{Ref}(\omega)|^2$ (open squares) and through the quantum well sample $|E_{QW}(\omega)|^2$ (circles). The solid line is $|E_{Ref}(\omega)|^2$ multiplied with the transmission of the quantum well sample $T(\omega)$ [$= |t(\omega)|^2 = 10^{-a(\omega)}$, where $a(\omega)$ is the absorbance shown in Fig. 4.1 (b) and $t(\omega)$ is the complex transmission coefficient]. (b) Spectral phase of $t(\omega) = E_{QW}(\omega)/E_{Ref}(\omega)$ (squares). The dashed line is a calculation using the approximation for a weak absorber [Eq. (4.2)].

$E_{QW}(\omega)$ is shown (squares). This curve corresponds to the phase of the complex transmission coefficient $t(\omega) = E_{QW}(\omega)/E_{Ref}(\omega)$. For an ideal, homogeneously broadened two-level system, the transmission coefficient is given by (approximation for weak absorber)

$$t(\omega) = 1 - \frac{0.5\, A_{abs}}{1 - i\,(\omega - \omega_0) \cdot T_2} \tag{4.2}$$

The dashed line in Fig. 4.8 (b) is the calculated phase of $t(\omega)$. The measured curve agrees quite well with the calculated one, which is another indication that the quantum well sample behaves like an ideal, homogeneously broadened two-level system. It is important to note that this information can not be obtained by static absorption measurements. Thus it demonstrates the potential of our new measurement technique.

Coherent control Now, we discuss the double pulse experiment [Fig. 4.6] in which coherent control of intersubband populations is demonstrated. The pulse energies are on the same order of magnitude as in the previous experiment. Hence, we are again in the linear regime.

The idea of this experiment in the Bloch picture [50] is shown in Fig. 4.9. The graphical interpretation of the Bloch vector $\vec{B}$ is depicted in which the occupation of the upper state is $n_{ex} = 1/2\,(1 + B_z)$ and the coherent intersubband polarization is $P_{Res} = B_x + i\,B_y$. An important quantity is the pulse area θ, which is the rotation angle in the Bloch sphere due to a partial Rabi cycle driven by the electric field. The first pulse E_1 rotates the vector by θ_1 out of the ground state leading to an intersubband polarization and, concomitantly, to an occupation of the upper state

$$n_{ex} = \frac{1}{2}\left(1 - \cos\theta_1\right), \quad \theta_1 = \frac{\mu \cdot (E_1)_{eff} \cdot \tau_{el}}{\hbar}$$

The occupation of the upper state is "switched on"with a pulse area θ_1. We assume that the occupation of the upper state remains unchanged for the interval between the pulses, i.e., negligible population decay, but the intersubband polarization decays by a factor of $\eta = \exp(-\tau_{12}/T_2)$. The second pulse provokes a further rotation $\theta_2 = \mu \cdot (E_2)_{eff} \cdot \tau_{el}/\hbar$ of

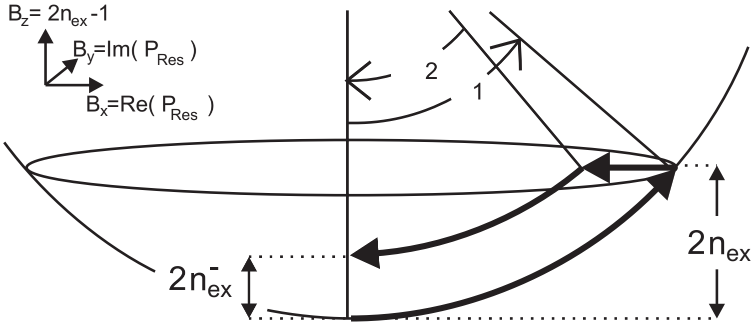

Figure 4.9: The effect of the mid-infrared pulse pair on the initially unexcited Bloch vector $\vec{B} = (0, 0, -1)$. The first pulse rotates $\vec{B}$ by θ_1 leading to an occupation n_{ex} of the upper state. The concomitant polarization decays because of dephasing, before pulse 2 with a destructive phase rotates $\vec{B}$ back by θ_2 leaving n^-_{ex} behind.

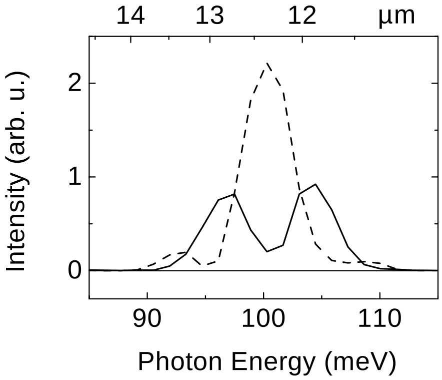

Figure 4.10: Spectra of two phase-locked mid-infrared pulses with 400 fs separation and relative phases of $\Delta\Phi = 0$ (dashed line) and $\Delta\Phi = \pi$ (solid line).

the Bloch vector either returning it back (“switch off”) towards the initial state or exciting more carriers, according to the relative phase between the pulses. The resulting maximum and minimum occupations of the upper state are [9]

$$n_{ex}^{\pm} = \frac{1}{2}\Big(1 - \cos\left(\theta_1 \pm \theta_2\right)\Big) \pm (\eta - 1)\,\sin\theta_1\,\sin\theta_2$$

For weakly excited systems, i.e., in the linear case, this yields

$$n_{ex}^{\pm} = \frac{1}{2}\left(\frac{\theta_1^2 - \theta_2^2}{2} \pm \eta\,\theta_1\,\theta_2\right)$$

n_{ex}^{-} is minimal for $\theta_2 = \eta\,\theta_1$. Thus, the maximum switch off is achieved if the second pulse has an amplitude of ($E_2 = \eta\,E_1$).

For phase-locked pulses with a relative phase $\Delta\Phi = 0$ [Fig. 4.6 (a)] the coherent polarization and, concomitantly, the occupation of the upper state created by the second pulse adds to the coherent excitation left from the first pulse resulting in a pronounced prolongation of the free induction decay [Fig. 4.6 (a), lower trace]. Here, the maximum occupation n_{ex}^{+} of the upper state is generated. Correspondingly, the spectrum of the applied field transient [dashed line in Fig. 4.10] has its maximum at the intersubband resonance [cf. Fig. 4.6 (a), upper trace]. For $\Delta\Phi = \pi$ [Fig. 4.6 (c)], destructive interference between the free induction decays induced by the two mid-infrared pulses results in a strong reduction of the amplitude of the coherent intersubband excitation after the second pulse. In this case, the minimum occupation n_{ex}^{-} of the upper state remains. In order to compensate for the partial decay of the coherent excitation in response to the first pulse the amplitude of the second excitation pulse has been adjusted to a smaller value ($E_2 \approx \eta\,E_1$). The corresponding spectra of the excitation pulses (solid line: Fig. 4.10) shows a pronounced dip at the intersubband resonance.

Our results clearly demonstrate the feasibility of coherent control of intersubband excitations with sub-picosecond dephasing times by weak mid-infrared transients. In particular, we have demonstrated ultrafast coherent “switch on”and “switch off”of the population in the excited state. Such a scheme is a promising candidate for future ultra high-bit rate telecommunication systems.

Coherent nonlinear propagation Now, we discuss the data shown in Fig. 4.7. In the linear regime, i.e., at low excitation densities, where the intersubband response cannot be distinguished from that of a harmonic oscillator, there is a parabolic relation between the degree of excitation n_{ex} and the polarization as shown in Fig. 4.11 (a, dashed line) [130]. As a result, the ratio between the amplitude of the free-induction decay E_{FID} and E_{Ref} after interaction with the sample is constant [Fig. 4.11 (b), dashed line]. The data plotted in Fig. 4.7 (c), however, show a distinct deviation from this linear behavior, i.e., the ratio E_{FID}/E_{Ref} decreases with increasing E_{Ref}. The quadratic relation between n_{ex} and P_{Res} is no longer valid and has to be replaced by the Bloch sphere [Fig. 4.11 (a, solid sphere)]. At small excitation pulse areas θ, i.e., in the linear case, the coherent polarization and the population of the upper states in the Bloch sphere picture are similar to those in the harmonic oscillator picture. The coherent polarization in the Bloch picture reaches its maximum at $\theta = 90°$ where all intersubband dipoles are perfectly aligned. For higher excitation pulse areas the polarization decreases again until it becomes zero in the case of total population inversion. Since the free induction decay is the light emitted by this coherent polarization, a saturation is expected with increasing excitation pulse areas. The solid line in Fig. 4.11 (b) is a calculation using the Maxwell-Bloch equations (see below). Our experimental data are in good agreement with this calculation as can be seen in Fig. 4.11 (b) .

This saturation can also be observed in Fig. 4.11 (c), where the spectra of the transients are plotted. The circles indicate the intensity spectrum of the incident field transient with a pulse energy of 0.1 pJ [Fig. 4.7 (a)] whereas the squares correspond to a pulse energy of 1.0 pJ [Fig. 4.7 (b)]. The solid line in Fig. 4.11 (c) is a calculated spectrum of a single pulse

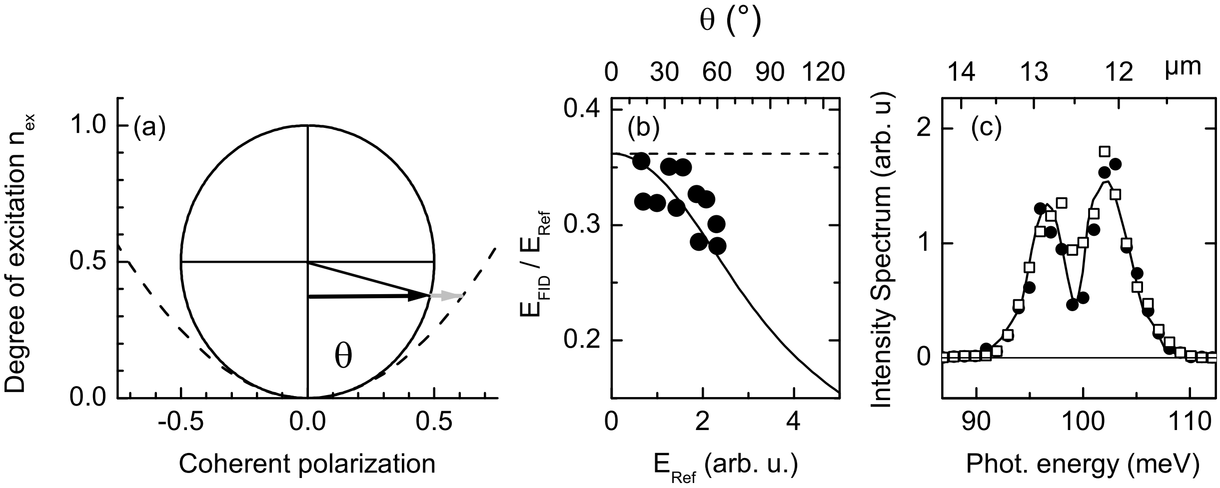

Figure 4.11: (a) Relationship between the degree of excitation n_{ex} and the coherent polarization in a harmonic oscillator picture (dashed parable) and in the Bloch picture (solid sphere). (b) Ratio between the amplitude of the free-induction decay E_{FID} and the amplitude of the excitation pulse E_{Ref} as a function of E_{Ref} determined from the experiment (symbols), derived from a harmonic oscillator picture (dashed line) and calculated in the Bloch picture using the Maxwell-Bloch equations (solid line). (c) Fourier transforms of the transients through the QW sample for a pulse energy of $I^{pulse} = 0.1$ pJ (circles) and a pulse energy of $I^{pulse} = 1$ pJ (squares) excitation. Solid line: FT of the transient through the reference sample multiplied by the linear transmission spectrum of the QW sample.

propagated through the quantum well sample. The calculation, which assumes a very low excitation degree (linear regime), is described above. The incident field transient with a pulse energy of 0.1 pJ is in good agreement with the calculated curve, but for a pulse energy of 1.0 pJ we observe a pronounced deviation from the linear behavior. This saturation exclusively is at the spectral position of the intersubband transition. The off-resonant wings of the two spectra are equal, i.e., not affected by the nonlinear response.

4.5.2 Quantitative analysis

4.5.2.1 Excitation density

For a quantitative analysis of the saturation observed in the previous experiment, we calculate the degree of excitation n_{ex} in the nonlinear experiment. We carry out two different calculations. First, we directly calculate n_{ex} with the help of the absorbance $a = 0.8$ [Fig. 4.1 (b)] treating the quantum well sample as a black box. Then we compare this result with a calculation taking into account the properties of the intersubband excitation in the picture of the quantum mechanical two-level system.

The cross section for the interaction with the sample in our beam geometry is [Fig. 4.12]

$$\sigma = \frac{A_{abs}}{n_{2D}\, N_{QW}\, A} = 2.8 \cdot 10^{-13}\,\mathrm{cm}^2$$

With the pulse energy $I^{pulse} = 1$ pJ in the sample and the focus diameter $d_{foc} = 70\,\mu$m the photon flux reads

$$\Phi = \frac{I^{pulse}}{h\,\frac{c}{\lambda}\,\pi\,\left(\frac{d_{foc}}{2}\right)^2}$$

and the degree of absorption

$$D = \frac{\int |E_{QW}(\omega)|^2\, d\omega}{\int |E_{Ref}(\omega)|^2\, d\omega} = 0.5$$

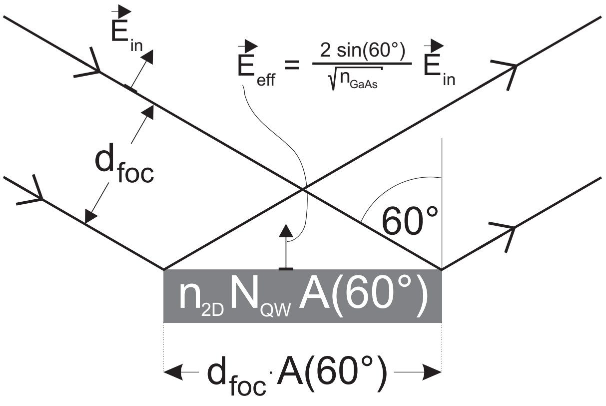

Figure 4.12: Schematics of the interaction with the sample. Φ is the photon flux, $\vec{E}_{in}$ is the incident electric field, $\vec{E}_{eff}$ is the effective electric field, d_{foc} is the focus diameter and A is the area enhancement factor. The effective two-dimensional carrier density is $n_{2D}\, N_{QW}\, A$.

Using these quantities the degree of excitation is calculated as

$$n_{ex} = \Phi\,\sigma\,D = 22.7\,\%$$

To confirm this result, we use a second, theoretical calculation. First, we calculate the dipole moment μ. With the cross section σ and using the Bloch equations [(2.5) and (2.6)] the dipole moment can be derived:

$$\mu = e\,\frac{\sqrt{n_{GaAs}}}{2\cdot\sin(60^\circ)}\,\sqrt{\frac{c\,\hbar\,\sigma\,\Delta E}{\epsilon_0\,2\,h\,\frac{c}{\lambda}}} = 2.5\,\mathrm{nm}\cdot e$$

where $\Delta E = 3.7$ meV is the intersubband linewidth [cf. Fig. 4.1 (b)]. This value for μ is in good agreement with a direct calculation using the envelope functions ζ_1 and ζ_2. With an effective electric field [Fig. 4.12]

$$E_{eff} = \frac{2\cdot\sin(60^\circ)}{\sqrt{n_{GaAs}}}\,\sqrt{2\,\frac{I^{pulse}}{c\,\epsilon_0\,\frac{\tau_{el}}{\sqrt{2}}\,\pi\,\left(\frac{d_{foc}}{2}\right)^2}} = 9\,\frac{\mathrm{kV}}{\mathrm{cm}}$$

where the duration of the Gaussian shaped electric field $\tau_{el} \approx 300$ fs [cf. Fig. 4.5 (a)], the pulse area yields

$$\theta = \frac{\mu\,E_{eff}\,\tau_{EL}}{\hbar} = 58^\circ$$

In the Bloch picture, we get the degree of excitation:

$$n_{ex} = \frac{1}{2}\Big(1 - \cos(\theta)\Big) = 23.5\%$$

This value is in good agreement with the one calculated above.

We have demonstrated that a strong nonlinear saturation (> 20 %) of the 1–2 intersubband excitation can be induced with incident pulses of only 1 pJ pulse energy. In the Bloch sphere picture, the strongest observed saturation of the free induction decay corresponds to a partial Rabi flop of up to 1/6 (60°) of the full cycle (360°) [Fig. 4.11 (b)].

4.5.2.2 Model calculations

Finally, we analyze the experimental data by model calculations using the Maxwell-Bloch equations for a homogeneously broadened two-level system [Eqs. (2.4)-(2.6)]. Our theoretical description is similar to that describing self-induced transparency experiments [131, 132]. In general the full spatial and time dependence in the Maxwell-Bloch equations have to be taken into account. In this case, Eqs. (2.4)-(2.6) have to be solved numerically. In the following, we will first treat the case of linear excitation. Finally, we consider the case of nonlinear excitation.

We make some approximations which simplify the problem considerably:

- In the prism geometry applied in our measurements, the electric field experienced by the electrons is nearly identical for all individual quantum wells, as is evident from the calculated intensity pattern in Fig. 4.3 (b). This fact allows for a simplified theoretical description with a position independent polarization $P_{Res}(z) \equiv P_{Res}$. Using the new coordinate system $x' = x$, $t' = t - x/v_{gr}$ (we will skip the primes in the following) Eq. (2.4) can be integrated along the interaction length L

$$E_{out} = E_{in} + i\,\frac{\Omega\,L}{2\,\epsilon_0\,c\,n}\,P_{Res} \tag{4.3}$$

- In the linear case n_{ex} is very small so that Eq. (2.6) can be neglected.
- Further, we assume that the amplitude of the re-emitted free induction decay is much smaller than the incident field amplitude, i.e.,

  $$|i\,\frac{\Omega\,L}{2\,\epsilon_0\,c\,n}\,P_{Res}| \ll E_{in} \tag{4.4}$$

  The experimental data indicate that the free induction decay [Fig. 4.5 (c)] has an amplitude which is approximately a factor of three times smaller than the amplitude of the incident field [Fig. 4.5 (a)]. Hence, this relation is not strictly satisfied. A direct comparison with the exact result for the linear case, however, justifies its application as will be shown below. With approximation (4.4), Eq. (2.5) can be treated independently from Eq. (2.4) considerably facilitating the solution of the Maxwell-Bloch equations.

The solution of Eq. (2.5) with an excitation field tuned to resonance ($\Delta\omega = 0$) is

$$P_{Res} = i\,\frac{\epsilon_0\,c\,n\,A_{abs}}{T_2\,\Omega\,L}\int_{-\infty}^{t} E_{in}(t')\,e^{\frac{t'-t}{T_2}}\,dt' \tag{4.5}$$

Putting (4.5) in (4.3) yields

$$E_{out} = E_{in} - \frac{A_{abs}}{2\,T_2}\int_{-\infty}^{t} E_{in}(t')\,e^{\frac{t'-t}{T_2}}\,dt' \tag{4.6}$$

In this calculation, the only free parameter is the incident field E_{in}. The absorption $A_{abs} = \ln(10)\cdot a$ is taken from the linear absorption measurement [Fig. 4.1 (b)] and the dephasing time $T_2 = 320$ fs is taken from four wave mixing experiments [69]. The second term of Eq. (4.6) is the re-emitted electric field, i.e., the free induction decay. It is emitted with a 180° phase shift so that it destructively interferes with the incident field E_{in} as mentioned above. The transmission coefficient [cf. Eq. (4.2)] is calculated by Fourier transforming Eq. (4.6)

$$t(\omega) = \frac{E_{out}(\omega)}{E_{in}(\omega)} = 1 - \frac{0.5\,A_{abs}}{1 - i\,(\omega - \omega_0)\cdot T_2} \tag{4.7}$$

Linear single pulse experiment To model the data, in a first step we fit a Gaussian to the reference electric field E_{Ref} [Fig. 4.5 (a)]. This yields the incident electric field E_{in} [Fig. 4.5 (d)]. Then, using Eq. (4.6) we calculate the field transient after transmission through the quantum well sample E_{out} [Fig. 4.5 (e)]. The free induction decay $E_{FID} = E_{out} - E_{in}$ is plotted in Fig. 4.5 (f). The experimental data [Fig. 4.5 (b)] agree well with the calculated transient.

Now, we come back to the question of the validity of the relation (4.4). We compare calculations with and without Eq. (4.4). Without this approximation, an analytic solution for the linear response can be found

$$E_{out} = E_{in} - \frac{A_{abs}}{T_2}\int_{-\infty}^{t} dt'\,e^{(t'-t)/T_2}\,E_{in}(t')\,\frac{J_1\left(\sqrt{2\,A_{abs}\,(t-t')/T_2}\right)}{\sqrt{2\,A_{abs}\,(t-t')/T_2}}$$

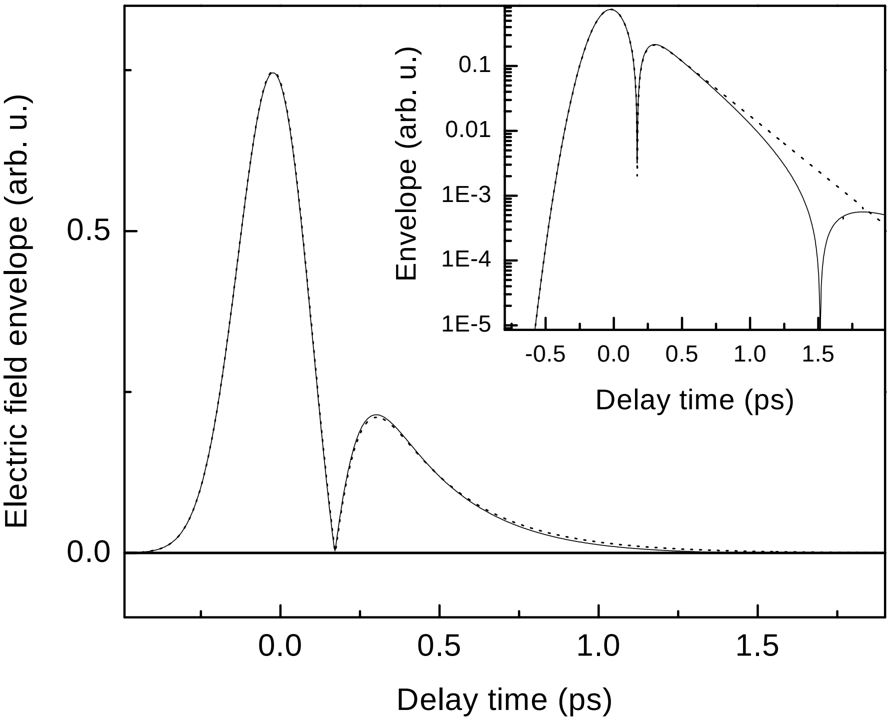

Figure 4.13: Calculated envelopes of electric field transients through the quantum well sample. The solid line indicates the full Maxwell-Bloch calculation using Bessel functions. The dotted line corresponds to a calculation where the approximation (4.4) was made. Inset: Field transient envelopes plotted on a logarithmic scale.

where J_1 is the first order Bessel function. In Fig. 4.13 the envelopes of the field transients calculated with and without approximation (4.4) are shown. A difference can only be observed on a logarithmic scale (inset of Fig. 4.13). This difference is much smaller than the noise in the measurement justifying a posteriori the application of Eq. (4.4) to model the experimental data.

Linear two pulse experiment In Figs. 4.6 (b) and 4.6 (d), the results of these model calculations in the case of two phase-locked incident pulses are shown. Such calculations are in excellent agreement with the data of Figs. 4.6 (a) and 4.6 (c).

Coherent nonlinear propagation In order to model the data shown in Fig. 4.7 it is important to note that the degree of excitation in (b) is rather high ($n_{ex} \approx 20$ %). Hence, in a model calculation using the Maxwell-Bloch equations the last Eq. (2.6) can not be neglected any more. However, as in the model for the linear case we can still assume that the amplitude of the re-emitted free induction decay is small compared to the amplitude of the incident field [Eq. (4.4)] so that the Bloch equations (2.5) and (2.6) can be treated independently from Eq. (2.4). For a given $E^{MIR}(t)$ we can calculate numerically $P_{Res}(t)$ using Eqs. (2.5) and (2.6). With Eq. (4.3) we then determine the electric field transient transmitted through the quantum well sample.

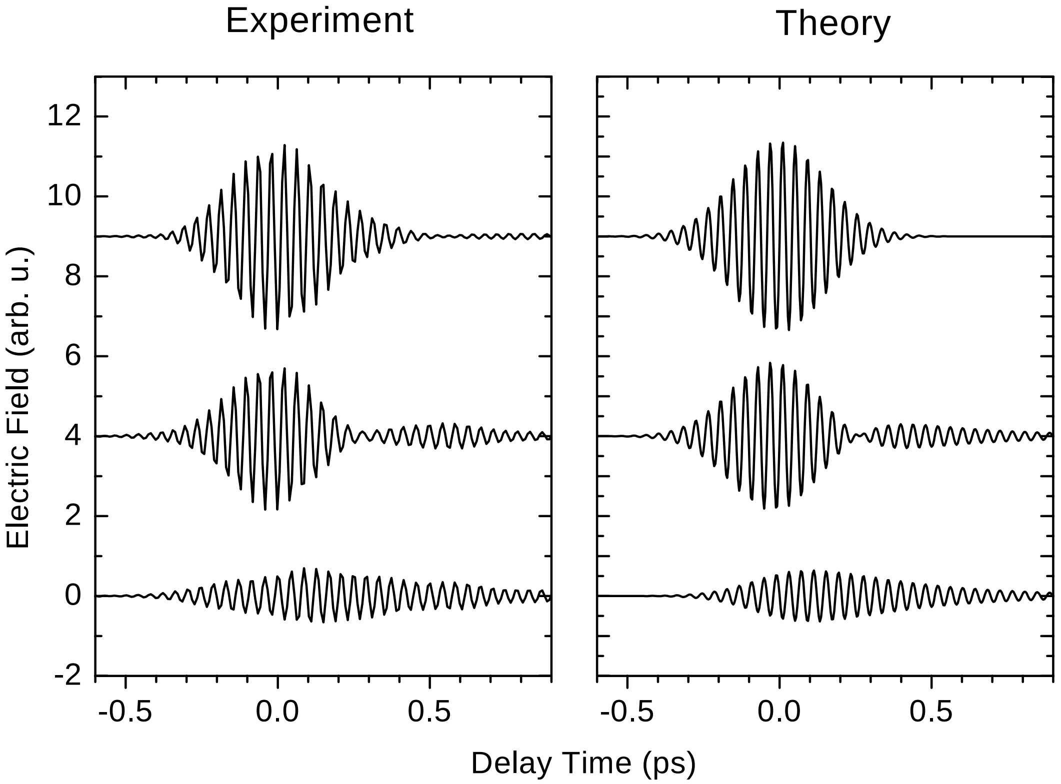

Figure 4.14: Measured and calculated electric field transients for high excitation ($I^{pulse} = 1.0$ pJ) through a reference sample (upper traces), through the quantum well sample (middle traces), and the free-induction decay (lower traces) of the intersubband excitation in response to a single pulse.

In Fig. 4.14 the calculated field transients for an incident pulse with energy $I^{pulse} = 1.0$ pJ are shown (right traces). It agrees well with the measured curves (left traces) [cf. Fig. 4.7 (b)]. The solid line in Fig. 4.11 (b) is the calculated ratio between the amplitude of the free-induction decay and the amplitude of the incident pulse E_{FID}/E_{in}. This curve fits also quite well the experimentally determined amplitude ratio [Fig. 4.11 (b), symbols].

In conclusion, we have demonstrated coherent control of linear intersubband polarizations with subpicosecond dephasing times by weak ultrafast electric field transients in the mid-infrared. A nonlinear response, i.e., a saturation of the polarization amplitude by up to 20 %, can be induced with pulses of only 1 pJ energy. This nonlinear response follows exactly the prediction of an ideal homogeneously broadened two-level system. This fact may facilitate the realization of ultrafast switching devices based on coherent intersubband polarizations.

Chapter 5

Direct measurement of electrically induced optical transmission changes in quantum cascade lasers

In this chapter, we present a direct study of optical transmission changes due to gain in an electrically driven quantum cascade structure. The normalized transmission change, i.e., $\big(T(I,\lambda) - T(0,\lambda)\big)/T(0,\lambda)$ is measured as a function of both applied current I and wavelength λ. The main motivation for this experiment is to develop a novel measurement technique which combines ultrafast spectroscopy with high-current electrical pumping of semiconductor device structures. This technique gives experimental access to fundamental questions of semiconductor physics which could not be obtained by other means. One important example, the physics of electron transport in semiconductor nanostructures in the presence of a dense electron plasma, will be discussed in the subsequent chapter.

The development of this technique implies considerable effort in the optical and electronic setup. Two things are very important. First, the light pulses have to penetrate highly doped, thick contact layers of the sample, which are necessary for electric pumping. Secondly, to prevent heating of the sample, the driving current has to be applied in pulsed mode. Thus, the combination of optical and synchronized electric pulses requires an elaborate electronic setup. For the experiments described in this chapter we use the cavity-dumped Ti:sapphire laser system presented in section 2.2.1 as it represents an easy tunable mid-infrared source.

Similar to the experiments discussed in the previous chapter we use a beam propagation geometry in which the optical beam is incident under an angle of 60°. This is an appropriate way to ensure a large coupling with the intersubband dipoles. To limit heat dissipation in the sample from the applied current, the quantum cascade structure is processed in circular mesas with a small surface. We have to take into account, however, that the mid-infrared light focus is rather large demanding a big mesa size for a suitable overlap. As a compromise, for the experiments discussed in this chapter we will use a sample which was originally developed for electroluminescence measurements. Here, the mesa has around half the size of the mid-infrared focus.

In the following we first introduce the quantum cascade sample. After the discussion of the effect of heating due to the electrical current, we will give a detailed explanation of the experimental realization to carry out a transmission change experiment. Then we present linear transmission change measurements to derive the gain coefficient. We analyze the data with respect to the effects resulting from the chosen beam propagation geometry. Taking these effects into account we will determine the gain coefficient of the quantum cascade structure and compare our results with work of other groups published in literature.

5.1 Sample properties

The sample used for the transmission change experiment (sample A_1) is a GaAs/Al$_x$Ga$_{1-x}$As quantum cascade structure (aluminum content: $x = 33$ %) grown at Thomson-CSF in Paris. It contains 10 periods of the active layer structure similar to the one in Ref. [99] and represents the layer structure of the first quantum cascade laser based on the GaAs/Al$_x$Ga$_{1-x}$As material system (aluminum content: $x = 33$ %). At this aluminum content AlGaAs is a direct gap semiconductor. The conduction band offset between AlGaAs and GaAs is $\Delta E_c = 295$ meV [133].

The conduction band diagram of the active region and the relevant wavefunctions are shown in Fig. 5.1. The active region consists of three coupled GaAs quantum wells. The injector is a graded superlattice containing five coupled GaAs quantum wells. The injector region and the active region are separated by a 6.2 nm thick AlGaAs injection barrier and a 3.4 nm thick AlGaAs exit barrier. The inset of Fig. 5.1 is a schematics of the injector and the active region under bias.

To reduce the lifetime of subband 2 (lower laser states), the 1–2 subband spacing corresponds to the energy of an LO phonon ($\hbar\,\omega_{LO} = 36$ meV). The calculated lifetimes of

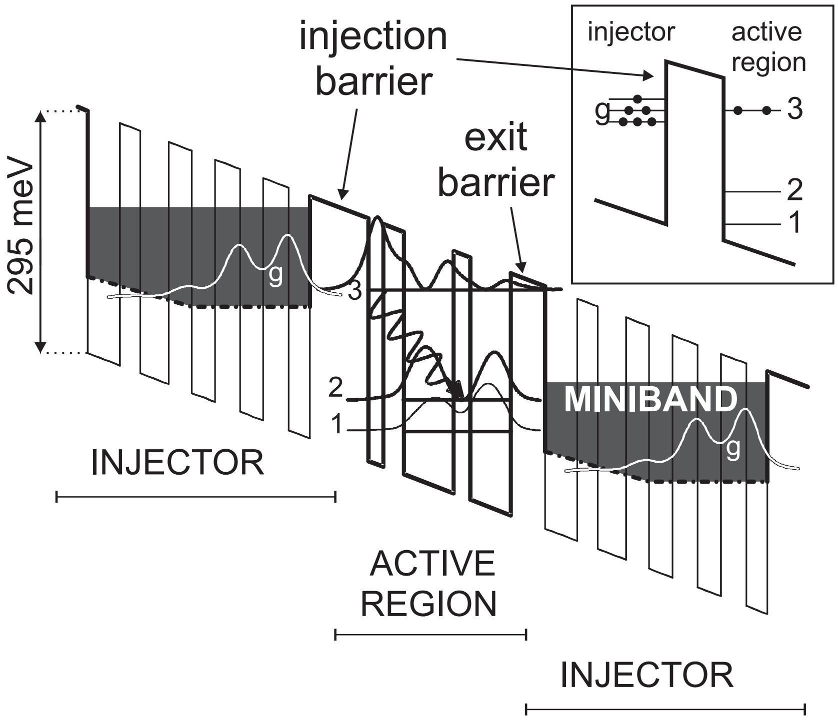

Figure 5.1: Conduction band diagram of sample A$_1$ for an applied electric field of 48 kV/cm. Probability densities $|\Psi(x)|^2$ are shown for the relevant wavefunctions ($|g\rangle$: ground state in the injector, $|3\rangle$: upper laser state, $|2\rangle$: lower laser state). The inset is a schematics of the injector and the active region divided by the injection barrier.

Table 5.1: Layer structure of sample A_1.

material	doping (Si)	thickness (nm)	
GaAs	2×10^{18} cm^{-3}	600	top contact
GaAs		20	
10 repetitions			
GaAs		3.2	injector
AlGaAs		2.0	
GaAs		2.8	
AlGaAs	4×10^{17} cm^{-3}	2.3	
GaAs	4×10^{17} cm^{-3}	2.3	
AlGaAs	4×10^{17} cm^{-3}	2.5	
GaAs	4×10^{17} cm^{-3}	2.3	
AlGaAs		2.5	
GaAs		2.1	
AlGaAs		6.2	active region
GaAs		1.5	
AlGaAs		2.0	
GaAs		4.9	
AlGaAs		1.7	
GaAs		4.0	
AlGaAs		3.4	
GaAs		3.2	injector
AlGaAs		2.0	
GaAs		2.8	
AlGaAs	4×10^{17} cm^{-3}	2.3	
GaAs	4×10^{17} cm^{-3}	2.3	
AlGaAs	4×10^{17} cm^{-3}	2.5	
GaAs		20	bottom contact
GaAs	2×10^{18} cm^{-3}	1000	
SI GaAs substrate (300 μm)			

subband 3 and subband 2 are $\tau_3 = 1.5$ ps and $\tau_2 = 0.3$ ps [99]. The complete layer structure is shown in Table 5.1.

The active region is sandwiched between two heavily n-doped ($n_{Si} = 2 \times 10^{18}$ cm^{-3}) GaAs contact layers [Fig. 5.2 (a)]. The quantum cascade sample is processed into round mesas with a mesa radius $R_m = 60\,\mu$m [Fig. 5.2 (c)], which is the size typically used for electroluminescence measurements. The mesa and the surrounding area are covered with a AuGe/Ni/Au alloyed contact.

This structure shows electroluminescence due to spontaneous emission from subband 3 to subband 2 in the biased case and photo-current due to absorption from subband 1 to subband 3 in the unbiased situation as shown in Fig. 5.3 (a). At a cryostat cold-finger temperature $T_{CF} = 77$ K and for a current density of 1.8 kA/cm^2 (dashed line) a single electroluminescence peak can be seen, which is centered at 10.4 μm. The width is 13 meV

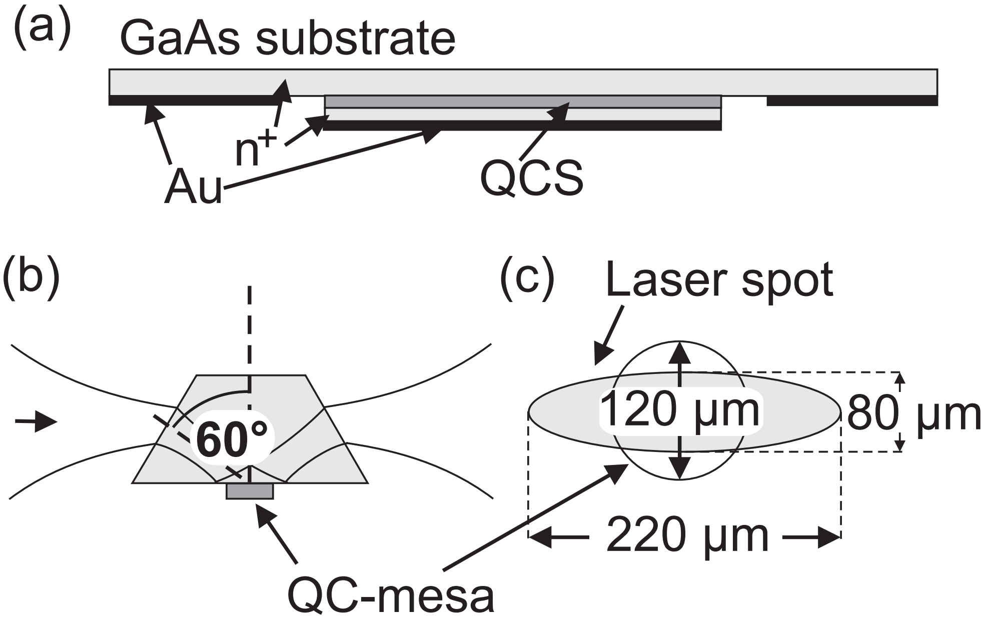

Figure 5.2: (a) The active region of the quantum cascade structure (QCS) is sandwiched between two n-type GaAs layers ($n = 2 \times 10^{18}$ cm^{-3}, thicknesses: 1 μm and 0.6 μm). (b) Geometry of beam propagation through the prism shaped sample. (c) Partial overlap between the mid-infrared laser spot and the disc shaped quantum cascade structure (QC-mesa).

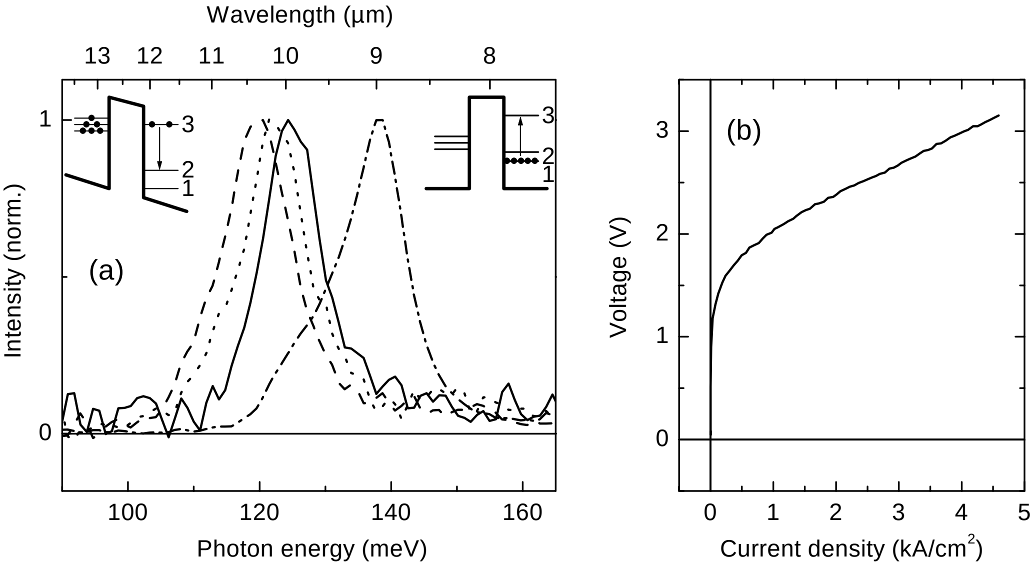

Figure 5.3: (a) Electroluminescence for different current densities (dashed line: 1.8 kA/cm^2, dotted line: 3.5 kA/cm^2, solid line: 7.1 kA/cm^2) and photocurrent (dash-dotted line) spectra of sample A$_1$ measured at $T_{CF} = 77$ K [134]. Left inset: Injector and active region with applied bias. Spontaneous emission from subband 3 to subband 2 leads to the shown electroluminescence spectra. Right inset: Injector and active region without bias. 1–3 absorption leads to photocurrent. (b) Current–voltage characteristics measured at a cryostat cold-finger temperature $T_{CF} = 77$ K with 400-ns current pulses at a repetition rate of 10 kHz [134].

(FWHM). At a current density of 7.1 kA/cm^2 (solid line) the electroluminescence peak shifts to 10.0 μm and the width is 10 meV. For increasing voltage the tilting of the bandstructure becomes stronger. As a result, the subbands in the active region move apart leading to the observed blue shift of the electroluminescence. The photo-current is peaked at a wavelength of 9.0 μm. In Fig. 5.3 (b) the current-voltage characteristics is shown. For voltages up to 1.5 V there is very low current. This voltage is needed for the alignment of the injector and the active region.

To measure the transmission change due to 3–2 population inversion, we use mid-infrared light resonant to this intersubband transition. For an efficient coupling of the intersubband dipoles with the electric field of the optical beam, we use a beam propagation geometry [Fig. 5.2 (b)] with an angle of incident $\alpha = 60°$ as discussed in the previous chapter. The substrate thickness is 300 μm. According to the considerations of section 4.2 this results in a length of $a = 790\,\mu$m for the base plane of the prism.

The laser device mentioned above (ridge waveguide, 2.5 mm × 24 μm) with 30 periods of a similar layer structure but with an injection barrier thickness of 5.8 nm has a threshold current density of $I_{th} = 7.3$ kA/cm^2 at 77 K. This laser works up to a temperature of $T_{th} = 140K$. We want to drive our sample with current densities up to I_{th} and below T_{th}. Hence, a careful consideration of the heat dissipation due to the current is important.

5.2 Heat dissipation due to electrical current

The current density $I_{th} = 7.3$ kA/cm^2 corresponds to a dissipated thermal power of $P_{th} = U(I_{th})\, I_{th}\, \pi\, R_m^2 \approx 3.5$ W. The cryostat we use has only a cooling power of ≈ 1 W. Hence, we have to electrically drive the sample in pulsed mode with a duty cycle of at most 25 %. The question now is the sample heating within a single current pulse.

Thermal conductivity For an applied current pulse with current density I we want calculate the lattice temperature T of the sample as a function of time t. The relevant equation is the equation of thermal conductivity

$$\frac{\partial T(\vec{r},t)}{\partial t} = \frac{\lambda\big(T(\vec{r},t)\big)}{\rho\, c_p\big(T(\vec{r},t)\big)}\,\Delta T(\vec{r},t) + \frac{1}{\rho\, c_p\big(T(\vec{r},t)\big)}\,\eta(I,\vec{r})$$

where λ is the thermal conductivity, ρ the density, c_p the heat capacity, η the dissipated heat per volume and Δ the Laplace operator. Because of the temperature dependence of λ and ρ (see Fig. 5.4) there is no analytic solution of this equation. Here, we will just treat the two extreme cases at very long times and at very short times. This will allow us to give a sufficient estimation for the lattice temperature of our sample.

- In the first case we consider the (quasi-stationary) thermal equilibrium, i.e., $\frac{\partial T}{\partial t}|_{t=\infty} = 0$, which is reached after "long"times. We calculate the average temperature in the mesa $T_{eq} \equiv T(t=\infty)$. The equation of thermal conductivity then yields the Poisson equation

  $$\Delta T(\vec{r}) = -\frac{\eta(I,\vec{r})}{\lambda} \qquad (5.1)$$

  A strong simplification of the problem can be achieved if we assume that the quantum cascade mesa (radius R_m) is a semi sphere with a surface which is equal to the surface

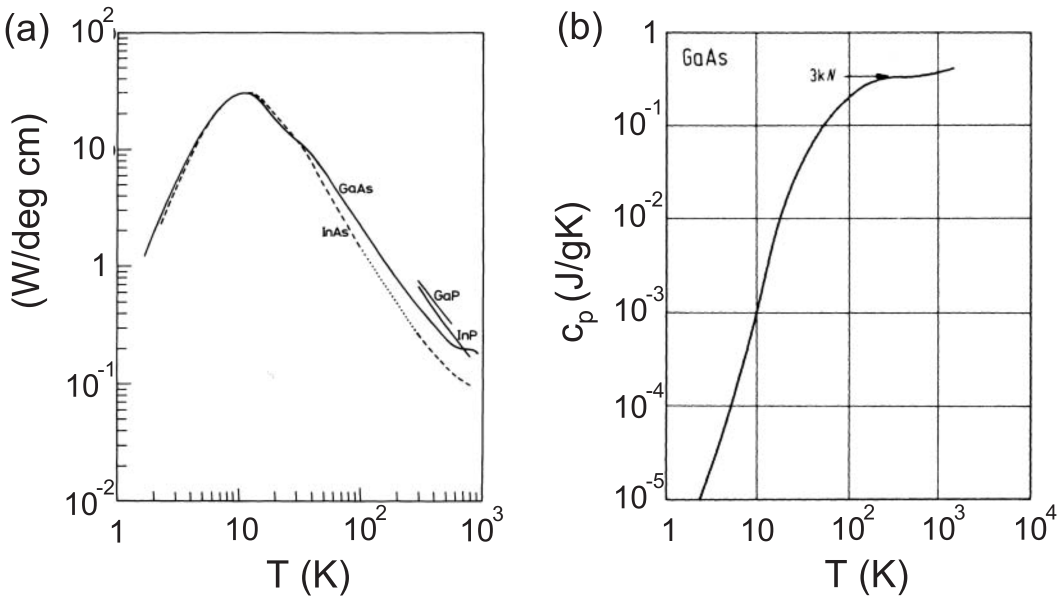

Figure 5.4: (a) Thermal conductivity [135] and (b) heat capacity [136] of GaAs as a function of temperature.

of the circular mesa disc. The radius of this sphere is $R_s = \frac{R_m}{\sqrt{2}}$. In that way the thermal flux, which is the essential quantity for thermal conductivity, is the same in both geometries. For symmetry reasons we can consider a total spherical situation, where r is the distance from the center. The boundary condition is $T(r = \infty) = T_{CF}$ where T_{CF} is the temperature of the cold-finger of the cryostat. The solution of this spherical problem for $\lambda = const.$ is

$$\begin{aligned} r \geq R_s: \quad T(r) &= \frac{1}{3} \frac{\eta R_s^3}{\lambda r} + T_{CF} \\ r \leq R_s: \quad T(r) &= -\frac{1}{6} \frac{\eta r^2}{\lambda} + \frac{1}{2} \frac{\eta R_s^2}{\lambda} + T_{CF} \end{aligned}$$

We are interested in the average mesa temperature

$$T_m(I, R_m) \equiv \frac{T(R_s) + T(0)}{2} = \frac{5}{12} \frac{\eta(I) R_s^2}{\lambda} + T_{CF}$$

The heat dissipation per volume in the semi-sphere due to the electric current in the quantum cascade laser reads

$$\begin{aligned} r \leq R_s: \quad & \eta(I, r) = \eta(I) = \frac{U(I)\, I\, \pi R_m^2}{\frac{2}{3} \pi R_s^3} = 3\sqrt{2} \frac{U(I)\, I}{R_m} \\ r > R_s: \quad & \eta(I, r) = 0 \end{aligned}$$

This yields finally

$$T_{eq}(I, R_m) = \frac{5}{4\sqrt{2}} \frac{U(I)\, I}{\lambda} R_m + T_{CF} \tag{5.2}$$

Note that the temperature in the thermal equilibrium depends on the mesa radius R_m.

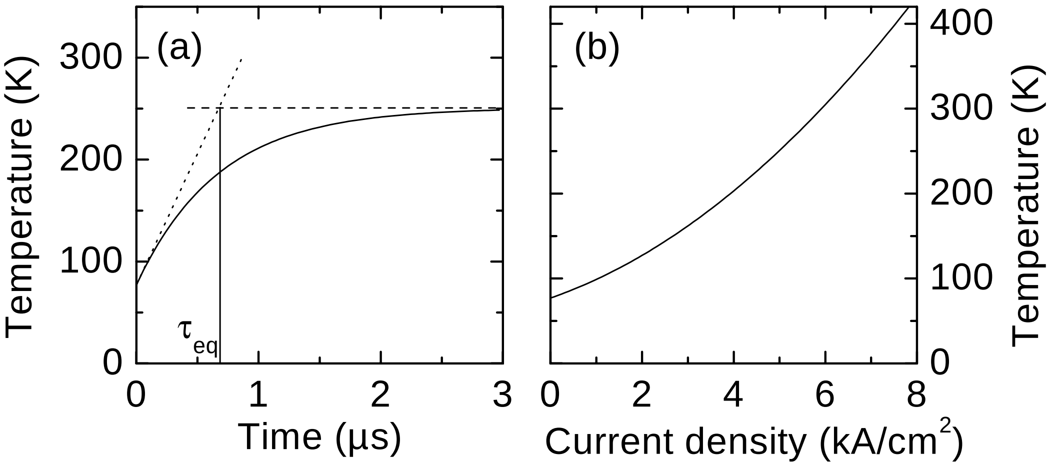

Figure 5.5: (a) Temperature at the quasi-stationary equilibrium T_{eq} (dashed line), temperature dependence at early times T_s (dotted line) and an exponential behavior (solid line) as a function of time for a quantum cascade mesa with radius $R_m = 60\,\mu$m and for a current density of $I = 5$ kA/cm^2. τ_{eq} is the time constant reaching the quasi-stationary equilibrium. (b) Temperature at the quasi-stationary equilibrium as a function of current density ($R_m = 60\,\mu$m).

- In the second case, at very short times, the term with the thermal conductivity can be neglected, i.e., $\Delta T = 0$. The equation of thermal conductivity can be easily solved for $c_p = const.$

  $$T_s(t, I) = \frac{\eta(I)}{\rho\, c_p}\, t + T_{CF} = \frac{U(I)\, I}{\rho\, c_p\, L}\, t + T_{CF} \tag{5.3}$$

  where L is the mesa thickness and $\eta(I) = \frac{U(I)\,I}{L}$. Note that Eq. 5.3 does not depend on the mesa radius R_m.

For a quantum cascade mesa with $R_m = 60\,\mu$m and a current density of $I = 5$ kA/cm^2 these two regimes are depicted in Fig. 5.5 (a). The cold-finger temperature is $T_{CF} = 77$ K. The thermal conductivity is taken to be $\lambda = \lambda(250\text{ K}) = 0.5\,\frac{\text{W}}{\text{K cm}}$ [cf. Fig. 5.4 (a)], the heat capacity as $c_p(100\text{ K}) = 0.2\,\frac{\text{J}}{\text{g K}}$ [cf. Fig. 5.4 (b)] and the density of GaAs is $\rho = 5.3$ g/cm^3. The temperature in the mesa is shown as a function of time. The dashed line represents the temperature T_{eq} which will be reached after long times. The dotted curve indicates the temperature dependence for very short times T_s. These calculations are "worst case"calculations and the true temperature will be somewhere below (solid line). Nevertheless, with these calculations we can estimate a time constant $\tau_{eq} \approx 700$ ns reaching the quasi-stationary equilibrium. Comparing (5.2) and (5.3) one can see that this time constant does not depend on the current. In Fig. 5.5 (b) the current dependence of the temperature T_{eq} is shown. We get room temperature $T_{eq} = 300$ K for a current density of 6 kA/cm^2. The maximum working temperature of the laser based on the laser structure of our sample is $T_{th} = 140$ K. It is reached already at 2.5 kA/cm^2.

It is important to note that the temperatures calculated above describe the temperature of the lattice of the quantum cascade structure. In general, these temperatures are not

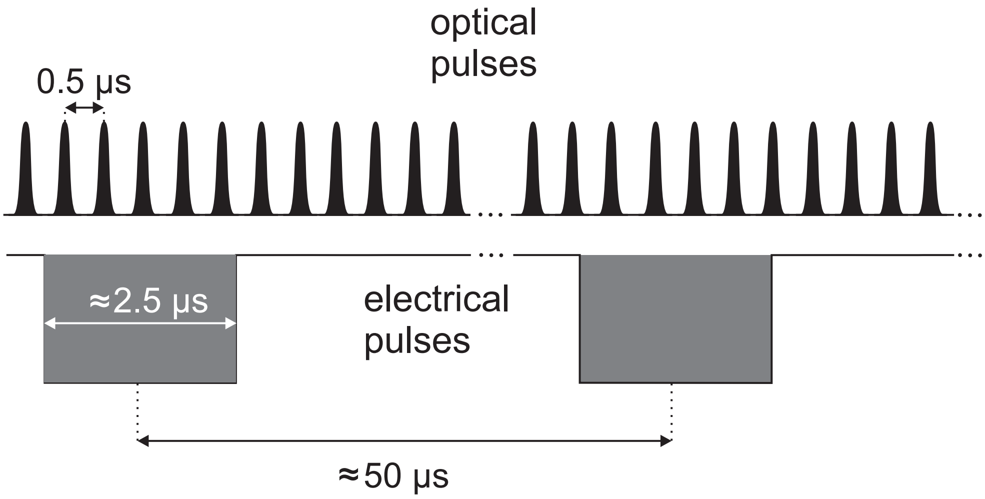

Figure 5.6: Timing of electrical and optical pulses. The electrical pulses are applied with a repetition rate of 23.8 kHz and a duty cycle of 5 %. The optical pulses have a repetition rate of 2.1 MHz.

valid for the carrier system. The electron distribution in electrically driven quantum cascade structures will have a temperature far above the lattice temperature (cf. chapter 3).

Electrical pulse length For the experiment we use the 2 MHz cavity-dumped Ti:sapphire system as described in section 2.2.1. To ensure a lattice temperature on the order of the cold-finger temperature the ideal electrical pumping would be to use very short pulses with pulse lengths on the order of $\tau_{eq}/10 \approx 70$ ns [Fig. 5.5 (a)] in combination with a synchronization of the current with the mid-infrared pulses. This is not possible, however, since high-current pulser providing current pulses with such elevated repetition rates are not available. For the experiments presented in this chapter we use a scheme as depicted in Fig. 5.6 with current pulses being longer than the inverse repetition rate of the optical pulses. Now, the transmission change signal is proportional to the electrical pulse length. We use a repetition rate for the electrical pulses of 23.8 kHz with a duty cycle of 5 % which corresponds to a pulse length of approximately $2.5\,\mu$s. Within this time, quasi-stationary equilibrium of the lattice temperature is attained [Fig. 5.5 (a)]. From Fig. 5.5 (b) we see that $T_{th} = 140$ K is reached already at a current density of 2.5 kA/cm^2. Therefore it makes only sense to use this method applying low currents.

5.3 Sample configuration

Sample holder geometry The combination of ultrafast spectroscopy with an electrically driven sample at cryogenic temperatures implies several requirements for the sample holder. One restriction results from the cryostat geometry. As a small optical focus is needed in the experiment we use a focussing optics with a small focal length. This requires a cryostat chamber with a small volume. For the experiment presented in this chapter, we have used a home-built liquid-nitrogen cold-finger cryostat. Since this cryostat has no heating facility, for the subsequent experiments we have used a commercial helium flow cryostat (Oxford,

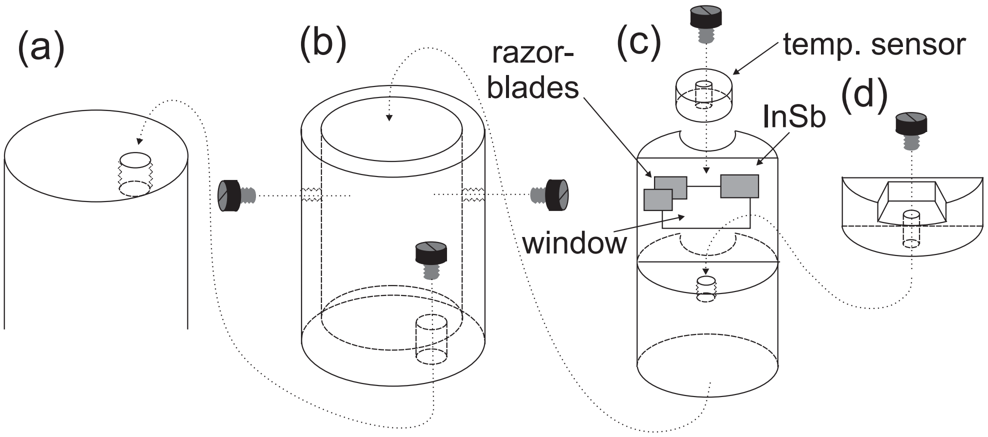

Figure 5.7: Sample holder consisting of three (b-d) parts attached to the cold-finger (a). The razor-blades and the InSb piece are fixed with part (c). Additionally, (c) contains the temperature sensor. The holder (d) carries the sample and the bond pads.

Optistat) which allows for adjustable temperatures from room temperature down to 4 K. Both cryostats have a similar chamber with a diameter of approximately 7 cm and a maximum sample holder diameter of 22 mm. In developing the sample holder we have to consider the following important points:

To find the optical focus and the spatial overlap between the pump beam and the probe beam we have to fix two crossed razor blades close to the sample. Further, we need a thin InSb plate for a cross-correlation experiment to find the temporal overlap of the pump pulse and the probe pulse. Then, two bond pads are required for the electric contacts providing the current through the sample. Another two bond pads are needed for the voltage measurement. These pads should have a good thermal contact to the cold-finger.

We use a sample holder consisting of three parts. The first part is a tube [Fig. 5.7 (b)], directly attached to the cold-finger [Fig. 5.7 (a)]. The second part contains the razor blade, the InSb plate, and the temperature sensor (Cryovac, DT-470 CD) as shown in Fig. 5.7 (c). It is fixed with the first part on a variable height. The sample and the bond pads are mounted on a separate holder [Fig. 5.7 (d)]. This holder is attached to the second part.

Processing The GaAs/AlGaAs sample is grown by molecular beam epitaxy on a 300 μm thick, mono-crystalline, and semi-insulating GaAs substrate. After the growth the samples are processed. Processing consists of three steps, etching, metallization structuring, and finalization. First, the sample is etched so that round mesas remain containing the grown layers [see Fig. 5.8 (a)].

By metallization structuring, the sample is contacted. The finalization contains cutting and polishing. The sample is cut in bars [see Fig. 5.8 (a), dashed lines] by cleaving along one crystal coordinate. The next step is to polish the side facets of the sample so that the sample becomes prism shaped. We glue a sample bar with a removable glue (Canada Balsam) with the mesas upside down on a glass prism [Fig. 5.8 (b)]. Then, the sample is polished along the prism sides [dashed lines in Fig. 5.8 (b)].

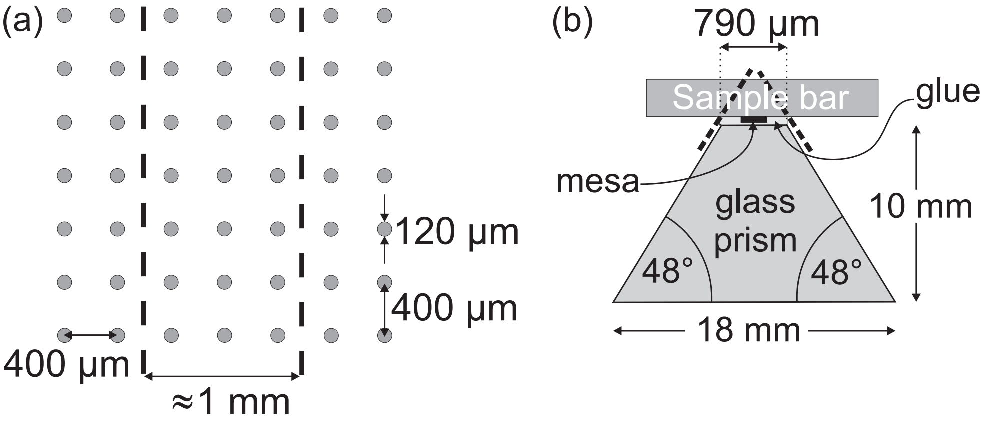

Figure 5.8: (a) Geometry of the sample surface. The round mesas contain the active layers. The sample is cut into ≈ 1 mm broad bars along the dashed lines. (b) The sample bar is glued on a glass prism with the mesas upside down and polished along the prism sides (dashed lines).

Mounting the sample The next step is to mount the sample onto the sample holder. The polished sample is glued using removable glue (Canada Balsam) on a plane iron plate with the mesas upside down. The sample holder is fixed with double sided tape on a linear translation stage [see Fig. 5.9 (a)]. One edge of the sample is covered with low temperature glue with a large thermal conductivity (Cryovac, Stycast Epoxy). The sample holder is moved down until it touches the sample. One has to wait about 24 h to have the glue dried out. Next, we heat the iron plate so that the wax gets liquid. Then, the sample holder with the sample can be removed. To get rid of the wax sticking on the sample we clean the sample with acetone and ethanol soaked cotton wool. The sample is glued onto the sample holder only at one side to prevent strain when cooling the sample [Fig. 5.9 (b)].

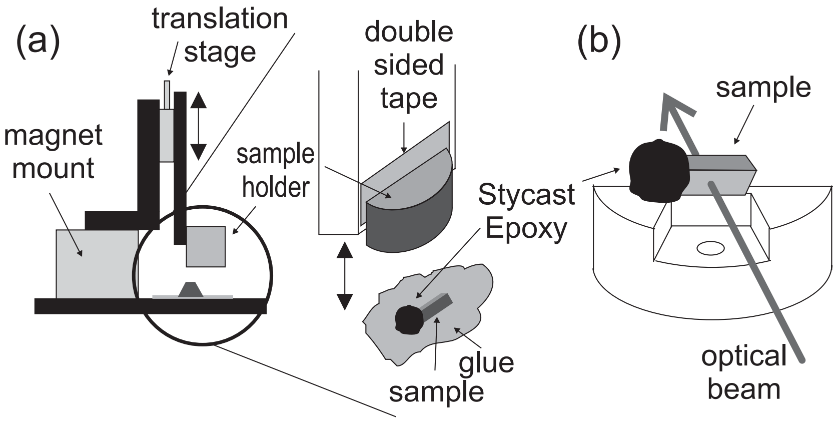

Figure 5.9: (a) Mounting of the sample. (b) To prevent strain due to cooling, the sample is fixed only at one side with the holder.

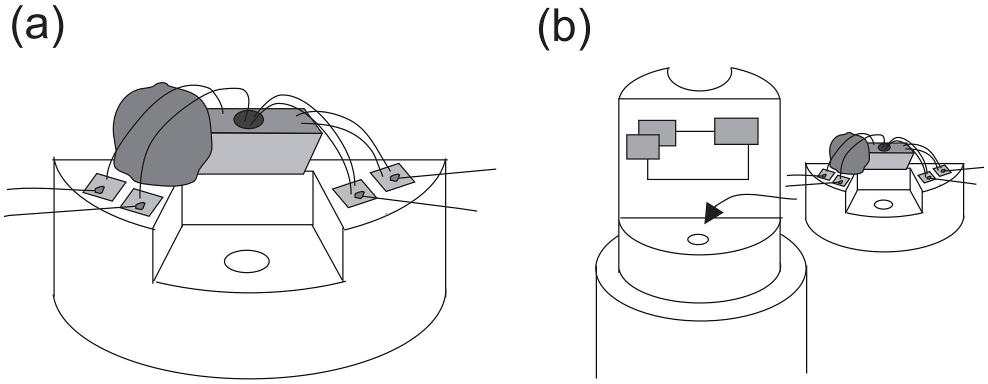

Figure 5.10: (a) Electric wiring of the sample. (b) Fixation with the other parts of the sample holder.

Electric wiring Electric wires are glued with conducting glue onto the contact pads [Fig. 5.10 (a)]. Then, the sample is bonded with aluminum wires (20 μm diameter). After this, the sample holder is fixed with the cryostat cold finger [Fig. 5.10 (b)]. Finally, we solder each of the wires to the core of a $50\,\Omega$ co-axial cable.

5.4 Experimental setup

Electronic setup The electronic setup is shown schematically in Fig. 5.11. We use the lock-in technique for noise reduction. The optical pulses are chopped with the frequency F_1, the sample is driven with electrical pulses with a repetition rate F_2 and the signal is detected at the sum-frequency (SF) $F_3 = F_1 + F_2$. In this dual frequency technique, we get a signal at the sum frequency F_3 only if both the current is applied and the probe beam is "switched on". This is necessary to prevent the signal from being disturbed by the electroluminescence and by heat radiation. The three frequencies F_1, F_2 and F_3 are generated by a home built frequency divider using the programmable logic chip ispLSI 1016-60LJ from Lattice. The clock frequency $F = 1$ MHz is divided by $n_1 = 23 \times 21$, $n_2 = 23 \times 2$ and $n_3 = 21 \times 2$ to yield the frequencies

$$F_1 = \frac{F}{n_1} = 2.1 \text{ kHz} \quad , \quad F_2 = \frac{F}{n_2} = 21.7 \text{ kHz} \quad , \quad F_3 = \frac{F}{n_3} = 23.8 \text{ kHz}$$

The pulses with frequency F_2 are used to trigger the current pulser (HP pulse generator 8114 A) which generates rectangularly shaped current pulses up to 1 A. A pulse length of $\Delta t = 2.5\,\mu$s which corresponds to a duty cycle of $5\,\%$ is used. The current is measured via the voltage drop on a $R = 50\,\Omega$ series resistance.

The light beam chopper controller is triggered with the frequency F_1. The chopped mid-infrared beam is measured with a HgCdTe detector (MCT). This signal is amplified with a high-frequency current pre-amplifier (GRASEBY INFRARED DP-8000) and sent to the signal input (SIG) of the lock-in (ITHACO 3961B). Additionally, the near-infrared beam is detected with a fast photodiode (PD: Electro Optics Technology, ET2000). This signal is amplified (HMS electronics 564) and sent to the signal input (SIG) of the lock-in. It is used to determine the phase of the signal (see below).

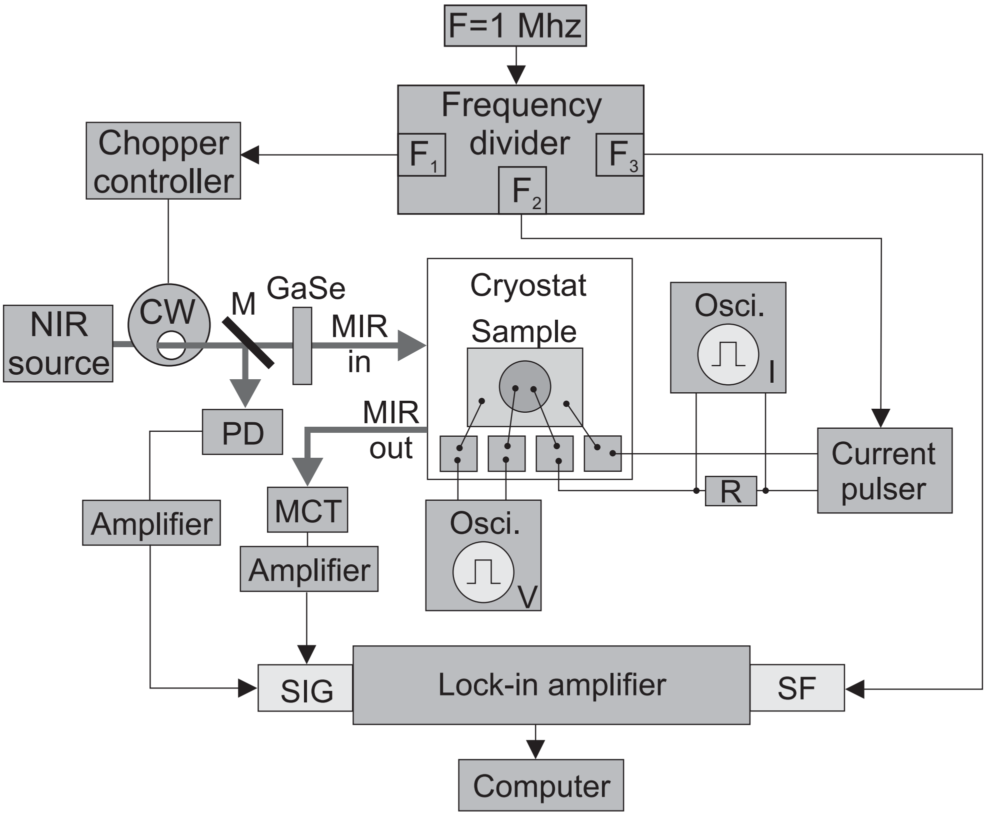

Figure 5.11: Electronic setup for the transmission-change measurement of an electrically driven quantum-cascade laser. A dual-frequency lock-in technique is used to suppress the electroluminescence and heat radiation signal. R - 50 Ω resistance, PD - photo diode, CW - chopper wheel, M - repositionable mirror, MCT - mercury cadmium telluride detector, SIG - signal input of the lock-in, SF - trigger input of the lock-in.

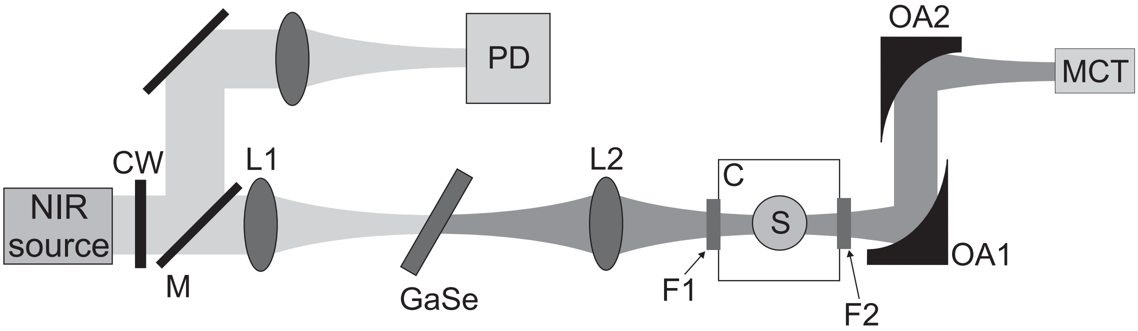

Figure 5.12: Optical setup for the transmission-change measurement. For the determination of the phase of the signal, i.e., transmission increase or decrease, the optical beam is reflected with a repositionable mirror (M) onto a photodiode (PD). CW - chopper wheel, L1/L2 - KBr lenses (f=50 mm), F1,F2 - 5 mm thick KBr windows, C - cryostat, S - sample, OA1/OA2 - gold coated 2″, 90° off-axis mirrors, MCT - mercury cadmium telluride detector.

Optical setup The optical setup is illustrated in Fig. 5.12. The output of a cavity-dumped Ti:sapphire oscillator is used to generate tunable mid-infrared pulses via phasematched difference frequency mixing in GaSe (see chapter 2.2.1.2). These pulses are focussed with a KBr lens (L2) onto the nitrogen-cooled sample (S). The transmitted light is collected with a gold coated 2″, 90° off-axis mirror (OA1) and focussed with another gold coated 2″, 90° off-axis mirror (OA2) onto a nitrogen cooled mercury cadmium telluride detector (MCT, model EG&G J15D16). Alternatively, using a repositionable mirror (M), the chopped near-infrared beam is measured with a fast photodiode (PD). The relative phase of the photodiode signal and the MCT signal determines the sign of the transmission change signal. If the phase of the PD signal is the same as the phase of the MCT signal then a transmission increase is measured. If the phase is retarded by 180° than the MCT signal corresponds to transmission decrease. The spectral information is obtained by tuning the center frequency of the mid-infrared beam via rotating the GaSe crystal.

5.5 Experimental data

In this section we present the results of linear transmission change experiments [Figs. 5.13 (a-c)]. In Fig. 5.13 (a), the transmission of pulses at $\lambda_{MIR} = 10.5\,\mu$m through the quantum cascade structure with zero bias is plotted as a function of the lateral distance between the mesa containing the quantum cascade structure and the mid-infrared beam (squares). The transmission through the sample decreases by a factor of about 4 for optimum spatial overlap of the mid-infrared beam with the mesa. For forward bias and in-plane (P) polarization of the mid-infrared beam, one observes an increase of transmission at $\lambda_{MIR} = 10.5\,\mu$m with the spatial profile plotted in Fig. 5.13 (a) (circles). This profile peaks at the center of the mesa, the full width at half maximum is $125\,\mu$m. Such a signal is exclusively found for in-plane

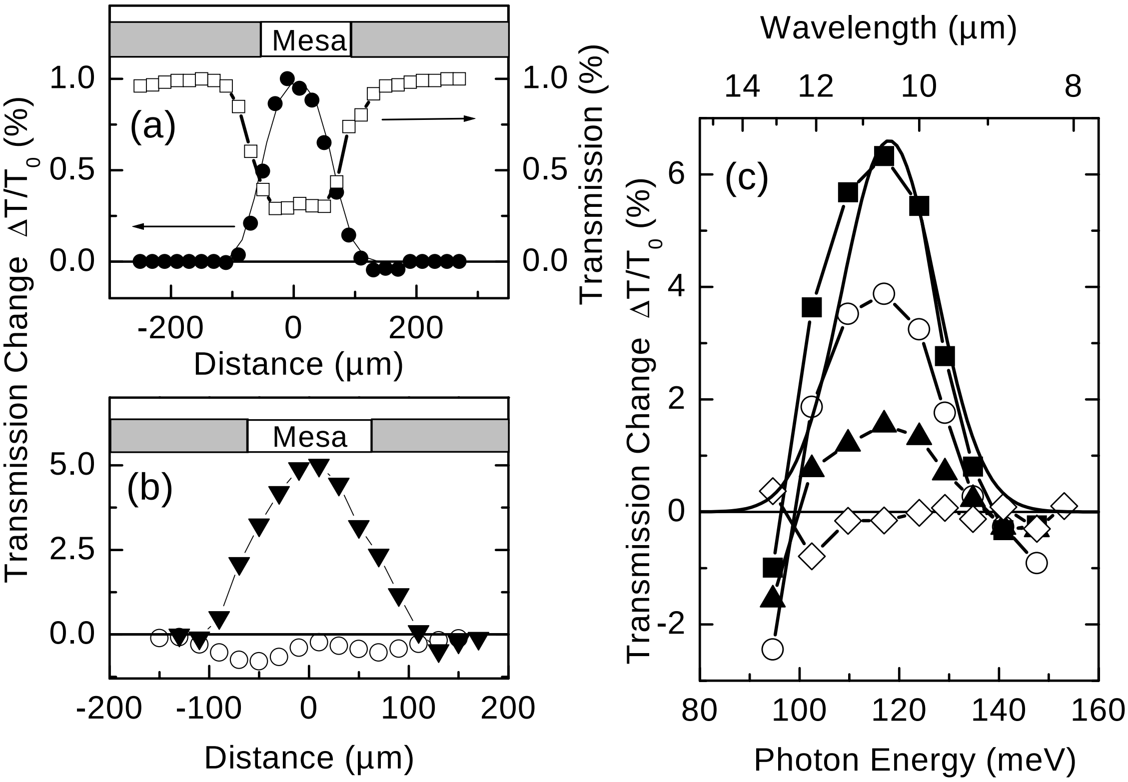

Figure 5.13: (a) Lateral profiles of the sample transmission (squares) and of the transmission change $\Delta T/T_0 = [T(I)-T(I=0)]/T(I=0)$ (circles) as a function of the separation between the laser spot and the quantum cascade structure. The solid lines are the convolution of the disc-shaped quantum cascade structure with the elliptical mid-infrared beam. (b) Polarization dependence of the electrically induced transmission change for P polarization (triangles) and for S polarization (circles) of the mid-infrared beam as a function of the separation between the laser spot and the quantum cascade structure for $\lambda = 10.5\,\mu$m. (c) Spectral dependence of the electrically induced transmission change $\Delta T/T_0$ at $T_{CF} = 77$ K for applied current densities of 0 kA/cm^2 (diamonds), 1.8 kA/cm^2 (triangles), 3.1 kA/cm^2 (circles), and 4.5 kA/cm^2 (squares). Solid line: gain spectrum calculated from the electroluminescence spectrum and convoluted with the spectral envelope of the mid-infrared pulses.

(P) polarization of the mid-infrared pulses. Signals with S polarization are negligibly small as can be seen in Fig. 5.13 (b). The spectral characteristics of the transmission increase at $T_{CF} = 77$ K is presented in Fig. 5.13 (c), displaying spectra measured for different injection currents (symbols). We have measured for current densities up to 4.5 kA/cm^2. The signal amplitude follows monotonically the applied current I for forward bias and reaches very high values of up to 6 %. It is centered at $\lambda = 10.5\,\mu$m.

5.6 Discussion

The electrically induced transmission change measurements represent the first measurements combining the techniques of ultrafast spectroscopy with high-current electrical pumping of a quantum cascade structure. We will now evaluate the experimental data to derive the gain coefficient.

5.6.1 Qualitative analysis

A first question in the evaluation of the experiment is whether the measured transmission change signals can be attributed to stimulated emission due to the 3 to 2 intersubband population inversion in the quantum cascade structure. The spatial dependence [Fig. 5.13 (a)] shows that the signal comes exclusively from the quantum cascade structure. As the signal is dominantly P-polarized [Fig. 5.13 (b)] there is strong evidence that the observed transmission change is due to an intersubband transition.

Now, we compare the spectral transmission change data [Fig. 5.13 (c)] with the electroluminescence data [Fig. 5.3 (a)]. Gain and electroluminescence both result from radiative intersubband transitions between the upper laser subband 3 and the lower laser subband 2. The fundamental difference between the two quantities is that gain is due to stimulated emission whereas the electroluminescence results from spontaneous emission. The probability of an electron to emit spontaneously a photon of energy $\hbar\,\omega$ depends on the density of photon states which is proportional to ω^2. In a single particle picture, i.e., neglecting many-body effects, the gain coefficient $g(\hbar\,\omega)$ and the electroluminescence intensity $I_{EL}(\hbar\,\omega)$ read [50]

$$\begin{aligned} g(\hbar\,\omega) &\sim \omega \sum_{\vec{k}} |\vec{r}_{3,2,\vec{k}}|^2 \Big(f(|3,\vec{k}\rangle) - f(|2,\vec{k}\rangle) \Big)\, \delta\Big(E_3(k) - E_2(k) - \hbar\omega \Big) \qquad (5.4) \\ I_{EL}(\hbar\,\omega) &\sim \omega^4 \sum_{\vec{k}} |\vec{r}_{3,2,\vec{k}}|^2 \Big(1 - f(|2,\vec{k}\rangle) \Big)\, f(|3,\vec{k}\rangle)\, \delta\Big(E_3(k) - E_2(k) - \hbar\omega \Big) \end{aligned}$$

where $\vec{r}_{3,2,\vec{k}}$ is the 3–2 dipole matrix element and f is the occupation probability for the upper laser states $|3,\vec{k}\rangle$ and the lower laser states $|2,\vec{k}\rangle$ with in-plane momentum $\vec{k}$.

In first order the two subbands are parallel so that details of the in-plane distributions have only a minor influence on the spectral lineshape of the gain. In this case gain is observed whenever the total population in subband 3 is larger than in subband 2, i.e.,

$$\sum_{\vec{k}} f(|3,\vec{k}\rangle) > \sum_{\vec{k}} f(|2,\vec{k}\rangle)$$

However, in general in the single particle picture nonparabolic subband dispersion can not be neglected.

In contrast, the intensity of electroluminescence is essentially determined by the total population in subband 3, since the factor $\left(1 - f(|2, \vec{k}\rangle)\right)$ is almost one for hot, i.e., nondegenerate electron distributions in subband 2. According to this discussion, the occurrence of electroluminescence does not automatically imply population inversion resulting in optical gain.

Nevertheless, the spectral shape of the gain coefficient can—in good approximation—be determined from the wavelength dependence of the electroluminescence $g(\hbar\,\omega) \sim I_{EL}(\hbar\,\omega)/\omega^3$. The solid line in Fig. 5.13 (d) represents the function $I_{EL}(\hbar\,\omega)/\omega^3$. The good agreement between the spectral shape of the experimental data and the calculated curve clearly demonstrates that the observed transmission increase is due to optical gain on the 3–2 lasing transition of the quantum cascade structure.

Note that the gain increases even for current densities higher than 2.5 kA/cm^2, where the sample temperature is above 140 K [Fig. 5.5 (b)]. At these temperatures the corresponding laser device with similar layer structure does not work [99].

5.6.2 Quantitative analysis

For a quantitative determination of the gain coefficient $g(I)$ we need a more detailed analysis of the observed signal. After interaction with the electrically driven quantum cascade structure the mid-infrared intensity yields

$$S(I, \lambda) = S_0 \times e^{(g(I,\lambda)-\alpha(I,\lambda)-\alpha_o)\,l}$$

where $S_0(\lambda)$ is the incident mid-infrared intensity, I the current density, α the current dependent absorption (e.g., the 1–3 absorption), α_o the current independent absorption (e.g., free carrier absorption from the contact layers) and l the interaction length. In the experiment, we measure the electrically induced transmission change, i.e., the normalized difference between the transmission with $[T(I \neq 0, \lambda)]$ and without $[T(I = 0, \lambda)]$ applied bias. For $g(I)\,l$, $\alpha(I)\,l \ll 1$ we get

$$\begin{aligned} \frac{\Delta T}{T_0}(I, \lambda) &= \frac{T(I,\lambda) - T(0,\lambda)}{T(0,\lambda)} = \frac{\frac{S(I,\lambda)}{S_0} - \frac{S(0,\lambda)}{S_0}}{\frac{S(0,\lambda)}{S_0}} = \frac{e^{\left(g(I,\lambda)-\alpha(I,\lambda)-\alpha_o\right)l} - e^{\left(g(0,\lambda)-\alpha(0,\lambda)-\alpha_o\right)l}}{e^{\left(g(0,\lambda)-\alpha(I,\lambda)-\alpha_o\right)l}} \\ &= \left[g(I,\lambda) - \left(\alpha(I,\lambda) - \alpha(0,\lambda)\right)\right] l \end{aligned} \tag{5.5}$$

Certainly, there is no gain at zero bias, i.e., $g(0, \lambda) \equiv 0$, but there is current dependent absorption. From the photocurrent spectrum [Fig. 5.3 (a)] we infer that for $\lambda < 10\,\mu$m there is 1–3 absorption at zero bias. This absorption is “bleached”in the biased case. For $\lambda > 10\,\mu$m the 1–3 absorption at $I = 0$ can be neglected, i.e., $\alpha(I, \lambda) - \alpha(0, \lambda) = 0$. At these wavelengths the gain coefficient $g(I, \lambda)$ can be determined directly from the transmission change signal if we know the interaction length l. However, it is difficult to determine the interaction length l in our beam propagation geometry. To solve this problem we have to look at the beam propagation geometry in more detail.

On one hand, we have to pay attention to the beam propagation through the multiple layer system of the contacts and the bare active region, which leads to multiple reflections and—near the angle of total reflection—to an evanescent wave. The thorough treatment of this effect with the help of the transfer matrix formalism provides a tool for the calculation of the gain coefficient from transmission change data as we will see later.

On the other hand, there is only a partial overlap of the laser spot with the quantum cascade structure [see Fig. 5.2 (c)], i.e., only part of the mid-infrared beam interacts with the mesa whereas the other part is reflected by the surrounding gold layer. Since the mid-infrared beam has a high spatial coherence, interference within the infrared beam has to be taken into account in the calculation of the gain coefficient.

These two beam propagation effects are discussed in more detail in the following before we finally determine the gain coefficient from our data.

Multiple layer effect The quantum cascade structure represents a multiple layer system. The parameters of optical propagation, i.e., transmission, reflection, and absorption or gain, are complex functions of the properties of the individual layers and the interplay among them. In our quantum cascade structure, the *n*-type GaAs contact layers play a crucial role. The electron plasma with a doping of $n_{3D} = 2 \times 10^{18}\,\mathrm{cm}^{-3}$ and the plasma frequency $\omega_p = \sqrt{\frac{n_{3D}\, e^2}{\epsilon_\infty\, m_{eff}}}$ causes a decrease of the refractive index $[n_{n-GaAs}(\omega)]$ compared to the semi-insulating GaAs substrate ($n_{SI-GaAs}$) in the spectral range around $10\,\mu$m. This results in a frequency dependent angle of total reflection

$$\alpha_{tot}(\omega) = \arcsin\left(\frac{n_{n-GaAs}(\omega)}{n_{SI-GaAs}}\right)$$

which yields for $\lambda = 10.5\,\mu$m

$$\alpha_{tot}(\frac{2\,\pi\, c}{10.5\,\mu\mathrm{m}}) = 59^\circ$$

It is close to the angle of incidence α of the mid-infrared beam in our prism geometry. In addition, the total width of the quantum cascade structure sandwiched between the two *n*-type GaAs layers is $d = 2.1\,\mu$m which is very close to $\frac{\lambda_\perp}{4} = \frac{\lambda_{vac}}{4\,n\,\cos\alpha} = 1.83\,\mu$m of the standing mid-infrared wave developing in the quantum cascade structure parallel to the stack axis.

As depicted schematically in Fig. 5.14, multiple reflections between the substrate/*n*-type layer interface and *n*-type layer/gold contact interface lead to an enhanced interaction intensity of the light field with any absorber/emitter [137]. For a quantitative analysis of

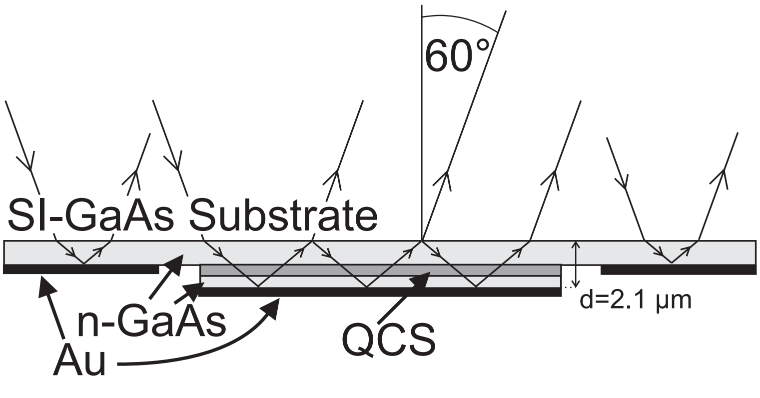

Figure 5.14: Close to the angle of total reflection ($\alpha_{tot} = 59^\circ$ for $\lambda_{MIR} = \lambda_{IS} = 10.5\,\mu$m) an evanescent wave and multiple reflections develop in the structure leading to a strong enhancement of the transmission change in the quantum cascade structure (QCS).

this effect, we apply the matrix transfer formalism (see, e.g., Ref. [129]). In this formalism the transmission and reflection at each interface between two layers is taken into account. In that way the field intensity in the structure and the transmission of the complete layer system can be calculated. To account correctly for the properties of intersubband transitions in quantum wells which are polarized parallel to the plane of incidence (P polarized), we include the anisotropic dielectric functions of the quantum cascade structure. We consider 4 different frequency dependent dielectric tensors $\epsilon_{ik}(\omega)$ describing the response of the different layer materials:

- The isotropic dielectric tensor for the semi-insulating GaAs substrate. Here, we take into account the GaAs reststrahl band at $\omega_{TO}^{GaAs} = 2\,\pi\,c/37\,\mu$m. With the dielectric constants $\epsilon_{st} = 12.9$ below ω_{TO}^{GaAs} and $\epsilon_\infty = 10.9$ above ω_{TO}^{GaAs} we get ($\gamma_1 = 10^{12}$ s^{-1})

$$(\epsilon_{SI-GaAs})_{ik} = \delta_{ik}\left(\epsilon_\infty + (\epsilon_{st} - \epsilon_\infty)\frac{(\omega_{TO}^{GaAs})^2}{(\omega_{TO}^{GaAs})^2 - \omega^2 + i\,\gamma_1\,\omega}\right) \quad , \quad i,k\,\epsilon\,\{x,y,z\}$$

- The isotropic dielectric tensor for the n-type GaAs contact layers ($n_1 = 2\times10^{18}$ cm^{-3}). In addition to the dielectric tensor above we have to consider the interaction with the electron plasma. With $\omega_p^{n_1} = \sqrt{\frac{n_1\,e^2}{\epsilon_0\,m_{eff}}}$ and $\gamma_2 = 2\times10^{13}$ s^{-1} (free carrier absorption [138]) we get

$$\Big(\epsilon_{n-GaAs}(\lambda)\Big)_{ik} = \delta_{ik}\left(\epsilon_\infty - \frac{(\omega_p^{n_1})^2}{\omega^2 - i\,\gamma_2\,\omega} + (\epsilon_{st} - \epsilon_\infty)\frac{(\omega_{TO}^{GaAs})^2}{(\omega_{TO}^{GaAs})^2 - \omega^2 + i\,\gamma_1\,\omega}\right)$$

- The isotropic dielectric tensor for the gold contact [139]

$$(\epsilon_{Au})_{ik} = \delta_{ik}\,(-2800 - 1300\,i)$$

- The anisotropic dielectric tensor of the quantum cascade structure. First, we consider the tensor components for the polarization perpendicular to the stack axis having no coupling to the intersubband dipole. The electrons can move freely in the plane of the layers, hence we have to take into account plasma oscillations with $\omega_p^{n_2} = \sqrt{\frac{n_2\,e^2}{\epsilon_0\,m_{eff}}}$, where $n_2 = 1\times10^{17}$ cm^{-3} is the average electron density. Further we average over the dielectric function of the AlGaAs barriers and the GaAs wells. With the AlGaAs reststrahl band at $\omega_{TO}^{AlGaAs} = 2\,\pi\,c/30\,\mu$m, the static dielectric constant of AlGaAs $\eta_{st} = 10.06$ below ω_{TO}^{AlGaAs} and the value above $\eta_\infty = 8.16$ we get

$$\begin{aligned}(\epsilon_{qcs})_{xx} = (\epsilon_{qcs})_{yy} \;&=\; 0.16\left(\eta_\infty + (\eta_{st} - \eta_\infty)\frac{(\omega_{TO}^{AlGaAs})^2}{(\omega_{TO}^{AlGaAs})^2 - \omega^2 + i\,\gamma_1\,\omega}\right)\\ &\quad +0.84\,(\epsilon_{SI-GaAs})_{xx} - \frac{(\omega_p^{n_2})^2}{\omega^2 - i\,\gamma_2\,\omega}\end{aligned}$$

  Secondly, we take the tensor component for the polarization parallel to the stack axis. Here, the intersubband dipole is taken into account having a Lorentzian shape centered at the $3-2$ intersubband transition $\omega_{IS} = 2\,\pi\,c/10.5\,\mu$m with the same width $\hbar\,\Gamma = 13$ meV as the corresponding electroluminescence spectrum [Fig. 5.3 (a)] and an oscillator strength related to the current dependent gain coefficient $g(I)$. The electrons can not move freely parallel to the stack axis, hence, plasma oscillations do not have to be taken into account. We get

$$\begin{aligned}(\epsilon_{qcs})_{zz} \;=\;& 0.16\Big(\eta_\infty + (\eta_{st}-\eta_\infty)\frac{(\omega_{TO}^{AlGaAs})^2}{(\omega_{TO}^{AlGaAs})^2-\omega^2+i\,\gamma_1\,\omega}\Big)\\ &+0.84\,(\epsilon_{SI-GaAs})_{xx} - \frac{g(I)\,c\,\Gamma\,\sqrt{\epsilon_\infty}}{\omega_{IS}^2-\omega^2+i\,\Gamma\,\omega} \qquad (5.6)\end{aligned}$$

In Fig. 5.15 (a) we show standing wave patterns of the mid-infrared intensity which were calculated for a collinear beam at a wavelength of $\lambda_{MIR} = 10.5\,\mu$m incident under different angles. The intensity in the active region (QCS) depends strongly on the angle of incidence. For an angle of incidence of 60°, i.e., the one chosen in our beam propagation geometry, a strong enhancement of the mid-infrared intensity is observed.

With the matrix transfer formalism and the exact anisotropic dielectric tensors we are now able to calculate the expected transmission change signal $\big(T(I,\lambda,\alpha)-T(0,\lambda,\alpha)\big)/T(0,\lambda,\alpha)$ for a given gain coefficient $g(I)$. A normalized transmission change signal calculated as a function of the angle of incidence and of the photon energy is shown in Fig. 5.15 (b). In the latter calculation the spectrum of the mid-infrared pulses used in the experiment was taken into account. As already mentioned above, we observe a pronounced correlation between the angle of incidence and the frequency of the mid-infrared beam. The main physical reason is the strong frequency dependence of the real part of the refractive index in the heavily doped layers. The strongest enhancement for all relevant frequencies is observed for an angle of incidence of around 60°. For our beam geometry this effect leads to a significant signal enhancement.

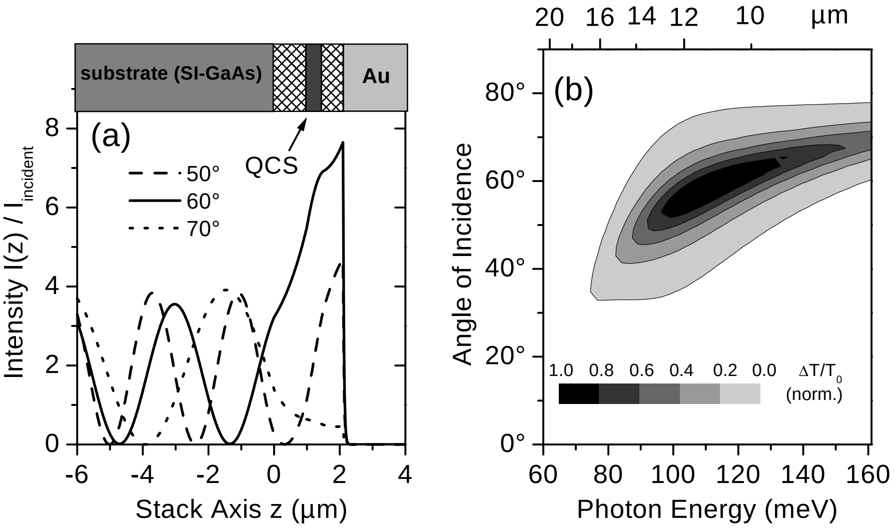

Figure 5.15: (a) Calculated standing wave between incident and reflected wave perpendicular to the stack axis of the multiple layer system for various angles of incidence at $\lambda = 10.5\,\mu$m. Between the substrate/n-type GaAs interface and the gold contact layer an evanescent wave and multiple reflections develop enhancing strongly the interaction with the quantum cascade structure. (b) Contour plot of calculated signal $\Delta T/T_0$ normalized to its peak value as a function of both the angle of incidence α and the photon energy $\hbar\,\omega$ of the mid-infrared light.

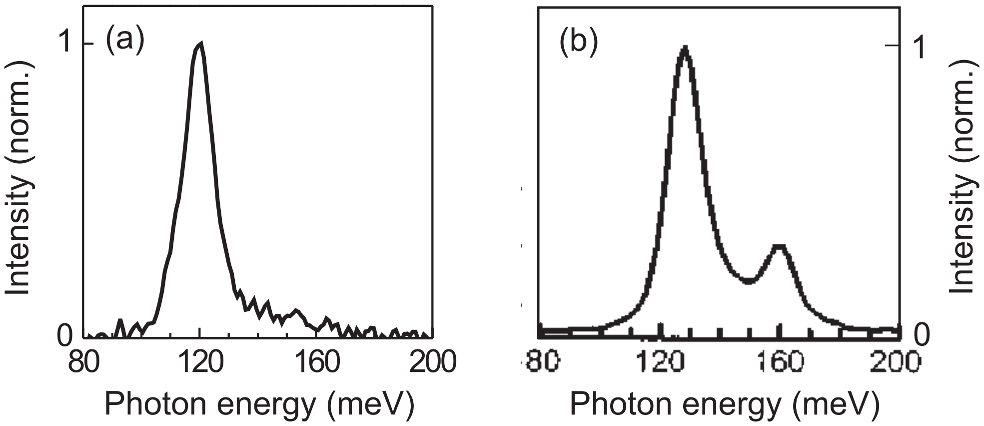

Figure 5.16: (a) Electroluminescence spectrum of sample A_1 measured at a current density of 1.8 kA/cm^2 at 77 K. A wave propagation geometry with an angle of incidence of 45° is used [134]. (b) Electroluminescence of a laser device with a layer structure similar to sample A_1 (barrier thickness 5.8 nm) for a current density of ≈ 1.7 kA/cm^2 at 77 K. The device is 24 μm wide and 2.5 mm long [99].

Strong evidence for the relevance of this effect is given by the electroluminescence data measured for different beam propagation geometries as shown in Fig. 5.16. In Fig. 5.16 (a) the electroluminescence spectrum of the mesa sample is shown. It is measured using a similar wave propagation geometry as discussed above with an angle of incidence of 45°. The electroluminescence measured for a laser with similar layer structure but processed into a ridge waveguide is depicted in Fig. 5.16 (b). Here, a wave propagation geometry parallel to the lasers is used. In both spectra the main peak is centered around a photon energy of around 120 meV. It corresponds to the 3–2 transition. The electroluminescence in Fig. 5.16 (b) shows a pronounced second peak at a photon energy of 160 meV corresponding to the 3–1 transition. This peak is strongly suppressed in the data measured for the mesa shaped structure [Fig. 5.16 (a)]. This behavior can be explained by the multiple layer effect. From Fig. 5.15 (b) we can see that for an angle of incidence of 45° the signals at photon energies larger than 120 meV are strongly suppressed. Apart from the minor difference in the exact layer structure, this might also explain the red-shift of the main peak in the electroluminescence spectrum observed for the 45° beam propagation geometry [Fig. 5.16 (a)].

Diffraction effect In Fig. 5.17 the diffraction of the mid-infrared beam and the corresponding diffraction pattern in the plane of the detector is shown. Fig. 5.17 (a) illustrates the spatial mid-infrared intensity in the plane of the mesa. The shape of the diffraction pattern depends on the phase shift ϕ between light reflected by the mesa and light reflected by the surrounding gold layer. This phase shift is a function of the angle of incidence and of the wavelength. With the methods discussed above we simulate the beam propagation in the multiple layer systems of the mesa and of the surrounding area. For an angle of incidence of 60° and a wavelength of $\lambda_{IS} = 10.5\,\mu$m the phase shift is close to 180° so that there is a minimum in the center of the diffraction pattern [Fig. 5.17 (b)]. The spatial transmission

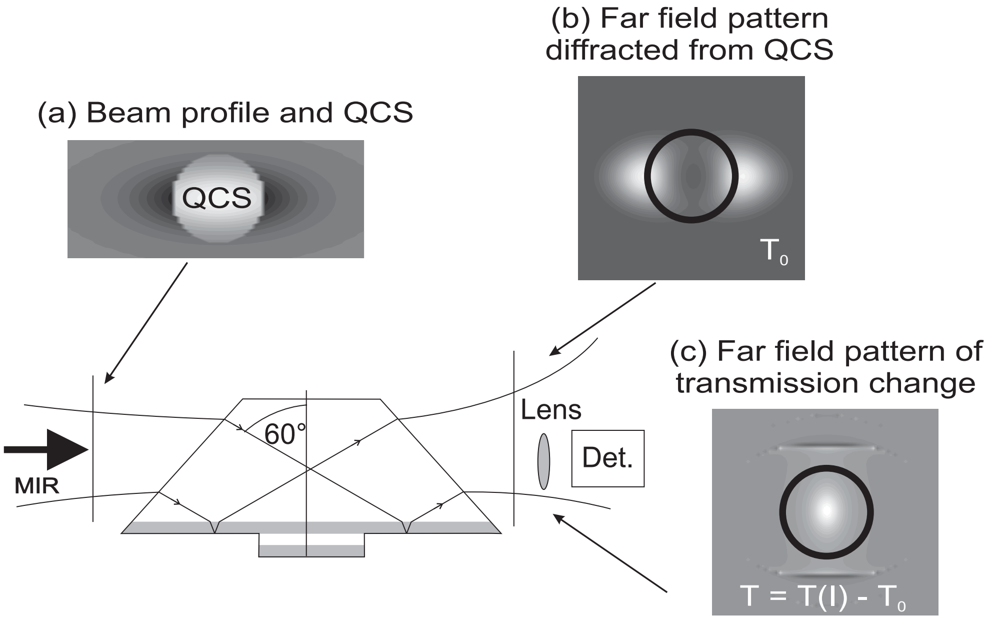

Figure 5.17: Diffraction of the mid-infrared beam at the mesa and corresponding diffraction pattern. (a) Spatial mid-infrared intensity in the plane of the layers. The mesa (QCS) is indicated by the enlightened circle. (b) Diffraction pattern of the mid-infrared beam in the plane of the detector. (c) Spatial transmission change signal in the plane of the detector. The area of the detector is indicated in (b) and (c) by the black ring.

change signal in the plane of the detector is shown in Fig. 5.17 (c). Since the detector can only collect a fraction of the entire diffraction pattern, the apparent transmission of the sample at the position of the mesa is strongly reduced [see Fig. 5.18 (a)]. Such a transmission decrease is observed experimentally as can be seen in Fig. 5.13 (a) (squares).

For the exact determination of this effect, the phase ϕ and the fraction $a = \sqrt{I_{surr}/I_{mesa}}$, which is the square root of the sum of photons re-emitted from the mesa surrounding divided by the sum of photons re-emitted from the mesa, are important. Further, the collection efficiency, i.e., the fraction of the diffraction pattern measured by the detector is crucial. To elucidate this we consider two extreme cases.

First, we assume that the collection efficiency is very low, i.e., only the center of the diffraction pattern is measured. Then, the measured transmission change signal as a function of ϕ and a reads

$$\frac{\Delta T}{T_0}(\phi, a) = \frac{|t_m + a\, e^{i\,\phi}|^2}{|1 + a\, e^{i\,\phi}|^2} - 1 \tag{5.7}$$

where t_m is the transmission coefficient of the active region [$t_m = \sqrt{S_{out}/S_{in}} = \sqrt{\exp(g\,l)}$]. For a phase shift of $\phi = 170°$, which is a realistic value in our experiment, the signal is plotted as solid line in Fig. 5.18 (b). We can see that a signal enhancement of a factor of more than 3 occurs for $a = 0.8$ and that positive and even negative signals can be observed depending sensitively on a. Hence, the advantage of an enhanced signal has to be paid for with the uncertainty of the exact enhancement factor.

Now, we consider the extreme case of 100 % collection efficiency. Here, the signal is not

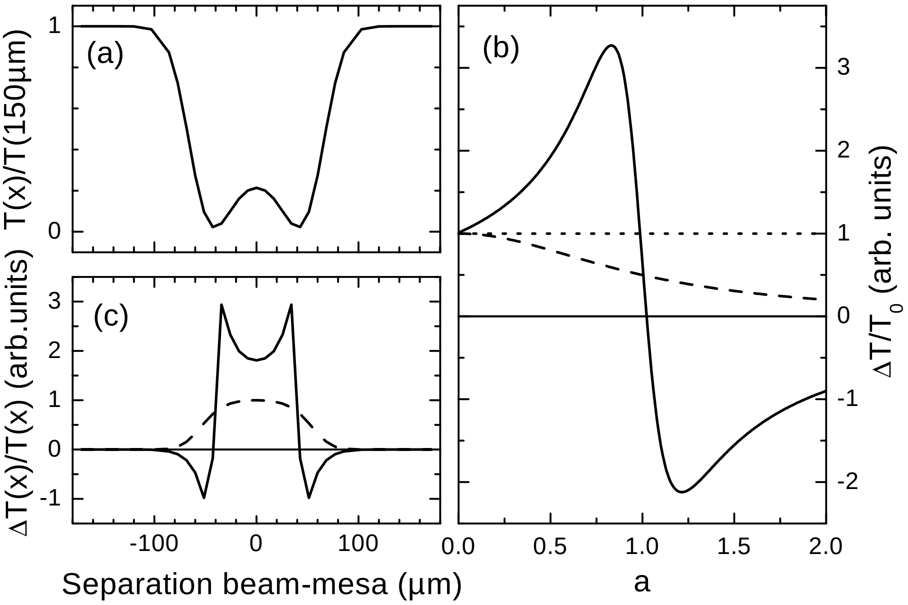

Figure 5.18: (a) Calculated transmission of the sample measured by a detector with a realistic size as a function of the separation between the center of the beam focus and the mesa. (b) Transmission change signal for the extreme case of a very low detector collection efficiency (solid line) and of a 100 % collection efficiency (dashed line) as a function of $a = \sqrt{I_{surr}/I_{mesa}}$, i.e., the square root of the sum of photons re-emitted from the mesa surrounding divided by the sum of photons re-emitted from the mesa. A phase shift of 170° between the light reflected by the mesa and the light reflected by the surrounding gold layer is assumed. The dotted curve indicates the transmission change signal of the active region for an infinitely large mesa. (c) Calculated transmission change signal for a realistic detector size (solid line). The dashed curve indicates the normalized transmission change signal measured by collecting the total diffraction pattern.

ϕ dependent. It reads as a function of a

$$\frac{\Delta T}{T_0}(a) = \frac{|t_m|^2 + a^2}{1 + a^2} - 1 = \frac{t_m^2 - 1}{1 + a^2}$$

This signal is plotted as the dashed line in Fig. 5.18 (b). It is monotonically decreasing with increasing a.

In both cases, if all the light is transmitted exclusively through the mesa ($a = 0$), then the “true”transmission change is measured. This suggests that for the measurement of the transmission change a bigger mesa diameter should be used. To get rid of the diffraction effect, the mesa has to have a diameter at least twice as large as the focus diameter. However, a larger mesa means a higher current and, thus, an increased heating. As a result, we are forced to compromise between the heating of the sample and the diffraction effect.

To minimize the diffraction effect, in the next chapter we will use quantum cascade samples with a bigger mesa size. One sample which will be investigated has a mesa diameter of 350 μm. In the setup used there the mid-infrared focus projected on the plane of the layers has the dimensions 130 μm × 340 μm [Fig. 6.2 (a)]. Due to the considerably bigger focus compared to the one obtained in the setup used in this chapter, the mid-infrared light is much less diffracted so that the collection efficiency of the detector is much bigger. For the second sample we will further optimize the mesa size by taking an elliptically shaped mesa with the dimensions 400 μm × 200 μm [Fig. 6.2 (b)].

To illustrate the relevance of the diffraction effect, in Fig. 5.19 we show the transmission for the latter two structures as a function of lateral position. For the circular sample, where the distance of the edges between two subsequent mesas is 150 μm [cf. inset of Fig. 5.19 (a)], a higher transmission was measured in the center of the mesa than in between two neighboring mesas [Fig. 5.19 (a)] in contrast to the transmission measurement carried out in this chapter on the identical quantum cascade structure. The reason for this is that the distance between two subsequent mesas is much smaller than the mesa diameter so that here the diffraction effect becomes relevant at the position between the mesas. The inverse situation is observed for elliptically shaped mesas with a lateral diameter of 200 μm [Fig. 5.19 (b)], where the distance of the edges between two subsequent mesas is 200 μm [cf. inset of Fig. 5.19 (b)].

For the evaluation of the transmission change signal $\Delta T/T_0$ with respect to the gain coefficient, it is important to take this diffraction effect into account. In Fig. 5.18 (c) calculated transmission change signals are shown for different detector sizes as a function of the spatial separation between the beam and the mesa. The dashed curve is the transmission change curve for a detector which is capable to collect the complete diffraction pattern. It represents a signal without diffraction effects. For a realistic detector size as indicated in Fig. 5.17 we get the solid curve. These calculations show that we can expect a signal enhancement of a factor of two to three. A more accurate value, however, can not be given as it depends sensitively on the fraction of the diffraction pattern collected by the detector and on the exact values for a and ϕ in Eq. 5.7, which can be estimated only roughly.

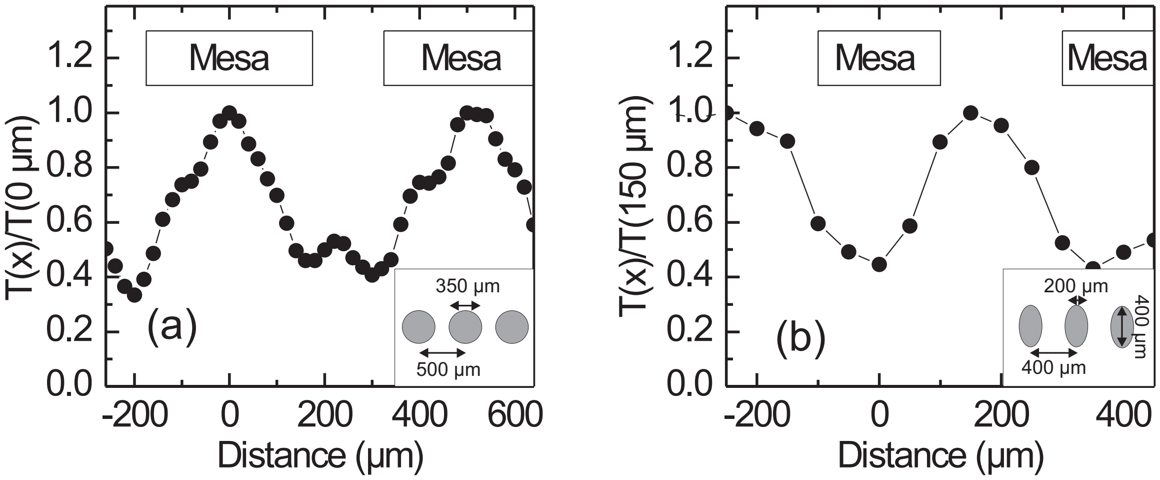

Figure 5.19: Lateral profiles of the sample transmission as a function of separation between the laser spot and the quantum cascade mesa for circular mesas (a) and elliptically shaped mesas (b). The mesa geometry is shown in the insets.

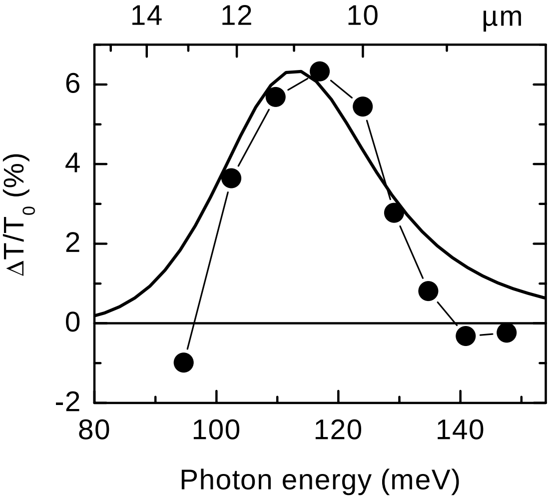

Figure 5.20: Transmission change spectrum calculated with the transfer matrix method with a gain coefficient of $\bar{g} = 225$ cm^{-1} (solid line) compared with the experimental data for a current density of 4.5 kA/cm^2 [cf. Fig. 5.13 (c)].

The gain coefficient In the beam propagation geometry chosen for this experiment it is difficult to define a proper interaction length to derive the gain coefficient $g(I)$ from the transmission change data [cf Eq. (5.5)]. To circumvent this problem we use the transfer matrix method with frequency dependent dielectric tensors. With this method we can calculate the expected transmission change signal. For a given angle of incidence and incident pulse spectrum the only free parameter in this calculation is the gain coefficient $g(I)$ [cf. Eq. (5.6)]. The gain coefficient $\bar{g} = 225$ cm^{-1} yields the best fit for the observed $\Delta T/T_0 = 0.06$ for an injection current of 4.5 kA/cm^2 (Fig. 5.20). In that way the correct beam propagation geometry in the multiple layer system is taken into account. In addition, a signal enhancement of a factor of 3 due to the diffraction effect is assumed. This yields finally a gain coefficient of $g = \bar{g}/3 = 75$ cm^{-1} for the bare active region corresponding to a gain coefficient per current density of $g^* = g(I)/I = 15 \pm 10$ cm/kA.

Comparison with other gain measurements We want to compare our technique and the results with other gain measurements in literature. Essentially three techniques were used to measure the gain coefficient on electrically driven quantum cascade laser structures.

The first technique was applied by Sirtori et al. [116] to GaAs/AlGaAs quantum cascade lasers with a bare active region similar to the one used in our experiment. It is based on a plot of the threshold current density versus reciprocal cavity length ($1/L$). At threshold, the gain overcomes the resonator losses, i.e., the mirror losses α_M ($R = e^{\alpha_M L}$, R: facet reflectivity, α_W: waveguide losses). Hence, the threshold condition reads $g^* I_{th} \Gamma = \alpha_M + \alpha_W$ where Γ is the overlap factor, i.e., the part of the laser mode overlapping with the bare active region. In Fig. 5.21 (a) data for the threshold current density as a function of the reciprocal cavity length $1/L$ is shown. From the slope $I'_{th}(1/L)$ of the fit curve below gain saturation one obtains the gain coefficient $g^* = \ln(R)/[I'_{th}\,\Gamma]$. With a calculated facet reflectivity R and mode overlap factor Γ the authors derive a gain coefficient $g^* = 16$ cm/kA.

The second technique is the so-called Hakki-Paoli technique [118]. It was applied to a

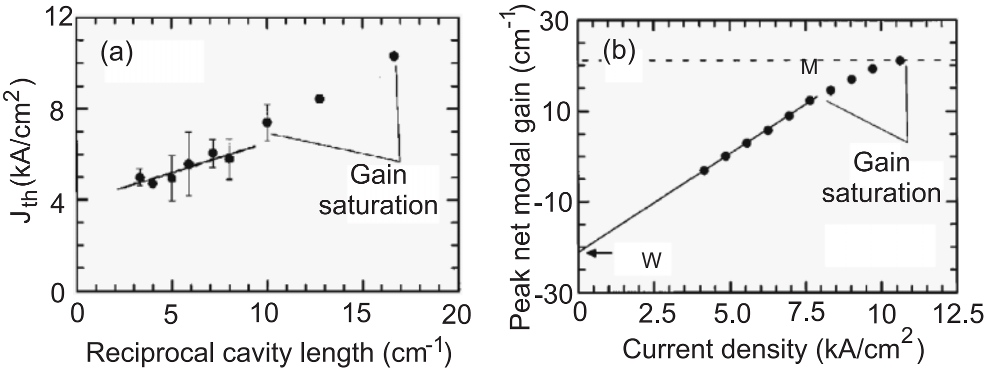

Figure 5.21: (a) Measured threshold current density I_{th} versus reciprocal cavity length at 77 K. The solid line is a fit to the data below saturation. From its slope and intercept the modal gain and the waveguide loss are determined [116]. (b) Net peak modal gain $G_M(\lambda_{peak}) - \alpha_W$ as deduced from the subthreshold emission spectra is plotted as a function of the current density I at 10 K. The slope and intersection of the fit, prior to saturation, give G_M and α_W [116].

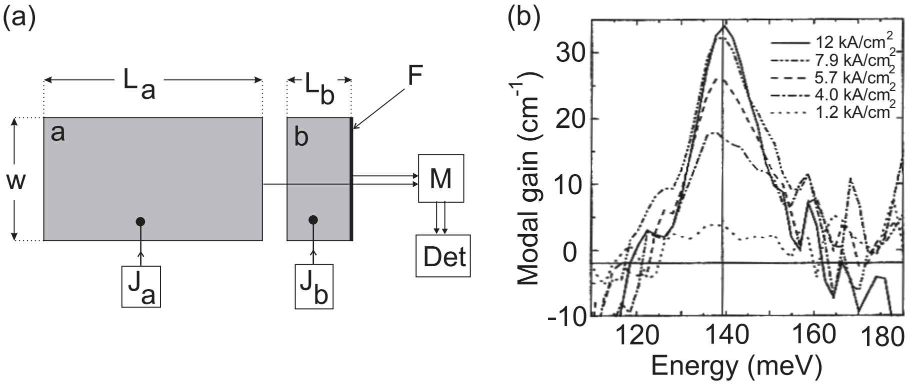

Figure 5.22: (a) Setup of the two-section cavity technique with two identical waveguide ridges a and b. The output light is spectrally resolved with a monochromator (M) and detected with a suitable detector (Det). (b) Modal gain versus photon energy at 4 K measured with the two-section cavity technique. I_a is kept fixed at 550 A/cm^2 [117].

quantum cascade laser with bare active region similar to ours by Sirtori et al. [116]. Here, the modal gain $[G_M(\lambda) = g(\lambda)\, I\, \Gamma]$ is extracted from the fringe contrast of the Fabry-Perot modes of the cavity below threshold using a Fourier analysis of the subthreshold spectra. In Fig. 5.21(b) the peak net modal gain $[= G_M(\lambda) - \alpha_W]$ is plotted as a function of the current density. Below gain saturation a linear dependence is observed. From the slope of the curve the gain coefficient is extracted. In that way, again using a calculated Γ, a gain coefficient $g^* = 14$ cm/kA was derived.

The third technique is the so-called two-section cavity technique. It was applied to a quantum cascade laser with a layer structure similar to ours by Barbieri et al. [117]. Two identical waveguide ridges with lengths L_a and L_b as depicted in Fig. 5.22 (a) are used. Each of them is considered as an independent light source of intensity $S_a(I_a, \lambda)$ and $S_b(I_b, \lambda)$ by applying currents I_a and I_b at the respective ridges. The output light $S_{tot}(I_a, I_b, \lambda)$ from the facet F is detected. By keeping I_a fixed and varying I_b the modal gain G_M can be determined. The result of this measurement is shown in Fig. 5.22 (b). A gain of $g^* = 13$ cm/kA was derived.

The latter three techniques measure the gain coefficient in a beam propagation geometry parallel to the layers. This entails the problem of the determination of the mirror losses α_M and the determination of the mode overlap with the laser-active region Γ. We want to mention that these two quantities are only known with large uncertainty.

In conclusion, the gain coefficient obtained with our technique is in good agreement with the values derived by those measurements. It is important to note that the exact determination of the gain coefficient with the measurement technique developed in this chapter is difficult. On one hand, the signal enhancement due to the multiple layer effect strongly depends on the exact doping concentration of the contact layers, which itself is not known exactly. On the other hand, the diffraction effect induces further uncertainties. Nevertheless, the important result is that the measured transmission change of an electrically driven quantum cascade structure can unambiguously be contributed to 3–2 population inversion, i.e., to gain. With this experiment, we have successfully combined the techniques of ultrafast spectroscopy with electrically pumping of quantum cascade structures. This new technique provides the means for a time-resolved electron transport measurement which will be presented in the next chapter.

Chapter 6

Ultrafast coherent electron transport in quantum cascade structures

Electron transport plays an important role for the performance of semiconductor devices under bias. In unipolar two-dimensional semiconductor nanostructures a central question is whether and to what extent the electron transport perpendicular to the layers is coherent. The aim of the experiment presented in this chapter is to study the mechanisms governing vertical charge transport in quantum cascade structures.

The quantum cascade laser structure is an important prototype system for studying carrier transport, in particular tunneling and wave packet propagation, at elevated carrier densities. The lasing transition is an ideal localized optical marker providing the means for the investigation of such phenomena. With the experimental technique developed in the previous chapter we are now able to carry out the first time-resolved pump-probe study of an electrically driven quantum cascade structure.

For the electron transport studies we apply pseudo two-color pump-probe spectroscopy (cf. section 2.1.2). In contrast to the linear spectroscopy carried out in the previous chapter, for this nonlinear experiment we need mid-infrared pulse energies far above the pulse energies provided by the 2 MHz laser system. Thus, here we have used the high-intensity, 1 kHz mid-infrared laser system introduced in section 2.2.2.

First, we present the basic principle of the experiment. We explain how the time-resolved detection of the electrically induced transmission change is used to determine the physics of electron transport. After this, we introduce the samples used in the experiments. In order to reduce the diffraction effect, which occurs because of the partial overlap of the optical focus with the quantum cascade mesa, we use much bigger mesas than in the experiment discussed in the previous chapter. However, this entails the problem of an increased heating of the sample. We address this problem before we explain the entire experimental setup. Subsequently, we present the experimental results. Finally, we analyze the data in order to determine the underlying physics of electron transport in quantum cascade structures.

6.1 Principle of measurement

The goal of the experiment is to determine the characteristics of electron transport from the injector through the injection barrier into the active region of a quantum cascade structure. In an ideal Gedanken experiment one would prepare an electron wavepacket localized in the

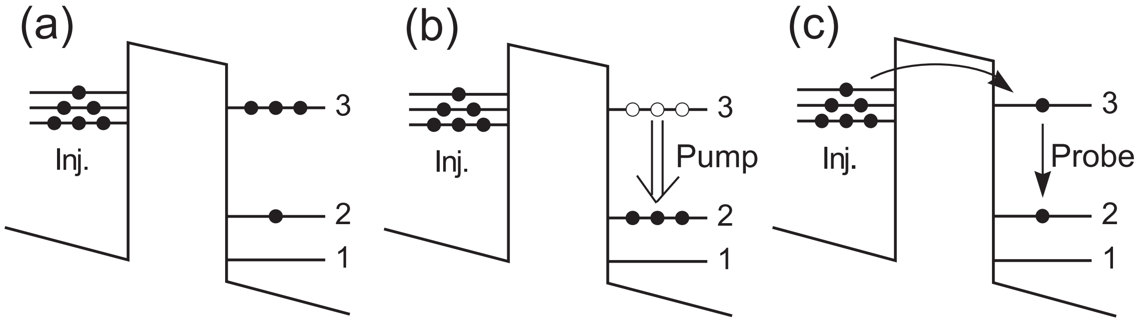

Figure 6.1: Experimental concept for the electron transport measurement. (a) Under forward bias the electronic system is in a quasistationary nonequilibrium state. (b) A strong pump pulse depletes the electrically induced optical gain and (c) a weak probe pulse monitors the subsequent gain recovery.

injector of an electrically driven quantum cascade structure and monitor subsequently the motion of this wavepacket. Of course, today there is no experimental technique to carry out such an experiment. The experiment discussed in the following, however, gets quite close to this ideal Gedanken experiment.

A quantity we have access to is the transmission change $\Delta T/T_0$ as shown in the previous chapter. This quantity is directly connected to the gain. The experimental concept is depicted in Fig. 6.1. Under appropriate forward bias the electron gas in the quantum cascade structure is in a quasistationary nonequilibrium state [Fig. 6.1 (a)]. A strong pump pulse depletes the electrically induced optical gain [Fig. 6.1 (b)] via stimulated emission promoting carriers from subband 3 into subband 2. A weak probe pulse monitors the subsequent gain recovery [Fig. 6.1 (c)] as a function of pump–probe delay t_D. The gain is proportional to the population difference between subbands 3 and 2 and gives direct information on the transport of electrons into subband 3 and out of subband 2.

Table 6.1: Structural parameters of the GaAs/Al$_x$Ga$_{1-x}$As samples A$_2$, B, and C.

	A$_2$	B	C
nominal Al-fraction (%)	33	45	45
inj. barrier width (nm)	6.2	4.0	4.6
exit barrier width	3.4	2.8	2.8
number of periods	10	10	10
sheet density per period (cm^{-2})	4×10^{11}	4×10^{11}	4×10^{11}
conduction band offset ΔE_c (meV) [99, 105]	295	390	390
τ_3 (ps) [99, 105]	1.5	1.4	1.4
τ_2 (ps) [99, 105]	0.3	0.3	0.3
mesa shape	round	elliptical	elliptical
mesa dimensions	Ø350 μm	200 μm×400 μm	200 μm×400 μm

6.2 Sample properties

We carry out transport studies on three different samples. The structural parameters of all samples are summarized in Table 6.1.

One sample, which will be called sample A_2 in the following, has the identical layer structure as sample A_1 (see Table 5.1). The only difference is the size of the mesa. In order to reduce the diffraction effects discussed in the previous chapter we use a circular mesa with a radius of $R_m = 175\,\mu\text{m}$ which is now larger than the laser beam focus (FWHM) in the mesa plane [see Fig. 6.2 (a)].

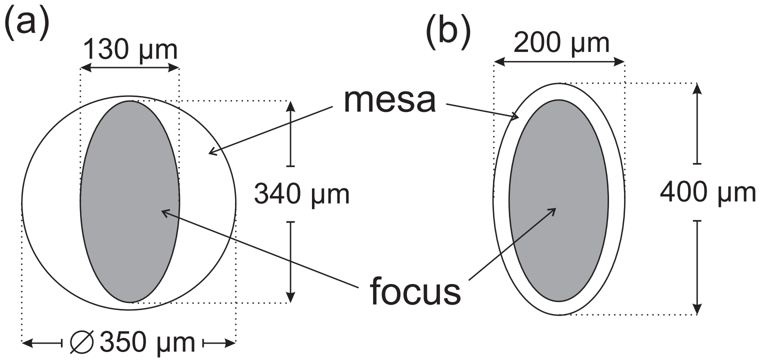

Figure 6.2: Mesa and beam shapes for sample A_2 (a) and samples B and C (b). The grey area indicates the mid-infrared beam focus in the plane of the mesas.

Samples B and C were grown at the TU Wien. The layer structures of these samples are similar to that of the GaAs/$Al_xGa_{1-x}As$ quantum cascade laser presented in Ref. [105]. It is the first GaAs-based quantum cascade laser working at room temperature. The aluminum content of this structure is $x = 45$ %. The conduction band offset $\Delta E_c \approx 390$ meV for Γ-valley electrons at this aluminum content is 95 meV higher compared to the offset at 33

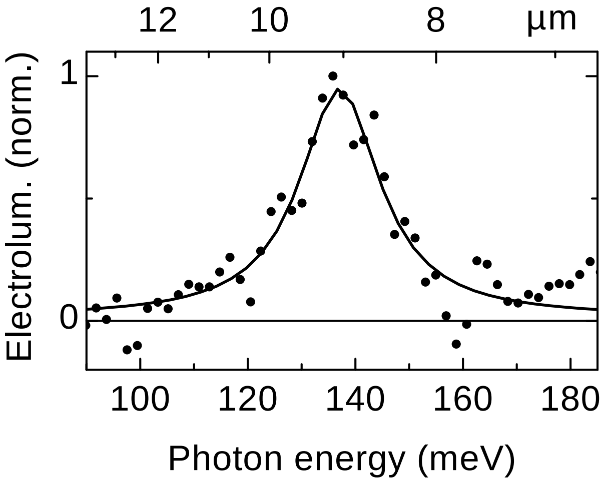

Figure 6.3: Electroluminescence spectrum of sample B measured at $T_{CF} = 77$ K obtained under a forward current of $I = 7.0\ \text{kA/cm}^2$ [140].

Table 6.2: Layer structure of samples B and C.

material	doping (Si)	thickness (nm)	
GaAs	2×10^{18} cm^{-3}	100	top contact
GaAs		4.8	injector
AlGaAs		2.8	
GaAs		3.4	
AlGaAs		1.7	
GaAs		3.0	
AlGaAs	2.75×10^{17} cm^{-3}	1.8	
GaAs	5×10^{17} cm^{-3}	2.8	
AlGaAs	2.75×10^{17} cm^{-3}	2.0	
GaAs	5×10^{17} cm^{-3}	3.0	
AlGaAs		2.6	
10 repetitions			
GaAs		3.0	active region
AlGaAs		4.0 (4.6) [sample B (C)]	
GaAs		1.9	
AlGaAs		1.1	
GaAs		5.4	
AlGaAs		1.1	
GaAs		4.8	
AlGaAs		2.8	injector
GaAs		3.4	
AlGaAs		1.7	
GaAs		3.0	
AlGaAs	2.75×10^{17} cm^{-3}	1.8	
GaAs	5×10^{17} cm^{-3}	2.8	
AlGaAs	2.75×10^{17} cm^{-3}	2.0	
GaAs	5×10^{17} cm^{-3}	3.0	
AlGaAs		2.6	
GaAs	2×10^{18} cm^{-3}	1000	bottom contact
SI GaAs substrate (500 μm)			

% aluminum content[105]. The active region consists of three GaAs quantum wells. The injector contains five GaAs quantum wells. Hence, the layer sequence is the same as for sample A_1 [Fig. 5.1]. The calculated lifetimes of subband 3 and subband 2 are $\tau_3 = 1.4$ ps and $\tau_2 = 0.3$ ps [105]. The peak output power of a laser device (ridge waveguide, 2 mm × 30 μm) with 36 periods is 1.3 W and the threshold current density is 4 kA/cm^2 at 77 K. The laser works up to a temperature of 308 K [105]. The only difference in the active layer structure between the laser and the samples investigated in this thesis is the number of periods which is 10 in our case and the injection barrier thickness which is $d_b = 4.0$ nm for sample B and $d_b = 4.6$ nm (identical to the laser) for sample C. The complete layer structure is shown in Table 6.2. For the mesas we have chosen an elliptical shape (400 μm × 200 μm) as shown in Fig. 6.2 (b). This gives an ideal overlap of the beam focus with the mesa.

The electro-luminescence spectrum for sample B measured at a cold finger temperature of $T_{CF} = 77$ K with a current of $I = 7$ kA/cm^2 is shown in Fig. 6.3. It is centered around $\lambda = 9.0\,\mu$m and has a width (FWHM) of 17 meV. The substrate thickness is 500 μm. According to the considerations of section 4.2 this results in a length of $a = 1320\,\mu$m for the base plane of the prism.

6.3 Synchronized electrical pulses

The drawback of a bigger mesa is an increased heating of the quantum cascade structure under bias. We have seen in section 5.2 that applying long current pulses the lattice temperature of the mesa in quasistationary equilibrium depends linearly on the mesa diameter for a given current density. Even for the small mesa used in the previous experiment the lattice temperature was considerably enhanced compared to the cold finger temperature. It is clear, that with the bigger mesa, now, we can not apply long current pulses any longer.

Instead, we shall apply very short current pulses. In Fig. 6.4 (a) the calculated transient lattice temperature T_L for the first 100 ns (sample A$_2$) is shown taking into account the full temperature dependence of c_p [cf. Fig. 5.4 (b)] and neglecting thermal conductivity into the substrate (current density: $I = 7.0$ kA/cm^2, cold finger temperature: $T_{CF} = 4$ K). This temperature represents the maximum lattice temperature. The true lattice temperature can be somewhat smaller due to thermal conductivity. Since the heat capacity of GaAs below 30 K is extremely small the sample heats up to $T_L = 30$ K within a few nanoseconds. We decided to carry out the optical experiment at 30 ns. In Fig. 6.4 (b) we plot the lattice temperature after 30 ns as a function of the cold finger temperature for a current density of $I = 2.1$ kA/cm^2 (dotted line), $I = 4.6$ kA/cm^2 (dashed line), and $I = 7.0$ kA/cm^2 (solid line). Above $T_{CF} = 100$ K the lattice temperature is nearly equivalent to the cold finger temperature and independent of the current density.

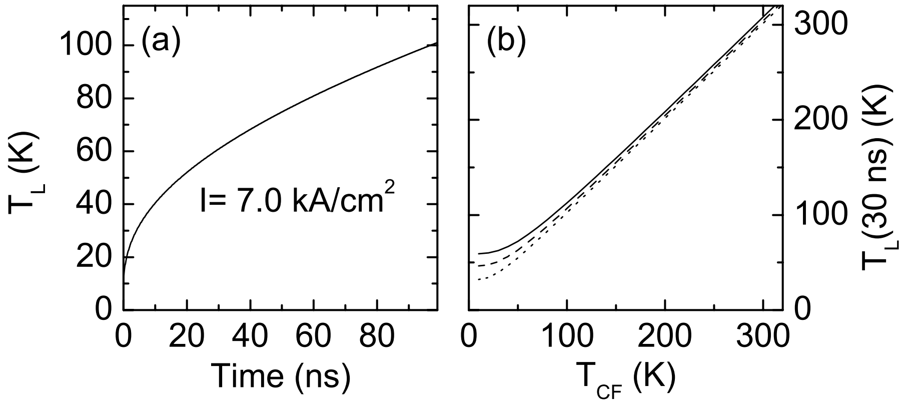

Figure 6.4: (a) Lattice temperature T_L of sample A$_2$ as a function of time of the applied current pulse with a current density of $I = 7.0$ kA/cm^2 ($T_{CF} = 4$ K). (b) Lattice temperature after 30 ns as a function of the cold finger temperature T_{CF} for current densities $I = 2.1$ kA/cm^2 (dotted line), $I = 4.6$ kA/cm^2 (dashed line), and $I = 7.0$ kA/cm^2 (solid line).

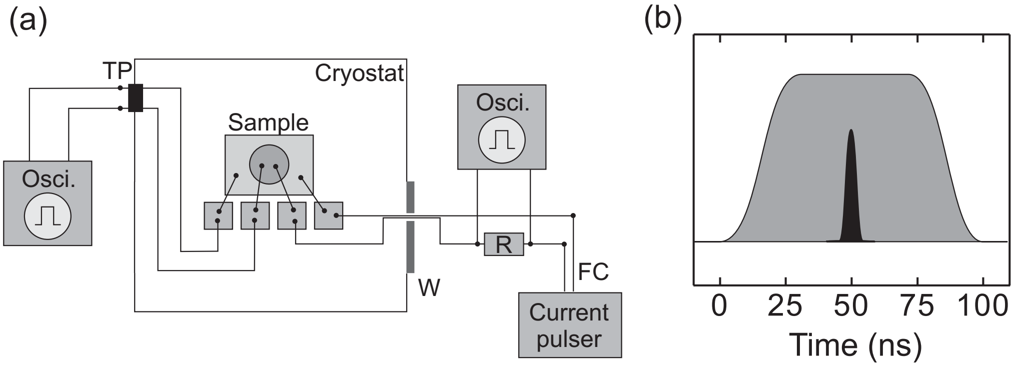

Figure 6.5: (a) Electrical wiring. For the voltage measurement we use coaxial cables with 50 Ω impedance which are led through the electrical throughput TP. The current cables are led through the window (W) of the cryostat to obtain a better impedance matching (FC: 1 Ω impedance flat-band cable). The $R = 1\,\Omega$ resistance is used to measure the current. (b) The electrical pulse (grey area) is ≈ 60 ns long with a rise time of 20 ns. The optical experiment sketched by the black area is carried out in the center of the current pulse.

In the experiment we use a high-current pulser (AVTECH AVOZ-A3-C-OP2) which is able to generate current pulses of up to 100 A with a pulse length ranging from 10 ns to 3 μs and a repetition rate of up to 20 kHz. The current cable is a 1 Ω impedance flat-band cable. For current pulses with a pulse length of less than 100 ns we need a very good impedance matching. For this we led the current cable from the sample holder directly through the cryostat window to the flat-band cable as shown in Fig. 6.5 (a). With this method we are able to get current pulses with a rise time of around 20 ns. The optical experiment is then carried in the center of the current pulse [Fig. 6.5 (b)].

6.4 Experimental setup

In the time-resolved pump-probe experiments we use the laser system presented in section 2.2.2 providing high-intensity mid-infrared pulses at 1 kHz repetition rate. At this low repetition rate we are able to synchronize the optical pulses with the current pulses as shown in Fig. 6.6. A delay generator generates rectangularly shaped pulse pairs at a repetition rate of 500 Hz. The first pulse of this electrical pulse pair is used to trigger the current pulser, which subsequently generates short high-current pulses. In this way, only every second optical experiment is carried out under bias. The second pulse of the trigger pulse pair is recorded by the gated integrator of our data acquisition system. In that way we obtain the information whether the optical experiment is carried out under bias or not. Finally, a computer calculates the normalized transmission change $[S(I)-S(0)]/S(0) = \Delta T/T_0$, where $S(I)$ is the measured signal with applied current I.

The low repetition rate in combination with the short current pulses leads to a very low average heat dissipation even for the bigger mesa size and the highest applied current densities. For a current density of 7.3 kA/cm^2, an electrical pulse length of 60 ns and a mesa with 175 μm radius the average dissipated power is only 1.5 mW.

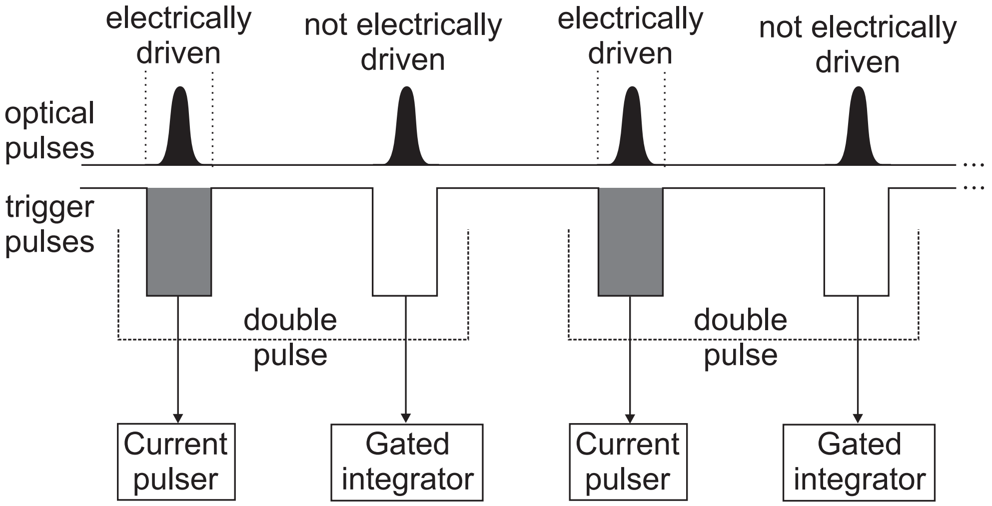

Figure 6.6: Time scheme for the electrical driving of the quantum cascade sample. The electrical pulses are 60 ns long. They are applied for every second optical experiment.

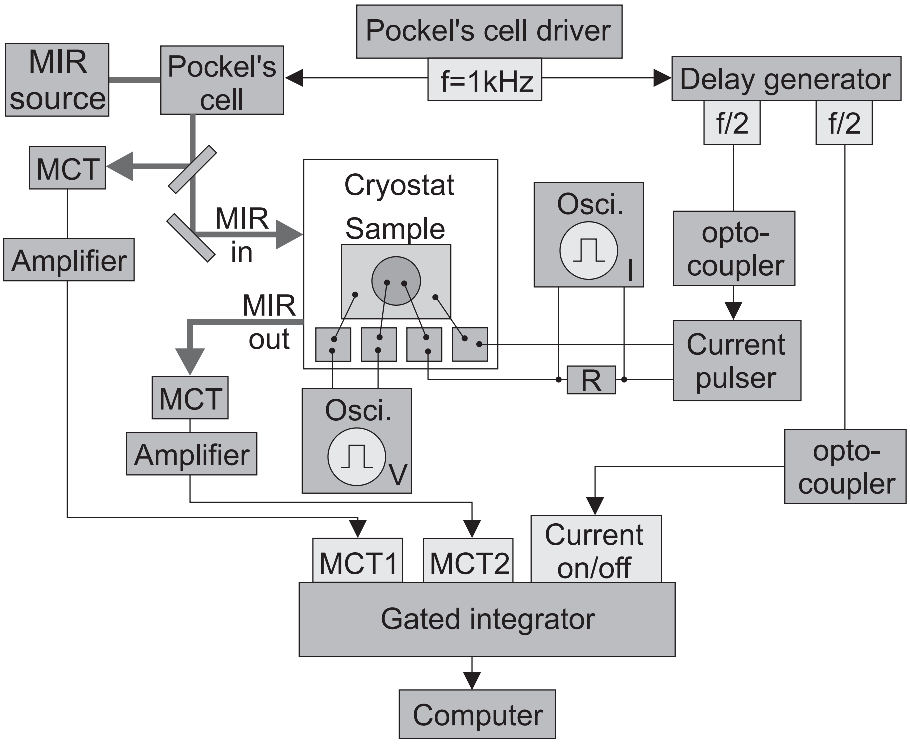

Figure 6.7: Electronic setup for the pump-probe experiment using a gated integrator. (MCT: HgCdTe detector, R: 1 Ω resistance)

Electronic setup The electronic setup supplying synchronized electrical pulses is illustrated in Fig. 6.7. The Pockel's cell driver (MEDOX E.-O.) of the Ti:sapphire regenerative amplifier delivers the trigger pulses synchronized with the optical pulses. The trigger signal is approximately 2 μs advanced with respect to the optical pulses. It triggers a delay generator (SRS DG535) which is used to adjust the overlap between the current and the optical pulses and to generate the pair of trigger pulses. The current pulser (AVTECH AVOZ-A3-C-OP2) delivers 60 ns long current pulses of variable peak current. We use a 1 Ω series resistance to measure the current.

The mid-infrared pulses are detected by liquid-nitrogen-cooled HgCdTe detectors (MCT). The resulting electric signal is amplified by a current amplifier (FEMTO, HVA-S) and sent into the gated integrator (signal input MCT1 and MCT2). MCT1 measures the mid-infrared reference pulses and MCT2 the mid-infrared probe pulses after interaction with the quantum cascade sample. Finally, a computer calculates the normalized transmission change signal from two subsequent experiments according to the timing sequence shown in Fig. 6.6:

$$\Delta T/T_0 = \left(\frac{\mathrm{MCT2}}{\mathrm{MCT1}}(\text{Current on}) - \frac{\mathrm{MCT2}}{\mathrm{MCT1}}(\text{Current off})\right) \Big/ \frac{\mathrm{MCT2}}{\mathrm{MCT1}}(\text{Current off})$$

Shielding Because of the very short and intense current pulses (up to 7 A) and a non-ideal impedance matching of the current cables, we have to face electromagnetic radiation emitted from these cables. This leads to high electrical pick-up effects in the measurement cables superimposed on the optical signal. To minimize this effect we shield the detectors with thick copper plates and use double shielded co-axial cables. Further, using opto-couplers we decouple the electronics of the gated integrator from that of the current pulser and from that of the delay generator (cf Fig. 6.7). In this way, we could sufficiently suppress the electric pick-up effects.

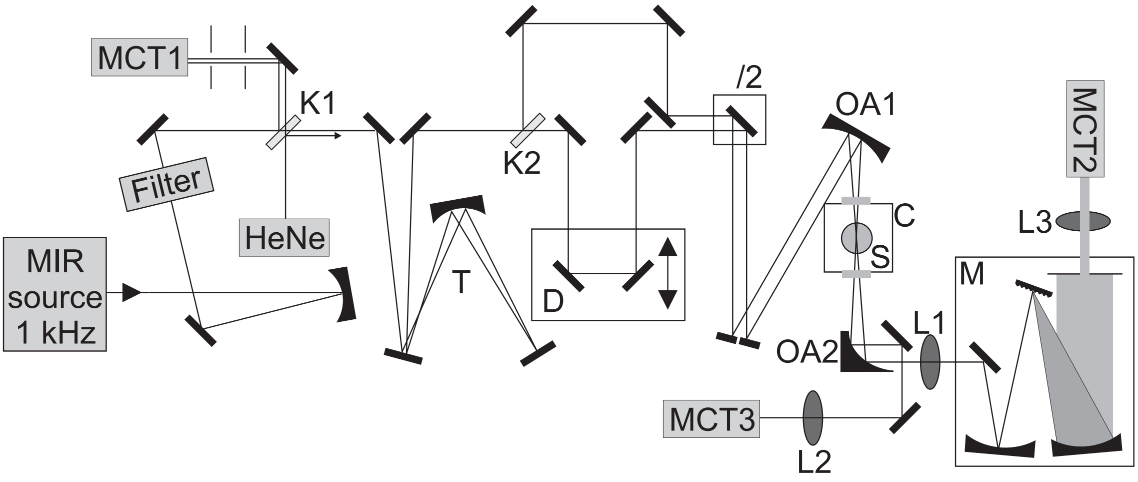

Figure 6.8: Optical setup of the mid-infrared pump-probe measurement [Filter: long-wavepass-filter, HeNe: helium-neon laser, K1: KBr wedge plate, K2: KBr 10% beam splitter, T: telescope with spherical gold mirror, D: delay stage, $\lambda/2$: periscope, OA1: 30° off-axis gold mirror (f = 100 mm), OA2: 90° off-axis gold mirror (f=100 mm), C: cryostat, S: quantum cascade sample, L1-3: f = 100 mm KBr lenses, M: monochromator]

Optical setup The optical setup of the pseudo two-color pump-probe measurement is shown in Fig. 6.8. The mid-infrared beam passes a long-wavepass-filter to block the residual near-infrared components. A weak reference beam is split off at a KBr wedge plate (K1) and focused onto the HgCdTe reference detector (MCT1). To pre-align the subsequent optical elements a visible HeNe beam is set parallel to the mid-infrared beam. The mid-infrared beam entering this setup is strongly astigmatic (because of the tilting of the GaSe crystal). This astigmatism is compensated by a tilted incidence on the spherical mirror (T). The telescope (T) is also used to increase the beam waist in order to get a small focus in the sample. A 10% fraction of the beam is split off at a KBr plate (K2) and used as probe beam. The residual pump beam passes a delay stage (D). The polarization of both beams is rotated by a periscope ($\lambda/2$). In this way, the pulses are P-polarized with respect to the layers of the quantum cascade sample (S). The pump beam and the probe beam are focused by a gold coated, 30° off-axis mirror (OA1) into the sample (S) and subsequently recollimated by a 90° off-axis gold mirror (OA2). The pump beam is focused onto a HgCdTe detector (MCT3). The probe beam is focused with a KBr lens (L1, $f = 50$ mm) into a monochromator (M) and with a spectral resolution of 150 nm it is detected with the signal detector (MCT2).

6.5 Experimental data

In this section we present femtosecond time-resolved transients for samples A_2, B, and C. In all transients the current-induced optical transmission change $\Delta T/T_0$ is plotted as a function of the time delay t_D between the pump and probe pulses. The pulse length (FWHM) of the pump and probe pulses is $\tau_p = 120$ fs [cf. Fig. 2.11 (b)]. We start with the presentation of data obtained from sample A_2. If not stated otherwise, the nominal lattice temperature, i.e., the lattice temperature at zero bias (cf. section 6.3), is held at $T_L = 10$ K, the detection wavelength is tuned to $\lambda_{det} = 10.0$ μm (resonant to the 3–2 transition of sample A_2 at $I = 7$ kA/cm^2), and the pulse energies of the pump and probe pulses are 7500 pJ and 250 pJ, respectively.

Experimental results for different current densities I are presented in Fig. 6.9. One finds

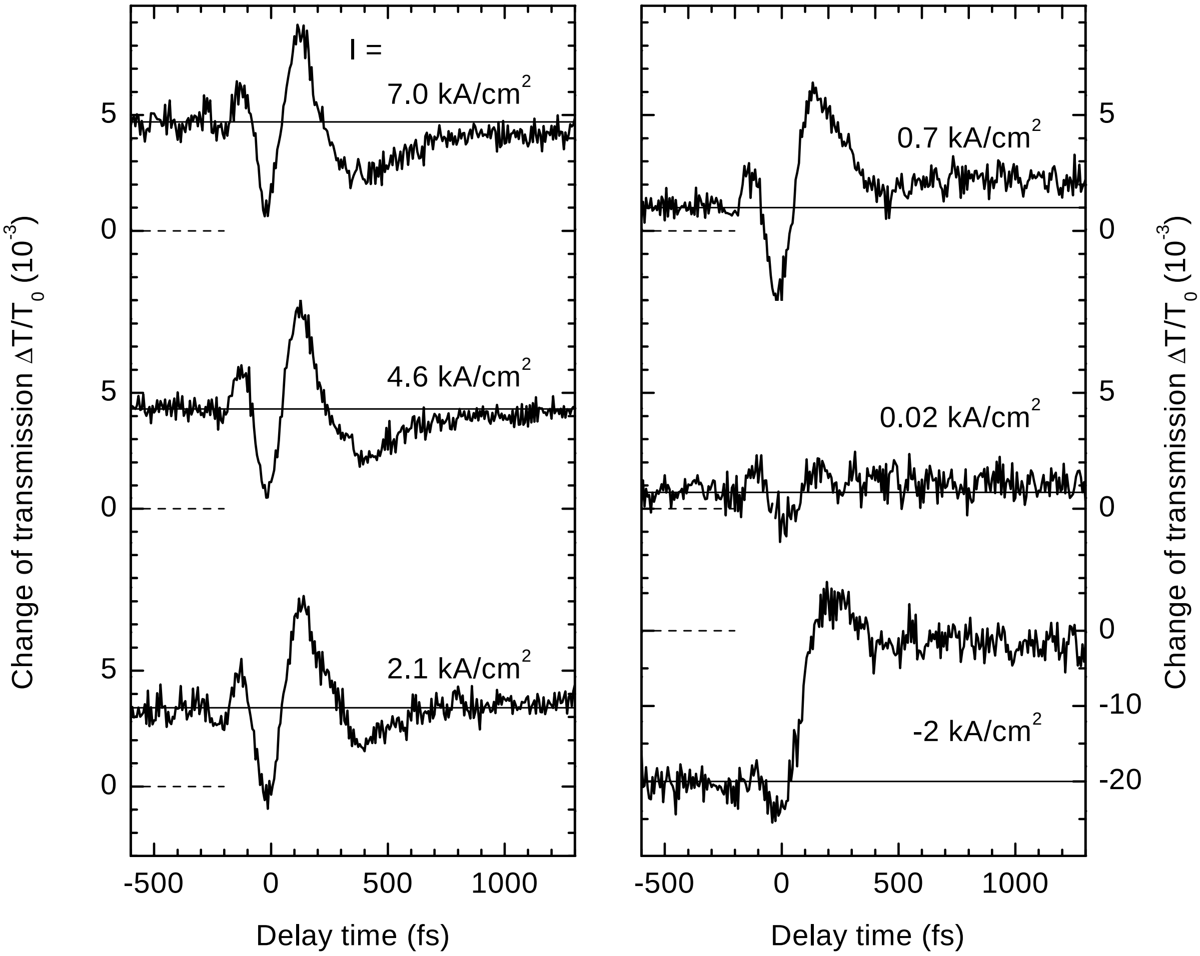

Figure 6.9: Pump-probe transients for sample A_2 measured at a detection wavelength of $\lambda_{det} = 10.0$ μm for various current densities I (nominal lattice temperature: $T_L = 10$ K). The current-induced optical transmission change $\Delta T/T_0 = T(I)/T(I = 0) - 1$ is plotted as a function of the time delay between pump and probe pulses [$T(I)$: transmission for an applied current I]. The pump pulse energy is 7500 pJ and the probe pulse energy is 250 pJ. The pump pulse is centered at 9.9 μm.

distinctly different transients for forward bias ($I > 0$) than for reverse bias ($I < 0$). At negative delay times all transients show a nonvanishing signal. For sufficient forward bias ($I > 0.4$ kA/cm^2) we observe an ultrafast saturation, which is followed by a pronounced oscillation with a period of $\approx$ 400 fs before it recovers almost exponentially on a time scale of several hundred femtoseconds. The shape of the pump-probe transients is nearly independent of the current density for $I > 2$ kA/cm^2. All transients for weak forward biases ($I = 0.02$ kA/cm^2) are dominated by a coherent artifact around delay zero. We use it to determine the time delay zero. For reverse bias, the transients show a distinctly different dynamics. The transmission at negative delay times is strongly decreasing. Upon ultrafast excitation we observe a step-like increase of the sample transmission within 200 fs, which recovers on a much longer time scale (not shown).

The excitation density dependence of the transmission change dynamics obtained at $\lambda_{det} = 10.5$ μm is addressed in Fig. 6.10 (current density: 4.6 kA/cm^2). For a probe pulse energy of 250 pJ we have varied the pump pulse energies E_{pump}. Increasing E_{pump} from 250 pJ to 2500 pJ, we observe an almost linear increase of the signal without changing its temporal shape. Around $E_{pump} = 2500$ pJ we observe saturation of the pump-probe signal amplitude. For the highest $E_{pump} = 7500$ pJ, one observes also a small change in the shape of the transient. The amplitude of the oscillation is smaller. It is followed by an exponentially decaying component at later times (> 400 fs), which is not observed for lower pump pulse energies.

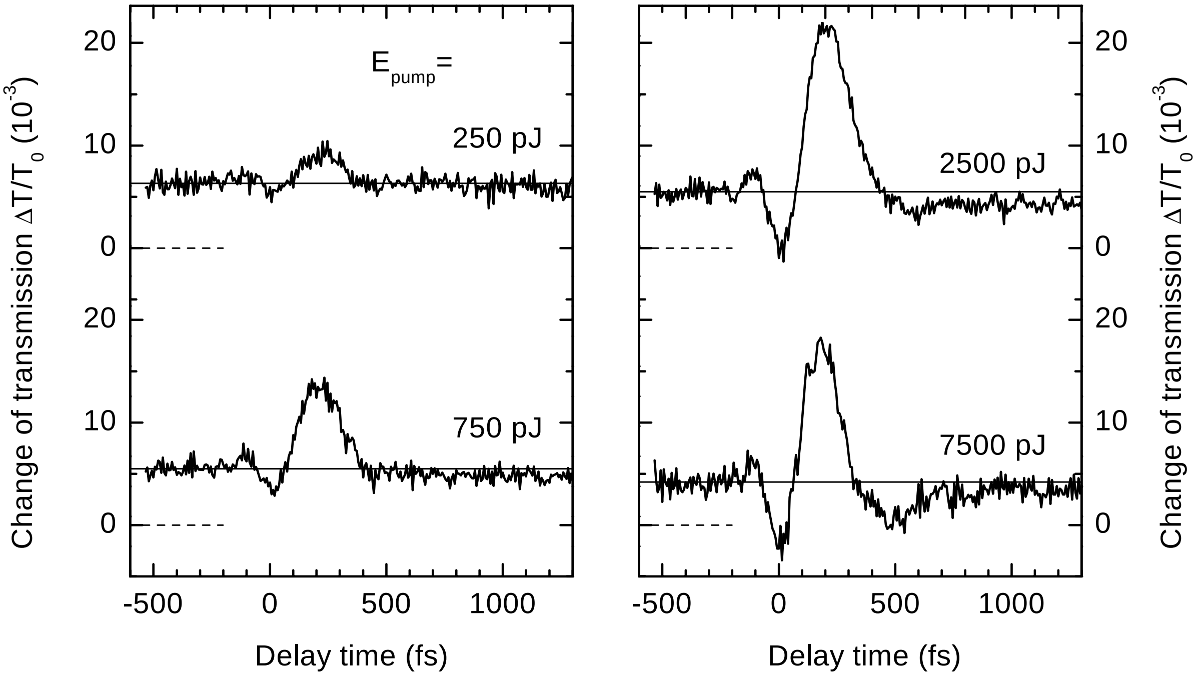

Figure 6.10: Excitation density dependence of the dynamics of the transmission change for sample A_2 measured at $\lambda_{det} = 10.5$ μm for different pump pulse energies E_{pump}, obtained for probe pulses with 250 pJ and a current density of 4.6 kA/cm^2 at $T_L = 10$ K.

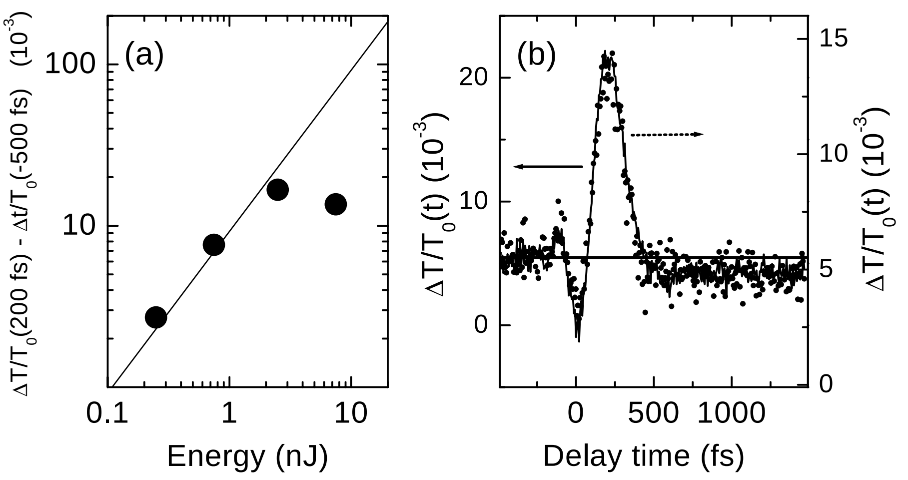

Figure 6.11: (a) Relative oscillation amplitudes, i.e., transmission changes before time delay zero subtracted from the maximum values at t = 200 fs as a function of the pump pulse energy (see Fig. 6.10). The probe pulse energy is $E_{probe} = 250$ pJ. The solid line represents a linear dependence on the pump pulse energy. (b) Direct comparison between the shapes of the transients for $E_{pump} = 750$ pJ (dots) and $E_{pump} = 2500$ pJ (solid line). The ordinate of the curve for $E_{pump} = 750$ pJ (right ordinate) is scaled by a factor of 2.2 compared to the one for $E_{pump} = 2500$ pJ (left ordinate).

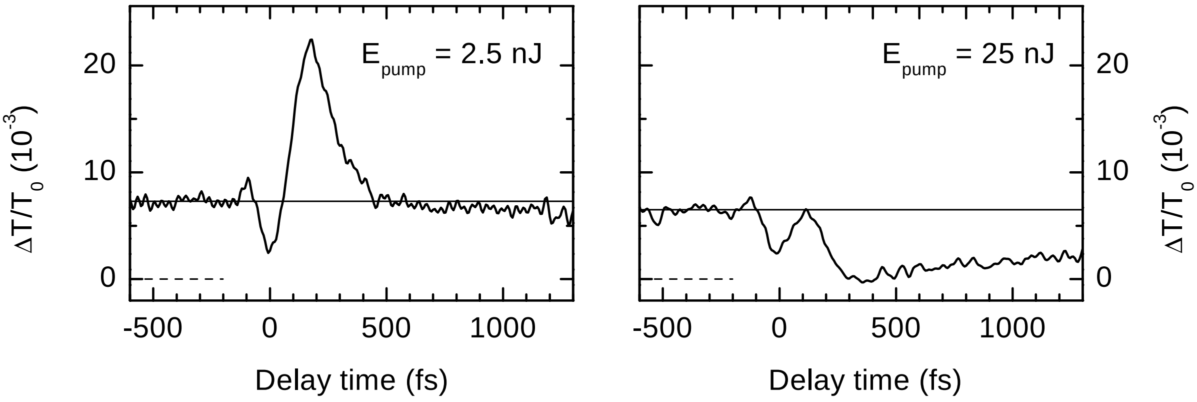

Figure 6.12: Excitation density dependence of the pump-probe signal for sample A_2 measured at $\lambda_{det} = 10.0$ μm for a low (left panel) and an extremely high pump pulse energy E_{pump} (right panel), obtained for a current density of 7 kA/cm^2 at $T_L = 10$ K. The probe pulse energy in the left panel is 75 pJ and in the right panel 750 pJ.

In Fig. 6.11 (a) the relative oscillation amplitudes as a function of the pump pulse energy are shown. They are obtained by subtracting the constant transmission change before time delay zero ($t_D < -500$ fs) from the peak of the oscillatory part at $t_D = 200$ fs. A linear increase of the signal is observed for pump pulse energies $E_{pump} < 2500$ pJ. At higher pump pulse energies the signal amplitude decreases slightly. This indicates a strong saturation of the excitation induced by pump pulses with $E_{pump} > 2500$ pJ. In Fig. 6.11 (b) the normalized shapes of the transients for $E_{pump} = 2500$ pJ and $E_{pump} = 750$ pJ are directly compared. This

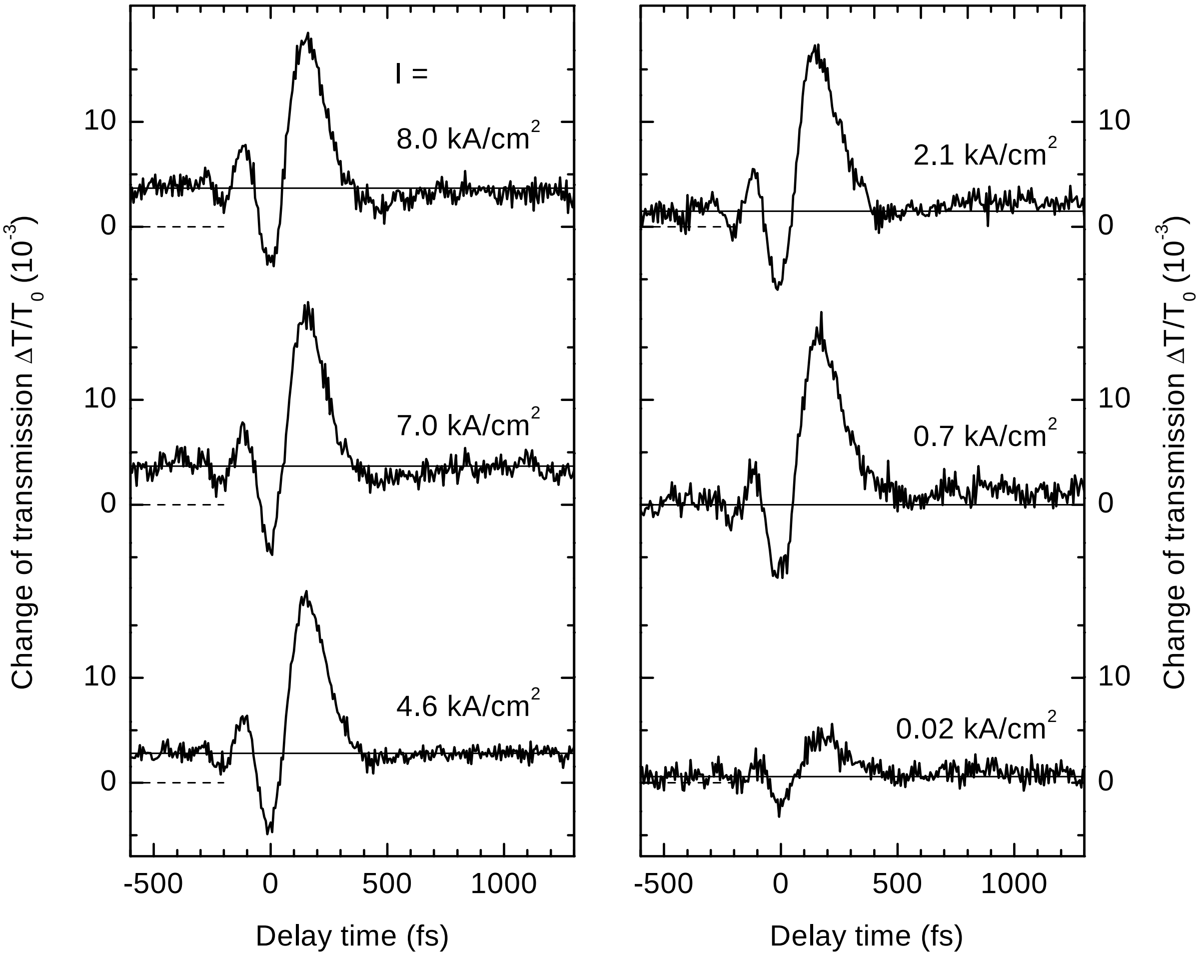

Figure 6.13: Pump-probe transients for sample A_2 measured at a detection wavelength of $\lambda_{det} = 10.0$ μm for various current densities I (nominal lattice temperature: $T_L = 10$ K). The pump pulse energy is 2500 pJ and the probe pulse energy is 75 pJ. The pump pulse is centered at 9.8 μm.

demonstrates that the temporal shapes do not change for pump pulse energies $E_{pump} \leq 2500$ pJ.

The excitation density dependence of the transmission change dynamics obtained at $\lambda_{det} = 10$ μm for low and very high pump pulse energies is addressed in Fig. 6.12 (current density: 7 kA/cm^2). For a pump pulse energy of 2.5 nJ we observe the oscillatory behavior as mentioned above. For a pump pulse energy of 25 nJ, i.e., at very strong saturation, the oscillation is strongly damped and at later times $t_D > 400$ fs there is an exponential recovery with a very long recovery time.

In Fig. 6.13 the current dependent pump-probe transients are shown for decreased pump and probe pulse energies ($E_{pump} = 2.5$ nJ, $E_{probe} = 75$ pJ) compared to those of Fig. 6.9. Qualitatively, the same features as in Fig. 6.9 are observed. Quantitatively, the oscillation amplitude is larger and the exponentially decaying component at later times is smaller.

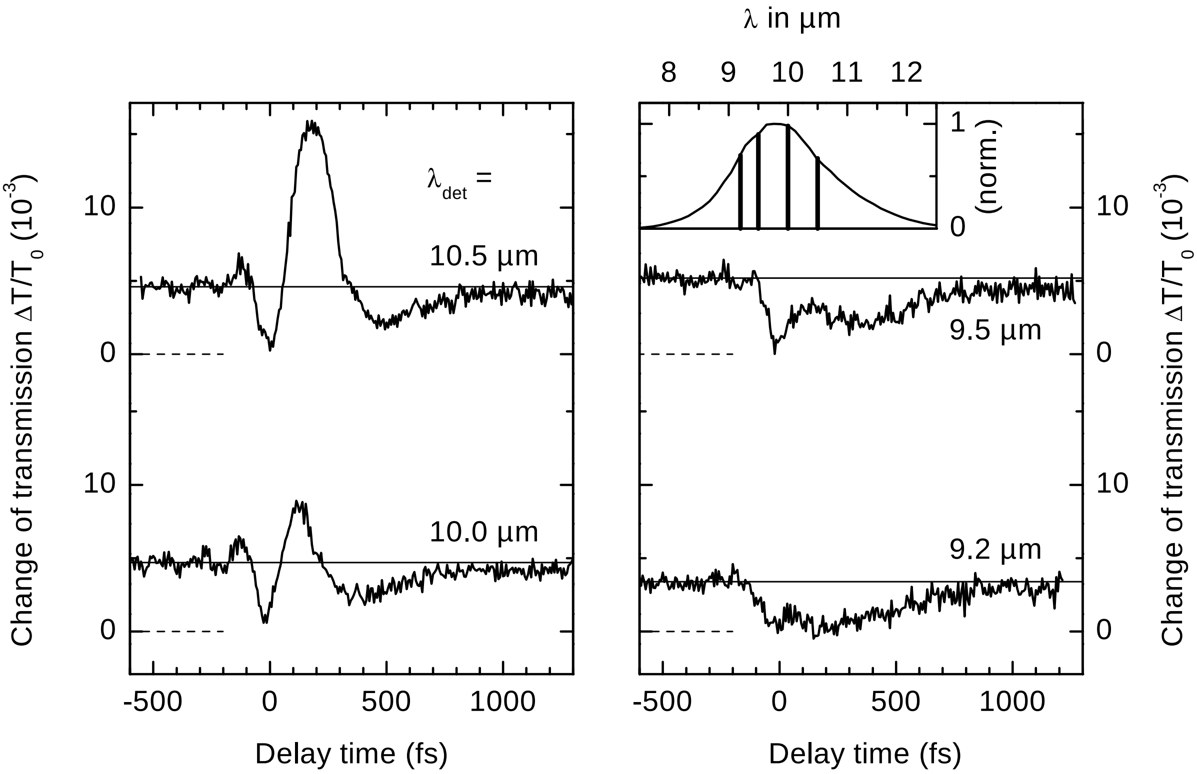

Figure 6.14: Spectral dependence of the dynamics of the transmission change for sample A_2 for various detection wavelengths λ_{det} (current density: 7 kA/cm^2, T_L = 10 K). The individual transients have been corrected for a small chirp of the probe pulses. The pump pulse energy is 7500 pJ and the probe pulse energy is 250 pJ. Inset: Power spectrum of the pump pulse (centered at 9.9 μm). The vertical lines indicate the detection wavelengths λ_{det}. The spectral resolution is 150 nm.

Pump-probe transients for a current density of 7 kA/cm^2 are shown in Fig. 6.14 for several detection wavelengths λ_{det}. Due to a small chirp of the mid-infrared pulse there is a shift of the time delay zero for different probe frequencies. To account correctly for this we have to determine the chirp of the pulse at the sample position. To do this, we have replaced the quantum cascade sample by an InSb crystal to measure spectrally resolved cross correlation signals via two-photon absorption. Since two-photon absorption has a minor spectral dependence the observed spectral characteristics can be calculated quite accurately using a simple model. It is used to determine the chirp of the pulse at the position of the sample as described in [141]. The individual transients shown in Fig. 6.14 have been corrected according to this procedure. At long detection wavelengths (λ_{det} = 10.5 μm) the signal is determined by an ultrafast saturation, which is followed by a pronounced oscillation. For shorter λ_{det}, an additional contribution to the pump-probe signals occurs. The transient measured at λ_{det} = 9.2 μm shows a fast rise within the time resolution and decays subsequently within 1 ps. This type of transient differs strongly from the oscillatory behavior of the transients observed at longer λ_{det}.

We present experimental data for different nominal lattice temperatures T_L in Fig. 6.15. The transients have been taken at $\lambda_{det} = 10.0\,\mu$m and for a current density of 7 kA/cm^2. Starting with 10 K we see the current-induced pump-probe signal as described above. In-

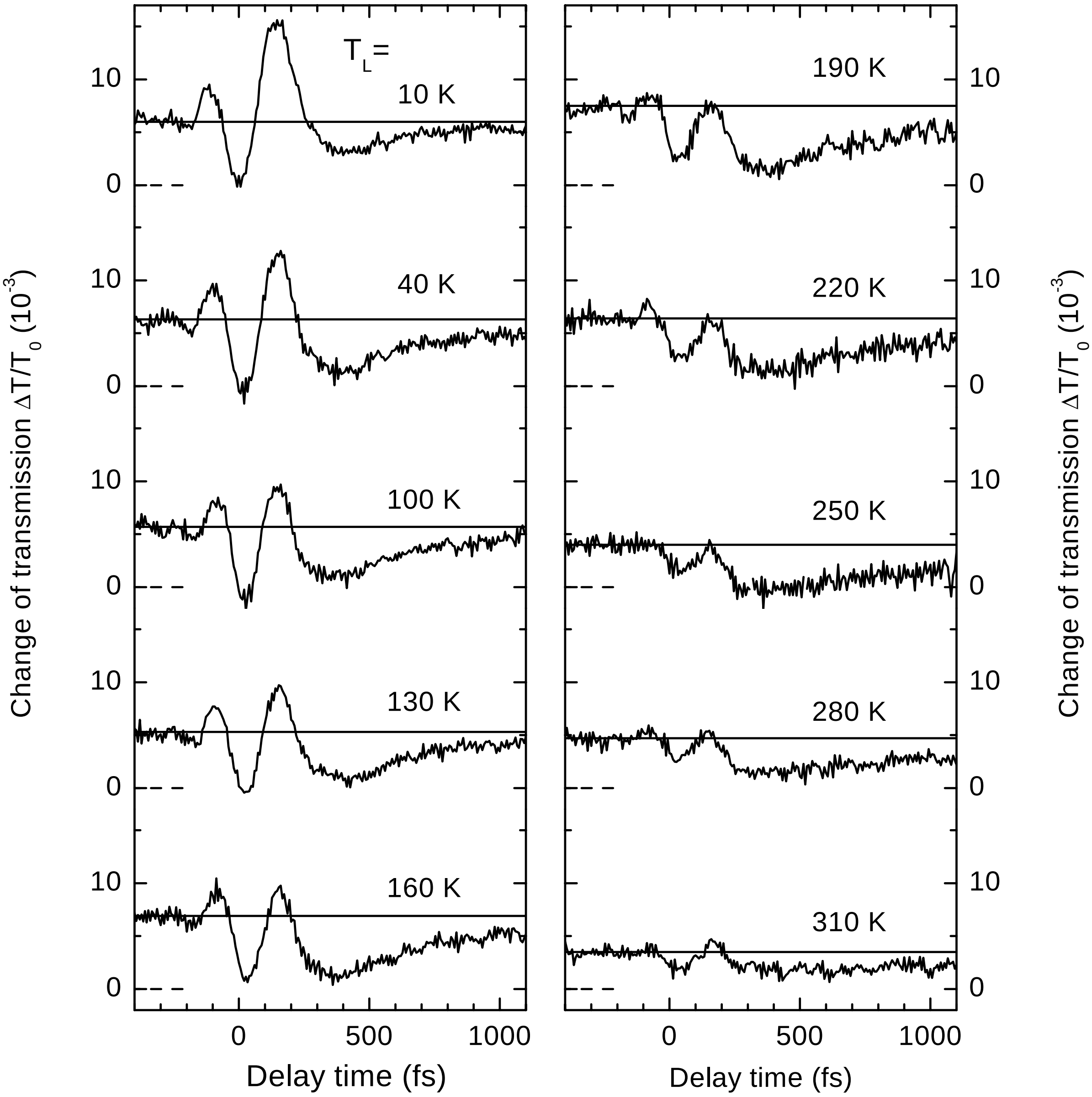

Figure 6.15: Ultrafast dynamics of $\Delta T/T_0$ for sample A_2 as a function of the nominal lattice temperature T_L as indicated. The transients have been measured for forward bias ($7\,\mathrm{kA/cm^2}$) at $\lambda_{det} = 10.0\ \mu$m. The pump pulse energy is 7500 pJ and the probe pulse energy is 250 pJ. The pump pulse is centered at 9.5 μm.

creasing the temperature to 100 K we observe a decrease of the oscillation amplitude and, concomitantly, an increase of the exponentially decaying contribution at later times. At a temperature of 220 K the oscillatory component has significantly weakened and the recovery time of the exponential contribution at later times increases. Both features practically vanish for temperatures above 300 K. For the stationary transmission change signal ($t_D < -400$ fs) we observe the tendency to decrease for increasing lattice temperatures for $T_L > 200$ K. For each pump-probe transient the sample had to be realigned since a variation of the temperature was accompanied by a variation of the length of the cold finger. This realignment resulted in a slightly different beam propagation geometry which influences strongly the stationary transmission change signal as discussed in the previous chapter. Hence, a quantitative comparison of the stationary transmission change for the various temperatures is difficult and will not be carried out.

In the following we present data for samples B and C. In Fig. 6.16 time resolved transmission changes for different current densities are plotted. The nominal lattice temperature is held at $T_L = 150$ K, the detection wavelength is tuned to $\lambda_{det} = 9.0$ μm and the pump and probe pulse energies are 750 pJ and 75 pJ, respectively.

Similar to sample A_2, for sufficient bias ($I > 4$ kA/cm^2) we observe an ultrafast saturation of the transmission change, which is followed by a pronounced oscillation with a period of $\approx$ 250 fs before it recovers almost exponentially on a time scale of several hundred femtoseconds. We observe that the period of the oscillation is nearly independent on the current density for $I > 4$ kA/cm^2. For increasing current, the oscillatory part becomes weaker and the exponentially decaying contribution increases.

The frequency of the oscillation for forward bias shows a pronounced dependence on the width of the injection barrier. In Fig. 6.17 pump-probe transients of the transmission change saturation and recovery are shown for samples B [Fig. 6.17 (a)] and C [Fig. 6.17 (b)]. Both transients were measured at a detection wavelength of $\lambda_{det} = 9.0$ μm, a nominal lattice temperature of $T_L = 150$ K, a current density $I = 4.8$ kA/cm^2 and a pump and probe pulse energy of 750 pJ and 75 pJ, respectively.

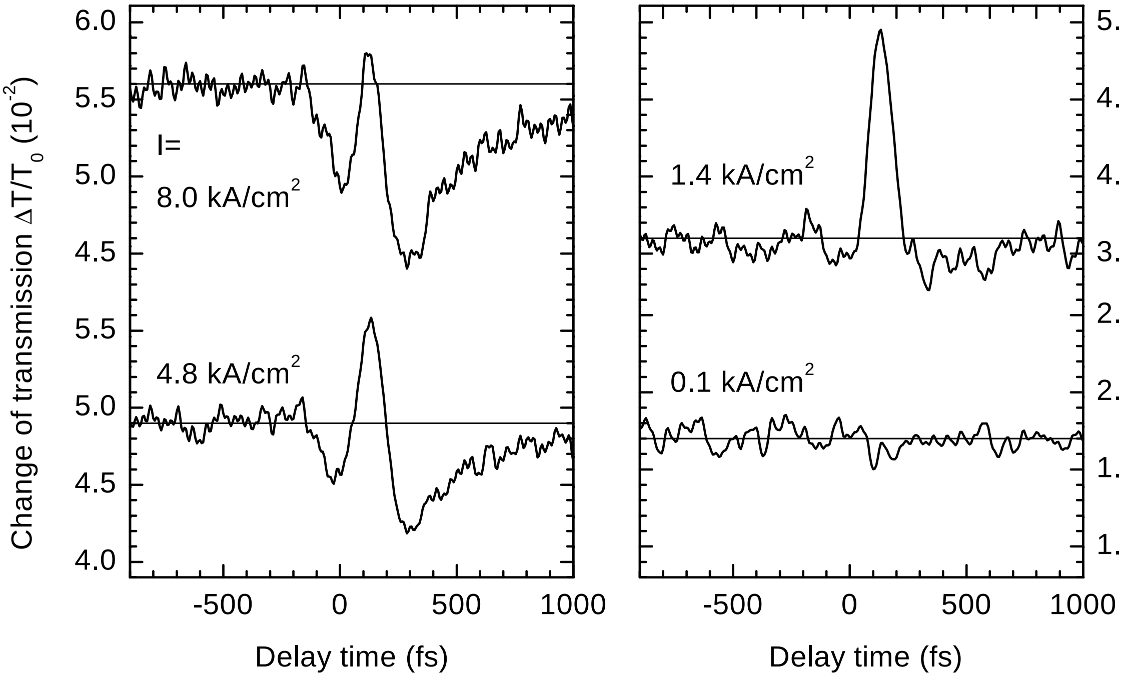

Figure 6.16: Pump-probe transients for sample B measured at a detection wavelength of $\lambda_{det} = 9.0$ μm for various current densities (nominal lattice temperature: $T_L = 150$ K). The pump pulse energy is 750 pJ and the probe pulse energy is 75 pJ. The pump pulse is centered at 9.0 μm.

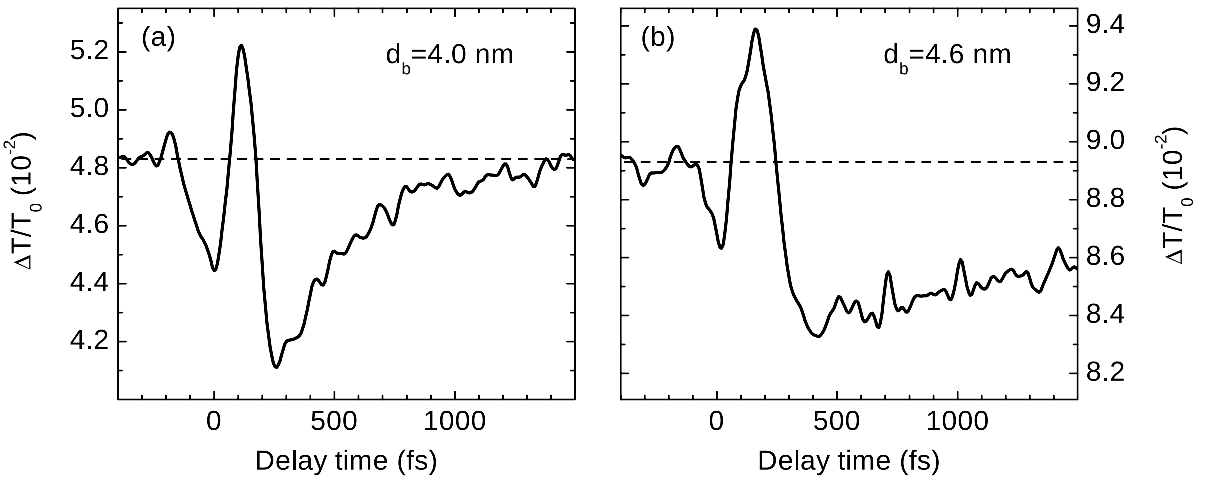

Figure 6.17: Dynamics of the transmission change $\Delta T/T_0$ for different barrier widths d_b [(a) sample B and (b) sample C] measured at a detection wavelength of $\lambda_{det} = 9.0$ μm for a current density $I = 4.8$ kA/cm^2 and a nominal lattice temperature of $T_L = 150$ K. The pump pulse energy is 750 pJ and the probe pulse energy is 75 pJ. The pump pulse is centered at 9.0 μm.

6.6 Discussion

At the beginning of the discussion of the experimental data we want to recall the basic working principle of the quantum cascade laser. Under appropriate bias, electrons are transferred from an n-doped injector through the injection barrier into the active region [Fig. 6.18 (a)]. Under steady-state conditions, a population inversion builds up between subbands 3 and 2, resulting in optical gain on the 3–2 intersubband transition (see inset of Fig. 6.18). Subband 2 is depopulated very efficiently by emission of longitudinal optical phonons, transferring carriers into energetically lower subbands, e.g., into subband 1. Electrons leave the active region by tunneling through a thin exit barrier into the next injector region. The states $|g\rangle$ and $|3\rangle$ designate the injector ground state and the upper laser state, respectively. $|2\rangle$ is called the lower laser state. It is important to note that the injector ground state $|g\rangle$ and the upper laser state $|3\rangle$ are eigenstates of the electronic Hamiltonian *without* the tunnel coupling through the injection barrier. Hence, these states are either localized in the injector or in the active region. At resonance the expectation values for the energy of the non-stationary states $|g\rangle$ and $|3\rangle$ are equal.

However, this is a simplified picture since more subbands in a quantum cascade structure play a non-negligible role. In Fig. 6.18 (b) a complete set of energy eigenstates of the electronic potential for one period *including* the tunnel coupling is plotted. Two points are important to note:

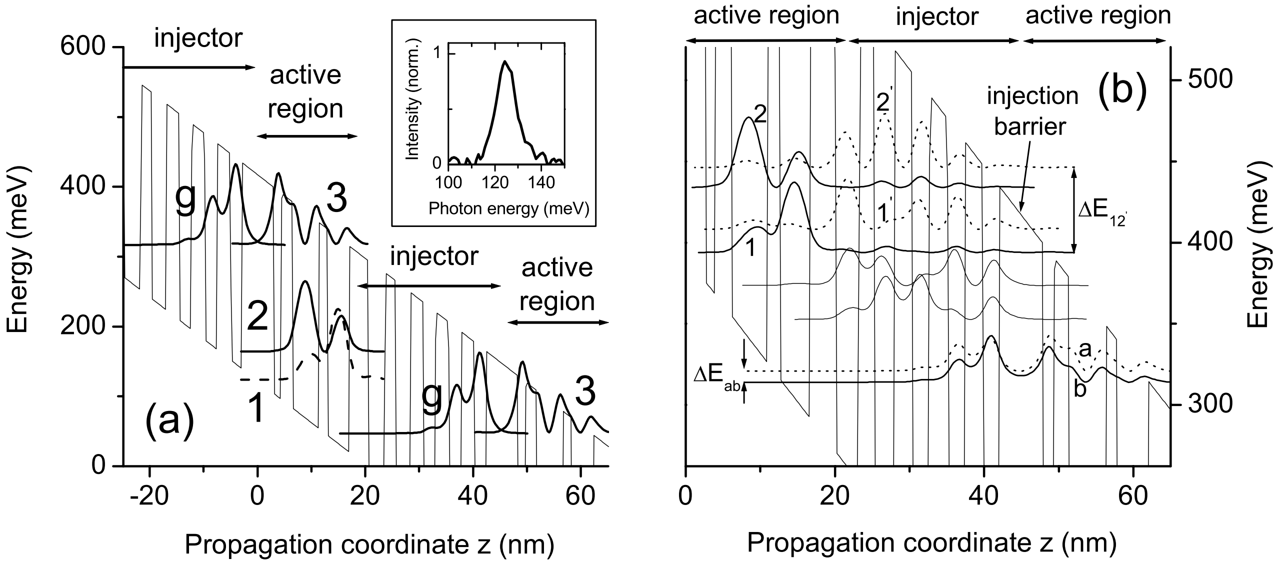

Figure 6.18: (a) Conduction band diagram of sample A_2 for an applied electric field of 60 kV/cm. Probability densities $|\zeta(x)|^2$ are shown for the wavefunctions relevant for the quantum cascade laser dynamics: $|g\rangle$ (ground state in the injector), $|3\rangle$ (upper laser state), $|2\rangle$ (lower laser state), and $|1\rangle$ are eigenstates of the electronic Hamiltonian *without* the tunnel coupling through the injection barrier. Inset: Electroluminescence spectrum due to spontaneous emission from subband 3 to subband 2. (b) Complete set of energy eigenfunctions (probability densities) of the electronic Hamiltonian *with* the tunnel coupling in the lowest miniband of one period. The probability densities are obtained from an eight-band $\mathbf{k}\cdot\mathbf{p}$ bandstructure calculation [74].

- We see that—at resonance—the upper laser state $|3\rangle$ and the injector ground state $|g\rangle$ form binding $|b\rangle$ and anti-binding $|a\rangle$ superpositions, which are delocalized over both the injector and the active region. ΔE_{ab} is the energy splitting between these states. The nonstationary states $|g\rangle$ and $|3\rangle$ in Fig. 6.18 (a) are coherent superpositions of energy eigenstates $|a\rangle$ and $|b\rangle$:

  $$|g\rangle = \frac{|b\rangle + |a\rangle}{\sqrt{2}} \quad , \quad |3\rangle = \frac{|b\rangle - |a\rangle}{\sqrt{2}}$$

  The non-stationary character of $|g\rangle$ and $|3\rangle$ is essential for the understanding of electron transport from the injector into the active region as we will see later.

- Not only states $|2\rangle$ and $|1\rangle$ have significant probability density in the active region. In particular, states $|2'\rangle$, $|2\rangle$, $|1'\rangle$, and $|1\rangle$ have a non-negligible optical dipole matrix element with $|3\rangle$ and are delocalized from the active region over the exit barrier into the injector. The very broad electroluminescence spectrum with a double peak structure shown in Fig. 5.16 (b) already gives direct evidence for a multi-subband structure of the lower laser state[1]. These points have to be taken into account in the evaluation of our experiment since the pump pulse has a large bandwidth.

After these preconsiderations we will now analyze the data starting with the stationary transmission change signal observed at zero delay times.

6.6.1 Electrically induced gain and degree of saturation

At negative delay times, the probe pulse interacts with the sample long before the pump pulse so that this signal is independent of the latter. In Fig. 6.19 the current dependence of the transmission change signal of sample A_2 at negative delay times (squares) is plotted [cf. Fig. 6.9]. For forward bias ($I > 0$) a positive transmission change is observed which monotonically increases with increasing current up to $\Delta T/T_0 = 0.5$ % at $I = 7.0$ kA/cm^2. This transmission increase is due to current-induced gain on the 3–2 lasing transition of the quantum cascade structure as discussed in the previous chapter.

For reverse bias we observe a large transmission decrease of $\Delta T/T_0 = -2$ % for $I = -2.0$ kA/cm^2. This behavior can be explained with the calculated gain and absorption spectra for various current densities plotted in the inset of Fig. 6.19. The calculations were carried out by Lee and Wacker using the Green's function formalism [121, 142]. At $I = 7$ kA/cm^2 there is gain which is peaked at a photon energy of 130 meV (solid line). The gain vanishes at low current densities. At $I = 0.17$ kA/cm^2 (dashed-dotted line) a weak absorption centered at 155 meV is observed. This absorption corresponds to the 1–3 intersubband excitation of electrons residing in subband 1 at very low bias. Decreasing the current further a red shift and an increase of the 1–3 absorption is observed. For a current density of $I = -2$ kA/cm^2 (dotted line) we observe a pronounced absorption centered at 120 meV with an amplitude which is a factor of five larger than that of the gain for $I = 7$ kA/cm^2 as observed in the experiment. The circles in Fig. 6.19 represent the calculated transmission change signal according to the theoretical work of Lee and Wacker [142]. It is evident that this theory curve is in excellent agreement with our experiment.

---

[1] In the beam propagation geometry of the quantum cascade mesa the double peak structure of the electroluminescence spectrum is strongly suppressed because of the multiple layer effect (see the discussion in the previous chapter).

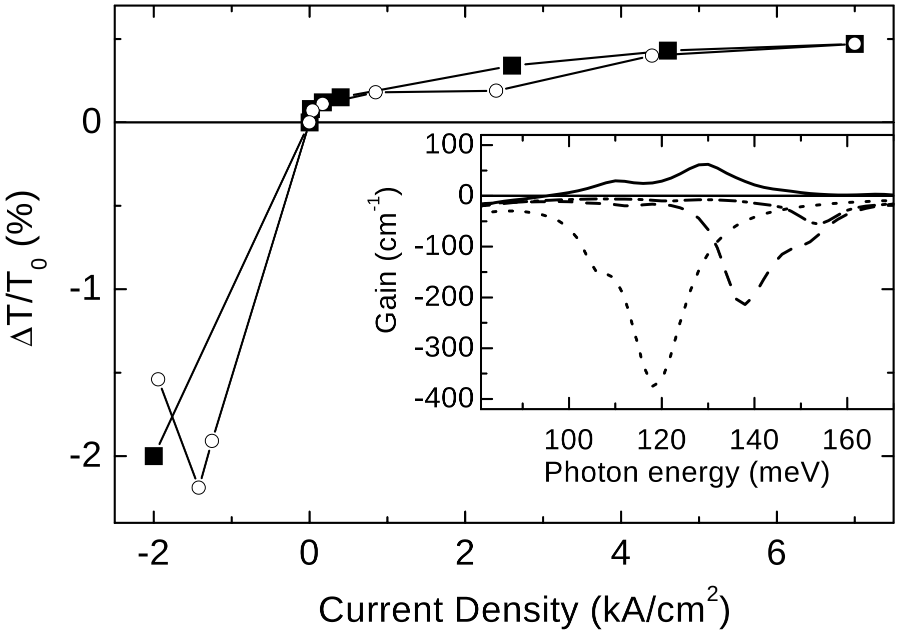

Figure 6.19: Transmission change signal at negative delay times ($t_D = -1$ ps) as a function of current density measured at $\lambda_{det} = 10.0\ \mu$m (photon energy 124 meV) (squares) and calculated using the Green's function formalism (circles) [142]. Inset: Calculated gain and absorption (negative gain) spectra for current densities of 7 kA/cm^2 (solid line), 0.17 kA/cm^2 (dashed-dotted line), 0 kA/cm^2 (dashed line), and -2 kA/cm^2 (dotted line) [142].

In the following we will estimate the saturation of the stationary gain induced by the strong pump pulse.

Degree of saturation For a quantitative determination of the degree of saturation we estimate the effective cross section of the intersubband transition from the upper laser subbands a and b into the lower laser subband 2. The stationary transmission change (light amplification) at $\lambda = 10.0\,\mu$m and for a current density of $I = 4.6$ kA/cm^2 is $G \equiv \Delta T/T_0 = 5 \times 10^{-3}$ (Fig. 6.10). Since the current from the injector into the active region is distributed over two channels, i.e., subband a and subband b, the electron densities n^b_{2D} and n^a_{2D} in the upper laser subbands b and a read:

$$n^b_{2D} = \tau_b \cdot (\Phi_{el}/2) = 2\,\tau_3 \cdot (\Phi_{el}/2) \quad \text{and} \quad n^a_{2D} = \tau_a \cdot (\Phi_{el}/2) = 2\,\tau_3 \cdot (\Phi_{el}/2)$$

where $\Phi_{el} = I/e$ is the total electron flux. With the focus area enhancement $A = 2.63$ the cross section yields

$$\sigma = \frac{G}{N_{QW}\left(n^b_{2D} + n^a_{2D}\right) A} = 1.8 \cdot 10^{-15}\,\text{cm}^2$$

With these considerations we are able to estimate the degree of saturation n_{ex} for an optical pulse energy E_{pulse}. The photon flux for a focus diameter $d_{foc} = 130\ \mu$m at $\lambda = 10.5\ \mu$m reads

$$\Phi_{ph}(E_{pulse}) = \frac{E_{pulse}}{h\,\frac{c}{\lambda}\,\pi\left(\frac{d_{foc}}{2}\right)^2}$$

and the spectral overlap is

$$D = \frac{\int \Phi_{MIR} \cdot \Phi_{Gain} \, d(\hbar\omega)}{\int \Phi_{MIR} \, d(\hbar\omega)} = 0.4$$

where Φ_{MIR} is the optical pulse spectrum and Φ_{MIR} is the normalized gain spectrum derived from the electroluminescence in units of photons per frequency interval. With these quantities the degree of excitation yields

$$n_{ex}(E_{pulse}) = \Phi_{ph}(E_{pulse}) \cdot \sigma \cdot D \qquad (6.1)$$

In the experiments carried out with sample A_2 we used pump pulses with an energy of 2500 pJ and 7500 pJ. For a pulse energy of 2500 pJ we calculate a degree of saturation of $n_{ex}(2500\,\text{pJ}) = 70$ %. This is in good agreement with the measurements carried out for various pump pulse intensities (Fig. 6.10). For the probe pulse we used pulse energies of 250 pJ which results in an excitation density of $n_{ex}(250\,\text{pJ}) = 7\,\%$. Hence, this pulse energy is well below saturation.

It is important to note that this simple estimate is correct only for a small degree of excitation, i.e., in the linear regime. For a more accurate calculation the interaction of the optical pulse with a quantum mechanical multiple-level system has to be taken into account as shown in chapter 4, where a two-level system was investigated. Nevertheless Eq. (6.1) gives a good estimate for the degree of saturation induced by the strong optical pump pulse.

6.6.2 Dynamics of the transmission change

Now, we want to discuss the key points of our time-resolved measurements. All transients measured at wavelengths where stimulated emission dominates the nonlinear transmission changes show three dominant characteristics. We discuss those with the transient measured at a bias of 7 kA/cm^2 and at a detection wavelength $\lambda_{det} = 10.0\,\mu$m shown in Fig. 6.20.

Before time delay zero, there is a positive transmission change. Since the electronic system resides in a quasi-stationary equilibrium with population inversion between subband 3 and subband 2 [Fig. 6.20 (a)] this positive signal is attributed to current-induced gain. At zero delay, we observe an ultrafast gain saturation induced by the strong pump pulse [Fig. 6.20 (b)], which is followed by a gain recovery within 1 ps [Fig. 6.20 (c)]. It is evident that this gain recovery shows a pronounced oscillatory behavior which indicates coherent phenomena in the underlying gain recovery processes.

Before we continue with the discussion of the underlying physics we want to show that the interpretation given above is correct, i.e., that the observed pump-probe features can exclusively be attributed to the dynamics of the current-induced gain. There are several possible alternative effects which have to be excluded:

- First, we want to emphasize that the structures investigated in this thesis consist only of the amplifier portion of the quantum cascade laser. This is in distinct contrast to the majority of gain dynamics experiments carried out on semiconductor interband laser amplifiers with long interaction lengths of the light field with the gain medium (see, e.g., Ref. [143]). Our structures are free from effects which result from the interaction of the gain medium with the resonator modes. Since the interaction length in our sample geometry is only $\approx 2\ \mu$m (cf. Fig. 5.2), corresponding to 20 fs transit time, we can also exclude any propagation effects, which have been observed in travelling wave semiconductor amplifiers [144].

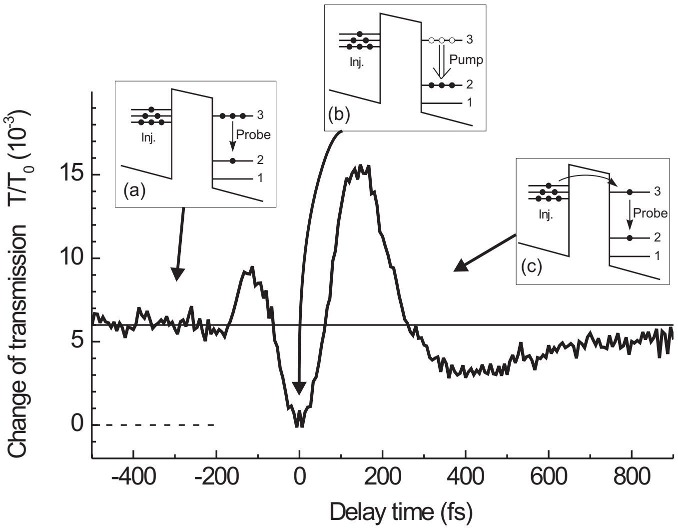

Figure 6.20: Pump-probe signal measured at a detection wavelength of $\lambda_{det} = 10.0\,\mu$m ($I = 7$ kA/cm^2, $T_L = 10$ K, cf. Fig. 6.15). (a) Quasi-stationary equilibrium with population inversion between subband 3 and subband 2. (b) Ultrafast gain saturation induced by the strong pump pulse. (c) Gain recovery with pronounced oscillatory behavior.

- An important question is the influence of the n-type contact layers on the pump-probe signal. For this, we evaluate the time resolved experiments for various current densities (Fig. 6.9). One finds completely different transients for forward ($I > 0$) and for reverse bias ($I < 0$). This pronounced dependence on the direction of the current excludes current-induced contributions from the n-type contact layers since the latter would be independent of the polarity of the bias. Thus, we conclude that the observed pump-probe signal is exclusively caused by the dynamics of intersubband transitions in the active region.

- Since our transmission change signal is the difference between the transmission change with bias minus that without bias, we have to consider also a possible pump-probe contribution at zero bias. The data presented in Fig. 6.14 show a strong spectral dependence of the transmission change signal. At $\lambda_{det} = 9.2$ μm a transient is observed which strongly differs from that measured at $\lambda_{det} = 10.0$ μm. We interpret the transient at $\lambda_{det} = 9.2\,\mu$m as follows: The photocurrent spectrum is peaked near $\lambda = 9.2\,\mu$m (cf. Fig. 6.21, dashed-dotted line), i.e., there is 1–3 absorption at zero bias, whereas the electroluminescence for forward bias is negligible at this spectral position. Thus, the transient measured at $\lambda_{det} = 9.2$ μm (Fig. 6.14) is the sign-inverted bleaching and recovery of the 1–3 intersubband absorption present at zero bias. It shows a fast rise within the time resolution of the experiment and decays subsequently within 1 ps, which is a typical value for intersubband relaxation [78, 69].

  A completely different behavior occurs at $\lambda_{det} = 10.0\,\mu$m, i.e., at the center of the electroluminescence spectrum. Here, the photocurrent data show that there is negligible 1–3 absorption for $\lambda_{det} \geq 10.0$ μm. From the electroluminescence spectrum we infer that at this wavelength the pump-probe signal is dominated by the saturation and

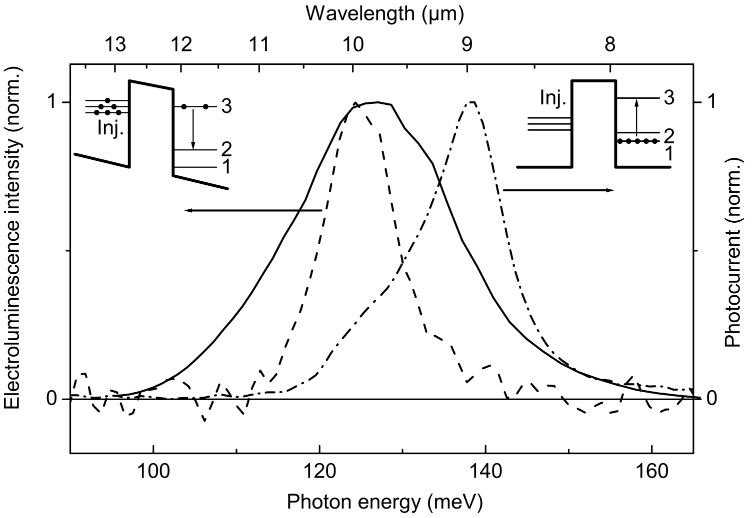

Figure 6.21: Mid-infrared pulse spectrum (solid line) in comparison with the electroluminescence spectrum for $I = 7.1$ kA/cm^2 (dashed line) and the photocurrent spectrum (dashed-dotted line) for sample A$_2$.

recovery of the current-induced 3–2 gain.

This discussion demonstrates that the oscillations exclusively observed at spectral positions around the gain maximum and for sufficient forward bias are an intrinsic property of the gain recovery dynamics. Since gain is due to the difference of the population in the upper and lower laser subbands [Eq. (5.4)] we expect two contributions to the pump-probe signal, a contribution from the electron dynamics in the upper and a contribution from the electron dynamics in the lower laser subbands. The pump-induced contribution from the lower laser subbands is of minor importance for the following reasons:

- In the pump-probe signal (Fig. 6.20) we observe an extremely fast increase of the gain after saturation at zero delay. At $t_D = 70$ fs it has already reached the stationary level and it further increases up to more than twice the stationary value within $t_D = 120$ fs. This behavior is only possible if the electrons promoted to the lower laser states leave these states extremely fast within the time-resolution of our experiment.

- This picture is supported by the fact that the quantum cascade structure was intentionally designed so that the lifetime of the lower laser states is much smaller than the lifetime of the upper laser state in order to get sufficient population inversion for laser action.

- Due to the large bandwidth of the pump pulse a wavepacket is generated in the lower laser subbands. The huge bandwidth of $\Delta E_{12'} = 60$ meV of the lower laser subbands with non-negligible dipole matrix elements with the upper laser state [cf. Fig. 6.18 (b)] corresponds to an exit time of only $h/(2E_{12'}) = 30$ fs. The resonant LO phonon coupling of the subbands 2, 2′ and 1, 1′ and the ultrafast thermalization due to electron-electron scattering in the injector [126] lead to a fast dephasing of this wavepacket preventing any recurrence in the active region.

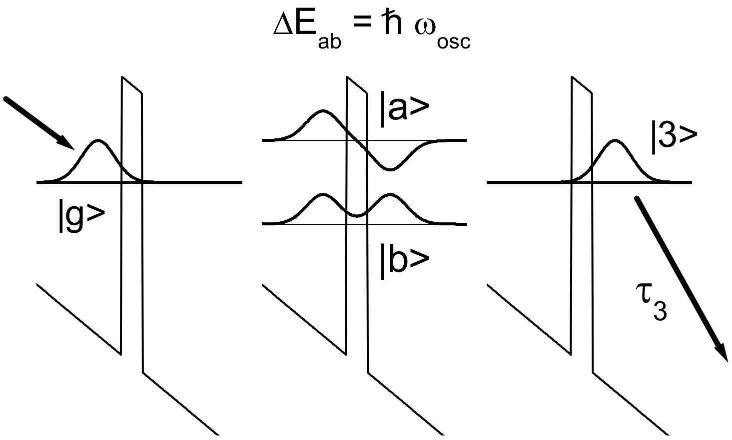

Figure 6.22: Schematics of the coherent transport of electrons from $|g\rangle$ into $|3\rangle$ in the dynamic picture of resonant tunneling. $|b\rangle$ and $|a\rangle$ are the binding and anti-binding energy eigenstates of the electronic Hamiltonian *including* the tunnel coupling. $|g\rangle$ and $|3\rangle$ are coherent superpositions of $|b\rangle$ and $|a\rangle$: $|g\rangle = 1/\sqrt{2}\left(|b\rangle + |a\rangle\right)$, $|3\rangle = 1/\sqrt{2}\left(|b\rangle - |a\rangle\right)$.

Hence, the contribution from the de-excited electrons is negligible for $t_D > 100$ fs. Consequently, the gain saturation and recovery dynamics is dominated by the population dynamics in the upper laser subband 3. This population dynamics is influenced by two mechanisms, the electron transport between the injector and the active region and the relaxation into the lower laser subbands. Since the observed gain recovery and in particular the oscillation is much faster than the lifetime of subband 3 ($\tau_3 = 1.4$ ps [99]), the pump-probe signal is mainly determined by the transport dynamics of the electrons.

Now, we discuss the physical mechanism underlying the transport dynamics of electrons in a quantum cascade structure. We have seen that the oscillation observed in the data measured at $\lambda_{det} = 10.0\,\mu$m gives evidence for coherent electron transport from the injector through the injection barrier into the upper laser subband. This can be described in the picture of resonant tunneling as suggested in the theoretical work of Kazarinov and Suris [98, 127] (cf. section 3.3): In the dynamic picture of resonant tunneling (Fig. 6.22) coherent superpositions of states $|a\rangle$ and $|b\rangle$,

$$|\Psi_{ab}\rangle(t) = \frac{1}{\sqrt{2}}\left(|b\rangle + |a\rangle\, e^{i\frac{\Delta E_{ab}}{\hbar}\,t}\right)$$

represent the basis for wave packet propagation from the injector ground state

$$|g\rangle = |\Psi_{ab}\rangle(0) = \frac{|b\rangle + |a\rangle}{\sqrt{2}}$$

into the upper laser state

$$|3\rangle = \frac{|b\rangle - |a\rangle}{\sqrt{2}}$$

In our time-resolved experiment, the femtosecond pump pulse depletes subband 3 [Fig. 6.23 (a)] and, concomitantly, initiates a coherent wavepacket motion by which electrons initially residing in the injector subband g tunnel through the barrier into the upper laser

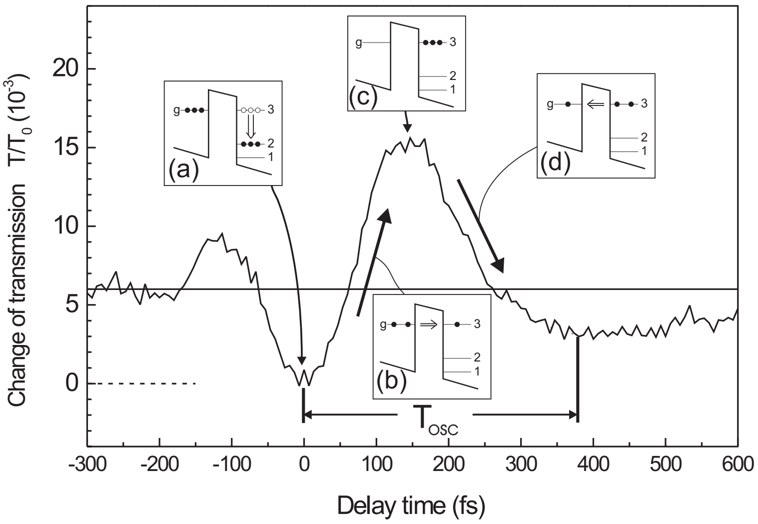

Figure 6.23: Schematics of the different processes underlying the observed pump-probe signal [cf. Fig. 6.15, 10 K]. (a) At delay time zero the pump pulse depletes subband 3 completely. (b)-(c) Concomitantly, the electrons tunnel from subband g into subband 3. (d) Since the lifetime of subband 3 is longer than the oscillation period, a large portion of the electrons will tunnel back into the injector.

subband 3 [Fig. 6.23 (b)]. According to the energy splitting ΔE_{ab} between the binding and anti-binding energy eigenstates $|b\rangle$ and $|a\rangle$, the tunneling carriers arrive after half the oscillation period $T_{osc} = h/\Delta E_{ab}$ in the subband 3 of the active region [Fig. 6.23 (c)]:

$$|3\rangle = |\Psi_{ab}\rangle(\frac{T_{osc}}{2})$$

Note, that now the gain is much higher than the stationary value. We will come back to this point later. As the lifetime $\tau_3 = 1.4$ ps [99] of state $|3\rangle$ is substantially longer than $T_{osc}/2$, a large portion of the electrons will move back into the injector resulting around $t_D = T_{osc}$ again in a gain depletion [Fig. 6.23 (d)]:

$$|g\rangle = |\Psi_{ab}\rangle(T_{osc})$$

So far, we have seen that the oscillation observed can qualitatively be understood in the picture of resonant tunneling. This interpretation rises several questions. The first one is the oscillation frequency $\nu_{osc} = 1/T_{osc}$, which is directly correlated with the energy splitting ΔE_{ab} according to the picture of resonant tunneling. Then there is the question of the damping of the oscillation. This point is important to determine the degree of coherence of the underlying transport. Another question is the explanation of the large gain overshoot at $t_D = 150$ fs above the stationary level. We will address these points in the following.

6.6.3 Oscillation frequency

From single particle band structure calculations we know that different injection barrier widths result in different coupling strengths between the injector and the active region, i.e., in a variation of the tunnel splitting ΔE_{ab}. Thus, the picture of resonant tunneling suggests that the oscillation frequency $\nu_{osc} = 1/T_{osc} = \Delta E_{ab}/h$ strongly depends on the injection barrier width d_b.

To investigate this we have carried out measurements on two quantum cascade structures (structures B and C) differing only in the barrier width. In Fig. 6.24 we plot the data presented in Fig. 6.17 which have been obtained from sample B (d_b = 4.0 nm) and C (d_b = 4.6 nm) for forward bias and a detection wavelength centered at the peak of the electroluminescence spectrum. For a better comparison we have subtracted the stationary gain from both transients. We observe that the oscillation frequencies for the two samples are distinctly different. The sample with the smaller injection barrier width (sample B) shows a larger oscillation frequency than the sample with the higher barrier width (sample C). According to the picture of resonant tunneling a smaller barrier width results in a stronger coupling and, concomitantly, in a higher oscillation frequency $\nu = 1/T_{osc}$. It is evident that the data for sample B and C (Fig. 6.24) agree with this picture. This comparison strongly supports the picture of resonant tunneling as the main transport process between the injector and the active region. It is important to note that this difference in the oscillation period is clearly seen though the barrier width variation is only 15 % corresponding to two monolayers. This strong dependence is explained by the fact that tunneling is an effect which depends exponentially on the barrier width [4].

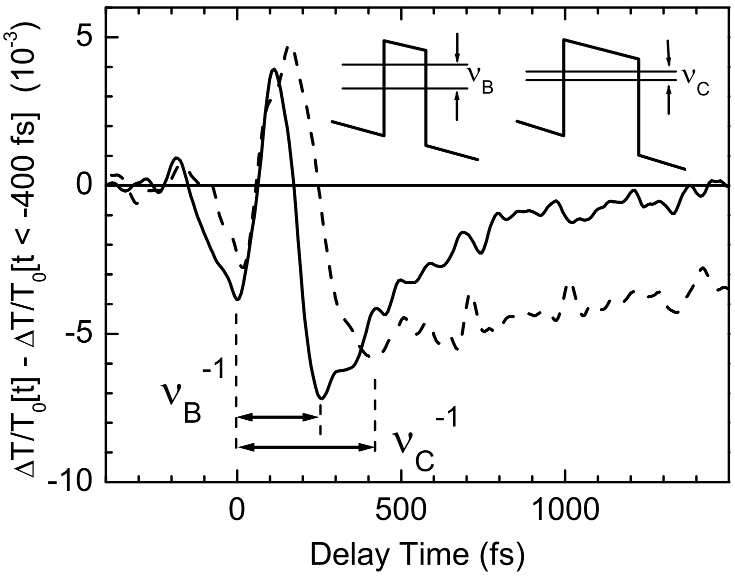

Figure 6.24: Pump-probe transients of the gain saturation and recovery for sample B with a 4.0-nm thick injection barrier (solid line) and sample C with a 4.6-nm thick injection barrier (dashed line). For better comparison we have subtracted the signals at negative delay times $t_D < -400$ fs. The arrows indicate the corresponding oscillation periods ν_B^{-1} and ν_C^{-1} (cf. Fig. 6.17).

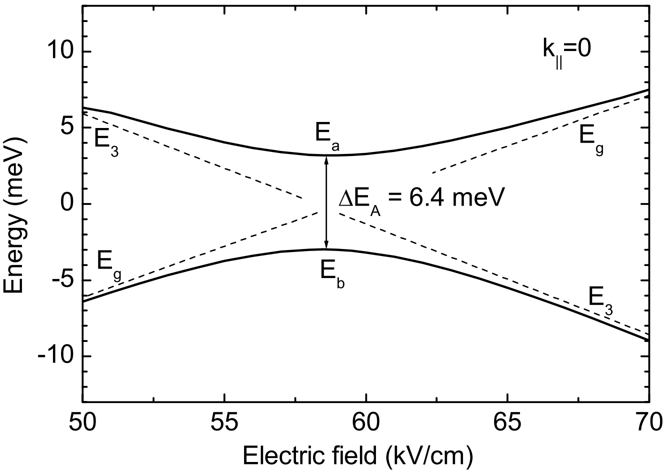

Figure 6.25: Calculated fan chart for the energies of the binding (E_b) and anti-binding (E_a) states of sample A_2 for $k_{||} = 0$. E_3 and E_g are the energies of the nonstationary states $|3\rangle$ and $|g\rangle$ without tunnel coupling.

After this qualitative discussion we will now present results from eight-band $\mathbf{k} \cdot \mathbf{p}$ bandstructure calculations [74]. With these calculations subband nonparabolicities are taken into account in a single particle picture. We have calculated the energy splitting ΔE_{ab} between the binding and the anti-binding states as a function of the applied electric field per period, in-plane momentum, and barrier width. For sample A_2 at $k_{||} = 0$ the energy splitting at resonance is $\Delta E_{ab}^A = 6.4$ meV [Fig. 6.25]. It is evident that ΔE_{ab} depends strongly on the bias. According to our calculations, at higher in-plane momenta we observe an increase of the energy splitting. For $k_{||} = k_{||}(30 \text{ meV})$ the energy splitting is increased by 15 % compared to the value at $k_{||} = 0$. For samples B and C bandstructure calculations yield an energy splitting at resonance ($k_{||} = 0$) of $\Delta E_{ab}^B = 8.3$ meV and $\Delta E_{ab}^C = 5.6$ meV, respectively. This behavior is qualitatively in good agreement with the experimental results.

Now we quantitatively analyze the oscillation frequencies and compare those with the bandstructure calculations. In Fig. 6.26 results for samples A_2, B, and C are shown. The spectra are obtained by the Fourier transforms of the transients. They clearly show maxima at the frequencies $\nu_A = 2.2$ THz, $\nu_B = 2.8$ THz, and $\nu_C = 2.1$ THz corresponding to an energy splitting of $\Delta E_{ab}^A = h\,\nu_A = 9.1$ meV, $\Delta E_{ab}^B = 11.6$ meV, and $\Delta E_{ab}^C = 8.7$ meV. Sample A_2 has a lower injection barrier (reduced Al content) than those of samples B and C, but it has a larger barrier width of $d_b = 6.2$ nm, resulting in an oscillation period similar to sample C.

Comparing these values with the results from the bandstructure calculations (see Table 6.3) we observe that the ratios of the oscillation frequencies $\nu_B/\nu_C = 1.4$ and $\nu_B/\nu_A = 1.3$ are in good agreement with the calculations which yield $\nu_B/\nu_C = 1.5$ and $\nu_B/\nu_A = 1.3$. The absolute numbers, however, are in all cases around 50 % larger than the theoretically predicted values.

The main reason for this is that the pump-probe signal [cf. Fig. 6.27 (a)] shows also strong oscillations before and around delay zero, i.e., for $t_D < 100$ fs. As already discussed in chapter 2, this time range is dominated by the perturbed free induction decay and pump-probe coupling contributions. Those oscillations are not caused by the a–b quantum coherence

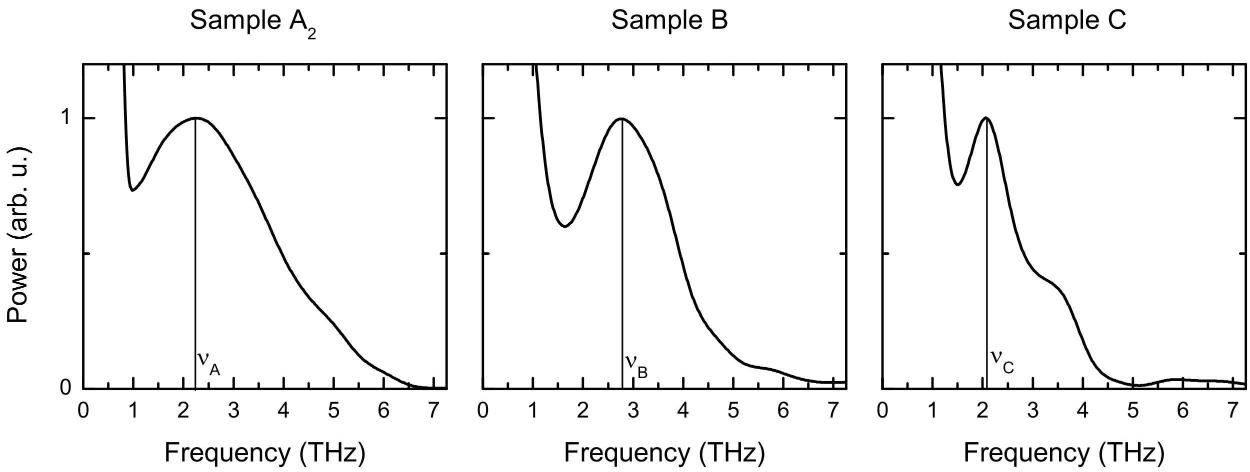

Figure 6.26: Power spectra of the transients measured for sample A_2 [cf. Fig. 6.9, I = 7 kA/cm^2], sample B [cf. Fig. 6.17 (a)], and sample C [cf. Fig. 6.17 (a)]. The spectra show a pronounced peak at $\nu_A = 2.2 \pm 0.1$ THz, $\nu_B = 2.8 \pm 0.1$ THz, and $\nu_C = 2.1 \pm 0.1$ THz, respectively.

Table 6.3: Structural parameters and experimentally and theoretically determined energy splittings for samples A_2, B, and C. The experimentally evaluated numbers designate the peak position of the Fourier transforms of the transients. The calculated numbers are gained from eight-band $\mathbf{k} \cdot \mathbf{p}$ bandstructure calculations [74].

Sample	Injection barrier width (nm)	Al-content	Experiment		Theory
			ν (THz)	ΔE_{ab} (meV)	ΔE_{ab} (meV)
A_2	6.2	33 %	2.2 ± 0.1	9.1 ± 0.5	6.4
B	4.0	45 %	2.8 ± 0.1	11.6 ± 0.5	8.3
C	4.6	45 %	2.1 ± 0.1	8.7 ± 0.5	5.6

but by detuning effects of λ_{det} relative to the center of the gain band. The transition from detuning oscillations for $t_D < 100$ fs to quantum beats for $t_D > 0$ leads to a pronounced chirp of the oscillation frequency. This chirp can be seen well in Fig. 6.27 (b) where the instantaneous frequency of the transient is plotted (circles). It is the time derivative of the phase of the complex extension of the transient[2]. For $t_D < 150$ fs oscillation frequencies are observed which are much higher than those at later times. For $t_D > 200$ fs the frequency is nearly stationary and the absolute value is in good agreement with the calculated one (solid line). This demonstrates that for a quantitative analysis of the quantum beat frequency the pump-probe signal should not be analyzed for $t_D < 100$ fs.

---

[2] The complex extension is obtained in the following way: First, the transient is Fourier transformed. Then the negative frequencies are cut off. The Fourier back-transform of this function is the complex extension of the transient.

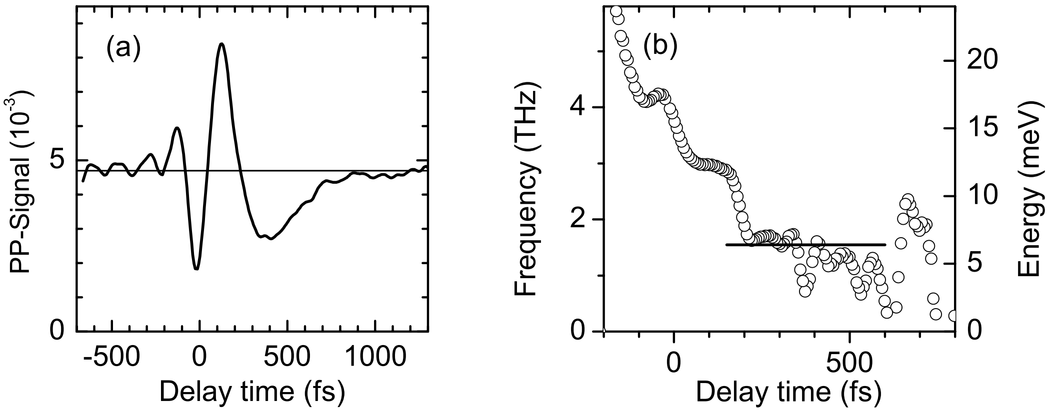

Figure 6.27: (a) Pump-probe signal measured for sample A_2 for $I = 7.0$ kA/cm^2 (cf. Fig. 6.9). (b) Time derivative of the phase, i.e., the instantaneous frequency, of the complex extension of the transient (circles). The solid line indicates the theoretically predicted oscillation frequency.

In the following we describe a method to analyze the data taking into account this point. As an example we evaluate the transient for $I = 7.0$ kA/cm^2 (cf. Fig. 6.9) measured for sample A_2 at $\lambda_{det} = 10.0\,\mu$m. The power spectrum obtained by Fourier transform is plotted as dashed line in Fig. 6.28 (a). First, with a Gaussian filter we separate the spectral components corresponding to the oscillatory part of the transient (solid line) from the low frequency part (dotted line). The filter is chosen so that the intersection of the solid line and the dotted line is at the same frequency as the local minimum of the dashed line. We will discuss the low frequency component later. The solid line in Fig. 6.28 (b) indicates the Fourier back-transform of this spectrum. In the next step we analyze the data only for $t_D > 100$ fs with the help of the Wigner function [23]

$$A(\omega, t) = \int d\tau\, e^{i\,\omega\,\tau}\, S^*(t + \tau/2)\, S(t - \tau/2)$$

where S is the complex extension of the time transient. The Wigner function is the Fourier transform of the autocorrelation signal $S^*(t + \tau/2) \cdot S(t - \tau/2)$. Its basic property is that its time integral is proportional to the spectral intensity of the transient and its frequency integral is proportional to the square of the envelope of the transient:

$$\begin{aligned} \int dt\, A(\omega, t) &\sim |\hat{S}(\omega)|^2 \\ \int d\omega\, A(\omega, t) &\sim |S(t)|^2 \end{aligned}$$

In Fig. 6.28 (c) the Wigner function is plotted as a function of time t_D and energy $\hbar\,\omega$. The pronounced time dependence of the frequency for $t_D < 200$ fs indicates a strong chirp as mentioned above. In order to cut out the frequency components occurring for $t_D < 100$ fs we integrate the Wigner function for $t_D > 100$ fs. The solid line in Fig. 6.28 (d) is the power spectrum generated in such a way. The dashed line indicates the full power spectrum obtained by the integration over the complete time range. Since the new spectrum does not contain the high frequency oscillations observed for $t_D < 100$ fs, a shift towards lower frequencies and a decrease of the width is observed.

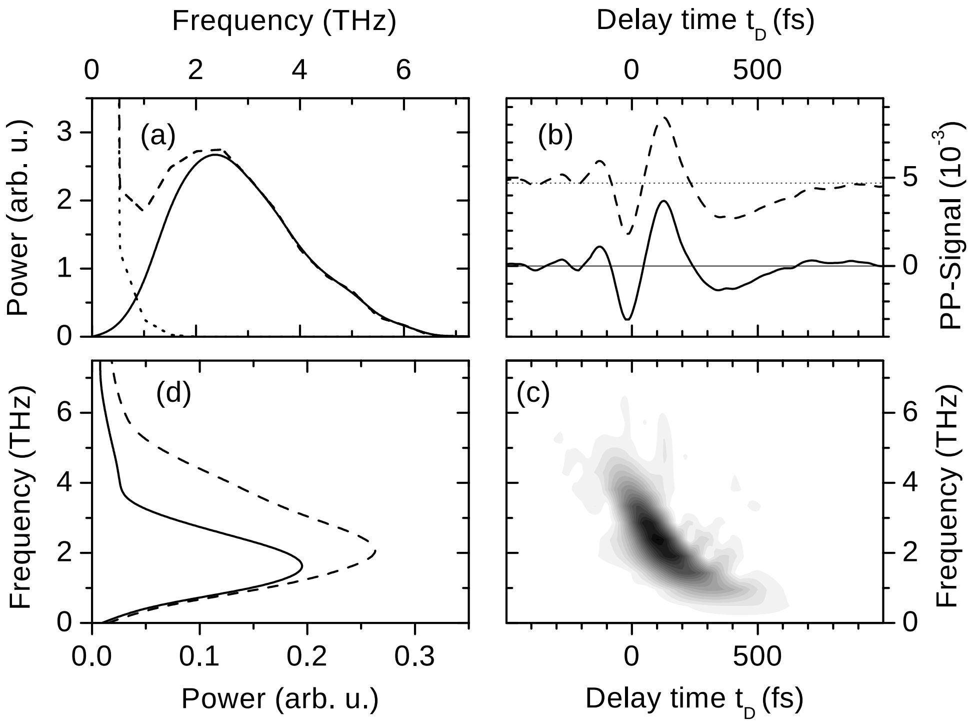

Figure 6.28: (a) Power spectrum of the time transient measured for sample A_2 for $I = 7.0$ kA/cm^2 (Fig. 6.9) at the center of the 3–2 laser transition ($\lambda_{det} = 10.0\,\mu$m). The full spectrum (dashed line) is the sum of a purely oscillatory part (solid line) and a low frequency part (dotted line). (b) The Fourier back-transformation of the oscillatory part of the spectrum (solid line) compared with the original time transient (dashed line). (c) Real part of the Wigner function $A(\omega, t) = \int d\tau\, e^{i\omega\tau}\, S^*(t + \tau/2)\, S(t - \tau/2)$. S is the complex extension of the transient indicated by the solid line in (b). (d) Power spectrum obtained by the time integration of the Wigner function over the full time range (solid line) and over $t_D > 100$ fs.

Table 6.4: Evaluated and calculated energy splitting for samples A$_2$, B, and C. The experimentally evaluated numbers are gained from an analysis using the Wigner function.

	Experiment		Theory
	ν (THz)	ΔE_{ab} (meV)	ΔE_{ab} (meV)
A$_2$	1.6 ± 0.1	6.6 ± 0.5	6.4
B	2.3 ± 0.1	9.5 ± 0.5	8.3
C	1.7 ± 0.1	6.9 ± 0.5	5.6

In Fig. 6.29 the power spectra of the transients of sample A$_2$, B, and C using this evaluation technique are plotted. The oscillation frequencies ν and the corresponding energy splittings ΔE_{ab} are plotted in Table 6.4. For comparison we have also plotted ΔE_{ab} gained from bandstructure calculations mentioned above. The value for sample A$_2$ is in good agreement with the theoretically predicted one. The evaluated energy splittings for samples

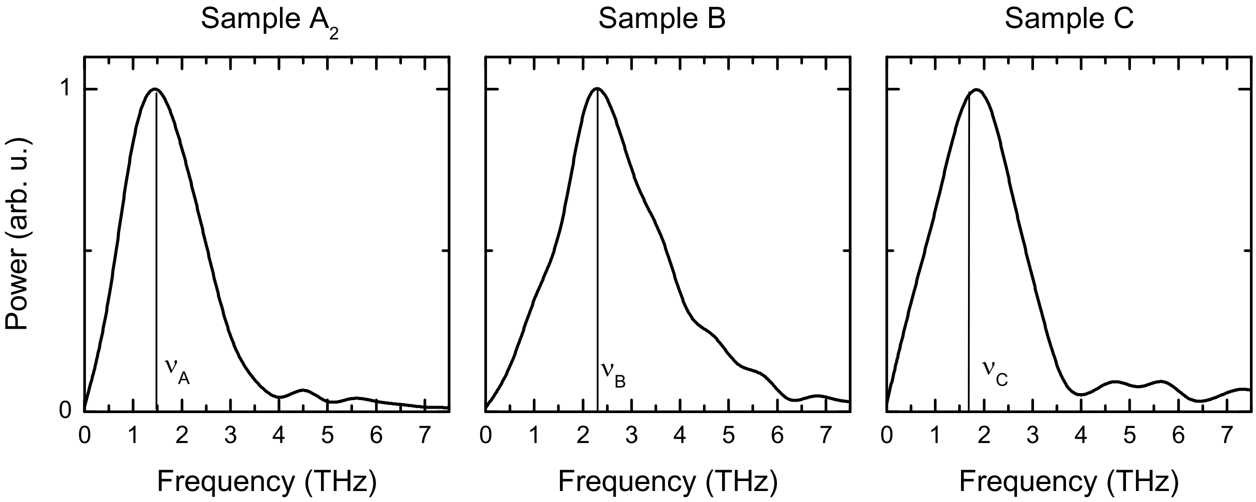

Figure 6.29: Power spectra evaluated for $t_C > 100$ fs with the help of the Wigner function. Sample A$_2$ [cf. Fig. 6.9, $I = 7$ kA/cm^2]: $\nu_A = 1.6 \pm 0.1$ THz, sample B [cf. Fig. 6.17 (a)]: $\nu_B = 2.3 \pm 0.1$ THz, sample C [cf. Fig. 6.17 (a)]: $\nu_C = 1.7 \pm 0.1$ THz.

B and C are approximately 20 % higher than the calculated ones.

Many-body effects For the comparison of the experimentally determined oscillation frequencies with these calculations it is important to note that the latter are based on a single particle picture. The effects of Coulomb interaction between the carriers, i.e., many-body effects, are neglected. A well known many-body effect which should be taken into account is the depolarization shift [75, 76]. The generation of a macroscopic electron wavepacket in the injector after pump depletion is inherently connected with a collective charge density oscillation. The concomitant Coulomb potential leads to an additional back-driving force resulting in a considerable shift of the oscillation frequency.

In the local density approximation [145, 146, 147] the depolarization shift E_{shift} can be simply calculated assuming parabolic subbands:

$$E_{shift} = \sqrt{\Delta E_{ab}^2 + E_{pl}^2} - \Delta E_{ab}$$

E_{pl} is a plasma energy given by

$$E_{pl}^2 = \frac{2\, e^2\, \Delta n_{ba}\, \Delta E_{ab}}{\epsilon_0\, \epsilon_r}\, S$$

where $\Delta n_{ba} = n_b - n_a$ is the difference of the electron densities in subbands b and a. S is the depolarization integral

$$S = \int_{-\infty}^{\infty} \left[\int_{-\infty}^{z} \zeta_a(z')\, \zeta_b(z')\, dz' \right]^2 dz$$

ζ_b and ζ_a are the wavefunctions of the states $|b\rangle$ and $|a\rangle$. Since the wavefunctions ζ_b and ζ_a are delocalized over many quantum wells [cf. Fig. 6.18 (b)] the depolarization integral is very large (2.2 nm). For the determination of the depolarization shift the exact difference

Δn_{ba} of the electron densities in b and a is important. This, however, is not exactly known. If $\Delta n_{ba} = 0$ then the depolarization shift vanishes. Assuming all carriers in b, i.e., $\Delta n_{ba} = n_s$ (total sheet density), results in a very large depolarization shift of $E_{shift} = 8$ meV. This large shift is a rather alarming feature since it is on the order of E_{ab}. Under typical working conditions in a quantum cascade laser, $\Delta n_{ba} \ll n_s$ and E_{shift} is somewhere in-between these two extreme cases. Hence, this simple estimation shows that we expect a depolarization shift towards higher frequencies as observed in our experiment. This strongly suggest that many-body effects should not be neglected in model calculations of electron transport in quantum cascade structures.

Current dependence In Fig. 6.30 the oscillation frequencies for different current densities are plotted. The evaluated transients are those of Fig. 6.9, measured for sample A_2. Only a minor dependence of the oscillation frequency on the current can be observed. A variation of the applied bias should strongly influence the energy splitting as can be seen in Fig. 6.25 (a). A possible explanation for the observed behavior is given by the VI-characteristics shown in Fig. 6.30 (b). For a current density exceeding 0.5 kA/cm^2 the characteristics is very flat, i.e., a further increase of the current results only in a weak increase of the voltage of the entire structure including the contact layers (solid line). Since this characteristics includes the voltage drop at the contact layers we assume that the VI-characteristics for the active region is even flatter. The dashed line in Fig. 6.30 (b) is a calculated VI-characteristics where a constant series resistance of 0.3 Ω—which is a realistic value [99]—for the contact layers is assumed. Thus, a change of the current yields only a minor difference of the voltage drop in the active region.

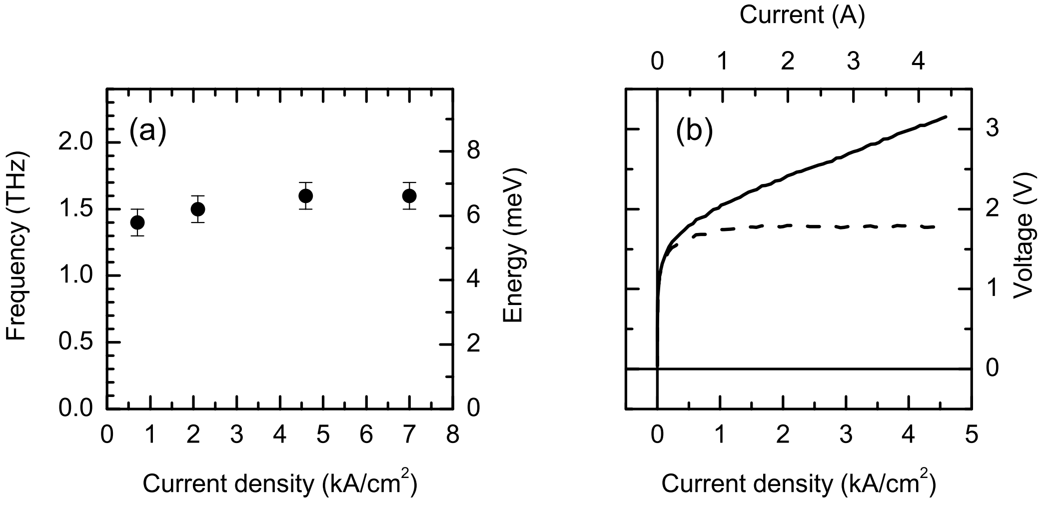

Figure 6.30: (a) Oscillation frequency as a function of the current density. Each value is gained from the power spectra evaluated for $t_C > 100$ fs with the help of the Wigner function. The analyzed transients are the ones shown in Fig. 6.9 ($\lambda_{det} = 10.0\,\mu$m). (b) VI-characteristics of sample A_2. The solid line indicates the measured VI-characteristics of the quantum cascade mesa including the contact layers [134]. The dashed line is the VI-characteristics of the active region which is calculated assuming a series resistance of 0.3 Ω for the contact layers.

So far, we have evaluated the oscillation with respect to the oscillation frequency. We have observed a pronounced peak in the power spectra obtained by Fourier transforms of the transients for all samples investigated. In a further evaluation of the spectra we used the Wigner function to cut off those frequencies occurring at delay times < 100 fs, where the data are superimposed by coherent artifacts. In this way we extract oscillation frequencies which are in good agreement with those from bandstructure calculations. This confirms the interpretation that the electron transport through the injection barrier of a quantum cascade laser can be described in terms of wavepacket oscillations via coherent resonant tunneling. A central question now is the degree of coherence of the electron transport. To answer this question, in the following we address the damping of the oscillation.

6.6.4 Damping of the oscillation

The fact that only one oscillation period is observed in the transients indicates strong damping. Now, we will analyze the damping quantitatively. Exemplarily we determine the decay time τ_{decay} of the oscillation observed in the pump-probe data measured for sample A_2 for an applied bias of $I = 7.0$ kA/cm^2 at a detection wavelength of $\lambda_{det} = 10.0\,\mu$m (cf. Fig. 6.13). In Fig. 6.31 we plot the oscillatory part (solid line) of the transient, which is separated from the original data by the method discussed in the previous section. The symbols indicate the envelope of the transient. An exponential decay with a decay time $\tau_{decay} = 200$ fs convoluted with the cross-correlation of the pump and probe pulses (dashed line in Fig. 6.31) fits the envelope of the transient quite well. We have applied this method also to other transients measured for samples A_2, B, and C at low temperatures. Here, we have found decay times in the range $\tau_{decay} = 200 - 300$ fs.

The envelope shows directly the decay of the macroscopic intersubband polarization P_{ba}. The decay of P_{ba} is determined by two mechanisms: (i) inhomogeneous broadening, i.e., the destructive interference between polarizations with different transition frequencies in

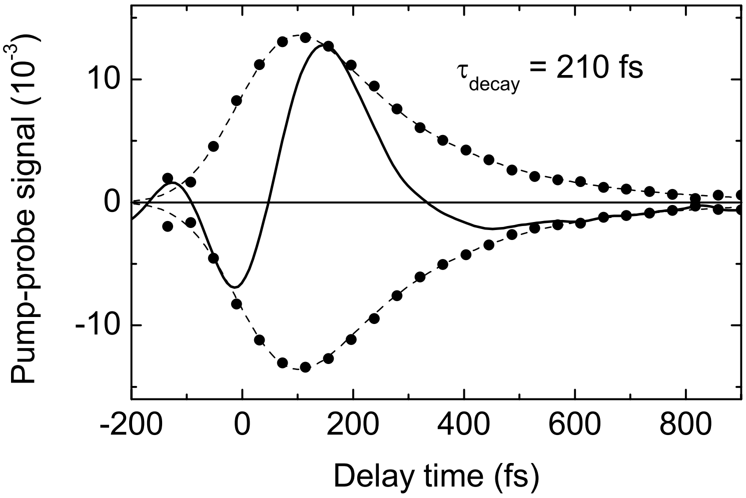

Figure 6.31: Envelope (symbols) of the transient (solid line) and fit curve (dashed line) with a rise time corresponding to the cross-correlation width of the pump and probe pulses (200 fs) and with an exponential decay of $\tau_{decay} = 210$ fs.

an inhomogeneously broadened ensemble and (ii) homogeneous broadening, i.e., the irreversible phase relaxation of the intersubband polarization due to scattering processes, e.g., electron-phonon, electron-electron, and electron-impurity scattering. With our experimental technique we can not directly distinguish between homogeneous and inhomogeneous broadening. However, our data set gives some indication for the relevance of the various dephasing mechanisms. This will be analyzed in the following.

(i) Inhomogeneous broadening There are several mechanisms of inhomogeneous broadening in quantum cascade structures. The influence of structural inhomogeneities like alloy disorder and monolayer fluctuations can be estimated directly from our experiments. We have seen that the oscillation frequency for sample B is 50 % higher than the oscillation frequency for sample C. The two samples are identical except for the barrier width, which differs by only two monolayers (see Table 6.3). It is evident that we can expect a large inhomogeneous contribution in our signal from barrier width fluctuations, since even in state of the art devices fluctuations of at least one monolayer are unavoidable.

The oscillation frequency observed for sample A_2 is in-between the oscillation frequencies of samples B and C though the barrier width of A_2 is more than 30 % bigger than for the latter. This can be explained by the different aluminum content (33 % for sample A_2, 45 % for sample C), which results in a different barrier height. This clearly demonstrates that statistical alloy disorder, which is unavoidable in the growth process, accounts for a non-negligible inhomogeneous broadening in our pump-probe signal.

Besides these structural inhomogeneities, there is inhomogeneous broadening even in a perfect structure. The reason for this is the in-plane momentum dependence of ΔE_{ab} due to the nonparabolic subband dispersion as can be determined from $\mathbf{k} \cdot \mathbf{p}$ bandstructure calculations.

From these considerations we conclude that inhomogeneous broadening plays an important role for the decay of the macroscopic intersubband polarization P_{ab}.

(ii) Homogeneous broadening As discussed in chapter 2, in the simplest approach homogeneous broadening is described by the dephasing time T_2. For a comparison between T_2 and the experimentally observed decay time τ_{decay} we have to take into account that the latter includes both, homogeneous and inhomogeneous broadening. However, T_2 can not be shorter than τ_{decay}, i.e.,

$$T_2 > \tau_{decay} = (250 \pm 50)\,\text{fs} \quad , \quad \frac{1}{T_2} < (0.4 \pm 0.1) \times 10^{13}\,\text{s}^{-1}$$

We are now able to determine the degree of coherence of the underlying electron transport. According to the definition discussed in section 3.3 electron transport is coherent if the dephasing rate is smaller than the angular frequency of the oscillation, i.e., $1/T_2 < \omega_{osc} = 2\,\pi/\nu_{osc}$. For the samples investigated we get

$$\omega_{osc} = 2\,\pi \times 1.6\,\text{THz} = (1.0 \pm 0.1) \times 10^{13}\,\frac{1}{\text{s}} > \frac{1}{T_2}$$

This demonstrates that electron transport in quantum cascade structures is coherent according to the definition given above.

The lower limit of (200 ± 50) fs for T_2 rules out sub-100 fs dephasing times as claimed in Ref. [113]. Such a dephasing time was extracted from the electroluminescence width. We want to mention again that the electroluminescence width is determined by the dephasing of polarizations between the upper and lower laser states. Additionally it is broadened by structural inhomogeneities. a–b intersubband dephasing is irrelevant. Hence, it is evident that the dephasing time T_2 cannot be determined by the electroluminescence width. This explains also the question why there is no doublet structure observed in the electroluminescence spectrum resulting from b–2 and a–2 transitions [Fig. 6.21]. For sample A_2 the oscillation frequency is $\nu_{osc} = 1.6\ \mathrm{s}^{-1}$ corresponding to an energy splitting of $\Delta E_{ab} = 6.4$ meV. The strong broadening of the electroluminescence spectrum ($FWHM = 13$ meV) smears out such a line structure.

6.6.4.1 Scattering processes

An irreversible phase loss of coherent superpositions of states $|b\rangle$ and $|a\rangle$ leads to homogeneous broadening. Now we want to discuss various possible scattering mechanisms contributing to homogeneous broadening and their relevance for the transport processes observed in our femtosecond experiment.

In general one can distinguish between two different kinds of scattering processes, namely *inter*subband and *intra*subband scattering as schematically shown in Fig. 6.32 (a). Intrasubband scattering corresponds to transitions of electrons between two states within the same subband [A in Fig. 6.32 (a)] whereas intersubband scattering represents a transition between different subbands [B in Fig. 6.32 (a)]. There are a number of different scattering mechanisms relevant in quantum cascade structures. The most important ones are electron-electron, electron-LO phonon, and electron-impurity scattering.

Electron-impurity scattering The ionized donors in the injector region of the quantum cascade structure provide Coulomb potentials which can act as scattering centers for the electrons. Since the impurities are immobile such scattering events are elastic, i.e., there is no energy exchange. Nevertheless, those lead to momentum relaxation as depicted in Fig. 6.32 (b). Because of the small wavefunction overlap, *inter*subband electron-impurity scattering is very weak. Hence, this scattering mechanism leads mainly to *intra*subband momentum relaxation.

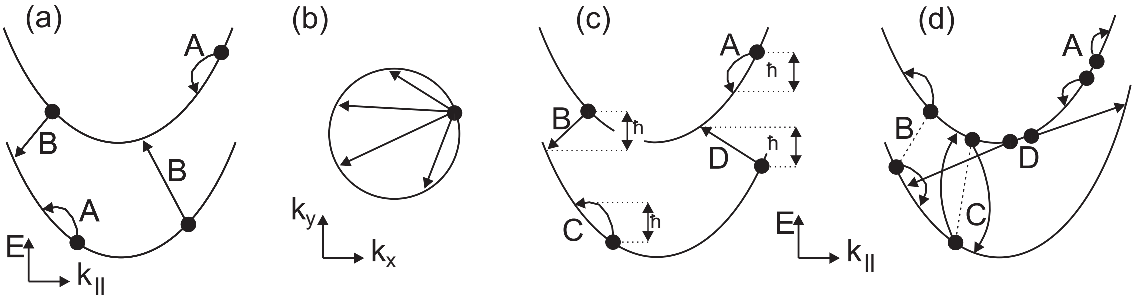

Figure 6.32: (a) Schematics of *inter*subband (A) and *intra*subband (B) scattering. (b) Electron-impurity scattering is an elastic scattering mechanism, i.e., there is only momentum but no energy relaxation. (c) Electron-LO phonon scattering leads to intraband transitions (A and C) or intersubband transitions (B and D). (d) Various Coulomb scattering processes between two electrons.

Electron-LO phonon scattering An important scattering mechanism is the scattering of electrons with LO phonons. Here, energy and momentum are exchanged. Due to the small energy dispersion, LO phonons have a nearly k-independent energy of $\hbar\omega_{LO} = 36$ meV in GaAs. Scattering between a LO phonon and an electron leads to the exchange of the energy $\hbar\omega_{LO}$. Both inter- and intrasubband scattering are possible as shown in Fig. 6.32 (c). Two different scattering processes can be distinguished, LO phonon emission [A and B in Fig. 6.32 (c)] and LO phonon absorption [C and D in Fig. 6.32 (c)]. The scattering rate for LO phonon emission is proportional to $1 + n_{LO}(T_L)$, where

$$n_{LO}(T_L) = \frac{1}{\exp\left(\frac{\hbar\omega_{LO}}{k_B T_L}\right) - 1}$$

is the thermal LO phonon population determined by the Bose distribution. The LO phonon absorption rate is proportional to $n_{LO}(T_L)$. Electrons being at least $\hbar\omega_{LO}$ above the respective subband minimum can spontaneously emit a LO phonon with a rate of 10^{13} s^{-1} [148, 81, 4].

LO phonon scattering is the dominant energy exchange process between the electron gas and the lattice.

Electron-electron scattering The Coulomb interaction causes scattering among the electrons. It is strongly modified by screening in the presence of other mobile charges in the electron gas. Scattering events among the electrons are accompanied by momentum and energy exchange. Electron-electron scattering is the dominant mechanism for thermalization within a single subband and between different subbands. Since the Coulomb interaction is a long-range interaction the electron gas represents a complicated, coupled many-body system. In the simplest approximation, electron-electron scattering is described in terms of independent two-electron interactions. In this approximation the possible inter- and intrasubband processes are depicted in Fig. 6.32 (d) [149]. (A) There are pure intrasubband processes where the interactions and the transitions occur within a single subband. This is the dominant process for intrasubband thermalization. (B) Interaction between two electrons, each in a different subband, can exchange energy and in-plane momentum while staying within the respective subbands after the interaction. (C) There are scattering processes where two electrons are initially in different subbands, and then exchange subbands. Processes B and C lead to thermalization *among* two subbands. (D) Finally, there are interactions where two electrons are initially in the same subband, but both move to another subband after the interaction.

However, this simple picture of electron-electron scattering via two-electron interaction is an approximation and an exact theoretical modelling requires a full quantum kinetic description including full dynamic screening [150, 151, 152]. This is still an unsolved problem for quasi-two dimensional electron plasmas.

Scattering in quantum cascade structures After this general consideration we will now discuss the relevance of the various scattering processes in quantum cascade structures as found in literature and compare these results with our experiment.

In Ref. [124] Harrison has carried out detailed calculations for electron-electron and electron-LO phonon scattering rates in quantum cascade structures using an approach based on Fermi's golden rule. According to these calculations intersubband scattering rates via

LO phonon emission are on the order of 10^{11} s^{-1} rising to 3×10^{12} s^{-1} between the strongly coupled subbands 2 and 1. At the same time the electron-electron intersubband rates are on the order of $10^9 - 10^{10}$ s^{-1}. From this he claims that in quantum cascade structures *inter*subband scattering is dominated by LO phonon scattering. *Intra*subband scattering is dominated by electron-electron scattering, for which rates greater than 5×10^{13} s^{-1} were calculated. He concludes that these high scattering rates drive the system towards a thermalized electron distribution in each subband having the same electron temperature for all subbands. In these calculations the author has assumed a priori that the electron temperature is the same as the lattice temperature which was assumed to be 77 K. We want to emphasize that the temperature is a critical parameter for the various scattering mechanisms and that its determination is an important task.

The question of the relation between the lattice and carrier temperature was addressed by Iotti and Rossi [126]. The authors carried out Monte Carlo simulations taking into account electron-LO phonon and electron-electron scattering via two-electron interaction in a semiclassical approach. They confirmed the result of Harrison [124] that there is a thermalized electron distribution in each of the subbands and that the temperature is the same for all subbands. Assuming a lattice temperature of $T_L = 77\ K$ they calculated an electron temperature of $T_C = 600 - 700$ K.

However, a simple estimation suggests that this carrier temperature is too high: We assume a Boltzmann distribution for the electrons and an intrasubband electron-LO phonon scattering rate of $R_{LO} = 10^{13}$ s^{-1} [4]. Taking into account LO phonon emission *and* absorption according to the LO phonon population $n_{LO}(T_L)$ the carrier temperature T_C as a function of the current density I and lattice temperature T_L reads

$$T_C(I, T_L) = \frac{-\hbar\,\omega_{LO}}{k_B\,\ln\left(\frac{\frac{I\,U(I)}{N\,\hbar\,\omega_{LO}\,R_{LO}} + n_{LO}(T_L)}{n_{LO}(T_L)+1}\right)}$$

where N is the total 2-dimensional carrier density in the structure ($N = 4 \times 10^{11}$ cm^{-2}). In Fig. 6.33 the carrier temperature is plotted as a function of current density for various lattice temperatures. The carrier temperature increases more or less linearly with the current. For a lattice temperature of $T_L = 10$ K the carrier temperature is $T_C = 180$ K at $I = 7$ kA/cm^2 [Fig. 6.33, dashed line]. The carrier temperature is not essentially higher for $T_L = 100$ K [Fig. 6.33, dotted line]. This estimation demonstrates that we can assume a carrier temperature on the order of $T_C = 200$ K at low lattice temperatures. It increases linearly with higher lattice temperatures. The solid line in Fig. 6.33 indicates the carrier temperature for a lattice temperature of $T_L = 300$ K. At $I = 7$ kA/cm^2 we observe a carrier temperature on the order of $T_C = 400$ K. With a simple estimation we can also calculate the temperature increase after pump depletion. In the time-resolved experiment, the pump pulse promotes electrons into the lower subbands of the active region. These subbands are energetically around $\Delta E_{2g} = 120$ meV above the subbands a and b [cf. Fig. 6.18 (b)]. Due to the strong carrier-carrier scattering with rates $> 10^{13}$ s^{-1} we can assume that the electron gas is thermalized within $t_D = 400$ fs. Using the estimation carried out in section 6.6.1 the electron density in the upper laser subband 3 is around 10 % of the total carrier density n_{tot}. We have seen that a pump pulse with an energy of 7.5 nJ saturates the gain completely. Thus, the number of de-excited electrons is $n_{ex} = 0.1\,n_{tot}$. Assuming no energy relaxation from the electron gas to the lattice, the additional energy input due to these electrons reads $E_{add} = \Delta E_{2g}\,n_{ex}$. With these consideration we can estimate the carrier temperature increase

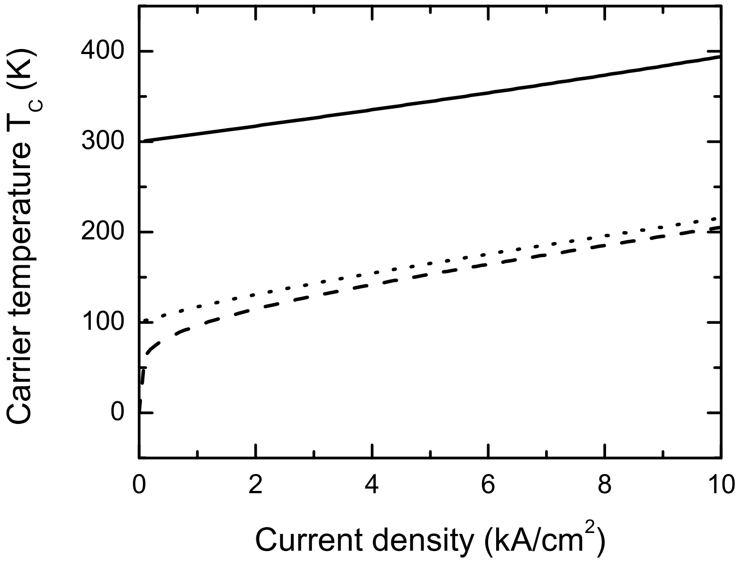

Figure 6.33: Carrier temperature T_C as a function of current density for various lattice temperatures T_L. The solid line indicates a lattice temperature of $T_L = 300$ K, the dotted line indicates $T_L = 100$ K, and the dashed line $T_L = 10$ K.

after pump depletion. For $E_{pump} = 7.5$ nJ and $T_L = 10$ K the carrier temperature increases from $T_C = 180$ K to $T_C = 300$ K.

Now we discuss the relevance of the various scattering mechanisms for the electron transport. In quantum Monte Carlo simulations taking into account electron-LO phonon scattering but neglecting electron-electron scattering Iotti and Rossi studied the dynamics of electron wavepacket dynamics in quantum cascade laser structures [128]. At $t = 0$ they prepared the system fully localized in the lowest injector subband. As time evolves, they observed wavepacket oscillations between the injector and the upper laser subband decaying on a time scale of several picoseconds. This dephasing time is an order of magnitude larger than the decay time observed in our experiment. Obviously, the reason for this is the neglect of electron-electron scattering in the calculations. The same authors also presented simulations including electron-electron scattering but using a semi-classical Monte Carlo approach. From these calculations they concluded that energy-relaxation and dephasing processes are strong enough to destroy *any* phase-coherence effect on a sub-picosecond time scale [128].

The rather high electron-electron scattering rate of $> 5\times10^{13}$ s^{-1} obtained from those theoretical calculations are much larger than the homogeneous dephasing rate $1/T_2 < 5\times10^{12}$ s^{-1} determined from our experiment. Obviously, only a fraction of scattering events leads to dephasing of the coherent superposition of states $|a\rangle$ and $|b\rangle$. This is in contrast to predictions of Fermi's Golden Rule, which assumes that particles are scattered into eigenstates of the unperturbed Hamiltonian. On short time scales, however, quantum mechanics allows also coherent superpositions of such final states, a concept known as scattering-induced coherence [153, 154].

6.6.4.2 Scattering-induced coherence

Qualitatively, the phenomenon of scattering-induced coherence can be understood in the following way. The coupling among electronic states in the injector, e.g., due to electron-electron or electron-phonon interaction, is much stronger than the coupling of states localized in the injector with states localized in the active region because of the small spatial overlap between them. Hence, at scattering rates higher than $1/T_{osc}$, electrons are mainly redistributed between states localized in the injector. The coherent superposition $|g\rangle$ of the electronic eigenstates $|a\rangle$ and $|b\rangle$ (Fig. 6.22) is among such localized states. As a result, scattering events populating $|g\rangle$ on a time scale much faster than T_{osc} generate a coherent excitation which is in phase with the oscillation induced by the pump pulse. Such an intraband coherence after energy relaxation was previously observed for Bloch oscillations at much lower electron densities [155].

The gain overshoot observed at half the oscillation period [Figs. 6.23 (c) and 6.24] gives additional evidence for scattering-induced coherence. Right after the gain depletion, electrons in subband g tunnel from the injector into the active region. This nonequilibrium depletion in subband g recovers on a time scale faster than the oscillation period, allowing for additional electrons to contribute in phase to the oscillatory gain, which is temporarily much higher than in the quasi-stationary equilibrium.

A general quantum kinetic theory for semiconductor nanostructures taking into account electron-phonon and electron-electron interaction has been presented in Ref. [156]. The application of this theory to quantum cascade structures with their elevated carrier densities, however, is very elaborate and has not yet been done so far. Nevertheless, quantum calculations including only electron-LO phonon scattering have been carried out by Iotti and Rossi [128]. In these calculations pronounced gain oscillations were observed pointing also to the phenomenon of scattering-induced coherence.

To demonstrate the physical concept of scattering induced coherence in appendix E we present a simple model calculation. A situation is considered, where an electron in a higher injector subband is scattered into subbands a and b due to the coupling with a third particle. As a model coupling mechanism we use electron-LO phonon coupling via the Fröhlich interaction. The main result of this calculation is that scattering-induced coherence increases the coherence of the electron transport from the injector into the active region.

It is important to note, however, that in quantum cascade structures electron-electron scattering is the dominant scattering mechanism owing to the high electron density. Hence, to correctly account for scattering-induced coherence a full quantum calculation including Coulomb scattering among the electrons is needed. Such calculations, however, are still missing and pose a challenging task for the future [157].

6.6.5 Resonant versus non-resonant tunneling

So far, we have considered exclusively the case of resonant tunneling. In this case the subbands g and 3 are iso-energetic. If there is an energy detuning $\hbar\,\Delta_{g3} \neq 0$ of subbands g and 3 we are out of resonance and non-resonant tunneling becomes important [Fig. 6.34 (a)]. In the following, we want to present a generalized picture containing both resonant- and non-resonant tunneling and discuss their relevance as observed in our data.

The starting point is the tight binding approximation using the states $|g\rangle$ and $|3\rangle$ localized in the injector and the active region, respectively. Here, both the tunnel coupling through

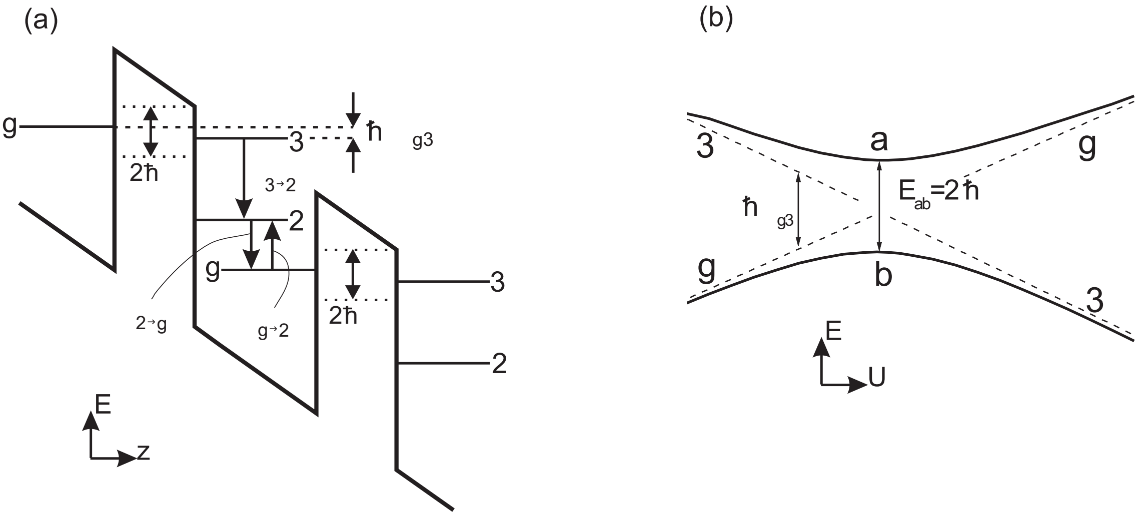

Figure 6.34: (a) Bandstructure and subbands considered in the model discussed in the text. $\hbar\,\Delta_{g3}$ is the detuning from resonance and $2\,\hbar\,\Omega$ is the tunnel coupling. (b) Schematics of the fan chart for subbands a, b, g, and 3.

the injection barrier $2\,\hbar\,\Omega$ ($= \Delta E_{ab}$ in resonance [Fig. 6.34 (b)]) and the scattering processes leading to dephasing of the coherent intersubband polarization P_{g3} are treated on the same level in terms of perturbations of the electronic Hamiltonian. This approximation is quite reasonable in our case since Ω and the dephasing rate $1/T_2$ are on the same order of magnitude as shown section 6.6.4. Kazarinov and Suris used the tight-binding approximation to derive a relation between current and voltage in quantum cascade structures [98, 127].

The underlying equations of motion for the dynamics of the coherent polarization P_{g3} and the populations n_2, n_3, and n_g in subbands 2, 3, and g are the following:

$$\begin{aligned}
\dot{P}_{g3} &= i\,\Delta_{g3}\,P_{g3} - \frac{P_{g3}}{T_2} + \Omega\,(n_g - n_3) \\
\dot{n}_3 &= -\Gamma_{3\to 2}\,n_3 + 2\,\Omega\,\mathrm{Re}(P_{g3}) \\
\dot{n}_g &= -\Gamma_{g\to 2}\,n_g + \Gamma_{2\to g}\,n_2 - 2\,\Omega\,\mathrm{Re}(P_{g3}) \\
\dot{n}_2 &= -\Gamma_{2\to g}\,n_2 + \Gamma_{3\to 2}\,n_3 + \Gamma_{g\to 2}\,n_g
\end{aligned}$$

$\Gamma_{3\to 2}$, $\Gamma_{2\to g}$, and $\Gamma_{g\to 2}$ are the in- and out-scattering rates of subband 2, which serves as an electron reservoir [Fig. 6.34 (a)]. We want to mention that in the quasi-stationary equilibrium ($\dot{n}_g = \dot{n}_3 = \dot{n}_2 = 0$) these equations yield the quasi-stationary current [Eq. (3.3)] derived in [98, 127]. To illustrate the difference between resonant and non-resonant tunneling, in Fig. 6.35 we present the results of calculations for the dynamics of the populations $n_g(t)$ and $n_3(t)$ in subbands g and 3. For simplification we neglect in- and out-scattering from/to subband 2, i.e., $\Gamma_{3\to 2} = \Gamma_{2\to g} = \Gamma_{g\to 2} = 0$. As starting condition we prepare all electrons to populate subband g. We consider two extreme cases, the case of exact resonance $\Delta_{g3} = 0$ and the case of strong detuning ($\Delta_{g3} \gg \Omega$). A tunnel coupling similar to the one of sample A_2 is assumed, i.e., $2\,\hbar\,\Omega = 6.4$ meV.

The case of zero detuning from resonance $\Delta_{g3} = 0$ is shown in Fig. 6.35 (a). The solid lines indicate the populations in subbands g and 3 for a relatively small dephasing

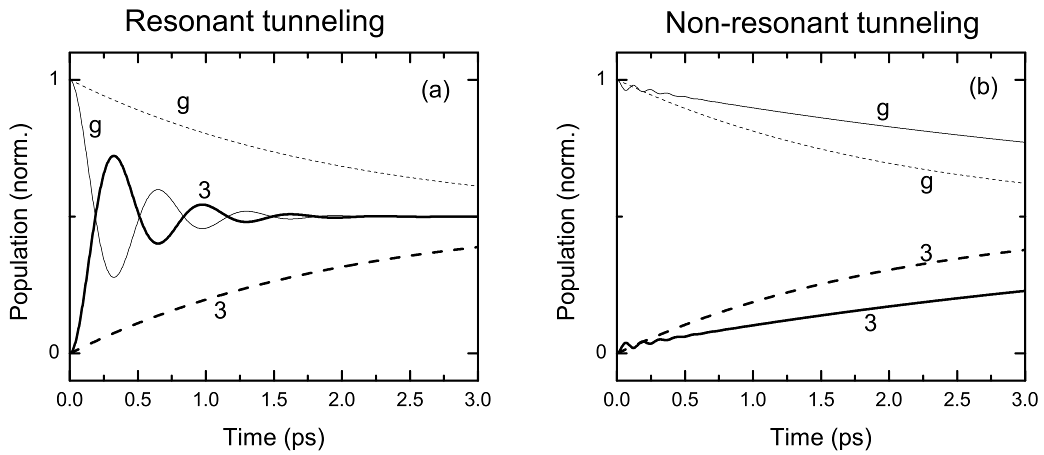

Figure 6.35: Calculated population in subbands g and 3 for the initial condition that all carriers are in subband g. A tunnel coupling similar to the one of sample A$_2$ ($2\hbar\Omega$ = 6.4 meV) is assumed. (a) Resonant case, i.e., $\Delta_{g3} = 0$. The solid lines indicate the coherent regime for a small dephasing rate $1/T_2 = \Omega$ whereas the dashed lines designate the fully incoherent regime for a very large dephasing rate $1/T_2 = 40 \cdot \Omega$. (b) Strongly nonresonant case, i.e., $\Delta_{g3} = 10 \cdot \Omega$. Again, the solid lines indicate the coherent regime for a small dephasing rate $1/T_2 = \Omega$ whereas the dashed lines designate the incoherent regime for a very large dephasing rate $1/T_2 = 40 \cdot \Omega$.

rate $1/T_2 = \Omega$. This case is similar to our experiment. We observe a pronounced coherent oscillation between the populations in g and 3. This coherence decays with the dephasing time T_2. At later times ($t > 2$ ps) the system is in equilibrium, i.e., equal population in g and 3. The dashed lines in Fig. 6.35 (a) show the case of a very large dephasing rate $1/T_2 = 40 \cdot \Omega$. Here, no oscillations are observed and the populations exponentially relax towards equilibrium on a much longer time scale. This represents the case of fully incoherent resonant tunneling, i.e., strongly damped P_{g3}. It is evident that dephasing is counterproductive in the case of resonant tunneling.

In Fig. 6.35 (b) a situation with strong detuning ($\Delta_{g3} = 10 \cdot \Omega$) is depicted. The case of a small dephasing rate $1/T_2 = \Omega$ (solid lines) and a large dephasing rate $1/T_2 = 40 \cdot \Omega$ (dashed lines) is shown. The dephasing rates are chosen to be equivalent to those of the respective curves in (a). The transport from g into 3 shows an exponential behavior in both cases. It is always slower than in the resonant case. For a small dephasing rate, we observe oscillations at early times indicating small coherence in the transport. These oscillations completely vanish for very large dephasing rates. We see that the transport via non-resonant tunneling is faster for larger dephasing rates. In contrast to the resonant case, here, strong dephasing leads to a larger tunnel current.

The transport from subband g into subband 3 via non-resonant tunneling is dominated by scattering-assisted tunneling [121] from g into 3 as depicted schematically in Fig. 6.36: It can be understood as tunneling into a virtual state followed by momentum relaxation within subband 3 [Fig. 6.36 (a)-(c)]. Momentum relaxation is necessary for the transport since subbands g and 3 are not isoenergetic. It is clear that nonresonant tunneling is faster for higher scattering rates in contrast to the resonant case and that transport via scattering-assisted tunneling is completely incoherent.

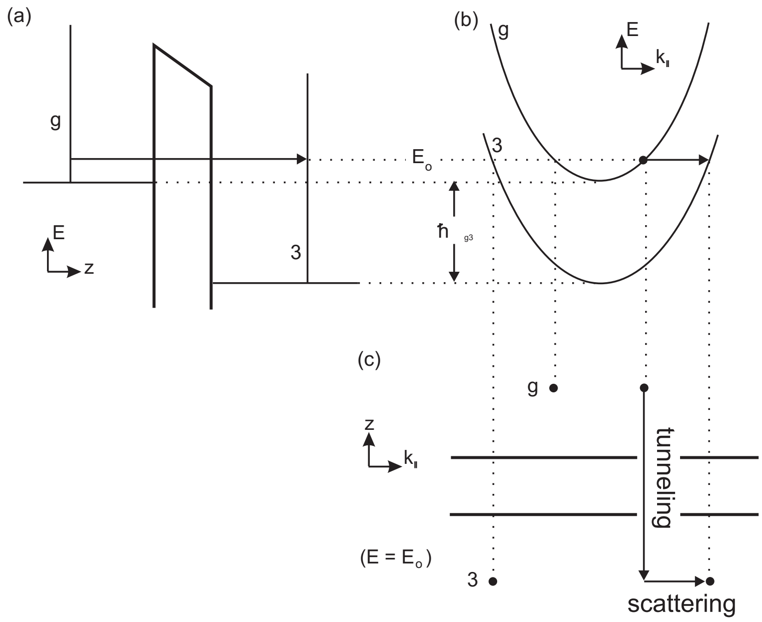

Figure 6.36: Scattering-assisted tunneling consists of two coupled processes, (a) iso-energetic tunneling from subband g through the barrier into a virtual state in the active region and (b) momentum relaxation with the dephasing rate $\Gamma = 1/T_2$ into a real state in subband 3. The combination of both processes in the $E = E_0$ plane (topview) is depicted in (c).

In conclusion it is evident that the most efficient transport from the injector into the active region occurs via coherent resonant tunneling.

Now we apply the picture of coherent/incoherent resonant and non-resonant tunneling to our experimental data. The pronounced oscillation observed for $t_D < 400$ fs, which is due to coherent resonant tunneling as discussed above, is followed by a non-oscillatory, exponential recovery at later times (cf. Fig. 6.20). In the following we want to investigate this exponential recovery in more detail. In Fig. 6.37 we compare data for different pump pulse energies, temperatures, and currents. We observe that for an increased pump pulse intensity [Fig. 6.37 (a) and (b)] the oscillation amplitude decreases and the exponential gain recovery increases at later times ($t_D > 400$ fs). The same behavior is observed for an increase of the nominal lattice temperature [Fig. 6.37 (c) and (d)] and an increase of the current [Fig. 6.37 (e) and (f)]. This behavior can be explained by the interplay between coherent/incoherent resonant and non-resonant tunneling. An increase of the pump pulse energy, the lattice temperature, or the current leads to an increase of the carrier temperature T_C. Since the various scattering processes are temperature dependent this results in an increased scattering rate leading to higher dephasing. Consequently, the degree of coherence of the transport decreases and incoherent resonant tunneling becomes more important, which explains the decrease of the oscillation amplitude. An increased carrier temperature additionally causes a higher population in the upper injector subbands [cf. Fig. 6.38]. Those carriers can only contribute via nonresonant tunneling. Both incoherent resonant tunneling and nonresonant tunneling lead to an exponential gain recovery as observed in our data for $t_D > 400$ fs.

In conclusion, for an increase of the carrier and lattice temperature the transport through the injection barrier becomes less efficient since the degree of coherent resonant tunneling

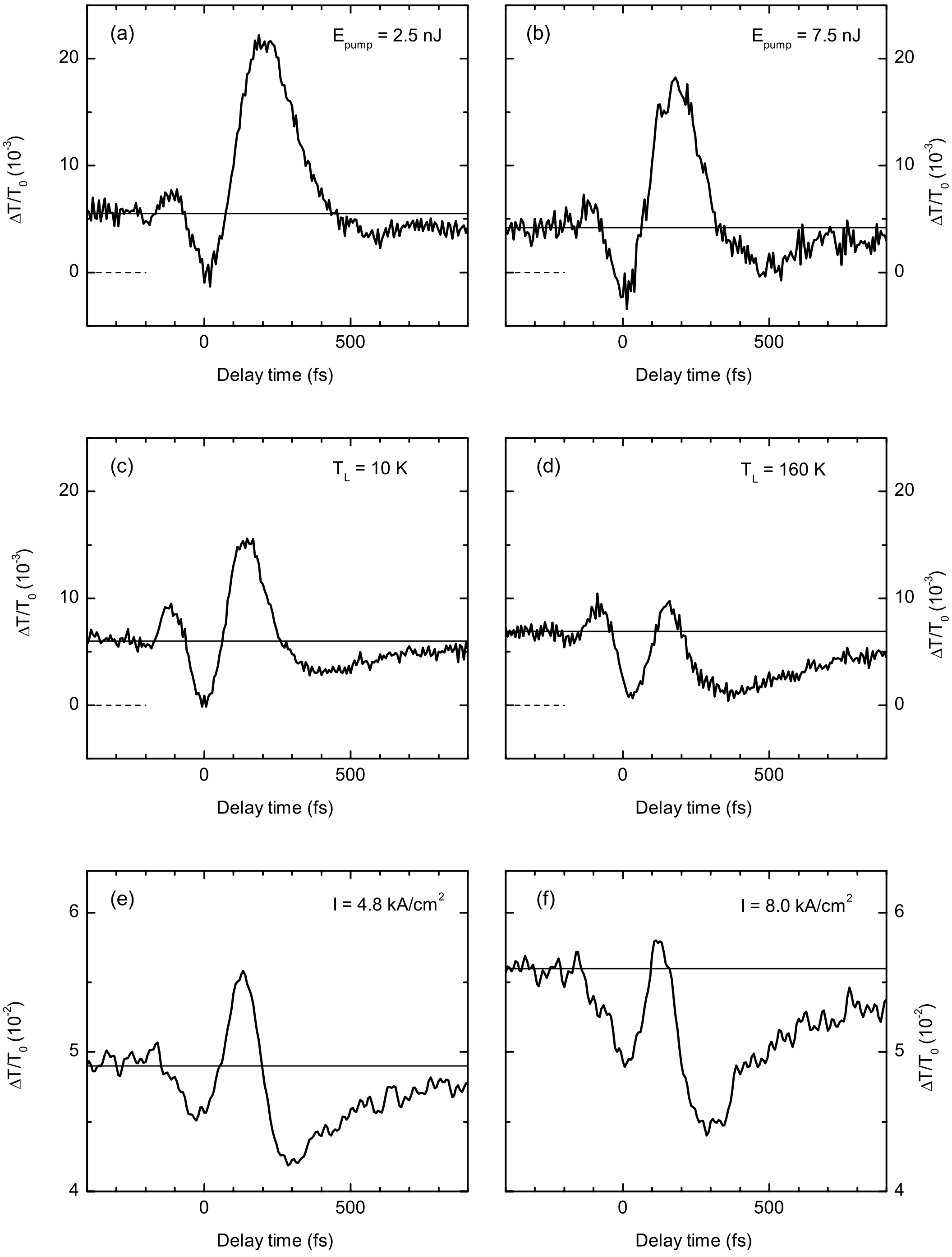

Figure 6.37: Pump-probe signal measured for sample A$_2$ for (a) $\lambda_{det} = 10.5\,\mu$m, $I = 4.6$ kA/cm^2, $E_{pump} = 2.5$ nJ, $T_L = 10$ K (cf. Fig. 6.10), (b) $\lambda_{det} = 10.5\,\mu$m, $I = 4.6$ kA/cm^2, $E_{pump} = 7.5$ nJ, $T_L = 10$ K (cf. Fig. 6.10), (c) $\lambda_{det} = 10.0\,\mu$m, $I = 7$ kA/cm^2, $E_{pump} = 7.5$ nJ (cf. Fig. 6.15), (d) $\lambda_{det} = 10.0\,\mu$m, $I = 7$ kA/cm^2, $E_{pump} = 7.5$ nJ (cf. Fig. 6.15). Pump-probe data measured for sample B for (e) $\lambda_{det} = 9.0\,\mu$m, $I = 4.6$ kA/cm^2, $E_{pump} = 750$ pJ, $T_L = 150$ K (cf. Fig. 6.16) and (f) $\lambda_{det} = 9.0\,\mu$m, $I = 8.0$ kA/cm^2, $E_{pump} = 750$ pJ, $T_L = 150$ K (cf. Fig. 6.16).

decreases for the benefit of incoherent resonant and nonresonant tunneling. Concomitantly, the refill of the upper laser subband is reduced leading to a lower gain.

The data measured for sample A_2 for various current densities (cf. Figs. 6.9 and 6.13) do not show such a pronounced increase of the exponential gain recovery with increasing current. For current densities $I > 2$ kA/cm^2 we observe no significant change in the shape of the transients. This can be ascribed to the leakage current occurring at these current densities in sample A_2. At current densities exceeding 2 kA/cm^2 the electron gas is heated and a considerable portion of the current is due to thermal activation into the continuum [105, 158]. Leakage current is strongly reduced in sample B due to the higher barriers. Hence, for this samples we observe a pronounced current dependent dynamics of the transmission change [cf. Fig. 6.37 (e,f)].

Strong heating The temperature dependent pump-probe signal (Fig. 6.15) shows a decreasing stationary gain for nominal lattice temperatures above $T_L = 200$ K. There are several possible contributions for this behavior:

- As discussed above, an increase of the lattice and carrier temperatures leads to a degradation of the injection efficiency due to incoherent resonant and nonresonant tunneling and due to thermal activation of electrons into continuum levels.
- An increased carrier temperature is connected with a redistribution of the population between the various injector subbands, i.e., a decrease of the population in subbands b and a and, concomitantly, a decrease of the gain. Strong heating leads to a thermal back-feeding of subband 2, additionally lowering the gain.
- Higher scattering rates and the occupation of states with larger in-plane momenta in the (nonparabolic) subband 3 broaden the 3–2 intersubband line resulting in a decreased gain even for a constant population inversion.

The pump depleted electrons considerably heat up the entire electron gas as shown by the estimation presented in section 6.6.4.1. Hence, for strong heating, we expect also a contribution to the pump-probe signal from the cooling of the heated electron gas. Schematically this is shown in Fig. 6.38 (a). In quasi-stationary equilibrium the carrier temperature is T_C^{eq} and a certain gain is observed. At zero delay time the pump pulse promotes the carriers from subband 3 into subband 2. These “hot”carriers thermalize on a sub-picosecond time scale [124, 126] and heat up the entire electron gas (T_C^{pump}) leading to a decrease of the gain for the reasons mentioned above. Subsequently, the electron distribution cools down until it has reached T_C^{eq} again. Now we compare this picture with our data.

In Fig. 6.39 transients are plotted for different pump pulse energies and different nominal lattice temperatures. For $T_L = 280$ K (Fig. 6.39, solid line in the left panel) we observe a very strong damping of the oscillation and a very slow gain recovery for $t_D > 400$ fs. After $t_D = 1.1$ ps the gain is still considerably below the stationary value. This is in contrast to the fast, exponential recovery observed at later times for $T_L = 100$ K (dotted line). The right panel in Fig. 6.39 shows pump-probe data measured at $T_L = 10$ K with a very large pump pulse energy of 25 nJ. At later times ($t_D > 400$ fs) this transient shows a very slow gain recovery similar to the one measured for a pump pulse energy of 7.5 nJ at $T_L = 280$ K. Also here, the gain is considerably lower than the stationary value after $t_D = 1.1$ ps. This behavior is schematically explained in Fig. 6.38 (b). At a lattice temperature of 100 K and

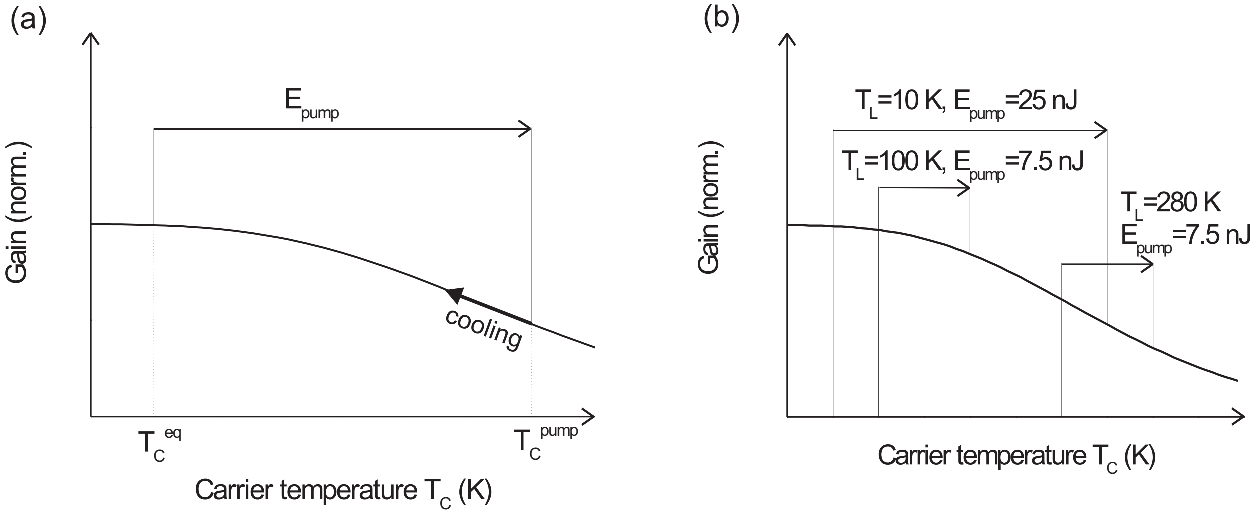

Figure 6.38: Schematics for the heating of the electron gas due to the strong pump-pulse. (a) In quasi-stationary equilibrium the carrier temperature is T_C^{eq}. The pump-depleted electrons thermalize and heat up the carrier distribution (T_C^{pump}) which subsequently cools down to t_C^{eq}. (b) Heating of the electron gas for several lattice temperatures and pump pulse energies.

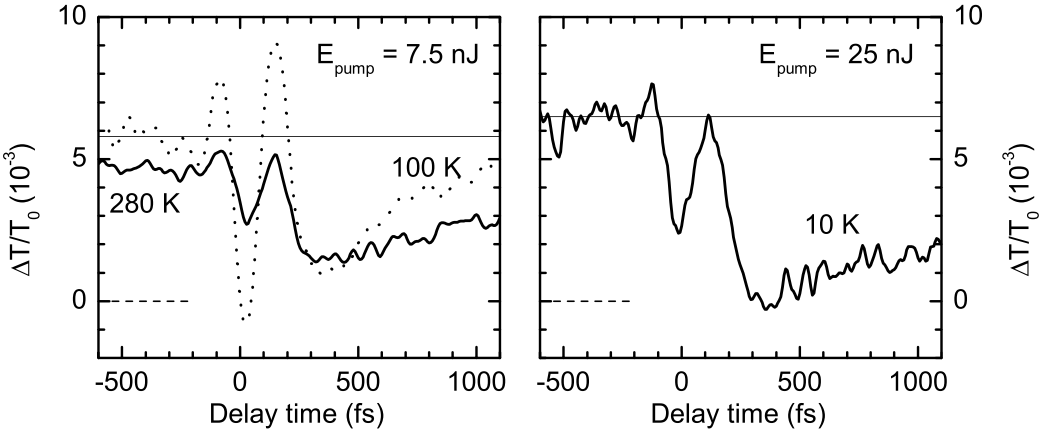

Figure 6.39: Pump-probe transients for various pump pulse energies and nominal lattice temperatures as indicated (left panel: cf. Fig. 6.15, right panel: cf. Fig. 6.12). The curves are measured at a detection wavelength of $\lambda_{det} = 10.0\,\mu$m and a current density of $I = 7$ kA/cm^2.

a pump pulse energy of 7.5 nJ the increase of the carrier temperature after pump depletion results only in a small gain decrease. Thus, only a weak contribution from the cooling of the electron gas is expected. Instead, the pump-probe signal is dominated by coherent and incoherent tunneling as discussed above. For higher lattice temperatures and for very large pump-pulse energies, however, the electron gas is strongly heated so that a considerable decrease of the gain is observed. Since cooling of a heated electron gas occurs on a time scale on the order of 10 ps [78], the gain at $t_D = 1$ ps has only partially recovered as observed in the experiments.

A more quantitative analysis of the observed gain recovery at later times ($t_D > 400$ fs) requires the knowledge of the exact electron distribution, which, however, is not known so far.

6.6.6 Conclusion

The investigations presented in this chapter represent the first time-resolved measurements on quantum cascade laser structures. These studies provide insight into the dynamics of electron transport from the injector into the upper laser subband of the active region, which can not be obtained by stationary measurements. In the following we summarize the main results discussed above:

- For forward bias and spectral positions around the gain maximum we observe pronounced gain oscillations. This gives direct evidence for a coherent wave packet motion from the injector into the upper laser subband via resonant tunneling even at the high electron density (4×10^{11} cm^{-2}) present in a quantum cascade laser structure. After saturation the electrically induced gain is completely recovered within 1 ps at low lattice and carrier temperatures.

- The ratios of the observed oscillation frequencies (1.5–2.5 THz) of all three samples are in good agreement with calculations of the energy splittings between the lowest injector state and the upper laser state at resonance. The absolute values, however, are somewhat higher than the calculated ones. This is probably due to a depolarization shift as a result of charge density oscillations after the strong pump depletion. Hence, our data suggest that many-body effects play an important role for the electron transport in quantum cascade structures.

- The oscillation frequencies depend sensitively on the width and the aluminum content of the barriers. A variation of the barrier width of only two monolayers results in oscillation frequencies differing by 50 %.

- The oscillation decays with a time constant of 200–300 fs, which represents a lower limit for the homogeneous dephasing time T_2 of the observed quantum coherence.

- The coexistence of a long dephasing time and high Coulomb scattering rates in the injector and the gain overshoot observed at half the oscillation period point to the occurrence of scattering-induced coherence, which is a quantum kinetic phenomenon.

- For higher carrier temperatures, which are obtained by increasing the lattice temperature, the pump pulse energy, or the electric current, an additional, exponential gain recovery contribution is observed. This contribution can be explained by incoherent resonant tunneling due to an increased dephasing rate and by nonresonant tunneling of electrons thermally activated into higher injector subbands.

- The sample with the lower aluminum content and, concomitantly, the lower barrier hight, shows only a weak current dependence of the pump-probe signal. This is in contrast to the strong current dependence observed for the samples with the higher barriers. This behavior is an indication for a leakage current due to thermal activation of electrons into continuum states for low barriers.

- Upon further heating of the electron gas, a very slow gain recovery on a picosecond time scale is observed. This can be explained by the cooling of the carrier distribution in the injector, which is heated by the thermalization of the pump-depleted electrons. Thus, the observed gain recovery is not exclusively determined by tunneling from the injector into the upper laser subband but also by the heating and cooling dynamics.

Chapter 7

Summary

In this thesis we investigate the ultrafast dynamics of carriers and coherent intersubband polarizations in quasi-two-dimensional semiconductor nanostructures and devices. In particular, we study n-type modulation doped multiple quantum wells and quantum cascade laser structures based on the GaAs/AlGaAs material system using ultrafast spectroscopy in the mid-infrared spectral range ($\lambda = 3 - 20\,\mu$m). To carry out the first coherent control experiment on intersubband polarizations, we have developed a tabletop system which includes the generation, shaping, and characterization of ultrashort mid-infrared field transients.

The results of the experimental studies are summarized in the following:

Generation, shaping, and characterization of ultrashort mid-infrared pulses

A novel experimental setup is developed allowing for the first time the controlled phase and amplitude shaping of ultrafast field transients in the mid-infrared wavelength range. The setup is based on a two-stage scheme: First the near-infrared pulses provided by a cavity-dumped Ti:sapphire oscillator are passed through a programmable pulse shaper. In this way, amplitude- and phase-shaped near-infrared pulses are generated. In the second step, phase-matched difference-frequency mixing of the various spectral components of these pulses in a GaSe crystal provides the femtosecond mid-infrared electric field transients. The electric field transients generated this way are directly measured using ultrafast electro-optic sampling.

- Various mid-infrared waveforms in a wavelength range centered around 14 μm are generated by applying a pair of phase-locked pump pulses.
- The shaped mid-infrared pulses have a pulse duration of 200–300 fs.
- The maximum pulse energy is 1 pJ at a repetition rate of 2 MHz.
- Our experimental data are in good agreement with a model describing phase-matched optical rectification.
- The scheme presented is extendable to more complex pulse shapes and to other wavelengths and other nonlinear crystals.

Ultrafast coherent control of intersubband transitions in quantum wells

We study the feasibility of coherent nonlinear control of intersubband polarizations. Amplitude and phase-controlled mid-infrared field transients at a wavelength of 12.5 μm from our new laser source induce resonant intersubband excitations in n-type modulation doped GaAs/$\mathrm{Al_{0.35}Ga_{0.65}As}$ quantum wells. The transmitted electric field transients are directly measured by ultrafast electro-optic sampling.

- We demonstrate for the first time coherent control of linear intersubband polarizations with subpicosecond dephasing times by applying two phase-locked pulses with variable relative phase.
- A saturation of the intersubband excitation by more than 20 % is achieved with mid-infrared pulses of only 1 pJ pulse energy.
- The experimental results are in excellent agreement with a simple model based on the Maxwell-Bloch equations. This verifies that the studied quantum well sample with an electron density of only 5×10^{10} cm^{-2} per quantum well behaves like an ideal, homogeneously broadened two-level system.
- These results may facilitate the realization of ultrafast switching devices based on coherent intersubband polarizations.

Ultrafast coherent electron transport in quantum cascade structures

We present for the first time a direct time-resolved experimental study on electrically driven quantum cascade laser structures. These studies provide insight into the dynamics of electron transport, which can not be obtained by stationary measurements. The ultrafast quantum transport of electrons from the injector through the injection barrier into the upper laser subband is investigated in femtosecond mid-infrared pump-probe experiments. In this way we directly monitor the ultrafast saturation and subsequent recovery of electrically induced gain. For the experiments we use three GaAs/$\mathrm{Al}_x\mathrm{Ga}_{1-x}\mathrm{As}$ samples with different aluminum contents ($x = 33$ % and $x = 45$ %) and different injection barrier widths.

- For forward bias and spectral positions around the gain maximum we observe pronounced gain oscillations. This gives direct evidence for a coherent wave packet motion from the injector into the upper laser subband via resonant tunneling even at the high electron density (4×10^{11} cm^{-2}) present in a quantum cascade laser structure. After saturation the electrically induced gain is completely recovered within 1 ps at low lattice and carrier temperatures.
- The ratios of the observed oscillation frequencies (1.5–2.5 THz) of all three samples are in good agreement with calculations of the energy splittings between the lowest injector state and the upper laser state at resonance. The absolute values, however, are somewhat higher than the calculated ones. This is probably due to a depolarization shift as a result of charge density oscillations after the strong pump depletion. Hence, our data suggest that many-body effects play an important role for the electron transport in quantum cascade structures.

- The oscillation frequencies depend sensitively on the width and the aluminum content of the barriers. A variation of the barrier width of only two monolayers results in oscillation frequencies differing by 50 %.

- The oscillation decays with a time constant of 200–300 fs, which represents a lower limit for the homogeneous dephasing time T_2 of the observed quantum coherence. The coexistence of a long dephasing time and high Coulomb scattering rates in the injector and the gain overshoot observed at half the oscillation period point to the occurrence of scattering-induced coherence, which is a quantum kinetic phenomenon.

- For higher carrier temperatures, which are obtained by increasing the lattice temperature, the pump pulse energy, or the electric current, an additional, exponential gain recovery contribution is observed. This contribution can be explained by incoherent resonant tunneling due to an increased dephasing rate and by nonresonant tunneling of electrons thermally activated into higher injector subbands. Upon further heating of the electron gas, a very slow gain recovery on a picosecond time scale is observed. This can be explained by the cooling of the carrier distribution in the injector, which is heated by the thermalization of the pump-depleted electrons. Thus, the observed gain recovery is not exclusively determined by tunneling from the injector into the upper laser subband but also by the heating and cooling dynamics.

Appendix A

Phasematched difference frequency mixing: model

Here, we derive a single formula allowing the calculation of the mid-infrared field generated via phasematched difference frequency mixing in a GaSe crystal with a single, weak near-infrared pulse. We start with some general considerations of difference frequency mixing and phase matching.

Difference frequency mixing is a second order nonlinear effect. Two electric fields $\vec{E}_1(\vec{r},\omega)$, $\vec{E}_2(\vec{r},\omega)$ generate the second order nonlinear polarization

$$P_i^{(2)}(\vec{r},\omega_0) = 2\,\epsilon_0 \sum_{j,k} d_{ijk}^{(2)}(\omega_0;\omega_1,\omega_2)\, E_{1,j}(\vec{r},\omega_1)\, E_{2,k}(\vec{r},\omega_2)$$

$d^{(2)}(\omega_0;\omega_1,\omega_2)$ is nonzero only for $\omega_0 = \omega_1 + \omega_2$ (sum-frequency generation) or $\omega_0 = \Delta\omega = |\omega_1 - \omega_2|$ (difference-frequency generation). In the following, we consider the case of difference frequency generation and assume that we are far away from any resonance so that the frequency dependence of $d^{(2)}(|\omega_1 - \omega_2|;\omega_1,\omega_2) \equiv d$ can be neglected.

The wave equation (2.1) in the frequency domain reads

$$\nabla \times \nabla \times \vec{E}(\vec{r},\omega) - \frac{\omega^2}{c^2\,\epsilon_0}\,\vec{D}^{(1)}(\vec{r},\omega) = \frac{\omega^2}{c^2\,\epsilon_0}\,\vec{P}^{(2)}(\vec{r},\omega) \tag{A.1}$$

where $\vec{D}^{(1)}$ is the linear part of the displacement field $\vec{D}$. The relation between $\vec{D}^{(1)}$ and $\vec{E}$ is given by the frequency dependent dielectric tensor $\epsilon_{ik}(\omega)$

$$D_i^{(1)}(\vec{r},\omega) \equiv \epsilon_0\, E_i(\vec{r},\omega) + P_i^{(1)}(\vec{r},\omega) = \epsilon_0\,\epsilon_{ik}(\omega)\, E_k(\vec{r},\omega)$$

For any plane wave $\vec{E}(\vec{r},t) = \vec{E}\cdot e^{i(\vec{k}(\omega)\,\vec{r} - \omega\, t)}$ with frequency ω one gets the following relation between the $\vec{k}$-vector and the electric field $\vec{E}$ of the wave using Eq. (A.1)

$$k^2(\omega)\, E_i - k_i(\omega)\, k_j(\omega)\, E_j = \frac{\omega^2}{c^2}\,\epsilon_{ij}(\omega)\, E_j$$

The solution of this equation is rather simple for uniaxial birefringent crystals ($\epsilon_{xx} = \epsilon_{yy} \neq \epsilon_{zz}$) like GaSe. Here one gets two equations for the $\vec{k}$-vector, one for the so-called ordinary

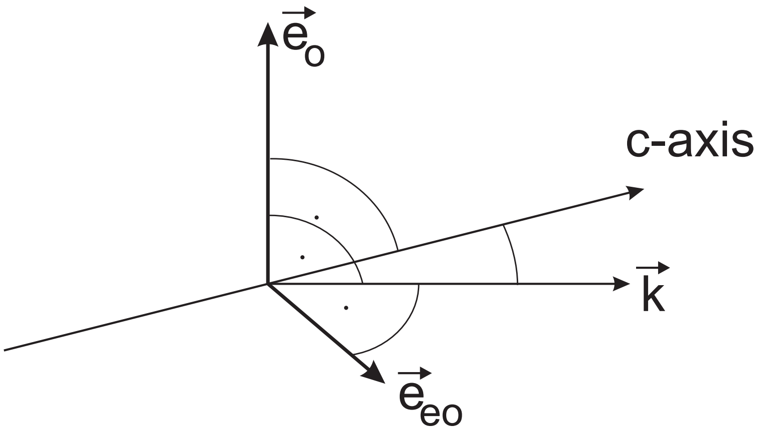

Figure A.1: Directions of ordinary polarization $\vec{e}_o$, extraordinary polarization $\vec{e}_{eo}$, $\vec{k}$ - vector and optical axis (c-axis).

(o) and one for the extraordinary (eo) wave

$$\begin{aligned} \frac{k_o^2(\omega)\,c^2}{\omega^2}\cdot\frac{1}{\epsilon_{xx}(\omega)} &= 1 \\ \frac{k_{eo}^2(\omega,\theta)\,c^2}{\omega^2}\cdot\left(\frac{\sin^2\theta}{\epsilon_{zz}(\omega)}+\frac{\cos^2\theta}{\epsilon_{xx}(\omega)}\right) &= 1 \end{aligned}$$

θ is the angle between the $\vec{k}$-vector and the optical axis (c-axis) as depicted in Fig. A.1. The ordinary polarization $\vec{e}_o$ is perpendicular to the c-axis and to the $\vec{k}$-vector, the extraordinary polarization $\vec{e}_{eo}$ is perpendicular to $\vec{e}_o$ and to $\vec{k}$.

To model the generation of mid-infrared pulses in a difference frequency mixing process the wave equation (A.1) has to be applied to a sum of three fields, the two generating fields $E^{NIR}(z,\omega_1)$ and $E^{NIR}(z,\omega_2)$ and the generated field $E^{MIR}(z,\Delta\omega)$, as there is interaction between all three waves. Hence, in general we have to solve three coupled wave equations. For the solution of this problem, we make the common ansatz of plane waves with a common $\vec{k}$-direction (collinear phasematching) parallel to the z-axis

$$\begin{aligned} E_o^{NIR}(z,\omega_1) &= \frac{1}{2}\,A_o^{NIR}(z,\omega_1)\,e^{i\,k_o(\omega_1)\,z}+cc. \\ E_{eo}^{NIR}(z,\omega_2,\theta) &= \frac{1}{2}\,A_{eo}^{NIR}(z,\omega_2,\theta)\,e^{i\,k_{eo}(\omega_2,\theta)\,z}+cc. \\ E_o^{MIR}(z,\Delta\omega) &= \frac{1}{2}\,A_o^{MIR}(z,\Delta\omega)\,e^{i\,k_o(\Delta\omega)\,z}+cc. \end{aligned}$$

$A(z,\omega)$ is complex, giving rise to an additional phase term. It is important to note that E_{eo}^{NIR} is the amplitude of the electric field parallel to $\vec{e}_{eo}$. The extraordinary wave has additionally a longitudinal component of the electric field, i.e. div $\vec{E}_{eo}\neq 0$ (but div $\vec{D}_{eo}=0$). In a so-called type-I process the second order nonlinear polarization is polarized along $\vec{e}_o$, $\vec{P}^{(2)}=P^{(2)}\,\vec{e}_o$, and it is generated by an extraordinary and an ordinary component of the electric field. In this case, the nonlinear polarization for the difference frequency mixing process can be expressed by means of the scalar relationship

$$P^{(2)}(z,\Delta\omega) = 4\,\epsilon_0\,d(\theta)\,E_o^{NIR}(z,\omega_1)\,E_{eo}^{NIR}(z,\omega_2,\theta)$$

$$= \epsilon_0 \, d(\theta) \, A_o^{NIR}(z,\omega_1) \, \left(A_{eo}^{NIR}(z,\omega_2,\theta)\right)^\star \, e^{i(k_o(\omega_1)-k_{eo}(\omega_2,\theta))z} + cc.$$

with the scalar second order susceptibility $d(\theta)$. For GaSe, which is used in our experiments, the only independent matrix element of the second order susceptibility tensor is $d_{22} = 54$ pm/V. For a type-I process, the scalar susceptibility can be expressed by [159]

$$d(\theta,\phi) \; = \; d_{22}\,\cos(\theta)\,\sin(3\phi)$$

where ϕ is the azimuthal angle between the propagation vector and the xz crystalline plane.

We use the approximation

$$\left|\frac{\partial^2}{\partial z^2} A_o^{MIR}(z,\Delta\omega)\right| \ll \left|k_o(\Delta\omega)\,\frac{\partial}{\partial z} A_o^{MIR}(z,\Delta\omega)\right|$$

which means that the fractional change in $A_o^{MIR}(z,\Delta\omega)$ within a distance of the wavelength $\frac{2\,\pi}{k_o(\Delta\omega)}$ is much smaller than unity, which is well satisfied in the cases discussed here. With the phase mismatch

$$\Delta k = k_{eo}(\omega_2,\theta) - k_o(\omega_1) - k_o(\Delta\omega)$$

the wave equation (A.1) yields

$$\frac{\partial}{\partial z} A_o^{MIR}(z,\Delta\omega) + cc. \; = \; \frac{2\,i\,\Delta\omega^2\,d(\theta)}{c^2\,k(\Delta\omega)} \, A_o^{NIR}(z,\omega_1)\left(A_{eo}^{NIR}(z,\omega_2,\theta)\right)^\star \, e^{i\,\Delta k\,z} + cc. \tag{A.2}$$

$$\frac{\partial}{\partial z} A_o^{NIR}(z,\omega_1) + cc. \; = \; \frac{2\,i\,\omega_1^2\,d(\theta)}{c^2\,k(\omega_1)} \, A_o^{MIR}(z,\Delta\omega) A_{eo}^{NIR}(z,\omega_2,\theta)\,e^{-i\,\Delta k\,z} + cc. \tag{A.3}$$

$$\frac{\partial}{\partial z} A_{eo}^{NIR}(z,\omega_2,\theta) + cc. \; = \; \frac{2\,i\,\omega_2^2\,d(\theta)}{c^2\,k(\omega_2)} \, A_o^{NIR}(z,\omega_1)\left(A_o^{MIR}(z,\Delta\omega)\right)^\star \, e^{-i\,\Delta k\,z} + cc. \tag{A.4}$$

If the generated mid-infrared light is very weak (as in the mid-infrared generation scheme presented in section 2.2.1), than in equations (A.3) and (A.4) the right hand sides can be neglected. In this case the amplitudes of the near-infrared plane waves become independent of z and equation (A.2) can be integrated along the crystal length L. For $z > L$ this results in

$$E_o^{MIR}(z,\Delta\omega) = \frac{2\,(\Delta\omega)^2\,d(\theta)}{c^2\,k_o(\Delta\omega)} \, A_o^{NIR}(\omega_1)\left(A_{eo}^{NIR}(\omega_2,\theta)\right)^\star \, \frac{e^{i\,\Delta k\,L}-1}{\Delta k}\, e^{-i\,k(\Delta\omega)\,z} + cc.$$

As we have spectrally broad near-infrared pulses, the same mid-infrared frequency is generated by a broad range of near-infrared frequencies. Integrating over all respective frequency doublets ($\omega_1 = \omega$ and $\omega_2 = \omega + \Delta\omega$), this yields the final expression

$$\begin{aligned} E_o^{MIR}(z,\Delta\omega) \; &= \; \frac{4\,\Delta\omega^2\,d(\theta)}{c^2\,k_o(\Delta\omega)}\, e^{-i\,k_o(\Delta\omega)\,z} \\ &\quad \cdot \int d\omega\, A_o^{NIR}(\omega)\left(A_{eo}^{NIR}(\omega+\Delta\omega,\theta)\right)^\star \, \frac{e^{i\,\Delta k\,L}-1}{\Delta k} + cc. \end{aligned}$$

Appendix B

The electro-optic effect

Generally, in anisotropic crystals the polarization induced by an electric field and the field itself are not parallel. The electric displacement vector $\vec{D}$ and the electric field $\vec{E}$ are related by the dielectric tensor $\boldsymbol{\epsilon}= 1+\chi^{(1)}$:

$$D_k = \epsilon_0\,\epsilon_{kl}E_l$$

As shown in appendix A, for an arbitrary wave vector $\vec{k}$ (where $\vec{k}\perp\vec{D}$; $\vec{D},\vec{E}$ and $\vec{k}$ lie in a single plane) there exist two linearly independent plane wave, linearly polarized, propagation modes (ordinary and extraordinary wave). These propagate with phase velocities $\pm\frac{c}{n_1}$ and $\pm\frac{c}{n_2}$ [160].

Given the dielectric tensor $\boldsymbol{\epsilon}$ and the wave vector $\vec{k}$, the question is how to find n_1, n_2 and the corresponding directions $\vec{D}_1$ and $\vec{D}_2$. Here, we apply a technique described, e.g., in [50] using the so called index ellipsoid or optical indicatrix. The index ellipsoid is defined by the equation

$$\frac{x^2}{n_x^2}+\frac{y^2}{n_y^2}+\frac{z^2}{n_z^2}=1 \tag{B.1}$$

where the refractive indices are connected with the dielectric tensor $\boldsymbol{\epsilon}$ via

$$n_x^2=\epsilon_{xx},\quad n_y^2=\epsilon_{yy},\quad n_z^2=\epsilon_{zz}$$

where ϵ_{xx}, ϵ_{yy}, ϵ_{zz} are the eigenvalues of $\boldsymbol{\epsilon}$. To determine n_1 and n_2 one has to find the intersection ellipse between a plane through the origin that is normal to $\vec{k}$ and the index ellipsoid (B.1). The two axes of the intersection ellipse are equal in length to $2n_1$ and $2n_2$. These axes are parallel to the directions of $\vec{D}_1$ and $\vec{D}_2$. x, y and z are called the principal dielectric axes, i.e., the directions along which $\vec{D}$ and $\vec{E}$ are parallel. If not all refractive indices are equal, the crystal is called birefringent.

Electro-optic effect The electro-optic effect is the change of the index ellipsoid that is caused by an applied electric field. It is called linear if this change depends linearly on the electric field. In an arbitrary coordinate system the index ellipsoid reads

$$\left(\frac{1}{n^2}\right)_1 x^2+\left(\frac{1}{n^2}\right)_2 y^2+\left(\frac{1}{n^2}\right)_3 z^2+2\left(\frac{1}{n^2}\right)_4 yz+2\left(\frac{1}{n^2}\right)_5 xz+2\left(\frac{1}{n^2}\right)_6 xy=1$$

The linear change in the coefficients

$$\left(\frac{1}{n^2}\right)_i,\ i=1,\ldots,6$$

due to an electric field $\vec{E} = (E_x, E_y, E_z)$ gives rise to the electro-optic tensor $\mathbf{r}$ (in its contracted form)

$$\Delta\left(\frac{1}{n^2}\right)_i = \sum_{j=1}^{3} r_{ij}\, E_j = \mathbf{r}\,\vec{E} \tag{B.2}$$

Equation (B.2) can be written in matrix form as

$$\begin{pmatrix} \Delta\left(\frac{1}{n^2}\right)_1 \\ \vdots \\ \Delta\left(\frac{1}{n^2}\right)_6 \end{pmatrix} = \begin{pmatrix} r_{11} & r_{12} & r_{13} \\ r_{21} & r_{22} & r_{23} \\ r_{31} & r_{32} & r_{33} \\ r_{41} & r_{42} & r_{43} \\ r_{51} & r_{52} & r_{53} \\ r_{61} & r_{62} & r_{63} \end{pmatrix} \begin{pmatrix} E_1 \\ E_2 \\ E_3 \end{pmatrix}$$

The linear electro-optic effect is a second order nonlinear effect (Pockels effect). Hence, it can also be expressed by the second order nonlinear susceptibility tensor $\mathbf{d}^{(2)}$. $\mathbf{r}$ and $\mathbf{d}^{(2)}$ are related by the equation

$$d^{(2)}_{ijk} = -\frac{\epsilon_i\,\epsilon_j}{2\,\epsilon_0} r_{ijk}$$

where ϵ_i and ϵ_j are the principal dielectric constants along i and j. r_{ijk} is the electro-optic tensor in its non-contracted form.

Appendix C

Polarization matrices

The matrix formalism is a very useful method to describe the evolution of the polarization vector of an electro-magnetic wave passing an optical element. Here, we want to explain the matrices used in this work. The general case is that of a wave with a wavelength λ and polarization $\vec{E}_{in} = (E_{in,x}, E_{in,y})$ passing an optical element of thickness L with the index ellipsoid shown in Fig. C.1. The question is, how does the polarization read at the exit of this optical element $\vec{E}_{out} = (E_{out,x}, E_{out,y})$. To calculate this we have to rotate the coordinate system by an angle of 45°. This means that the vectors $(1,0)$ and $(0,1)$ in the old coordinates x, y become $\frac{1}{\sqrt{2}}(1,-1)$ and $\frac{1}{\sqrt{2}}(1,1)$, respectively, in the new coordinates x', y' (Fig. C.1). The corresponding rotation matrix is

$$M(45^\circ) = \frac{1}{\sqrt{2}} \begin{pmatrix} 1 & 1 \\ -1 & 1 \end{pmatrix}$$

The backward rotation matrix $M(-45^\circ)$ then reads

$$M(-45^\circ) = \frac{1}{\sqrt{2}} \begin{pmatrix} 1 & -1 \\ 1 & 1 \end{pmatrix}$$

Now, the elements of the rotated polarization vector are subject to the refractive indices n_1 and n_2, respectively. Finally we have to rotate back the coordinate system. Altogether this yields

$$\vec{E}_{out} = \frac{1}{2} M(-45^\circ) \begin{pmatrix} e^{i\frac{2\pi}{\lambda} n_1 L} & 0 \\ 0 & e^{i\frac{2\pi}{\lambda} n_2 L} \end{pmatrix} M(45^\circ)\, \vec{E}_{in} + cc.$$

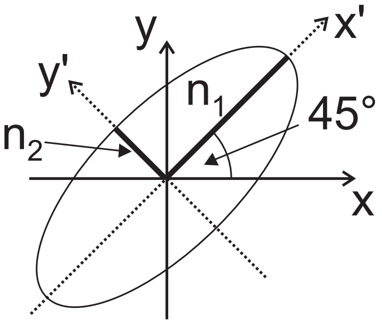

Figure C.1: Index ellipsoid of an optical element with the refractive indices n_1 and n_2.

$$= \frac{1}{2}\, M(n_1, n_2)\, \vec{E}_{in} + cc.$$

with

$$M(n_1, n_2) = e^{i\,\frac{2\pi}{\lambda}\,(n_1+n_2)\,L} \left(\begin{array}{cc} \cos\frac{\Gamma}{2} & e^{i\frac{\pi}{2}}\,\sin\frac{\Gamma}{2} \\ e^{i\frac{\pi}{2}}\,\sin\frac{\Gamma}{2} & \cos\frac{\Gamma}{2} \end{array} \right)$$

where $\Gamma = \frac{2\pi}{2}\, L\,(n_1 - n_2)$ is called the phase retardance. In most cases, the absolute phase-factor $e^{i\frac{2\pi}{\lambda}\,(n_1+n_2)\,L}$ can be neglected so that we get

$$M(\Gamma) = \left(\begin{array}{cc} \cos\frac{\Gamma}{2} & e^{i\frac{\pi}{2}}\,\sin\frac{\Gamma}{2} \\ e^{i\frac{\pi}{2}}\,\sin\frac{\Gamma}{2} & \cos\frac{\Gamma}{2} \end{array} \right)$$

For a $\lambda/4$-waveplate the retardance is $\Gamma = \frac{\pi}{2}$, so that the matrix $M_{\lambda/4}$ yields

$$M_{\lambda/4} = \frac{1}{\sqrt{2}} \left(\begin{array}{cc} 1 & e^{i\frac{\pi}{2}} \\ e^{i\frac{\pi}{2}} & 1 \end{array} \right)$$

For a $\lambda/2$-waveplate the retardance is $\Gamma = \pi$, hence

$$M_{\lambda/2} = \left(\begin{array}{cc} 0 & e^{i\frac{\pi}{2}} \\ e^{i\frac{\pi}{2}} & 0 \end{array} \right)$$

A polarizer, which polarizes light along the x axis or along the y axis, can be represented by the matrices P_x and P_y, respectively:

$$P_x = \left(\begin{array}{cc} 1 & 0 \\ 0 & 0 \end{array} \right) \qquad \text{and} \qquad P_y = \left(\begin{array}{cc} 0 & 0 \\ 0 & 1 \end{array} \right)$$

Appendix D

Maximum phase retardation

Here, we calculate the optimum polarization for the mid-infrared and the near-infrared pulses for which the maximum phase retardation is obtained with a thin ZnTe plate being $< 110 >$ oriented [32]. ZnTe is not birefringent for zero electric field, i.e., the index ellipsoid for $\vec{E}^{MIR} = 0$ is a sphere

$$\left(\frac{x}{n}\right)^2 + \left(\frac{y}{n}\right)^2 + \left(\frac{z}{n}\right)^2 = 1$$

The refractive index of ZnTe is well approximated for wavelengths $< 30\,\mu$m (reststrahl band) by the Sellmeier equation [161]

$$n_{ZnTe}(\lambda) = \sqrt{9.92 + \frac{0.42530}{\lambda^2 - 0.37766^2} + \frac{2.63580}{\frac{\lambda^2}{56.5^2} - 1}}\,,\ \lambda \text{ in } \mu\text{m}\,.$$

The non-vanishing components of the electro-optic tensor $\mathbf{r}_{ZnTe}$ for ZnTe at a mid-infrared wavelength of $10.6\,\mu$m [50] are

$$r_{41} = r_{52} = r_{63} = 3.9 \cdot 10^{-12}\,\frac{\text{m}}{\text{V}} \tag{D.1}$$

Hence, with applied field $\vec{E}^{MIR} = (E_1^{MIR}, E_2^{MIR}, E_3^{MIR})$ the index ellipsoid reads

$$\left(\frac{x}{n}\right)^2 + \left(\frac{y}{n}\right)^2 + \left(\frac{z}{n}\right)^2 + 2\,r_{41}\,E_1^{MIR}\,yz \quad + \quad 2\,r_{41}\,E_2^{MIR}\,xz + 2\,r_{41}\,E_3^{MIR}\,xy = 1 \tag{D.2}$$

Both the mid- and near-infrared propagation directions are chosen to be perpendicular to the ZnTe surface

$$\vec{E}^{NIR},\ \vec{E}^{MIR} \perp \begin{pmatrix} 1 \\ 1 \\ 0 \end{pmatrix} \Rightarrow \quad \vec{E}^{MIR} = \alpha \begin{pmatrix} 0 \\ 0 \\ 1 \end{pmatrix} + \frac{\beta}{\sqrt{2}} \begin{pmatrix} 1 \\ -1 \\ 0 \end{pmatrix}$$

The first task is to find the intersection plane between the index ellipsoid (D.2) and the plane of all possible mid-infrared polarizations

$$\left\{\left(\frac{x}{n}\right)^2 + \left(\frac{y}{n}\right)^2 + \left(\frac{z}{n}\right)^2 + 2\,r_{41}\left(\frac{\beta}{\sqrt{2}}(y-x)\,z + \alpha\,x\,y\right) = 1\right\} \cap \{x = -y\} \tag{D.3}$$

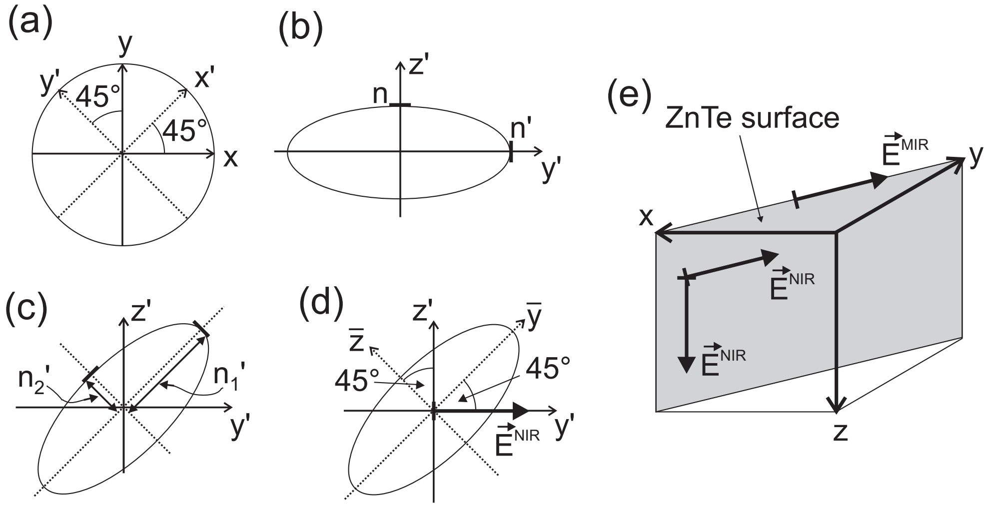

Figure D.1: The electro-optic effect. Coordinate rotations [(a) and (d)] are necessary to calculate the electro-optic effect from the index ellipsoid [(b) and (c)]. (e) ZnTe surface and polarizations of the near- and mid-infrared beam yielding the maximum effect (for the near-infrared beam there are two possibilities).

We introduce new coordinates x', y', z' which are related to x, y and z by a 45° rotation around the z axis as shown in Fig. D.1 (a).

$$x = \frac{1}{\sqrt{2}}\,(x' - y')\,, \quad y = \frac{1}{\sqrt{2}}\,(x' + y')\,, \quad z' = z$$

Successively, we treat the two linear independent cases of mid-infrared polarizations:

- $\alpha = E^{MIR}$, $\beta = 0$, i.e., $\vec{E}^{MIR}$ is polarized along the z-axis:

  Upon substitution (D.3) yields

  $$\left\{\left(\frac{1}{n^2} + r_{41}\,E^{MIR}\right)x'^2 + \left(\frac{1}{n^2} - r_{41}\,E^{MIR}\right)y'^2 + \left(\frac{z'}{n}\right)^2 = 1\,,\ x' = 0\right\}$$

  For $r_{41}\,E^{MIR} \ll \frac{1}{n^2}$, which is the case in the experiments, this results in

  $$\left\{\left(\frac{y'}{n'}\right)^2 + \left(\frac{z'}{n}\right)^2 = 1\,,\ x' = 0\right\} \quad \text{with} \quad n' = n + \frac{1}{2}n^3 r_{41} E^{MIR} \tag{D.4}$$

  The intersection of the index ellipsoid with the $x' = 0$ plane is shown in Fig. D.1 (b).

- $\alpha = 0$, $\beta = E^{MIR}$, i.e., $\vec{E}^{MIR}$ is polarized along the y'-axis:

  Now (D.3) yields

  $$\left\{\frac{1}{2}\left(\frac{1}{n^2} + r_{41}E^{MIR}\right)(y' + z')^2 + \frac{1}{2}\left(\frac{1}{n^2} - r_{41}E^{MIR}\right)(y' - z')^2 = 1\,,\ x' = 0\right\}$$

Again, for $r_{41}\,E^{MIR} \ll \frac{1}{n^2}$ this results in

$$\left\{\frac{1}{n_1'^2}\left(\frac{y'+z'}{\sqrt{2}}\right)^2 + \frac{1}{n_2'^2}\left(\frac{y'-z'}{\sqrt{2}}\right)^2 = 1\,,\; x' = 0\right\} \tag{D.5}$$

with

$$n_1' = n + \frac{1}{2}\,n^3\,r_{41}\,E^{MIR} \quad , \quad n_2' = n - \frac{1}{2}\,n^3\,r_{41}\,E^{MIR} \tag{D.6}$$

The intersection of the index ellipsoid with the $x' = 0$ plane is shown in Fig. D.1 (c).

Phase retardation So far, we have calculated the electro-optic effect induced by a mid-infrared field $\vec{E}^{MIR}$. The question now is how this modulation affects a near-infrared reference pulse. We choose the near-infrared beam propagating along the x'-axis and polarized along the y'-axis, $\vec{E}^{NIR} = E^{NIR}\,\vec{e}_{y'}$. Now, we follow the polarization of the near-infrared beam after entering the ZnTe crystal. For this, we have to carry out again a coordinate rotation so that the new coordinates coincide with the principal axes of the index ellipsoid [Fig. D.1 (d)].

$$\begin{aligned} y' &= \frac{1}{\sqrt{2}}\,(\bar{y} - \bar{z}) \quad , \quad & z' &= \frac{1}{\sqrt{2}}\,(\bar{y} + \bar{z}) \\ \vec{e}_{y'} &= \frac{1}{\sqrt{2}}\,(\vec{e}_{\bar{y}} - \vec{e}_{\bar{z}}) \quad , \quad & \vec{e}_{z'} &= \frac{1}{\sqrt{2}}\,(\vec{e}_{\bar{y}} + \vec{e}_{\bar{z}}) \end{aligned}$$

The field is incident along the x'-direction, i.e.,

$$\vec{E}^{NIR} = \frac{1}{2}\frac{E^{NIR}}{\sqrt{2}}\,(\vec{e}_{\bar{y}} - \vec{e}_{\bar{z}})\,e^{i\left(\omega t - \frac{\omega}{c} n_0 x'\right)} + cc. \equiv E^{NIR}_{\bar{y}}\,\vec{e}_{\bar{y}} + E^{NIR}_{\bar{z}}\,\vec{e}_{\bar{z}}$$

The phases of the polarization components in $\bar{y}$ and $\bar{z}$ direction develop according to the refractive indices for the $\vec{e}_{\bar{y}}$ and $\vec{e}_{\bar{z}}$ directions (D.6)

$$E^{NIR}_{\bar{y}} = \frac{1}{2}\frac{E^{NIR}}{\sqrt{2}}\,e^{\,i\left(\omega t - \frac{\omega}{c}\left(n + \frac{1}{2}\,n^3\,r_{41}\,E^{MIR}\right)x' + \varphi\right)} + cc. \tag{D.7}$$

$$E^{NIR}_{\bar{z}} = \frac{1}{2}\frac{E^{NIR}}{\sqrt{2}}\,e^{\,i\left(\omega t - \frac{\omega}{c}\left(n - \frac{1}{2}\,n^3\,r_{41}\,E^{MIR}\right)x' + \varphi\right)} + cc. \tag{D.8}$$

φ is an arbitrary phase at the entrance of the crystal at $x' = 0$. The phase difference at the output plane $x' = L$ is the retardance Γ. It is the difference of the exponents in (D.7) and (D.8)

$$\Gamma = \frac{\omega}{c}\,n^3\,r_{41}\,E^{MIR}\,L \tag{D.9}$$

With the same calculation one can see that the same phase difference occurs also for a near-infrared beam being polarized along the z'-axis. It causes an originally linearly polarized beam to become elliptically polarized. (D.9) is the maximum retardation for any polarization of the near-infrared field for the index ellipsoid (D.5). For the index ellipsoid (D.4) the maximum retardation is $\Gamma' = \frac{1}{2}\,\Gamma$.

In conclusion, we get the maximum phase retardation $\Gamma = \frac{\omega}{c}\,n^3\,r_{41}\,E^{MIR}\,L$ for a $< 110 >$ oriented ZnTe-crystal with a mid-infrared beam propagating along the $(1,1,0)$ direction being polarized along the $(1,-1,0)$ direction and the near-infrared field being polarized either along the $(1,-1,0)$ or the $(0,0,1)$ direction [Fig. D.1 (e)].

Appendix E

Scattering-induced coherence: quantum kinetic model

In order to illustrate the phenomenon of scattering-induced coherence we have carried out calculations based on a simple quantum kinetic model [153, 154]. We study the coupling of a higher injector state $|i\rangle$ with the localized states $|g\rangle$ and $|3\rangle$. As a model coupling mechanism we use electron-LO phonon coupling via the Fröhlich Hamiltonian H_F. The aim of this calculation is to study the time evolution of a single electron initially residing in state $|i\rangle$.

We will solve the time-dependent Schrödinger equation

$$i\hbar \frac{d}{dt} |\Psi\rangle = (H_e + H_F + H_{ph}) |\Psi\rangle$$

where H_e is the electron Hamiltonian, H_{ph} is the phonon Hamiltonian, $|\Psi\rangle$ is the state vector of the coupled electron-LO phonon system characterized by the electron quantum numbers $n \,\epsilon\, \{\, i,\, g,\, 3 \,\}$ and $\vec{k}$, and the phonon occupation number $N_{\vec{q}}$. We assume a lattice temperature of $T_L = 0$. Hence, only scattering via LO phonon emission is possible. The coupling matrix element between the electron-phonon product states reads

$$\begin{aligned} M_{ij}(\vec{q}) &= \langle \vec{k} = \vec{q}_{||},\, j,\, N_{\vec{q}} = 1 \,|\, H_F \,|\, \vec{k} = 0,\, i,\, N_{\vec{q}} = 0 \rangle \\ &= M_0 \int dz \, \frac{1}{|\vec{q}|} \, \zeta_i^*(z)\, \zeta_j(z)\, e^{i\, q_z\, z}\,, \quad j \,\epsilon\, \{\, g,\, 3 \} \end{aligned}$$

with a coupling constant M_0. In our model, we treat M_0 as a variable parameter which can be identified with an effective LO phonon scattering rate $1/\tau_{LO}$. M_{ij} couples the state $|\vec{k} = 0,\, i,\, N_{\vec{q}} = 0\rangle$ of an electron in $|i\rangle$ with $\vec{k} = 0$ and zero phonons to state $|\vec{k} = \vec{q}_{||},\, j,\, N_{\vec{q}} = 1\rangle$ with an electron in $|g\rangle$ or $|3\rangle$ with momentum $\vec{q}_{||}$ and a phonon with $\vec{q} = -\vec{q}_{||} + q_z\, \vec{e}_z$ (Fig. E.1). Due to the small spatial overlap of states $|i\rangle$ and $|3\rangle$ the matrix element M_{i3} is much smaller than M_{ig} and can be neglected.

There are several interesting points resulting from this quantum kinetic approach.

- State $|\vec{k} = 0,\, i,\, N_{\vec{q}} = 0\rangle$ is not an eigenstate of the total Hamiltonian $H_e + H_F + H_{ph}$. As time evolves it develops into a coherent superposition of states $|\vec{k} = 0,\, i,\, N_{\vec{q}} = 0\rangle$, $|\vec{k} = \vec{q}_{||},\, g,\, N_{\vec{q}} = 1\rangle$, and $|\vec{k} = \vec{q}_{||},\, 3,\, N_{\vec{q}} = 1\rangle$.

- Since we directly solve the Schrödinger equation , identical results are obtained using the delocalized states $|b\rangle$ and $|a\rangle$.

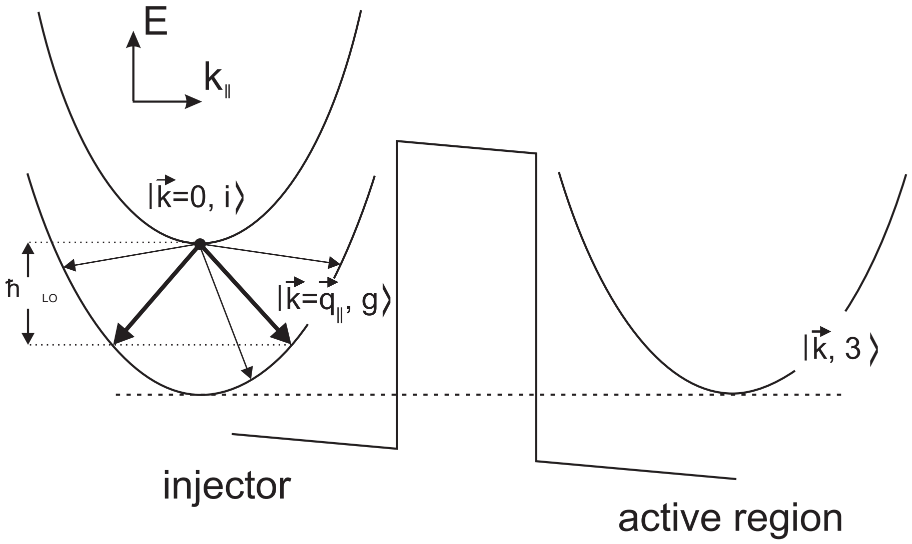

Figure E.1: An electron in state $|\vec{k} = 0,\, i\rangle$ is scattered into states $|\vec{k} = \vec{q}_{||},\, g\rangle$ via LO phonon emission. Scattering into states $|\vec{k} = \vec{q}_{||},\, 3\rangle$ is strongly suppressed because of the small overlap of the envelope functions of states in subbands i and 3. There is also coupling to states for which energy conservation is not satisfied.

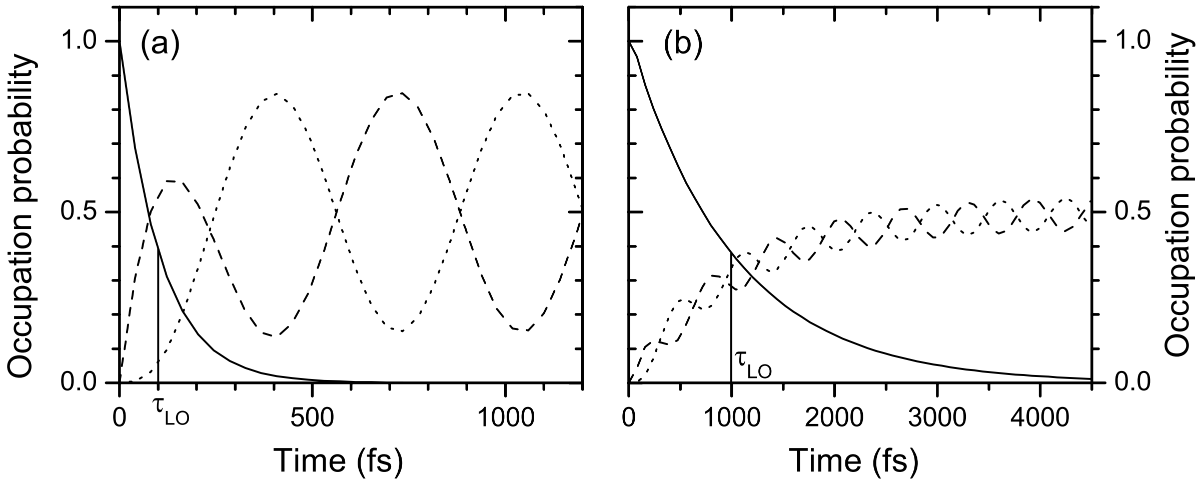

Figure E.2: Occupation probabilities of subband i (solid line), subband g localized in the injector (dashed line), and subband 3 localized in the active region (dotted line). Effective LO-phonon scattering times of (a) $\tau_{LO} = 100$ fs and (b) $\tau_{LO} = 1000$ fs and an energy splitting of $\Delta E_{ab} = 6.4$ meV are assumed.

- The time evolution of a pure electron-phonon product state remains a pure state. However, the partial trace of the density matrix $\rho(t) = |\Psi(t)\rangle\langle\Psi(t)|$ over the in-plane momentum results in a 3-level density matrix being in a statistical mixture.

In Fig. E.2 we present calculations for a single electron initially residing in state $|\vec{k} = 0,\, i,\, N_{\vec{q}} = 0\rangle$ for different effective LO-phonon scattering times τ_{LO}. An energy splitting between the binding and anti-binding states of $\Delta E_{ab} = 6.4$ meV is assumed similar to the value for the structure A_2. Since we are interested in the occupations of the electronic states with arbitrary in-plane momenta we project the product states onto the electronic subsystem, i.e., we sum over all those product states for which the quantum number of the electron subband is identical. This results in a 3-level density matrix being in a statistical mixture. In Fig. E.2 (a) various occupation probabilities are plotted as a function of time for an effective LO-phonon scattering time much shorter than the oscillation time: $\tau_{LO} = 100$ fs $< T_{osc} = 640$ fs. The solid line indicates the decay of the occupation probability of the upper injector state i. It decays exponentially with the decay time $\tau_{decay} \equiv \tau_{LO} = 100$ fs. At early times ($t < \tau_{decay}$) also the occupation probability of subband g (dashed line) increases exponentially with the rise time 100 fs. At later times a pronounced oscillation with an oscillation period of T_{osc} is observed. The occupation probability of subband 3 (dotted line) oscillates with a phase shift of 180°. This indicates that due to the strong LO-phonon scattering a wavepacket is generated oscillating between the injector and the active region. This oscillatory motion is strongly coherent, i.e., the scattering mechanism has induced a pronounced coherent superposition of the electronic eigenstates $|a\rangle$ and $|b\rangle$. What happens for longer LO phonon scattering times is depicted in Fig. E.2 (b). Here, a LO phonon scattering time $\tau_{LO} = 1000$ fs, which is longer than the oscillation time, is assumed. The solid line indicates the exponential decay of the occupation probability of the upper injector state i. In contrast to the situation above, the occupation probabilities of subband g (dashed line) and subband 3 (dotted line) increase uniformly with a time constant similar to τ_{LO} and only minor oscillations are observed. This indicates little coherence in the superposition of the electronic eigenstates $|a\rangle$ and $|b\rangle$.

With this model we have demonstrated that scattering processes are not necessarily phase destroying events. Even the opposite can occur, i.e., scattering-induced coherence. In our model we have seen that the induced coherence is even larger for higher scattering rates and that the occupation in subband g is much higher in the oscillation maxima than the average value similar to the gain overshoot observed in our experiment.

Bibliography

[1] L. Esaki and R. Tsu
Superlattice and negative differential conductivity in semiconductors
IBM J. Res. Develop. **14**, 61-65 (1970).

[2] B. F. Levine, K. K. Choi, C. G. Bethea, J. Walker, and R. J. Malik
New 10 μm infrared detector using intersubband absorption in resonant tunneling GaAlAs superlattices
Appl. Phys. Lett. **50**, 1092-1094 (1987).

[3] J. Faist, F. Capasso, D. L. Sivco, C. Sirtori, A. L. Hutchinson, and A. Y. Cho
Quantum Cascade Laser
Science **264**, 553-556 (1994).

[4] J. Shah
Ultrafast spectroscopy of semiconductors and semiconductor nanostructures (Springer, Berlin, 1999).

[5] T. Elsaesser and M. Woerner
Femtosecond infrared spectroscopy of semiconductors and semiconductor nanostructures
Phys. Rep. **321**, 253-305 (1999).

[6] *Ultrafast Phenomena XI*, edited by T. Elsaesser, J. G. Fujimoto, D. A. Wiersma, and W. Zinth (Springer, Berlin, 1998).

[7] *Ultrafast Phenomena XII*, edited by T. Elsaesser, S. Mukamel, M. M. Murnane, and N. F. Scherer (Springer, Berlin, 2001).

[8] W. S. Warren, H. Rabitz, and M. Dahleh
Coherent control of quantum dynamics: the dream is alive
Science **259**, 1581–1589 (1993).

[9] A. P. Heberle, J. J. Baumberg, and K. Köhler
Ultrafast coherent control and destruction of excitons in quantum wells
Phys. Rev. Lett. **75**, 2598-2601 (1995).

[10] M. Beck, D. Hofstetter, T. Aellen, J. Faist, U. Oesterle, M. Ilegems, E. Gini, and H. Melchior
Continuous wave operation of a mid-infrared semiconductor laser at room temperature
Science **295**, 301-305 (2002).

[11] R. Köhler, A. Tredicucci, F. Beltram, H. E. Beere, E. H. Linfield, A. G. Davies, D. A. Ritchie, R. C. Iotti, and F. Rossi
Terahertz semiconductor-heterostructure laser
Nature **417**, 156-159 (2002).

[12] S. Barbieri, C. Sirtori, H. Page, M. Stellmacher, and J. Nagle
Design strategies for GaAs-based unipolar lasers: Optimum injector-active region coupling via resonant tunneling
Appl. Phys. Lett. **78**, 282-284 (2001).

[13] A. Wacker
Semiconductor superlattices: a model system for nonlinear transport
Phys Rep. **357**, 1-111 (2002).

[14] J. Feldmann, K. Leo, J. Shah, D. A. B. Miller, J. E. Cunningham, T. Meier, G. von Plessen, A. Schulze, P. Thomas, and S. Schmitt-Rink
Optical investigation of Bloch oscillations in a semiconductor superlattice
Phys. Rev. B **46**, 7252 (1992).

[15] J. Stenger, D. Madsen, P. Hamm, E. T. J. Nibbering, and T. Elsaesser
Ultrafast vibrational dephasing of liquid water
Phys. Rev. Lett. **87**, 027401 (2001).

[16] J. Edler, P. Hamm, and A. C. Scott
Femtosecond study of self-trapped vibrational excitons in crystalline acetanilide
Phys. Rev. Lett. **88**, 067403 (2002).

[17] R. A. Kaindl, M. Woerner, T. Elsaesser, D. C. Smith, J. F. Ryan, G. Farnan, M. McCurry, and G. Walmsley
Ultrafast mid-infrared response of $YBa_2Cu_3O_{7-\delta}$
Science **287**, 470-473 (2000).

[18] R. A. Kaindl, S. Lutgen, M. Woerner, T. Elsaesser, B. Nottelmann, V. M. Axt, T. Kuhn, A. Hase, and H. Künzel
Ultrafast dephasing of coherent intersubband polarizations in a qusi-two-dimensional electron plasma
Phys. Rev. Lett. **80**, 3575-3578 (1998).

[19] L. D. Landau and E. M. Lifschitz
Lehrbuch der theoretischen Physik, Band VIII: Electrodynamik der Kontinua (Akademie-Verlag, Berlin, 1985).

[20] A. Messiah
Quantenmechanik Band 2 (Walter de Gruyter, Berlin, 1979).

[21] R. W. Boyd
Nonlinear Optics (Academic Press, San Diego, 1992).

[22] J.-C. Diels and W. Rudolph
Ultrashort laser pulse phenomena (Academic Press, San Diego, 1996).

[23] S. Mukamel
Principles of nonlinear optical spectroscopy (Oxford Univ., New York, 1995).

[24] H. Haug and S. W. Koch
Quantum theory of the optical and electronic properties of semiconductors, 3rd ed. (World Scientific, Singapore, 1996).

[25] A. Baltuška, T. Fuji, and T. Kobayashi
Visible pulse compression to 4 fs by optical parametric amplification and programmable dispersion control
Opt. Lett. **27**, 306-308 (2002).

[26] N. Zhavaronkov and G. Korn
Generation of single intense short optical pulses by ultrafast molecular phase modulation
Phys. Rev. Lett. **88**, 203901-1–4 (2002).

[27] M. Chachisvilis, H. Fidder, and V. Sundstrom
Electronic coherence in pseudo-2-color pump-probe spectroscopy
Chem. Phys. Lett. **234**, 141-150 (1995).

[28] W. T. Pollard, S.-Y. Lee, and R. A. Mathies
Wave packet theory of dynamic absorption spectra in femtosecond pump-probe experiments
J. Chem. Phys. **92**, 4012-4029 (1990).

[29] W. T.Pollard, S. L. Dexheimer, Q. Wang, L. A. Peteanu, C. V. Shank, and R. A. Mathies
Theory of dynamic absorption spectroscopy of nonstationary sates. 4. Application to 12-fs resonant impulsive Raman spectroscopy of bacteriorhodopsin
J. Phys. Chem. **96**, 6147-6158 (1992).

[30] M. Joschko
Ultraschnelle Dynamik von kohärenten Intervalenzbandpolarisationen in Galliumarsenid (PhD thesis, Humboldt-Universität zu Berlin, 1998).

[31] B. Fluegel, N. Peyghambarian, G. Olbright, M. Lindberg, S. W. Koch, M. Joffre, D. Hulin, A. Migus, and A. Antonetti
Femtosecond studies of coherent transients in semiconductors
Phys. Rev. Lett. **59**, 2588-2591 (1987).

[32] Q. Wu and X.-C. Zhang
Free-space electro-optics sampling of mid-infrared pulses
Appl. Phys. Lett. **71**, 1285-1286 (1997).

[33] D. H. Auston, K. P. Cheung, J. A. Valdmanis, and D. A. Kleinman
Cherenkov radiation from femtosecond optical pulses in electro-optic media
Phys. Rev. Lett. **53**, 1555-1558 (1984).

[34] M. S. Pshenichnikov, W. P. de Boeij, and D. A. Wiersma
Generation of 13-fs, 5-MW pulses from a cavity-dumped Ti:sapphire laser
Opt. Lett. **19**, 572-574 (1994).

[35] W. P. de Boeij
Ultrafast solvation dynamics explored by nonlinear optical spectroscopy (PhD thesis, University of Groningen, 1997).

[36] C. Spielmann, P. F. Curley, T. Brabec, and F. Krausz
Ultrabroadband femtosecond lasers
IEEE J. Quantum Electron. **30**, 1100–1114 (1994).

[37] R. A. Kaindl, D. C. Smith, M. Joschko, M. P. Hasselbeck, M. Woerner, and T. Elsaesser
Femtosecond infrared pulses tunable from 9 to 18 μm at an 88-MHz repetition rate
Opt. Lett. **23**, 861-863 (1998).

[38] A. Bonvalet, M. Joffre, J. L. Martin, and A. Migus
Generation of ultrabroadband femtosecond pulses in the mid-infrared by optical rectification of 15 fs light pulses at 100 MHz repetition rate
Appl. Phys. Lett. **67**, 2907-2909 (1995).

[39] M. Joffre, A. Bonvalet, A. Migus, and J. L. Martin
Femtosecond diffracting Fourier-transform infrared interferometer
Opt. Lett. **21**, 964-966 (1996).

[40] K. L. Vodopyanov and L. A. Kulevskii
New dispersion relationships for GaSe in the 0.65-18 μm spectral region
Opt. Commun. **118**, 375-378 (1995).

[41] R. A. Kaindl
Ultrafast mid-infrared studies of low-energy excitations in solids (PhD thesis, Humboldt-Universität zu Berlin, 2000).

[42] R. A. Kaindl, M. Wurm, K. Reimann, P. Hamm, A. M. Weiner, and M. Woerner
Generation, shaping and characterization of intense femtosecond pulses tunable between 3 and 20 μm
J. Opt. Soc. Am. B **17**, 2086-2094 (2000).

[43] J. Squier and G. Mourou
Tunable solid-state lasers create ultrashort pulses
Laser Focus World **28**, 51–52 (1992).

[44] J. A. Valdmanis, G. Mourou, and C. W. Gabel
Picosecond electro-optic sampling system
Appl. Phys. Lett. **41**, 211-212 (1982).

[45] B. H. Kolner and D. M. Bloom
Electrooptic sampling in GaAs integrated circuits
IEEE J. Quantum Electron. **22**, 79-93 (1986).

[46] J. A. Valdmanis and G. Mourou
Subpicosecond Electrooptic sampling: principles and applications
IEEE J. Quantum Electron. **22**, 69-78 (1986).

[47] D. H. Auston and M. C. Nuss
Electrooptic generation and detection of femtosecond electrical transients
IEEE J. Quantum Electron. **24**, 184-197 (1988).

[48] Q. Wu and X.-C. Zhang
Free-space electro-optic sampling of terahertz beams
Appl. Phys. Lett. **67**, 3523-3525 (1995).

[49] R. Huber, A. Brodschelm, F. Tauser, and A. Leitenstorfer
Generation and field-resolved detection of femtosecond electromagnetic pulses tunable up to 41 THz
Appl. Phys. Lett. **76**, 3191–3193 (2000).

[50] A. Yariv
Quantum Electronics (3rd ed.) (Wiley, New York, 1988).

[51] Q. Wu and X.-C. Zhang
7 terahertz broadband GaP electro-optic sensor
Appl. Phys. Lett. **70**, 1784–1786 (1997).

[52] J. P. Heritage, A. M. Weiner, and R. N. Thurston
Picosecond pulse shaping by spectral phase and amplitude manipulation
Opt. Lett. **10**, 609-611 (1985).

[53] A. M. Weiner, J. P. Heritage, and E. M. Kirschner
High-resolution femtosecond pulse shaping
J. Opt. Soc. Am. **5**, 1563-1572 (1988).

[54] C. W. Hillegas, J. X. Tull, D. Goswami, D. Strickland, and W. S. Warren
Femtosecond laser pulse shaping by use of microsecond radio-frequency pulses
Opt. Lett. **19**, 737-739 (1994).

[55] A. M. Weiner, D. E. Leaird, J. S. Patel, and J. Wullert
Programmable femtosecond pulse shaping by use of a multielement liquid-crystal phase modulator
Opt. Lett. **15**, 326-328 (1990).

[56] A. M. Weiner, D. E. Leaird, J. S. Patel, and I. I. Wullert JR
Programmable shaping of femtosecond optical pulses by use of 128-element liquid crystal phase modulator
IEEE J. Quantum Electron. **28**, 908–920 (1992).

[57] A. M. Weiner
Femtosecond pulse shaping using spatial light modulators
Rev. Sci. Instrum. **71**, 1929–1960 (2000).

[58] M. M. Wefers and K. A. Nelson
Generation of high-fidelity programmable ultrafast optical waveforms
Opt. Lett. **20**, 1047-1049 (1995).

[59] D. J. Kane and R. Trebino
Characterization of arbitrary femtosecond pulses using frequency-resolved optical gating
IEEE J. Quantum Electron. **29**, 571–579 (1993).

[60] C. Iaconis and I. A. Walmsley
Self-referencing spectral interferometry for measuring ultrashort optical pulses
IEEE J. Quantum Electron. **35**, 501-509 (1999).

[61] K. C. Chu, J. P. Heritage, R. S. Grant, K. X. Liu, A. Dienes, W. E. White, and A. Sullivan
Direct measurement of the spectral phase of femtosecond pulses
Opt. Lett. **20**, 904–906 (1995).

[62] A. Y. Cho and J. R. Arthur
Molecular beam epitaxy
Prog. Solid State Chem. **10**, 157-191 (1975).

[63] K. Ploog, in: H. C. Freyhardt (Ed.), Crystals: Growth, Properties and Applications, Springer, Berlin, 1980, p. 75.

[64] M. A. Hermann and H. Sitter
Molecular Beam Epitaxy - Fundamentals and Current Status (Springer Series in Materials Science, Vol. 7, Springer Verlag, 1995).

[65] G. B. Stringfellow
Organometallic vapor phase epitaxy: Theory and practice (Academic Press, New York, 1989).

[66] H. C. Liu, M. Buchanan, and Z. R. Wasilewski
How good is the polarization selection rule for intersubband transitions?
Appl. Phys. Lett. **72**, 1682-1684 (1998).

[67] L. C. West and S. J. Eglash
First observation of an extremely large-dipole infrared transition within the conduction band of a GaAs quantum well
Appl. Phys. Lett. **46**, 1156-1158 (1985).

[68] H. Lobentanzer, W. König, W. Stolz, K. Ploog, T. Elsaesser, and R. J. Bäuerle
Intersubband absorption in a modulation-doped GaInAs/AlInAs multiple quantum well structure
Appl. Phys Lett. **53**, 571-573 (1988).

[69] R. A. Kaindl, K. Reimann, M. Woerner, T. Elsaesser, R. Hey, and K. H. Ploog
Homogeneous broadening and excitation-induced dephasing of intersubband transitions in a quasi-two-dimensional electron gas
Phys. Rev. B **63**, 161308 (2001).

[70] A. Kamgar, P. Kneschaurek, G. Dorda, and J. F. Koch
Resonance spectroscopy of electronic levels in a surface accumulation layer
Phys. Rev. Lett. **32**, 1251-1254 (1974).

[71] P. Kneschaurek, A. Kamgar, and J. F. Koch
Electronic levels in surface space charge layers on Si(100)
Phys. Rev. B **14**, 1610-1622 (1976).

[72] M. Ramsteiner, J. D. Ralston, P. Koidl, B. Dischler, H. Biebl, J. Wagner, and H. Ennen
Doping density dependence of intersubband transitions in GaAs/AlGaAs quantum-well structures
J. Appl. Phys. **67**, 3900-3903 (1996).

[73] K. L. Campman, H. Schmidt, A. Imamoglu, and A. C. Gossard
Interface roughness contributions and alloy disorder scattering contributions of intersubband transition linewidths
Appl. Phys. Lett. **69**, 2554-2556 (1996).

[74] K. Reimann, R. A. Kaindl, and M. Woerner
Optical deformation-potential scattering of holes in multiple quantum well structures
Phys. Rev. B **65**, 045302 (2001).

[75] T. Ando, A. B. Fowler, and F. Stern
Electronic–properties of two–dimensional systems
Rev. Mod. Phys. **54**, 437-672 (1982).

[76] M. Zaluzny
Intersubband absorption line broadening in semiconductor quantum wells: Nonparabolicity contribution
Phys. Rev. B **43**, 4511-4514 (1991).

[77] S. Lutgen, R. A. Kaindl, M. Woerner, T. Elsaesser, A. Hase, and H. Künzel
Nonlinear intersubband absorption of a hot quasi–two–dimensional electron plasma studied by femtosecond infrared spectroscopy
Phys. Rev. B **54**, R17343 (1996).

[78] S. Lutgen, R. A. Kaindl, M. Woerner, A. Hase, and H. Künzel
Ultrafast heating and cooling of electon plasmas in GaInAs/AlInAs quantum wells after intersubband excitation
Solid State Commun. **106**, 425-429 (1998).

[79] M. Woerner and T. Elsaesser
in *Ultrafast nonequilibrium dynamics of intersubband excitations in quasi–two–dimensional semiconductors*, edited by K. T. Tsen (Springer, New York, 2001).

[80] M. A. Tischler and B. D. Parker
Effect of structural parameters on transport characteristics of GaInAs/AlInAs two–dimensional electron gases grown by molecular beam epitaxy
Appl. Phys. Lett. **58**, 1614-1616 (1991).

[81] Insook Lee and S. M. Goodnick
Microscopic calculation of the electron–optical-phonon interaction in ultrathin GaAs/AlGaAs alloy quantum-well systems
Phys. Rev. B **51**, 7046-7057 (1995).

[82] P. Lugli, P. Bordone, E. Molinari, H. Rucker, A. M. Depaula, A. C. Maciel, J. F. Ryan, and M. Shayegan
Interaction of electrons with interface phonons in GaAs/AlAs and GaAs/AlGaAs heterostructures
Semiconductor Sci. Technol. **7**, B116-B119 (1992).

[83] W. H. Knox, D. S. Chemla, G. Livescu, J. E. Cunningham, and J. E. Henry
Femtosecond Carrier Thermalization in Dense Fermi Seas
Phys. Rev. Lett. **61**, 1290-1293 (1988).

[84] D. A. B. Miller, D. S. Chemla, T. C. Damen, T. H. Wood, C. A. Burrus andA. C. Gossard, and W. Wiegmann
The quantum well self-electrooptic effect device: optoelectronic bistability and oscillation, and self-linearized modulation
IEEE J. Quantum Electron. **21**, 1462-1476 (1985).

[85] U. Keller, D. A. B. Miller, G. D. Boyd, T. H. Chiu, J. F. Ferguson, and M. T. Asom
Solid-state low-loss intracavity saturable absorber for Nd:YLF lasers: an antiresonant semiconductor Fabry–Perot saturable absorber
Opt. Lett. **17**, 505-507 (1992).

[86] D. Fröhlich, R. Wille, W. Schlapp, and G. Weimann
Optical quantum-confined Stark effect in GaAs quantum wells
Phys. Rev. Lett. **59**, 1748-1751 (1987).

[87] A. Hache, Y. Kostoulas, R. Atanasov, J. L. P. Hughes, J. E. Sipe, and H. M. van Driel
Observation of coherently controlled photocurrent in unbiased, bulk GaAs
Phys. Rev. Lett. **78**, 306-309 (1997).

[88] X. Hu and W. Pötz
Coherent control of optical gain from electronic intersubband transitions in semiconductors
Appl. Phys. Lett. **73**, 876-878 (1998).

[89] A. Neogi, O. Wada, Y. Takahashi, and H. Kawaguchi
Ultrashort-pulse-controlled all-optical modulation by interband and intersubband transitions in doped quantum wells
Opt. Lett. **23**, 1212-1214 (1998).

[90] A. Bonvalet, J. Nagle, V. Berger, A. Migus, J.-L. Martin, and M. Joffre
Femtosecond infrared emission resulting from coherent charge oscillations in quantum wells
Phys. Rev. Lett. **76**, 4392-4395 (1996).

[91] E. Dupont, P. B. Corkum, H. C. Liu, M. Buchanan, and Z. R. Wasilewski
Phase-controlled currents in semiconductors
Phys. Rev. Lett. **74**, 3596-3599 (1995).

[92] M. Tsuchiya, T. Matsusue, and H. Sakaki
Tunneling escape rate of electrons from quantum well in double-barrier heterostructures
Phys. Rev. Lett. **59**, 2356-2359 (1987).

[93] D. Y. Oberli, J. Shah, T. C. Damen, C. W. Tu, T. Y. Chang, D. A. B. Miller, J. E. Henry, R. F. Kopf, N. Sauer, and A. E. DiGiovanni
Direct measurement of resonant and nonresonant tunneling times in asymmetric coupled quantum wells
Phys. Rev. B **40**, 3028-3031 (1989).

[94] K. Leo, J. Shah, E. O. Göbel, T. C. Damen, S. Schmitt-Rink, and W. Schäfer
Coherent oscillations of a wave packet in a semiconductor double-quantum-well structure
Phys. Rev. Lett. **66**, 201-204 (1991).

[95] H. G. Roskos, M. C. Nuss, J. Shah, K. Leo, D. A. B. Miller, A. M. Fox, S. Schmitt-Rink, and K. Köhler
Coherent submillimeter-wave emission from charge oscillations in a double-well potential
Phys. Rev. Lett. **68**, 2216-2219 (1992).

[96] F. Bloch
Über die Quantenmechanik der elektronen in Kristallgittern
Z. Phys. **52**, 555-600 (1928).

[97] R. Martini, G. Klose, H. G. Roskos, H. Kurz, H. T. Grahn, and R. Hey
Superradiant emission from Bloch oscillations in semiconductor superlattices
Phys. Rev. B **54**, 14325 (1996).

[98] R. F. Kazarinov and R. A. Suris
Possibility of the amplification of electromagnetic waves in a semiconductor with a superlattice
Sov. Phys. Semicond. **5**, 707709 (1971).

[99] C. Sirtori, P. Kruck, S. Barbieri, P. Collot, J. Nagle, M. Beck, J. Faist, and U. Oesterle
GaAs/AlGaAs quantum cascade lasers
Appl. Phys. Lett. **73**, 3486-3488 (1988).

[100] J. Faist, F. Capasso C. Sirtori, D. L. Sivco, A. L. Hutchinson, and A. Y. Cho
Continuous wave operation of a vertical transition quantum cascade laser above T=80K
Appl. Phys. Lett. **67**, 3057-3059 (1995).

[101] J. Faist, F. Capasso C. Sirtori, D. L. Sivco, J. N. Baillargeon, A. L. Hutchinson, S.-N. G. Chu, and A. Y. Cho
High power mid-infrared ($\lambda \sim 5\,\mu$m) quantum cascade lasers operating above room

temperature
Appl. Phys. Lett. **68**, 3680-3682 (1996).

[102] J. Faist, C. Gmachl, F. Capasso C. Sirtori, D. L. Sivco, J. N. Baillargeon, and A. Y. Cho
Distributed feedback quantum cascade lasers
Appl. Phys. Lett. **70**, 2670-2672 (1997).

[103] G. Scamarcio, F. Capasso, C. Sirtori, J. Faist, A. L. Hutchinson, D. L. Sivco, and A. Y. Cho
High-power infrared (8-micrometer wavelength) superlattice lasers
Acience **276**, 773-776 (1997).

[104] G. Strasser, L. Hvozdara, S. Gianordoli, K. Unterrainer, E. Gornik, P. Kruck, and M. Helm
GaAs/AlGaAs quantum cascade intersubband and interminiband emitter
J. Cryst. Growth. **202**, 919-922 (1999).

[105] H. Page, C. Becker, A. Robertson, G. Glastre, V. Ortiz, and C. Sirtori
300 K operation of a GaAs-based quantum-cascade laser at $\lambda \approx 9\,\mu$m
Appl. Phys. Lett. **78**, 3529-3531 (2001).

[106] R. Paiella, F. Capasso, C. Gmachl, D. L. Sivco, J. N. Baillargeon, A. L. Hutchinson, A. Y. Cho, and H. C. Liu
Self-mode-locking of quantum cascade lasers with giant ultrafast optical nonlinearities
Science **290**, 1739-1742 (2000).

[107] C. Gmachl, D. L. Sivco, R. Colombelli, F. Capasso, and A. Y. Cho
Ultra-broadband semiconductor laser
Nature **415**, 883-887 (2002).

[108] C. Gmachl, Lucent Technol., Bell Labs (private communication).

[109] C. Becker, I. Prevot, X. Marcadet, B. Vinter, and C. Sirtori
InAs/AlSb quantum-cascade light-emitting devices in the 3-5 μm wavelength region
Appl. Phys. Lett. **78**, 3893-3895 (2001).

[110] H. Kuenzel, HHI Berlin, (private communication).

[111] M. Semtsiv, HU Berlin, (private communication).

[112] G. Dehlinger, L. Diehl, U. Gennser, H. Sigg, J. Faist, K. Ensslin, D. Grutzmacher, and E. Muller
Intersubband electroluminescence from silicon-based quantum cascade structures
Science **290**, 2277-2279 (2000).

[113] C. Sirtori, F. Capasso, J. Faist, A. L. Hutchinson, D. L. Sivco, and A. Y. Cho
Resonant tunneling in quantum cascade lasers
IEEE J. Quantum Electron. **34**, 1722-1729 (1998).

[114] L. R. Wilson, P. T. Keightley, J. W. Cockburn, J. P. Duck, M. S. Skolnick, J. C. Clark, G. Hill, M. Moran, and R. Grey
Spectroscopic determination of the electron distribution in a quantum cascade structure
Appl. Phys. Lett. **75**, 2079-2081 (1999).

[115] L. R. Wilson, P. T. Keightley, J. W. Cockburn, J. P. Duck, M. S. Skolnick, J. C. Clark, G. Hill, M. Moran, and R. Grey
Mid-infrared spectroscopic studies and lasing in GaAs-AlGaAs quantum cascade devices
Physica E **7**, 713-717 (2000).

[116] C. Sirtori, P. Kruck, S. Barbieri, H. Page, M. Beck, J. Faist, U. Oesterle, and J. Nagle
Low loss Al free waveguides for unipolar semiconductor lasers
Appl. Phys. Lett. **75**, 3911-3913 (1999).

[117] S. Barbieri, C. Sirtori, H. Page, M. Beck, J. Faist, and J. Nagle
Gain measurements on GaAs-based quantum cascade lasers using a two-section cavity technique
IEEE J. Quantum Electron. **36**, 736-741 (2000).

[118] B. W. Hakki and T. L. Paoli
Gain spectra in GaAs double-heterostructure injection lasers
J. Appl. Phys. **46**, 1299-1306 (1975).

[119] J. Faist, A. Tredicucci, F. Capasso, C. Sirtori, D. L. Sivco, J. N. Baillargeon, A. L. Hutchinson, and A. Y. Cho
High-power continuous-wave quantum cascade lasers
IEEE J. Quantum Electron. **34**, 336-343 (1998).

[120] A. Wacker and S.-C. Lee
Gain and loss in quantum cascade lasers
Physica B (2002).

[121] A. Wacker
in *Transport in nanostructures: A comparison between nonequilibrium Green functions and density matrices*, edited by B. Kramer (Springer, New York, 2001).

[122] M. Troccoli, G. Scamarcio, V. Spagnolo, A. Tredicucci, C. Gmachl, F. Capasso, D. L. Sivco, A. Y. Cho, and M. Striccoli
Electronic distribution in superlattice quantum cascade lasers
Appl. Phys. Lett. **77**, 1088-1090 (2000).

[123] M. Troccoli, G. Scamarcioand A. Valentini, G. Casamassima, and M. Striccoli
Hot electron distribution in quantum cascade and single stage GaAs/AlGaAs periodic superlattice structures
Opt. Mater. **17**, 223-225 (2001).

[124] P. Harrison
The nature of the electron distribution functions in quantum cascade lasers
Appl. Phys. Lett. **75**, 2800-2802 (1999).

[125] R. C. Iotti and F. Rossi
Microscopic theory of hot-carrier relaxation in semiconductor-based quantum-cascade lasers
Appl. Phys. Lett. **76**, 2265-2267 (2000).

[126] R. C. Iotti and F. Rossi
Carrier thermalization versus phonon-assisted relaxation in quantum-cascade lasers: A monte carlo approach
Appl. Phys. Lett. **78**, 2902-2904 (2001).

[127] R. F. Kazarinov and R. A. Suris
Electric and electromagnetic properties of semiconductors with a superlattice
Sov. Phys. Semicond. **6**, 120-131 (1972).

[128] R. C. Iotti and F. Rossi
Nature of charge transport in quantum-cascade lasers
Phys. Rev. Lett. **87**, 146603 (2001).

[129] M. V. Klein and T. E. Furtak
Optik (Springer, Berlin, 1988).

[130] R. Loudon
The quantum theory of light (3rd ed.) (Oxford Univ. Press, Oxford, 1983).

[131] S. L. McCall and E. L. Hahn
Self-induced transparency
Phys. Rev. **183**, 457-485 (1969).

[132] S. L. McCall and E. L. Hahn
Self-induced transparency by pulsed coherent light
Phys. Rev. Lett. **18**, 908-911 (1967).

[133] N. Chand, T. Henderson, J. Klem, W. T. Masselink, R. Fisher, Y.-C. Chang, and H. Morkoç
Comprehensive analysis of Si-doped $Al_xGa_{1-x}As$ ($x = 0$ to 1): Theory and experiments
Phys. Rev. B **30**, 4481-4492 (1984).

[134] S. Barbieri, Thomson-CSF (unpublished results).

[135] S. Adachi
Physical properties of III-V semiconductor compounds (Wiley, New York, 1992).

[136] *Landolt-Börnstein – Zahlenwerte und Funktionen aus Naturwissenschaften und Technik*, edited by O. Madelung (Springer, Berlin, 1987), Vol. III/22a.

[137] N. Marschall and B. Fischer
Dispersion of surface polaritons in GaP
Phys. Rev. Lett. **28**, 811-813 (1972).

[138] W. G. Spitzer and J. M. Whelan
Infrared absorption and electron effective mass in n-type gallium arsenide
Phys. Rev. **114**, 59-63 (1959).

[139] E. D. Palik
Handbook of optical constants of solids (Academic Press, San Diego, 1985).

[140] K. Unterrainer, TU Wien (unpublished results).

[141] S. A. Kovalenko, A. L. Dobryakov, J. Ruthmann, and N. P. Ernsting
Femtosecond spectroscopy of condensed phases with chirped supercontinuum probing
Phys. Rev. A **59**, 2369-2384 (1999).

[142] A. Wacker and T. Lee, TU Berlin (unpublished results).

[143] M. P. Kesler and E. P. Ippen
Subpicosecond gain dynamics in GaAlAs laser diodes
Appl. Phys. Lett. **51**, 1765-1767 (1987).

[144] A. Reale, A. Di Carlo, and P. Lugli
Gain dynamics in traveling-wave semiconductor optical amplifiers
IEEE J. Sel. Topics Quantum Electron. **7**, 293-299 (2001).

[145] M. S.-C. Luo, S. L. Chuang, S. Schmitt-Rink, and A. Pinczuk
Many-body effects on intersubband spin-density and charge-density excitations
Phys. Rev. B **48**, 11086-11094 (1993).

[146] M. Zaluzny
Influence of nonparabolicity on collective intersubband spin- and charge-density excitation spectra
Phys. Rev. B **49**, 2923-2926 (1994).

[147] R. J. Warburton, C. Gauer, A. Wixforth, J. P. Kotthaus, B. Brar, and H. Kroemer
Intersubband resonances in InAs/AlSb quantum wells: Selection rules, matrix elements, and the depolarization field
Phys. Rev. B **53**, 7903-7910 (1996).

[148] R. Ferreira and G. Bastard
Evaluation of some scattering times for electrons in unbiased and biased single- and multiple quantum well structures
Phys. Rev. B **40**, 1074-1086 (1989).

[149] S.-C. Lee and I. Galbraith
Intersubband and intrasubband electronic scattering rates in semiconductor quantum wells
Phys. Rev. B **59**, 15796-15805 (1999).

[150] H. Haug and C. Ell
Coulomb quantum kinetics in a dense electron gas
Phys. Rev. B **46**, 2126-2132 (1992).

[151] Q. T. Vu, H. Haug, W. A. Hügel, S. Chatterjee, and M. Wegener
Signature of electron-plasmon quantum kinetics in GaAs
Phys. Rev. Lett. **85**, 3508-3511 (2000).

[152] R. Huber, F. Tauser, A. Brodschelm, M. Bichler, G. Abstreiter, and A. Leitensdorfer
How many-particle interactions develop ultrafast excitation of an electron-hole plasma
Nature **414**, 286-289 (2001).

[153] H. Vaupel, P. Thomas, O. Kühn, V. May, K. Maschke, A. P. Heberle, W. W. Rühle, and K. Köhler
Dissipative tunneling in asymmetric double-quantum-well systems: A coherence phenomenon
Phys. Rev. B **53**, 16531-16542 (1996).

[154] S. A. Gurvitz, I. Bar-Joseph, and B. Deveaud
Quantum tunneling and relaxation in asymmetric coupled wells
Phys. Rev. B **43**, 14703-14706 (1991).

[155] F. Wolter, H. G. Roskos, P. H. Bolivar, G. Bartels, H. Kurz, K. Köhler, H. T. Grahn, and R. Hey
Influence of LO-phonon emission on Bloch oscillations in semiconductor superlattices
Phys. Status Solidi B **204**, 83-86 (1997).

[156] T. Kuhn
in *Theory of transport properties of semiconductor nanostructures*, edited by E. Schöll (Chapman & Hall, London, 1998).

[157] R. Iotti, INFM Torino, private communication.

[158] P. Kruck, H. Page, C. Sirtori, S. Barbieri, M. Stellmacher, and J. Nagle
Improved temperature performance of $\mathrm{Al}_{0.33}\mathrm{Ga}_{0.67}\mathrm{As}/\mathrm{GaAs}$ quantum-cascade lasers with emission wavelength at $\lambda \approx 11\,\mu\mathrm{m}$
Appl. Phys. Lett. **76**, 3340-3342 (2000).

[159] V. G. Dmitriev, G. G. Gurzadyan, and D. N. Nikogosyan
Handbook of Nonlinear Optical Crystals (Springer, Berlin, 1996).

[160] M. Born and E. Wolf
Principles of Optics (Macmillan, New York, 1964).

[161] *Handbook of Optics II*, edited by M. Bass (McGraw-Hill, New York, 1995).

Zusammenfassung

In dieser Arbeit untersuchen wir die ultraschnelle Dynamik von Ladungsträgern und kohärenten Intersubbandpolarisationen in quasi-zweidimensionalen Halbleiternanostrukturen und Halbleiterbauelementen. Insbesondere werden n-Typ modulationsdotierte multiple Quantentöpfe und Quantenkaskadenlaserstrukturen basierend auf dem Materialsystem GaAs/AlGaAs mit der Methode der ultraschnellen Spektroskopie im mittleren Infrarot ($\lambda = 3 - 20\,\mu$m) studiert. Zur erstmaligen Durchführung eines Experimentes zur kohärenten Kontrolle an Intersubbandpolarisationen haben wir ein System entwickelt, welches die Erzeugung, Formung und Charakterisierung von ultraschnellen Feldtransienten im mittleren Infrarot erlaubt.

Die Resultate der experimentellen Untersuchungen lassen sich wie folgt zusammenfassen:

Erzeugung, Formung und Charakterisierung von ultraschnellen Mittinfrarotpulsen

Ein neuartiger experimenteller Aufbau ist entwickelt worden, der zum ersten Mal das phasen- und amplitudenkontrollierte Formen von ultraschnellen Feldtransienten im mittelinfraroten Spektralbereich erlaubt. Der Aufbau basiert auf einem zweistufigen Schema: Zuerst werden nahinfrarote Pulse, die in einem resonatorgeschalteten Titan-Saphir Oszillator erzeugt wurden, durch einen programmierbaren Pulsformer geleitet. Auf diese Weise werden amplituden- und phasenkontrollierte Nahinfrarotpulse erzeugt. In einer weiteren Stufe wird durch phasenangepaßte Differenzfrequenzmischung der verschiedenen spektralen Komponenten dieses Pulses in einem GaSe Kristall der geformte Mittinfrarotpuls erzeugt. Die auf diese Weise erzeugten Feldtransienten werden direkt mit Hilfe des ultraschnellen elektro-optischen Abtastverfahrens gemessen.

- Mittels eines phasengekoppelten Pulspaares werden verschiedene Pulsformen in einem Wellenlängenbereich um 14 μm erzeugt.
- Die geformten Mittinfrarotpulse haben eine Pulslänge von 200–300 fs.
- Die maximale Pulsenergie ist 1 pJ bei einer Repetitionsrate von 2 MHz.
- Unsere experimentellen Daten sind in guter Übereinstimmung mit einem Modell, das phasenangepaßte optische Gleichrichtung beschreibt.
- Das präsentierte Schema ist auf komplexere Pulsformen, andere Wellenlängen und andere nichtlineare Kristalle erweiterbar.

Ultraschnelle kohärente Kontrolle von Intersubbandübergängen in Quantentöpfen

Wir untersuchen die Möglichkeit der kohärenten Kontrolle von Intersubbandübergängen. Amplituden- und phasenkonntrollierte Feldtransienten, die mit unserer neuen Laserquelle erzeugt werden, induzieren bei einer Wellenlänge von 12.5 μm resonante Intersubbandanregungen in n-Typ modulationsdotierten GaAs/AlGaAs Quantentöpfen. Die transmittierten elektrischen Feldtransienten werden mit Hilfe des ultraschnellen elektro-optischen Abtastverfahrens gemessen.

- Unter Anwendung zweier phasengekoppelter Mittinfarotpulse variabler relativer Phase zeigen wir erstmalig die kohärente Kontrolle an linearen Intersubbandpolarisationen mit Dephasierungszeiten unterhalb einer Pikosekunde.

- Eine Sättigung von mehr als 20 % wird bei einer Mittinfrarotpulsenergie von nur 1 pJ erreicht.

- Die experimentellen Resultate sind in exzellenter Übereinstimmung mit einem einfachen Modell, das auf den Maxwell-Bloch-Gleichungen basiert. Dies ist eine Bestätigung dafür, daß sich die untersuchte Quantentopfprobe mit einer Elektronendichte von nur 5×10^{10} cm^{-2} pro Quantentopf wie ein ideales, homogen verbreitertes Zweiniveausystem verhält.

- Diese Ergebnisse könnten die Realisierung ultraschneller Schalter, die auf kohärenten Intersubbandpolarisationen basieren, vereinfachen.

Ultraschneller Elektronentransport in Quantenkaskadenstrukturen

Es wird erstmalig ein direktes, zeitaufgelöstes Experiment an elektrisch betriebenen Quantenkaskadenstrukturen vorgestellt. Diese Untersuchung ermöglicht den Einblick in die Dynamik des Elektronentransports, der mit stationären Methoden nicht meßbar ist. Der ultraschnelle Quantentransport der Elektronen vom Injektor durch die Injektionsbarriere in das obere Lasersubband wird in Femtosekunden-Mittinfrarot-Anreg-Abtast-Experimenten untersucht. Auf diese Weise beobachten wir die ultraschnelle Sättigung und die nachfolgende Wiederherstellung des elektrisch induzierten Gains. Für die Experimente verwenden wir drei GaAs/Al$_x$Ga$_{1-x}$As Proben mit unterschiedlichem Aluminiumgehalt ($x = 33$ % und $x = 45$ %) und unterschiedlicher Injektionsbarrierenbreite.

- Wir beobachten ausgeprägte Gainoszillationen bei angelegtem Vorwärtsstrom und an spektralen Positionen am Gainmaximum. Dies ist ein direkter Beweis für eine kohärente Wellenpaketspropagation vom Injektor in das obere Lasersubband mittels resonantem Tunneln trotz der hohen Ladungsträgerdichte (4×10^{11} cm^{-2}) in Quantenkaskadenlasern. Nach der Sättigung ist der elektrisch induzierte Gain bei niedrigen Gitter- und Ladungsträgertemperaturen innerhalb einer Pikosekunde vollständig wiederhergestellt.

- Die Quotienten der beobachteten Oszillationsfrequenzen (1.5 – 2.5 THz) aller drei Proben sind in guter Übereinstimmung mit Berechnungen der Energieaufspaltungen zwischen dem niedrigsten Injektorzustand und dem oberen Laserzustand in der Resonanz. Die absoluten Werte sind jedoch etwas höher als die berechneten. Dies hat möglicherweise seine Ursache in der Depolarisationsverschiebung aufgrund von Ladungsdichteoszillationen nach starker Anregung. Aus diesem Grund legen es unsere Daten nahe, daß Vielteilcheneffekte eine wichtige Rolle für den Elektronentransport in Quantenkaskadenstrukturen spielen.

- Die Oszillationsfrequenzen hängen empflindlich von der Breite und dem Aluminiumgehalt der Barriere ab. Eine Veränderung der Barrierenbreite um nur zwei Monolagen hat einen Frequenzunterschied von 50 % zur Folge.

- Die Oszillation ist mit einer Zeitkonstante von 200–300 fs gedämpft. Diese Zeit stellt eine untere Grenze für die homogene Dephasierungszeit T_2 der beobachteten Quantenkohärenz dar. Die Koexistenz einer langen Dephasierungszeit und hoher Coulombstreuraten im Injektor sowie der Gainüberschwinger, der bei der halben Oszillationsperiode beobachtet wird, deuten auf das Auftreten streuinduzierter Kohärenz hin, welches eine quantenkinetische Erscheinung ist.

- Bei höheren Ladungsträgertemperaturen, welche bei einer Erhöhung der Gittertemperatur, der Anregpulsenergie oder des elektrischen Stroms entstehen, wird ein zusätzlicher, exponentieller Beitrag zur Wiederherstellung des Gains beobachtet. Dieser Beitrag kann mit inkohärentem, resonanten Tunneln aufgrund einer erhöhten Dephasierungsrate sowie mit nichtresonantem Tunneln thermisch aktivierter Elektronen in höheren Injektorsubbändern erklärt werden. Bei weiterem Aufheizen des Elektronengases wird ein sehr langsames Wiederherstellen des Gains auf einer Pikosekundenzeitskala beobachtet. Dies kann durch ein Abkühlen der Ladungsträgerverteilung im Injektor, welche durch das Thermalisieren der angeregten Elektronen aufgeheizt wird, erklärt werden. Aus diesem Grund ist die beobachtete Gaindynamik nicht ausschließlich durch das Tunneln vom Injektor in das obere Lasersubband sonder auch durch die Dynamik des Aufheizens und Abkühlens der Ladungsträger bestimmt.

Publications in conjunction with this thesis

Publications in refereed journals and books:

- R. A. Kaindl, F. Eickemeyer, M. Woerner, and T. Elsaesser, *Broadband phasematched difference frequency mixing of femtosecond pulses in GaSe: Experiment and theory*, Appl. Phys. Lett. **75**, 1060-1062 (1999).
- F. Eickemeyer, R. A. Kaindl, M. Woerner, and T. Elsaesser, *Large electrically induced transmission changes of GaAs/AlGaAs quantum-cascade structures*, Appl. Phys. Lett. **76**, 3254-3256 (2000)
- F. Eickemeyer, R. A. Kaindl, M. Woerner, T. Elsaesser, and A. M. Weiner, *Controlled shaping of ultrafast electric field transients in the mid-infrared spectral range*, Opt. Lett. **25**, 1472-1474 (2000)
- F. Eickemeyer, R. A. Kaindl, M. Woerner, and A. M. Weiner, *Coherently controlled shaping of ultrafast electric-field transients in the mid-infrared*, in: Ultrafast Phenomena XII, Springer, Berlin, 180-182 (2000)
- F. Eickemeyer, M. Woerner, A. M. Weiner, T. Elsaesser, R. Hey, K. H. Ploog, *Coherent nonlinear propagation of ultrafast electric field transients through intersubband resonances*, Appl. Phys. Lett. **79**, 165-167 (2001)
- M. Woerner, R. A. Kaindl, F. Eickemeyer, K. Reimann, T. Elsaesser, A. M. Weiner, R. Hey, and K. H. Ploog, *Coherent nonlinear dynamics of intersubband excitations in a two-dimensional electron gas*, Physica B **314**, 244-247 (2002)
- F. Eickemeyer, K. Reimann, M. Woerner, T. Elsaesser, S.-C. Lee, A. Wacker, S. Barbieri, C. Sirtori, and J. Nagle, *Ultrafast coherent electron transport in GaAs/AlGaAs quantum cascade structures*, Physica B **314**, 314-322 (2002)
- M. Woerner, R. A. Kaindl, F. Eickemeyer, K. Reimann, T. Elsaesser, R. Hey, and K. Ploog, *Ultrafast coherent nonlinear dynamics of intersubband excitations in a quasi-two-dimensional electron gas*, Physica E (2002) - in press
- F. Eickemeyer, K. Reimann, M. Woerner, T. Elsaesser, S. Barbieri, C. Sirtori, G. Strasser, T. Müller, R. Bratschitsch, and K. Unterrainer, *Ultrafast coherent electron transport in semiconductor quantum cascade structures*, Phys. Rev. Lett. **89**, 047402/1-4 (2002)

Conference contributions:

- R. A. Kaindl, F. Eickemeyer, M. Woerner, and T. Elsaesser, *Femtosecond infrared pulses widely tunable from 9 to 18 μm at high repetition rates*, Conference on Lasers and Electro-Optics (CLEO) in Baltimore, USA, May 1999 (invited)

- F. Eickemeyer, R. A. Kaindl, M. Woerner, and T. Elsaesser, *Electrically induced transmission-change characteristics of GaAs/AlGaAs quantum cascade structures*, Hot Carriers in Semiconductors XI (HCIS) in Kyoto, Japan, July 1999 (oral)
- F. Eickemeyer, R. A. Kaindl, M. Woerner, T. Elsaesser, S. Barbieri, P. Kruck, C. Sirtori, and J. Nagle, *Untersuchung der elektrisch induzierten optischen Verstärkung in einer GaAs/AlGaAs Quantenkaskadenstruktur*, DPG Frühjahrstagung in Regensburg, Germany, April 2000 (oral)
- F. Eickemeyer, R. A. Kaindl, M. Woerner, and A. M. Weiner, *Coherently controlled shaping of ultrafast electric field transients in the mid-infrared*, Conference on Lasers and Electro-Optics (CLEO) in San Francisco, USA, May 2000 (oral)
- F. Eickemeyer, R. A. Kaindl, M. Woerner, T. Elsaesser, S. Barbieri, P. Kruck, C. Sirtori, and J. Nagle, *Field-enhanced optical amplification in GaAs/AlGaAs quantum cascade structures*, Conference on Lasers and Electro-Optics (CLEO) in San Francisco, USA, May 2000 (poster)
- F. Eickemeyer, R. A. Kaindl, M. Woerner, and A. M. Weiner, *Coherently controlled shaping of ultrafast electric-field transients in the mid-infrared*, Ultrafast Phenomena XII in Charleston, USA, July 2000 (oral)
- F. Eickemeyer, R. A. Kaindl, M. Woerner, and A. M. Weiner, *Towards arbitrary shaping of mid-infrared pulses*, International Terahertz Workshop (ITW2000) in Sandbjerg Estate, Denmark, September 2000 (oral)
- M. Woerner, F. Eickemeyer, A. M. Weiner, T. Elsaesser, R. Hey, and K. H. Ploog, *Coherent nonlinear propagation of ultrafast electric field transient through intersubband resonances*, Conference on Lasers and Electro-Optics (CLEO) in Baltimore, USA, May 2001 (oral)
- M. Woerner, R. A. Kaindl, F. Eickemeyer, K. Reimann, T. Elsaesser, R. Hey, and K. Ploog, *Ultrafast coherent nonlinear dynamics of intersubband excitations in a quasi-two-dimensional electron gas*, 10th International Conference on Modulated Semiconductor Structures (MSS) in Linz, Austria, July 2001 (oral)
- F. Eickemeyer, K. Reimann, M. Woerner, T. Elsaesser, S. Barbieri, C. Sirtori, *Ultrafast coherent electron transport in GaAs/AlGaAs quantum cascade structures*, Alaska Meeting on Fundamental Optical Processes in Semiconductors, Girdwood, USA, August 2001 (invited)
- F. Eickemeyer, K. Reimann, M. Woerner, T. Elsaesser, S. Barbieri, C. Sirtori, *Ultrafast coherent electron transport in GaAs/AlGaAs quantum cascade structures*, Hot Carriers in Semiconductors XII (HCIS) in Santa Fe, USA, August 2001 (invited)
- F. Eickemeyer, K. Reimann, M. Woerner, T. Elsaesser, S. Barbieri, C. Sirtori, G. Strasser, T. Müller, R. Bratschitsch, and K. Unterrainer, *Ultrafast coherent electron transport in quantum cascade structures*, Workshop “Light Emitters Based on Intersubband Transitions”of the DFG-Forschergruppe in Berlin, Germany, February 2002 (oral)

- F. Eickemeyer, K. Reimann, M. Woerner, T. Elsaesser, S. Barbieri, C. Sirtori, G. Strasser, T. Müller, R. Bratschitsch, and K. Unterrainer, *Ultrafast coherent electron transport in quantum cascade structures*, Ultrafast Phenomena XIII in Vancouver, Canada, May 2002 (oral)
- F. Eickemeyer, K. Reimann, M. Woerner, T. Elsaesser, S. Barbieri, C. Sirtori, G. Strasser, T. Müller, R. Bratschitsch, and K. Unterrainer, *Ultrafast coherent electron transport in quantum cascade laser structures*, Conference on Lasers and Electro-Optics (CLEO) in Long Beach, USA, May 2002 (oral)
- F. Eickemeyer, K. Reimann, M. Woerner, T. Elsaesser, S. Barbieri, C. Sirtori, G. Strasser, T. Müller, R. Bratschitsch, and K. Unterrainer, *Ultrafast gain dynamics in quantum cascade laser structures*, 26th International Conference on the Physics of Semiconductors (ICPS) in Edinburgh, UK, July/August 2002 (oral)

Acknowledgement

The research work described in this thesis was carried out at the Max-Born-Institute for Nonlinear Optics and Short Pulse Spectroscopy in Berlin. In particular I wish to thank Prof. Dr. T. Elsässer who allowed me to work in his group. He has initiated the international collaborations which were indispensable in the success of this thesis.

Many thanks to Dr. Michael Wörner for his excellent supervising, the innumerable fruitful discussions, the friendly working atmosphere, and the critical reading of the manuscript. I am grateful to Prof. Dr. Klaus Reimann for many discussions and the careful reading of the manuscript. I want to thank Dr. Robert A. Kaindl introducing me into the lab-world of femtoseconds.

I am grateful to Dr. R. Hey and Prof. Dr. K. Ploog for growing the quantum well samples and their collaboration in the coherent control experiment.

Many thanks to Dr. Carlo Sirtori, Dr. Stefano Barbieri, Dr. J. Nagle, Dr. Peter Kruck, Dr. Shun-Chen Lee, Dr. Andreas Wacker, Dr. Rudolf Bratschitsch, Thomas Müller, Dr. Gottfried Strasser and Prof. Dr. Karl Unterrainer for the cooperation in the quantum cascade laser project.

I am grateful to Prof. Dr. A. M. Weiner for his support in the pulse shaping and the coherent control project.

I want to express my gratitude to the current and former members of the department including Valentina Emiliani, Francesca Intonti, Guillaume Cassabois, Matteo Rini, Jens Stenger, Kerstin Müller, Thomas Unold, and Roman Thiel for the nice working atmosphere. A particular thanks to Gabriele Kordass and Monika Tischer for the technical support. I am indebted to Margret Lehmann and Kathleen Triebler for the prompt settlement of any kind of administrative problem.

Last but not least, many thanks to B. Wunderle and T. Günther for the numerous Sunday brunch meetings, where the late-breaking topics in physics and non-physics were discussed.

Curriculum vitae

Name:	Felix Eickemeyer
Date and place of birth:	January 3rd 1973, Heidelberg
Nationality:	German

Education

1983–1992	Highschool “Hohenstaufengymnasium”, Bad Wimpfen, Germany
1993-1994	Physics major at TH Karlsruhe
1994-1997	Physics major at TU Dresden
1997-1998	Diploma thesis in the group of Prof. Dr. M. Wollenberg, Universität Leipzig Topic: *Über einfache kausale Netze auf der de Sitter Raum-Zeit*
March 1998	Diploma
since Sept. 1998	Ph. D. Student in the group of Prof. Dr. T. Elsässer, Max-Born-Institut, Berlin

Selbständigkeitserklärung

Hiermit erkläre ich, die vorliegende Arbeit selbständig ohne fremde Hilfe verfaßt zu haben und nur die angegebene Literatur und Hilfsmittel verwendet zu haben.

Felix Eickemeyer
27. Mai 2002